

ZZ PRODUCTION IN PROTON-PROTON COLLISIONS AT
 $\sqrt{s} = 13$ TeV IN FOUR-LEPTON EVENTS USING THE
CMS DETECTOR AT THE CERN LHC

by

Nathaniel Woods

A dissertation submitted in partial fulfillment of
the requirements for the degree of

Doctor of Philosophy
(Physics)

at the
UNIVERSITY OF WISCONSIN – MADISON
2017

Defended on X October 2017

Dissertation approved by the following members of the Final Oral Committee:

Wesley Smith · Bjorn Wiik Professor of Physics
Sridhara Dasu · Professor of Physics
Matthew Herndon · Professor of Physics
Someone · Professor of Physics
Someone · Professor of Something

Abstract

Acknowledgements

Contents

Abstract	i
Acknowledgements	ii
Contents	iii
List of Figures	viii
List of Tables	xii
1 The Standard Model	1
1.1 Introduction	3
1.2 Matter and Forces	3
1.3 Electroweak Symmetry Breaking and the Higgs Boson	9
1.4 Diboson and Multiboson Physics	12
1.4.1 Vector Boson Scattering	16
1.5 Limitations and Possible Extensions	16
1.5.1 Anomalous Gauge Couplings	18
1.6 Proton-Proton Collisions	20
1.7 ZZ Measurements in Context	22
2 ZZ Phenomenology and Previous Results	24
2.1 Nonresonant ZZ/Z γ^* Production and Decay	25

2.1.1	Vector Boson Scattering	27
2.1.2	Prior Measurements	28
2.2	Resonant $ZZ^*/Z\gamma^*$ Production	34
2.2.1	Z Boson Decays to Four Leptons	35
2.2.2	Higgs Boson Production	35
2.2.2.1	Prior Measurements	36
2.3	Anomalous Gauge Couplings	38
2.3.1	Previous Limits	40
2.4	Background Processes	42
3	The CMS Experiment and the CERN LHC	44
3.1	The CERN Large Hadron Collider	44
3.1.1	Accelerator Chain, Layout, and Detectors	46
3.1.2	Operating Parameters	49
3.1.2.1	Design	50
3.1.2.2	Run I	51
3.1.2.3	Run II	52
3.2	The Compact Muon Solenoid Detector	53
3.2.1	Terminology and Geometry	54
3.2.2	Magnet and Inner Tracking System	55
3.2.2.1	Pixel Detector	58
3.2.2.2	Strip Tracker	59
3.2.3	Electromagnetic Calorimeter	59
3.2.4	Hadronic Calorimeter	61
3.2.5	Muon Spectrometer	63
3.2.5.1	Drift Tubes	64

3.2.5.2	Cathode Strip Chambers	65
3.2.5.3	Resistive Plate Chambers	66
3.2.6	Data Acquisition and Trigger	67
3.2.6.1	Level-1 Trigger	68
3.2.6.2	High-Level Trigger	70
3.2.7	Luminosity Determination	71
4	Simulation	74
4.1	Monte Carlo Event Generation	74
4.1.1	Matrix Element and Hard Process Generation	75
4.1.2	Parton Shower, Hadronization, and Underlying Event	76
4.1.3	Pileup Simulation	78
4.1.4	Samples Used in this Analysis	78
4.2	Detector Simulation	79
5	Object Reconstruction and Selection	82
5.1	Track Reconstruction and Vertex Identification	83
5.2	Particle Flow Reconstruction	85
5.2.1	PF Candidates	86
5.2.1.1	Muons	87
5.2.1.2	Electrons and Prompt Photons	88
5.2.1.3	Charged and Neutral Hadrons	88
5.2.2	Jets	89
5.2.3	Missing Transverse Energy	91
5.3	Object Identification and Selection	91
5.3.1	Electrons	92
5.3.2	Muons	94

5.3.3	Final State Photon Radiation	95
5.3.4	Jets	96
5.3.5	Misidentified Objects	96
5.4	ZZ Candidate and Event Selection	97
5.4.1	Z/γ^* Candidate Selection	98
5.4.2	ZZ Candidate Selection	99
5.4.3	Dijet and VBS Signal Selection	100
6	Analysis Strategy	101
6.1	Background Estimation	101
6.2	Systematic Uncertainties	104
6.3	Fiducial and Total Cross Section Calculation	106
6.3.1	Signal Strength Extraction	109
6.3.2	$Z \rightarrow 4\ell$ Branching Fraction	109
6.4	Differential Cross Sections	110
6.4.1	Unfolding	111
6.4.2	Uncertainties	112
6.5	VBS Signal Extraction	112
6.6	Anomalous Gauge Coupling Searches	114
7	Results	116
7.1	Four-Lepton Yields and Inclusive Cross Sections	117
7.1.1	Full Spectrum	117
7.1.2	$Z \rightarrow 4\ell$ Resonance	117
7.1.3	Higgs Resonance	122
7.1.4	ZZ Production	123
7.2	Differential Cross Sections	133

7.3	Vector Boson Scattering	135
7.4	Anomalous Coupling Limits	135
8	Conclusions	153
8.1	Summary	153
8.2	Outlook	155
	Bibliography	157

List of Figures

1.1	Triple gauge boson coupling vertex	13
1.2	Quartic gauge boson coupling vertex	14
1.3	Higgs couplings to the gauge bosons	14
1.4	Higgs self couplings	15
1.5	Tree level Feynman diagrams for diboson production in fermion-anti-fermion collisions	15
1.6	Gluon-gluon fusion box diagram for general diboson production . . .	16
1.7	Unitarity violation in vector boson scattering without a Higgs boson	17
1.8	Neutral anomalous gauge coupling vertices	19
1.9	Neutral anomalous triple gauge coupling vertex	20
1.10	Parton distribution functions	22
2.1	Leading order $ZZ \rightarrow 4\ell$ production	26
2.2	Next-to-leading order $ZZ \rightarrow 4\ell$ production	27
2.3	Gluon-gluon fusion box diagram for $ZZ \rightarrow 4\ell$ production	28
2.4	Vector boson scattering diagrams	29
2.5	Measured $e^+e^- \rightarrow ZZ$ cross sections from OPAL.	30
2.6	Measured four-lepton mass spectrum from D0.	31
2.7	Measured four-lepton mass spectrum from CMS at $\sqrt{s} = 8$ TeV.	32

2.8	Measured four-lepton mass spectrum from ATLAS at $\sqrt{s} = 8$ TeV.	33
2.9	Feynman diagram for $Z \rightarrow 4\ell$ production	35
2.10	Higgs production mechanisms	37
2.11	Higgs boson SM cross section and branching ratio, as a function of m_H	38
2.12	Enhancements in p_T^Z and p_T^μ resulting from nonzero aTGCs	39
2.13	Lepton angular correlations resulting from nonzero aTGCs	40
2.14	Previous two-dimensional aTGC limits from CMS.	41
2.15	Example background diagrams	43
3.1	LHC dipole schematic	47
3.2	LHC accelerator and experiment layout	48
3.3	Integrated luminosity delivered to CMS in each LHC run period	52
3.4	CMS cutout schematic	54
3.5	Inner tracker layout	57
3.6	Tracker material budget in radiation lengths	58
3.7	ECAL geometry	60
3.8	HCAL geometry	62
3.9	Total material budget in nuclear interaction lengths	63
3.10	Muon system geometry	64
3.11	Trigger data flow	71
4.1	Comparison of data and simulation in e^+e^- events around the Z resonance	81
6.1	Misidentification rates for electrons and muons	103
7.1	Full four-lepton mass spectrum	118
7.2	Mass of all Z/γ^* candidates in the full spectrum selection	119

7.3	Mass of Z_1 candidates in the full spectrum selection	120
7.4	Scatter plot of m_{Z_2} vs. m_{Z_1} for data events in the full spectrum selection	121
7.5	Four-lepton mass in the $Z \rightarrow 4\ell$ selection	122
7.6	Scatter plot of m_{Z_2} vs. m_{Z_1} for data events in the $Z \rightarrow 4\ell$ selection .	123
7.7	Four-lepton mass spectrum around the Higgs resonance	124
7.8	Mass of Z_1 candidates in events near the Higgs resonance	125
7.9	Mass of Z_2 candidates in events near the Higgs resonance	126
7.10	Scatter plot of m_{Z_2} vs. m_{Z_1} for data events near the Higgs resonance	127
7.11	Four-lepton mass spectrum for events with both Z candidates on-shell	128
7.12	Mass of all Z/γ^* candidates in the on-shell selection	129
7.13	Jet multiplicity	130
7.14	Transverse momentum of the leading and subleading jets	131
7.15	Pseudorapidity of the leading and subleading jets	131
7.16	Dijet invariant mass	132
7.17	Dijet pseudorapidity separation	133
7.18	Total ZZ cross section as a function of center-of-mass energy	134
7.19	Normalized differential ZZ cross section as a function of four-lepton invariant mass	136
7.20	Normalized differential ZZ cross section as a function of four-lepton system p_T	137
7.21	Normalized differential ZZ cross section as a function of Z boson candidate p_T	138
7.22	Normalized differential ZZ cross section as a function of leading lepton p_T	139
7.23	Normalized differential ZZ cross section as a function of ΔR between the Z bosons	140

7.24	Normalized differential ZZ cross section as a function of $\Delta\phi$ between the Z bosons	141
7.25	Normalized differential ZZ cross section as a function of jet multiplicity	142
7.26	Normalized differential ZZ cross section as a function of dijet invariant mass	143
7.27	Normalized differential ZZ cross section as a function of dijet pseudorapidity separation	144
7.28	Normalized differential ZZ cross sections as functions of leading and subleading jet transverse momentum	145
7.29	Normalized differential ZZ cross sections as functions of leading and subleading jet pseudorapidity	146
7.30	Normalized differential four-lepton cross section as a function of four-lepton invariant mass with loosened Z mass cuts	147
7.31	VBS signal extraction GBDT output	148
7.32	ZZ invariant mass distribution with example aTGC working points .	149
7.33	Asymptotic one- and two-dimensional aTGC limits at 95% confidence level	150
7.34	One-dimensional aTGC limits as a function of the maximum ZZ invariant mass used in the calculation	151
7.35	ZZ invariant mass distribution for dijet events, with example aQGC working points	152

List of Tables

1.1	Particle content of the standard model	5
3.1	LHC beam parameters	51
6.1	Systematic uncertainties on the total yield	106
6.2	Fiducial phase space definitions	108
7.1	Expected and observed yields for $Z \rightarrow 4\ell$ production.	119
7.2	Expected and observed yields for Higgs boson production.	124
7.3	Expected and observed yields for doubly-resonant ZZ production.	127

⁰ Chapter 1

¹ The Standard Model

2 The mission of fundamental particle physics is an audacious one. An exercise in
3 reductionism taken to its logical extreme, the goal of the field is to find the minimal set
4 of mathematical precepts that underlie all interactions of matter and energy and from
5 which everything else in the universe is, in principle, an emergent property. Despite
6 the loftiness of its goals, the program has been extraordinarily successful, yielding
7 the standard model (SM), a remarkable theory which is elegant in its mathematical
8 formulation yet expansive and powerful in its predictions, most of which have been
9 verified in exquisite detail. Calculations done in the framework of the SM have
10 matched data within the precision of essentially every experiment over roughly four
11 decades, making it arguably the best-confirmed theory in the history of science. It is
12 generally believed to be self-consistent; future advances will likely add to it, explain
13 its free parameters, or find some deeper underlying structure, not contradict it.

14 And yet work remains. There are a few known phenomena that the SM does not
15 cover, and some of its features seem for now to be surprising coincidences (see Sec-
16 tion 1.5). One area of particular interest is the physics of the electroweak interaction,
17 which was the last piece to fall into place. Its final major component, the existence of

18 the Higgs boson, was definitively confirmed only as recently as 2012 and some details
19 remain hazy or unverified, from an experimental perspective. These statements will
20 be explained and made more precise here in Chapter 1, which gives an overview of
21 the SM with a focus on its electroweak sector, and describes some of the shortcomings
22 that motivate continued searches for new physics even now that it is complete. Chap-
23 ter 1 also describes diboson and multiboson processes, interactions involving multiple
24 instances of the particles underlying electroweak physics, which are valuable tools for
25 understanding how the bosons interact with each other. This thesis presents several
26 studies of the ZZ diboson process, intended to illuminate the behavior of the neutral
27 part of electroweak interactions. In particular, the focus of this work is the case in
28 which two Z bosons each decay to a pair of charged leptons. Such events are rare but
29 experimentally appealing. Two of the three charged leptons, electrons (e) and muons
30 (μ) can be reconstructed with high precision, and few physics processes aside from
31 ZZ result in four-lepton final states, so they provide an unmistakable experimental
32 signature that can be easily identified over small backgrounds. Details of ZZ physics
33 are described in Chapter 2, along with a review of previous literature.

34 High-energy particle collisions in a laboratory provide a way to investigate ZZ pro-
35 duction and other fundamental interactions in a controlled setting. CERN’s Large
36 Hadron Collider (LHC), a proton-proton collider in tunnels running beneath the
37 Swiss-French border near Geneva, provides collisions at record-breaking energies and
38 rates, which are used by the Compact Muon Solenoid (CMS) detector to study dibo-
39 son processes in unprecedented detail. These apparatus are described in Chapter 3.
40 Accurate simulations of physics and particles’ interactions with the detector are vital
41 to obtaining valid results; this process is described in Chapter 4. Chapter 5 describes
42 how physics objects are built from the detector signals, and how those appropriate
43 for analysis are selected. The strategy for performing the ZZ measurements presented

44 in this thesis is given in Chapter 6. New studies of four-lepton events in a sample of
45 proton-proton collisions are presented in Chapter 7.

46 **1.1 Introduction**

47 The standard model is a set of several related theories that together describe matter
48 and its interactions at a fundamental level. The following sections give a general
49 overview of the SM and related topics that serve as background material for the
50 four-lepton processes described in more detail in subsequent chapters. This includes
51 discussions of the particle content of the SM and the gauge structure that leads to
52 particle interactions, the spontaneous symmetry breaking mechanism that leads to
53 the specific structure of the electroweak sector of the SM, diboson processes, and
54 the SM’s limitations and how they might be addressed. Some details are also given
55 about the proton-proton collisions used to probe particle interactions at high energies.
56 More complete information may be found in a number of texts, including Refs. [1–5].
57 Everything that follows uses units such that $c = \hbar = 1$, where c is the speed of light
58 and \hbar is the reduced Planck’s constant $\hbar = h/2\pi$.

59 **1.2 Matter and Forces**

60 In the SM, matter is made of fermions (particles with half-integer spin; all SM fun-
61 damental fermions have spin $\frac{1}{2}$) which interact by exchanging gauge bosons (integer
62 spin; spin 1 for the SM force carriers). Table 1.1 lists the fundamental particles and
63 some of their properties. With the exception of the neutral bosons, all particles have
64 a corresponding antiparticle which is the same except that all its quantum numbers
65 have opposite sign. The fermions come in two categories, leptons and quarks. All

66 the quarks and half the lepton types carry electric charge and are therefore subject
 67 to interactions through the electromagnetic force, described by quantum electrodyn-
 68 namics (QED) [2]. In a QED interaction, two charged particles exchange a photon,
 69 which carries the momentum transferred from one to the other. The photon is a
 70 spin-1 gauge boson that is massless and electrically neutral itself, explaining why
 71 electromagnetic forces are long-range.

72 There are six types of quarks which fall into three “generations:” up and down
 73 (u and d, first generation); charm and strange (c and s, second generation); and top
 74 and bottom (t and b, third generation)¹. Quark masses increase with each successive
 75 generation. Up-type quarks (u, c, t) have electric charge $+2/3$ (in units of the positron
 76 charge e) while down-type quarks have $-1/3$. Quarks are the building blocks of
 77 hadrons, including $q\bar{q}'$ bound states called mesons and $qq'q''/\bar{q}\bar{q}'\bar{q}''$ bound states called
 78 baryons, of which protons (uud) and neutrons (udd) are the most familiar. Top
 79 quarks are too heavy to form bound states; the toponium ($t\bar{t}$ meson) weak decay
 80 width is larger than the spacing between its energy levels and its mean lifetime is
 81 an order of magnitude shorter than its orbital period so no resonance may form [5].
 82 Hadrons are bound by the strong nuclear force, described by the theory of quantum
 83 chromodynamics (QCD).

84 The mediator for the strong force is the gluon, which like the photon is a massless
 85 spin-1 gauge boson. The analog of electric charge is “color”, a notion originally
 86 introduced [6] as an ad hoc explanation of how identical quarks could exist in the
 87 symmetric bound state of a hadron despite the Fermi exclusion principle and later
 88 found to be the charge underlying the strong force [1, 7]. Unlike electric charge,
 89 there are three types of color charge, typically called red, green, and blue, though
 90 these names are arbitrary². The analogy with visible color comes primarily from

¹Top and bottom quarks are sometimes called truth and beauty.

²Antiquarks carry negative color charges, typically called antired, antigreen and antiblue.

Table 1.1: The particles of the standard model, and some of their properties. All fermions have a corresponding antiparticle with opposite sign for all quantum numbers. Quarks and leptons are grouped by generation. Note that the listed T^3 (the measured component of the weak isospin, described below) applies only to left-handed fermions; right-handed fermions have $T^3 = 0$ and do not couple to the W^\pm (right-handed neutrinos, if they exist, do not couple to the Z either).

Particle	Mass (GeV)	Charge (e)	T^3	Gauge couplings
Scalar boson (spin 0)				
H	125	0		W^\pm, Z
Fermion (spin 1/2)				
u	0.023	+2/3	+1/2	g, γ, Z, W^\pm
d	0.048	-1/3	-1/2	g, γ, Z, W^\pm
e	5.11×10^{-4}	-1	+1/2	γ, Z, W^\pm
ν_e	$< 2.2 \times 10^{-9}$	0	-1/2	Z, W^\pm
c	1.28	+2/3	+1/2	g, γ, Z, W^\pm
s	0.95	-1/3	-1/2	g, γ, Z, W^\pm
μ	0.105	-1	+1/2	γ, Z, W^\pm
ν_μ	$< 1.7 \times 10^{-4}$	0	-1/2	Z, W^\pm
t	172	+2/3	+1/2	g, γ, Z, W^\pm
b	4.2	-1/3	-1/2	g, γ, Z, W^\pm
τ	1.77	-1	+1/2	γ, Z, W^\pm
ν_τ	< 0.018	0	-1/2	Z, W^\pm
Vector boson (spin 1)				
g	0	0	0	g
γ	0	0	0	W^\pm
Z	91.2	0	0	W^\pm
W^\pm	80.4	± 1	± 1	γ, Z, W^\pm

91 the heuristic that natural states must be “colorless,” i.e. a hadron may have equal
92 parts color and corresponding anticolor as in a meson, but it may also be “white,”
93 containing red, blue, and green in equal measures as in a baryon. This implies that
94 a color charged object cannot exist on its own, a property known as confinement.

95 Confinement arises from the structure of QCD interactions and gluons themselves.
96 Among fermions, only quarks interact through the strong force, but gluons also carry
97 color charge and interact with each other. Because gluons self-interact, have no dis-
98 tinct antiparticle, and are massless, they can split and radiate infinitely. The resulting
99 soft gluon interactions around quarks lead to an anti-screening effect that causes the
100 strength of the strong force to change as a function of the distance between interacting
101 quarks, with close quarks interacting less strongly as far as a single gluon exchange
102 is concerned. As quark separation gets larger, the potential energy of strong inter-
103 actions rises rapidly, until it is energetically favorable for the gluon connecting them
104 to split into a $q\bar{q}$ pair that screens them and effectively breaks off the interaction.
105 A single colored particle will thus cause more colored particles to be produced from
106 vacuum until only colorless bound states remain, enforcing confinement. This pro-
107 cess is known as hadronization, and causes single quarks or gluons leaving a hard
108 scattering interaction to produce “jets” of many hadrons, each carrying a fraction of
109 the original parton momentum, that enter the detector in a conical shower. This is
110 why a free quark has never been observed, and is not expected to be found, and why
111 the strong interaction is short-range even though gluons are massless. It is also why,
112 for example, $qq\bar{q}$ bound states are not seen in nature. Conversely, close-range QCD
113 is relatively feeble, leading to “asymptotic freedom,” the property of partons within
114 hadrons that they may be considered independent in high-energy collisions, because
115 their interactions are weak enough that bound state effects may be neglected (see
116 Section 1.6).

117 Leptons may be electrically charged or neutral, and come in three generations,
118 each containing one lepton of each type, a charged lepton and a corresponding neu-
119 trino. In order of charged lepton mass, the generations are the electron and its
120 neutrino (e and ν_e), muon and its neutrino (μ and ν_μ), and tau and its neutrino (τ
121 and ν_τ). Taus decay quickly, with a mean lifetime of 2.9×10^{-13} s in their rest frame;
122 muons also decay, but their lifetime ($2.2 \mu\text{s}$) is long compared to other time scales
123 involved in particle collider experiments, so they are considered stable particles for
124 the purposes of this work. Neutrinos are known to have mass [8–10], and the masses
125 are known to be small but they have not been measured. All leptons and quarks
126 interact via the weak nuclear force, which is best known for causing the nuclear beta
127 decay reaction $n \rightarrow p + e^- + \bar{\nu}_e$. Neutrinos are notable for coupling to the rest of the
128 SM only through weak interactions, making them difficult to detect in practice. De-
129 tectors at particle colliders make no attempt to detect neutrinos, and their presence
130 is inferred only through the apparent momentum imbalance resulting from the fact
131 that they are not detected.

132 The weak force operates through two mechanisms, charged-current and neutral-
133 current interactions. Neutral-current interactions proceed through exchange of a Z
134 boson, an electrically neutral spin-1 mediator, and are analogous to electromagnetic
135 interactions except for two important differences. Unlike the γ , the Z has mass—in
136 fact, one of the largest known masses at 91 GeV [11]—giving it longitudinal polariza-
137 tion modes [2] and limiting the range of the force because it decays with a halflife on
138 the order of 10^{-25} s [11]. Also unlike QED, weak interactions do not respect parity
139 (P) symmetry. The Z boson couples more strongly to left-handed fermions (those
140 with helicity opposite their direction of motion) and right-handed antifermions than
141 to their opposite-spin counterparts. The degree of asymmetry varies by fermion type;
142 notably, the Z does not couple at all to right-handed neutrinos. Neutral-current inter-

143 actions are still symmetric under combined charge conjugation (C) and parity (CP)
 144 transformations, because processes that are odd under P are also odd under C.

145 Charged-current interactions proceed through exchange of an electrically charged
 146 boson, the W^\pm , which has a mass around 80 GeV [11]. Leptons couple to W^- bosons
 147 in $\ell^-, \bar{\nu}_\ell$ pairs (W^+ bosons likewise with their antiparticles), causing μ and τ decays.
 148 Lepton flavor is conserved in the sense that charged leptons couple to the W only in
 149 conjunction with the (anti-)neutrino from the same generation, so the total lepton
 150 number $N_\ell = n_{\ell^-} - n_{\ell^+} + n_{\nu_\ell} - n_{\bar{\nu}_\ell}$, where n_X is the number of X particles in existence,
 151 is conserved separately for $\ell \in (\text{e}, \mu, \tau)$. Flavor conservation does not hold for quarks
 152 undergoing charged weak interactions. An up-type quark always couples to the W
 153 in conjunction with a down-type quark, as it must to obey conservation of electric
 154 and color charge. The pairings are in general described by a unitary 3×3 matrix
 155 known as the Cabibbo–Kobayashi–Maskawa (CKM) matrix which defines the inter-
 156 generational mixing [12, 13]. Flavor-changing currents allow heavy quarks to decay
 157 to lighter ones, and are thus responsible for the decay of hadrons that do not contain
 158 the $q\bar{q}$ pair necessary for strong or electromagnetic decays.

159 Charged-current interactions also do not respect parity symmetry, and in fact are
 160 maximally parity violating: the W couples only to left-handed fermions and right-
 161 handed antifermions. Because neutrinos interact only through the weak force³, and
 162 the Z also couples only to left-handed neutrinos, it is not clear that right-handed
 163 neutrinos even exist. If they do, they have no way to interact with other matter and
 164 they are not part of the SM. Unlike neutral-current interactions, charged-current
 165 interactions violate CP symmetry at a small but measurable rate. CP violation
 166 was first observed in neutral kaon mixing before the theory of the weak force was
 167 fully worked out [14]. After flavor-changing charged currents were formalized it was

³Aside from gravity, presumably, but this interaction is not experimentally accessible and is not covered by the standard model.

168 realized that CP violation could arise from a complex phase in the CKM matrix,
 169 which arises in models with at least three generations of quarks⁴ [13]. CP violation
 170 was subsequently confirmed by observation in a number of meson decays [15–20].

171 The quantum number analogous to electric charge and color charge for the weak
 172 interaction is the three-component weak isospin T^i , which is typically defined such
 173 that the measured component is T^3 . Left-handed fermions have $|T| = \frac{1}{2}$, the W^\pm
 174 has $|T| = \pm 1$, and all other particles have $|T| = 0$. Weak isospin is conserved in all
 175 electromagnetic, strong, and fermion-fermion weak interactions, but is not conserved
 176 in general because the Higgs boson (see below) carries weak isospin. Electric charge
 177 is always conserved, and is related to the measured component of the weak isospin
 178 by the weak hypercharge Y , which is

$$Y = 2(Q - T^3), \quad (1.1)$$

179 where Q is the electric charge. This connection between the electromagnetic and
 180 weak forces, and the parallels between the weak neutral-current interaction and QED
 181 hint at the intriguing possibility that the two forces could be unified under a single
 182 theory, but important differences—in particular, boson mass—must be explained.
 183 The mechanism for this is called electroweak symmetry breaking.

184 1.3 Electroweak Symmetry Breaking and the 185 Higgs Boson

186 The structures of the fundamental forces arise from symmetries in the underlying
 187 fields, specifically gauge invariance of the relevant terms in the SM Lagrangian. Much
 188 of the phenomenology of QCD, for example, arises from the SU(3) symmetry of

⁴At the time, only the first two generations were known, so the observed CP asymmetry was taken as an early indication of the existence of top and bottom quarks.

189 invariance under local color phase transformations, and the fact that the symmetry
 190 is non-Abelian (i.e. the transformation operators do not commute). Charges are
 191 the generators of the relevant symmetry group, the conserved currents of Noether's
 192 first theorem [21]. A full treatment of the SM's symmetry group structure and its
 193 connections to the theory's phenomenology is given in a number of books, including
 194 Refs. [2, 4, 5, 22]. The relevant point here is that the weak force arises from an $SU(2)$
 195 symmetry generated by the weak isospin T , and the electromagnetic force from a
 196 $U(1)$ symmetry generated by the electric charge Q , so a unified electroweak force
 197 should obey an $SU(2)_L \times U(1)$ symmetry, where the L indicates that only left-handed
 198 fermions transform under the $SU(2)$ symmetry. The resulting unified electroweak
 199 theory is known as the Glashow–Weinberg–Salam (GWS) model [23–25].

200 An unbroken $SU(2)_L \times U(1)$ symmetry implies four massless vector gauge fields:
 201 a triplet $W_\mu^i (i \in 1, 2, 3)$ which couple to fields with weak isospin (but only for left-
 202 handed particles), and a singlet B_μ which couples to weak hypercharge currents. This
 203 looks like the weak and electromagnetic forces discussed above, except that the weak
 204 gauge fields are massless and all three weak bosons are maximally P-violating. The
 205 gauge bosons can be given mass if the underlying symmetry is somehow broken in the
 206 theory's vacuum state. Symmetry breaking occurs via the Higgs mechanism⁵ [26–28],
 207 which introduces an isospin doublet of complex scalar fields

$$\phi = \begin{pmatrix} \phi^+ \\ \phi^0 \end{pmatrix}, \quad (1.2)$$

208 with a Lagrangian of the form

$$\mathcal{L}_H = (D_\mu \phi)^\dagger (D^\mu \phi) + \mu^2 \phi^\dagger \phi - \lambda^2 (\phi^\dagger \phi)^2 \quad (1.3)$$

⁵The Higgs mechanism is also called the Englert–Brout–Higgs–Guralnik–Hagen–Kibble mechanism to acknowledge more of the theorists who developed it, with Anderson and 't Hooft sometimes included as well.

209 where μ and λ are nonzero real numbers, D_μ is the covariant derivative invariant
 210 under $SU(2)_L \times U(1)_Y$,

$$D_\mu = \partial_\mu + igT_iW_\mu^i + i\frac{g'Y}{2}B_\mu, \quad (1.4)$$

211 and g and g' are the W_μ^i and B_μ coupling strengths. Because the potential in Eq. (1.3)
 212 is not minimized at 0, for small excitations around the vacuum expectation value
 213 (VEV) $v = \frac{\mu}{2\lambda} = 246$ GeV, in appropriately chosen coordinates, the doublet of com-
 214 plex scalar fields is reduced to

$$\phi = \frac{1}{\sqrt{2}} \begin{pmatrix} 0 \\ v + h(x) \end{pmatrix}. \quad (1.5)$$

215 Substituting Eq. (1.5) into Eq. (1.3) introduces mixing terms between the W_μ^i ,
 216 B_μ , and h fields. The new Lagrangian has mass eigenstates

$$\begin{aligned} W_\mu^\pm &= \frac{1}{\sqrt{2}} (W_\mu^1 \mp W_\mu^2) \\ Z_\mu &= \frac{gW_\mu^3 - g'B_\mu}{\sqrt{g^2 + g'^2}} = W_\mu^3 \cos \theta_W - B_\mu \sin \theta_W \\ A_\mu &= \frac{g'W_\mu^3 + gB_\mu}{\sqrt{g^2 + g'^2}} = W_\mu^3 \cos \theta_W + B_\mu \sin \theta_W \end{aligned} \quad (1.6)$$

217 where θ_W is the Weinberg electroweak mixing angle

$$\tan \theta_W = \frac{g'}{g}. \quad (1.7)$$

218 The newly defined fields are the gauge fields for the weak and electromagnetic forces,
 219 and in this basis, the Lagrangian has terms

$$\mathcal{L}_{m_V} = -\frac{v^2 g^2}{4} W_\mu^+ W^{-\mu} - \frac{v^2(g^2 + g'^2)}{8} Z_\mu Z^\mu, \quad (1.8)$$

220 which imply boson masses

$$\begin{aligned} m_W &= \frac{1}{2}vg \\ m_Z &= \frac{1}{2}v\sqrt{g^2 + g'^2} \end{aligned} \quad (1.9)$$

$$m_A = m_\gamma = 0,$$

221 and

$$\cos \theta_W = \frac{m_W}{m_Z}. \quad (1.10)$$

222 The original Higgs doublet in Eq. (1.2) had four degrees of freedom (two complex
 223 scalars), of which only one remains in the final Higgs field $H = h - v$, which is now
 224 a physical field with a corresponding massive scalar boson. The other three became
 225 the longitudinal polarization modes of the vector bosons.

226 Electroweak symmetry breaking thus explains the observed structure of the elec-
 227 tromagnetic and weak forces. Three bosons become massive, while one stays mass-
 228 less. Because the photon is massless, the theory retains the $U(1)_{EM}$ gauge symmetry
 229 observed in electromagnetic interactions and electric charge is conserved, while the
 230 $SU(2)$ symmetry is broken and its generator T^i is not. The W^\pm bosons still couple
 231 only to left-handed fermions, while the Z couples right- and left-handed fermions but
 232 not equally. The nonzero VEV even gives a convenient mechanism for generation of
 233 fermion masses in Yukawa couplings with Lagrangian terms of the form

$$\mathcal{L}_{m_f} = \sqrt{2} \frac{m_f}{v} (\bar{f}_L f_R + \bar{f}_R f_L). \quad (1.11)$$

234 It also controls off-diagonal terms in the Lagrangian that cause interactions between
 235 the electroweak bosons, the primary focus of this research.

236 1.4 Diboson and Multiboson Physics

237 In addition to the previously discussed boson mass terms introduced into the SM
 238 Lagrangian by electroweak symmetry breaking, boson interaction terms appear for
 239 trilinear gauge boson couplings

$$\begin{aligned} \mathcal{L}_{WWV} = & -ig [(W_{\mu\nu}^+ W^{-\mu} - W^{+\mu} W_{\mu\nu}) (A^\nu \sin \theta_W - Z^\nu \cos \theta_W) \\ & + W_\nu^- W_\mu^+ (A^{\mu\nu} \sin \theta_W - Z^{\mu\nu} \cos \theta_W)], \end{aligned} \quad (1.12)$$

240 which results in the vertices shown in fig 1.1; quartic gauge couplings

$$\begin{aligned}\mathcal{L}_{WWVV} = & -\frac{g^2}{4} \left\{ \left[2W_\mu^+ W^{-\mu} + (A_\mu \sin \theta_W - Z_\mu \cos \theta_W)^2 \right]^2 \right. \\ & - [W_\mu^+ W_\nu^- + W_\nu^+ W_\mu^- \\ & \left. + (A_\mu \sin \theta_W - Z_\mu \cos \theta_W) (A_\nu \sin \theta_W - Z_\nu \cos \theta_W) \right]^2 \left. \right\},\end{aligned}\quad (1.13)$$

241 (Fig. 1.2); Higgs couplings to the massive vector bosons

$$\mathcal{L}_{HV} = \left(g m_W H + \frac{g^2}{4} H^2 \right) \left(W_\mu^+ W^{-\mu} + \frac{Z_\mu Z^\mu}{2 \cos^2 \theta_W} \right), \quad (1.14)$$

242 (Fig. 1.3); and Higgs self-interactions

$$\mathcal{L}_{HH} = -\frac{g m_H^2}{4 m_W} H^3 - \frac{g^2 m_H^2}{32 m_W^2} H^4, \quad (1.15)$$

243 (Fig. 1.4).

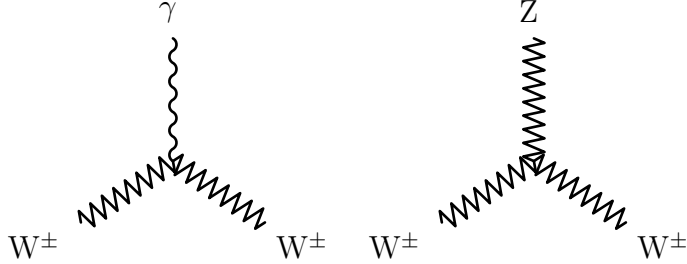


Figure 1.1: Vertex for the trilinear gauge boson couplings allowed at tree level in the SM.

244 The structure of the interactions shown in Figs. 1.1–1.4 depends on the details
 245 of the GWS model and spontaneous symmetry breaking, making multiboson interac-
 246 tions excellent probes of the SM electroweak and Higgs sectors. One can confirm the
 247 basic validity of the Higgs mechanism by observation of a Higgs boson, and its inter-
 248 actions with the massive gauge bosons can be probed in decays to ZZ* and W±W±*,
 249 which were in fact used in its discovery (see Section 2.2.2.1). The SM makes a num-
 250 ber of other testable predictions about the behavior of the electroweak bosons, the

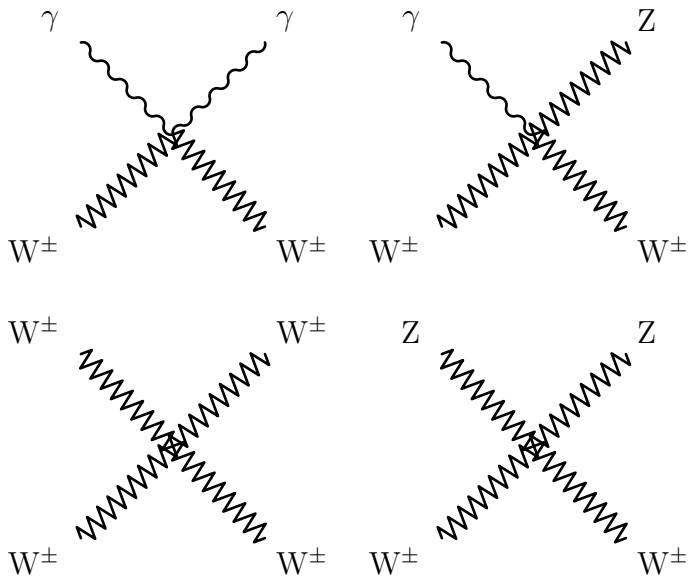


Figure 1.2: Vertices for the quartic gauge boson couplings allowed at tree level in the SM.

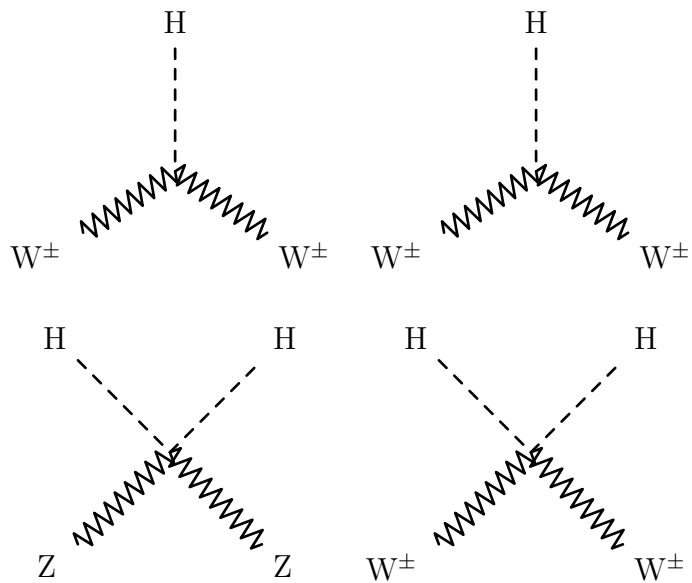


Figure 1.3: Vertices for Higgs boson couplings to gauge bosons allowed at tree level in the SM.

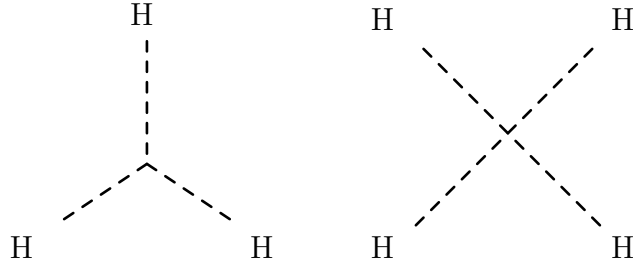


Figure 1.4: Higgs boson trilinear and quartic self-coupling vertices.

most easily testable of which are the multiboson production cross sections, i.e. the rates at which particle collisions result in final states with two or more electroweak gauge bosons. The tree-level diagrams for general diboson production in fermion-antifermion collisions ($f\bar{f} \rightarrow VV$) are shown in Fig. 1.5. The cross section for such a process will be strongly dependent on the gauge bosons' couplings to fermions, in the first diagram in Fig. 1.5, and their couplings to other gauge bosons in the second diagram (which does not contribute at all for neutral gauge bosons in the SM). Diboson production in gg collisions does not occur at tree level but may proceed through a quark loop as in the so-called box diagram of Fig. 1.6.

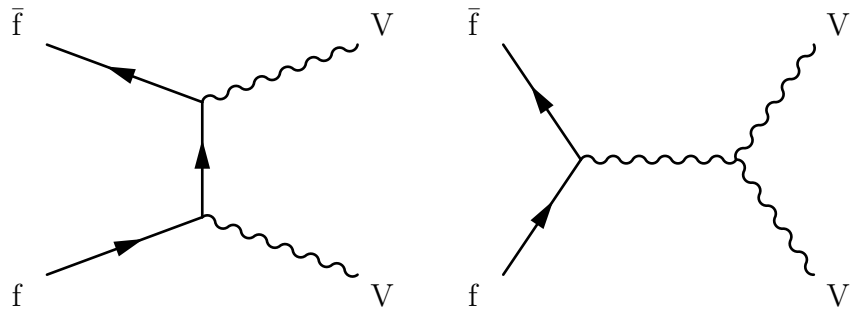


Figure 1.5: Tree-level Feynman diagrams for diboson production in fermion-antifermion collisions. The second diagram does not contribute for neutral gauge bosons in the SM.

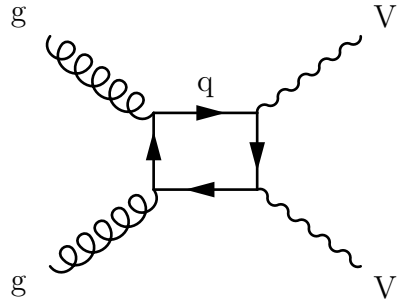


Figure 1.6: Leading order “box” diagram for diboson production through a quark loop in a gluon-gluon fusion event.

260 1.4.1 Vector Boson Scattering

261 Quasielastic vector boson scattering (VBS) interactions ($VV \rightarrow VV$) are sensitive
 262 to a number of features of the SM electroweak sector. If only the vector bosons are
 263 considered, the scattering amplitude for the process grows quadratically with the
 264 center-of-mass energy, violating unitarity [29]. Interference from diagrams involving
 265 the Higgs boson restores unitarity, as shown in Fig. 1.7. The VBS cross section is
 266 therefore sensitive to both the four-point gauge boson couplings of Fig. 1.2 and the
 267 structure of the Higgs field, and can be used to distinguish the SM from models
 268 without a Higgs boson and models with multiple particles that play its role.

269 1.5 Limitations and Possible Extensions

270 As noted above, the SM is believed to be fully self-consistent, but it has several notable
 271 omissions. It makes no mention of gravity, which is too weak to be probed at the
 272 level of individual particles at energies available in collider experiments. Neutrinos in
 273 the SM are massless, but they are found experimentally to oscillate between the three
 274 flavors in flight, which implies that the flavor eigenstates are not mass eigenstates,
 275 and thus that they have mass. Dark matter, the unidentified substance that makes up

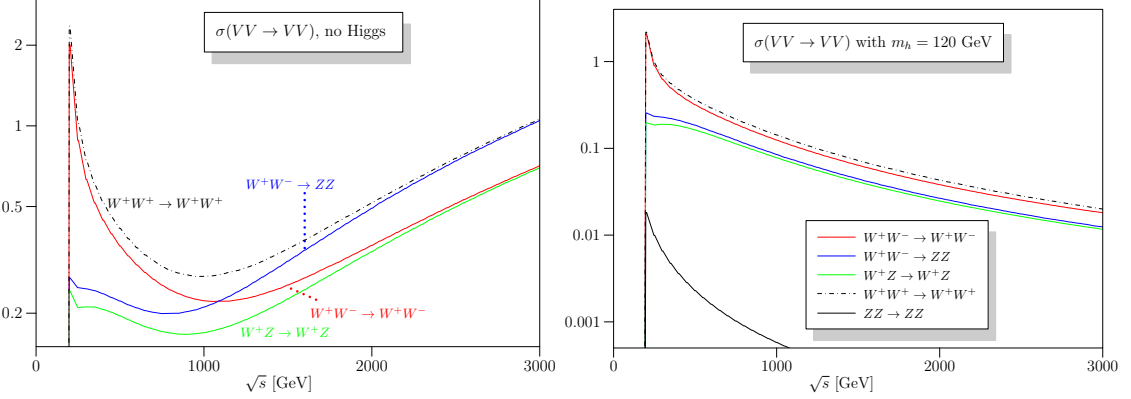


Figure 1.7: $VV \rightarrow VV$ scattering cross sections as a function of center-of-mass energy for the SM with no Higgs boson (left) and a Higgs boson with $m_H = 120$ GeV (right), reproduced from Ref. [29]. The model with no Higgs violates unitarity.

276 roughly 80% of the universe’s gravitationally interacting material [11, 30–32], is also
 277 not described. Some consider the SM to be “ad hoc” in the sense that the fermion
 278 masses, and a number of other parameters—19 in all—are completely unconstrained,
 279 and a more aesthetically satisfying theory would make predictions for all of them. A
 280 nicer theory would also offer thorough explanations for what seem now like remarkable
 281 coincidences. For example, the so-called hierarchy problem: it is intuitively surprising
 282 that the strengths of the fundamental forces vary by many orders of magnitude, and
 283 do so in such a way that large quantum corrections to the effective Higgs potential
 284 cancel almost exactly, causing the Higgs boson mass to be nonzero but much smaller
 285 than the scale of the corrections ($\mathcal{O}(10^{19} \text{ GeV})$) [33–35].

286 A number of theories have been proposed which modify or extend the SM [11,
 287 32], adding new symmetry groups, unifying the existing ones further, adding new
 288 particles, etc. A fourth generation of fermions would be a simple extension, but the
 289 fourth neutrino would have to have a mass more than half the Z boson mass to have
 290 escaped detection so far, which would be surprising given the small masses of the
 291 first three [11, 36]. Supersymmetric models, for example, posit a symmetry between

292 bosons and fermions, such that each particle would have a “superpartner” with the
 293 opposite spin statistics which would provide an opposite correction to the effective
 294 Higgs potential and thus a clean solution to the hierarchy problem [11, 37]. Despite
 295 extensive searches, no evidence of such models has been found [38].

296 1.5.1 Anomalous Gauge Couplings

297 Another simple extension to the SM would be a new force, with mediator gauge bosons
 298 analogous to the W and Z above the masses accessible at existing colliders. Such a
 299 force would originate from a previously undiscovered symmetry, which in many models
 300 could result from a higher symmetry which unifies all the fundamental forces at high
 301 energy but is broken and effectively reduces to the SM in the low-energy limit [11,
 302 33, 35, 39]. This, and several other possible extensions to the SM, would appear in
 303 practice as small deviations from the expected couplings of the gauge bosons. Such
 304 deviations from standard model interactions are called anomalous gauge couplings
 305 (aGC), and may involve anomalous trilinear (aTGC) or quartic (aQGC) vertices. Of
 306 particular interest here are the anomalous neutral couplings, which correspond to
 307 the vertices shown in Fig. 1.8. These interactions are forbidden in the SM. Their
 308 existence would increase the cross section for diboson production, and affect the cross
 309 section for $ZZ \rightarrow ZZ$ scattering, changing the requirements on the Higgs field needed
 310 to preserve unitarity.

311 Several theoretical frameworks exist for describing aGCs. For aTGCs, we use the
 312 effective Lagrangian approach described in Ref. [40–42]. In this parameterization, a
 313 ZZV coupling (where V may be Z or γ) has a vertex function corresponding to the
 314 vertex shown in Fig. 1.9 of the form

$$\Gamma_V^{\alpha,\beta,\delta}(q_1, q_2, P) = i \frac{\hat{s} - m_V^2}{m_Z^2} (f_4^V (P^\alpha g^{\delta\beta} + P^\beta g^{\delta\alpha}) + f_5^V \varepsilon^{\delta\alpha\beta\lambda} (q_1 - q_2)_\lambda), \quad (1.16)$$

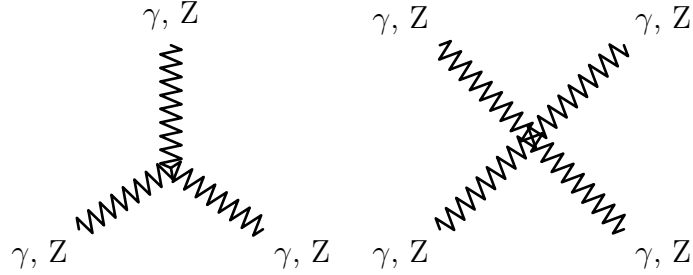


Figure 1.8: Fully-neutral gauge coupling vertices, for aTGCs (left) and aQGCs (right). These are forbidden in the SM.

315 where \hat{s} is the center of mass energy squared, $g^{\mu\nu}$ is the Minkowski metric and $\varepsilon^{\alpha\beta\gamma\delta}$ is
 316 the fully antisymmetric tensor with $\varepsilon^{0123} = 1$. Neutral aTGCs are then described by
 317 two parameters $f_4^{\gamma,Z}$ associated to CP-odd terms and two parameters $f_5^{\gamma,Z}$ associated
 318 to CP-even terms.⁶ The effective Lagrangians in use here are taken to be low-energy
 319 approximations invalid at high energy, and are not unitary at high $\sqrt{\hat{s}}$. In some
 320 previous literature (see Section 2.3.1), unitarity is enforced with a generalized dipole
 321 form factor [42, 43], such that the vertex factor takes an energy dependence,

$$f_i^V(\hat{s}) = \frac{f_{i,0}^V}{(1 + \hat{s}/\Lambda^2)^n}, \quad (1.17)$$

322 where Λ is the energy scale of the new physics process. No such form factor is applied
 323 in this work, to avoid adding unnecessary model dependence, so Λ is taken to be much
 324 larger than the energies accessible in the experiment and no form factor is applied.

325 For aQGCs, we adopt an effective field theory approach [44] which parameterizes
 326 the effects of new physics as a set of field operators [45]. The operators are chosen to
 327 be dimension-8, because this is the lowest dimension that can yield neutral quartic
 328 couplings, and the lowest dimension that can produce a theory with aQGCs but no
 329 aTGCs. Out of the large class of operators which control aQGCs in general, ZZ VBS

⁶There are, of course, analogous terms for all anomalous VVV couplings, where V may be any of the electroweak bosons, but only the ZZZ and ZZ γ terms are relevant to this work.

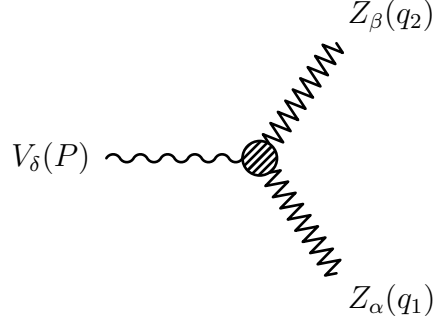


Figure 1.9: An anomalous neutral triple gauge coupling vertex, with momentum labels corresponding to Eq. (1.16).

330 is sensitive to five,

$$\begin{aligned}\mathcal{L}_{T0} &= \frac{f_{T0}}{\Lambda^4} \text{Tr} [\hat{W}_{\mu\nu} \hat{W}^{\mu\nu}] \times \text{Tr} [\hat{W}_{\alpha\beta} \hat{W}^{\alpha\beta}] \\ \mathcal{L}_{T1} &= \frac{f_{T1}}{\Lambda^4} \text{Tr} [\hat{W}_{\alpha\nu} \hat{W}^{\mu\beta}] \times \text{Tr} [\hat{W}_{\mu\beta} \hat{W}^{\alpha\nu}] \\ \mathcal{L}_{T2} &= \frac{f_{T2}}{\Lambda^4} \text{Tr} [\hat{W}_{\alpha\mu} \hat{W}^{\mu\beta}] \times \text{Tr} [\hat{W}_{\beta\nu} \hat{W}^{\nu\alpha}] \\ \mathcal{L}_{T8} &= \frac{f_{T8}}{\Lambda^4} B_{\mu\nu} B^{\mu\nu} B_{\alpha\beta} B^{\alpha\beta} \\ \mathcal{L}_{T9} &= \frac{f_{T9}}{\Lambda^4} B_{\alpha\mu} B^{\mu\beta} B_{\beta\nu} B^{\nu\alpha},\end{aligned}\tag{1.18}$$

331 where

$$\hat{W}_{\mu\nu} = \sum_j W_{\mu\nu}^j \frac{\sigma^j}{2},\tag{1.19}$$

332 and $\Lambda \gg \sqrt{s}$ is again the scale of the new physics causing the change in the effective
333 couplings.

334 1.6 Proton-Proton Collisions

335 Our experimental probe of all these interactions is proton-proton collisions. As dis-
336 cussed above, protons are bound states of three quarks (uud), known as the valence
337 quarks, held together by virtual gluon exchange. The proton constituents, quarks and
338 gluons, are collectively called partons. The gluons carry roughly half the total proton

339 momentum [2]. Because the number of gluons is not conserved, and they self-interact,
 340 the gluon structure of the proton is constantly evolving, and gluons produce virtual
 341 $q\bar{q}$ “sea quark” pairs which annihilate again on time scales of order $t_{virt} \sim 1/\Delta E$ [3].
 342 A sufficiently energetic color-charged particle colliding with a proton may therefore
 343 interact with any kind of quark or with a gluon, and interesting physics in a pp
 344 collision may be initiated by qq , $q\bar{q}$, qg , or gg scattering. A particle that scatters
 345 with a proton of energy P has a probability of interacting with a parton of a given
 346 type with momentum xP given by the parton distribution function (PDF) $f(x, Q^2)$,
 347 where x is the fraction of the proton momentum carried by the parton and Q is the
 348 momentum transfer of the interaction [3]. Heuristically, the PDF is a function of Q
 349 because it sets the wavelength of the mediating gauge boson and thus the scale on
 350 which the interaction can resolve constituent partons. PDFs are nonperturbative and
 351 have not been calculated from theory, so they are built from fits to experimental data
 352 from fixed-target and symmetric $e^\pm p$ deep inelastic scattering (DIS) data, and from
 353 hadron collider data [46]. The most recent PDFs from the NNPDF collaboration [46]
 354 are shown in Fig 1.10.

355 As mentioned previously, the rate at which a scattering process occurs is called its
 356 cross section σ , typically given in barns, a unit of area $b = 10^{-24} \text{ cm}^2$. The number
 357 of collisions is characterized by the luminosity \mathcal{L} such that the rate of events with
 358 final state X will be given by

$$\frac{dN_X}{dt} = \sigma(pp \rightarrow X) \mathcal{L} \quad (1.20)$$

359 as described in more detail in Section 3.1. If the initial protons each have momen-
 360 tum P and collide head on, such that their center-of-mass energy is $\sqrt{s} = 2P$, the
 361 interacting partons will have total energy $\sqrt{\hat{s}} = \sqrt{2x_1 x_2} P$ where x_1 and x_2 are the
 362 fraction of its proton’s momentum each incoming parton carried. The cross section

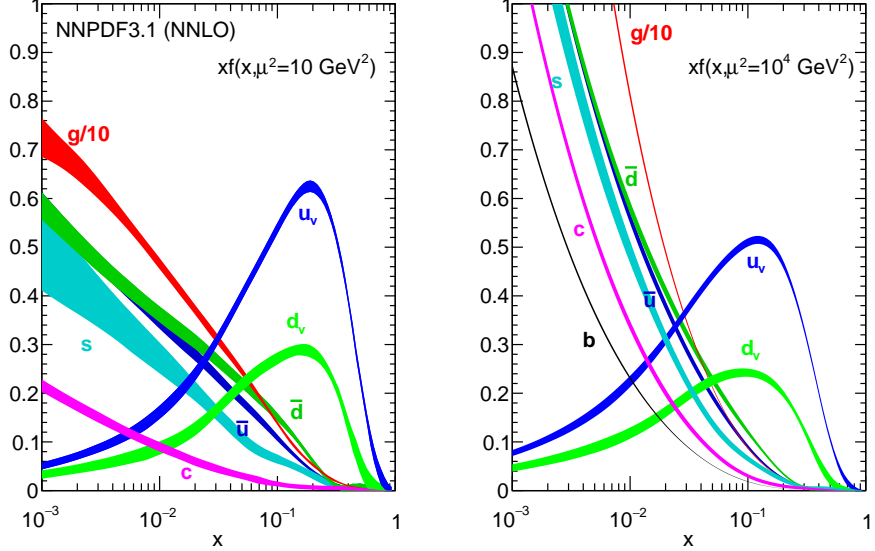


Figure 1.10: Parton distribution functions from NNPDF3.1, reproduced from Ref. [46], which used μ for the momentum transfer denoted Q in the text.

363 is given by

$$\sigma(\text{pp} \rightarrow X) = \sum_{p_1, p_2 \in q, \bar{q}, g} C_{p_1, p_2} \int dx_1 dx_2 f_{p_1}(x_1, Q^2) f_{p_2}(x_2, Q^2) \sigma_{\text{ME}}(p_1 + p_2 \rightarrow X), \quad (1.21)$$

364 where σ_{ME} is the matrix element-level cross section for the bare partons to scatter
 365 to final state X and C_{p_1, p_2} is a combinatoric factor based on the number of possible
 366 color combinations that varies based on the initial state particles p_1 and p_2 . This
 367 factorization into perturbative hard process physics and the nonperturbative PDF
 368 greatly simplifies calculations.

369 1.7 ZZ Measurements in Context

370 This is the context for the work described in the following chapters: the SM is in-
 371 complete, but it has been tested extensively and no discrepancies have been found

372 (a partial review of studies that did not exclude the SM can be found in Chapter 2).
373 Because the electroweak sector was the last to be confirmed experimentally and is
374 generally best explored at high energies, a number of aspects await detailed confir-
375 mation and remain a potential area where new physics might be found. This thesis
376 presents several studies of diboson events with $\ell^+\ell^-\ell'^+\ell'^-$ ($\ell, \ell' \in e, \mu$) final states
377 designed to probe the interactions of the neutral electroweak bosons. In particular,
378 as one can deduce from Eqs. (1.12)–(1.14), ZZ production processes are sensitive to
379 the details of the couplings between the gauge bosons and can therefore be used to
380 investigate the GWS model and the Higgs model and spontaneous symmetry break-
381 ing. Measurements of ZZ production have been made before, but measurements
382 in a new energy regime and with a very large dataset allow stringent new tests of
383 the SM and allow the potential observation of previously unseen phenomena within
384 and beyond it. The results presented here substantially expand our understanding
385 of ZZ production, with inclusive and differential cross section measurements at the
386 record-breaking center-of-mass energy of 13 TeV, the most precise measurement of
387 the $Z \rightarrow 4\ell$ branching fraction to date, and searches for vector boson scattering and
388 anomalous neutral gauge couplings.

⁰ Chapter 2

¹ ZZ Phenomenology and Previous ² Results

³ Four-lepton final states originate primarily from three physics processes: nonresonant
⁴ diboson production, resonant Higgs boson production which decays to ZZ^* , and res-
⁵ onant single-Z production. Multi-Z triboson production (WZZ and ZZZ) occurs at
⁶ negligible rates [47, 48]. Single-Z triboson production (WWZ) [48, 49] and $t\bar{t}Z$ pro-
⁷ duction result in final states with four prompt leptons, but are considered background
⁸ (see Section 2.4). The three signal processes can be distinguished by kinematics, such
⁹ as the four-lepton invariant mass distribution.

¹⁰ The signal processes all involve on- or off-shell Z bosons. The Z was first indirectly
¹¹ observed in 1973 when the Gargamelle bubble chamber experiment at CERN recorded
¹² an elastic muon antineutrino-electron ($\bar{\nu}_\mu + e^- \rightarrow \bar{\nu}_\mu + e^-$) scattering event [50]. Direct
¹³ observation in leptonic decays came roughly a decade later, from the UA1 experiment,
¹⁴ also at CERN [51]. Clean e^+e^- collisions at LEP and SLAC, where the center-of-mass
¹⁵ energy could be adjusted to produce Z bosons copiously, allowed its properties—and
¹⁶ a number of other parameters of the electroweak theory—to be measured with per-

17 mille precision or better [52]. Of particular importance to this study, the Z mass is
 18

$$m_Z = 91.1876 \pm 0.0021 \text{ GeV}, \quad (2.1)$$

19 its full width is

$$\Gamma_Z = 2.4952 \pm 0.0023 \text{ GeV}, \quad (2.2)$$

20 its width in leptonic decays is

$$\Gamma_Z(\ell^+ \ell^-) = 83.984 \pm 0.086 \text{ MeV}, \quad (2.3)$$

21 and it decays to a pair of charged leptons 3.3658% of the time for each lepton fla-
 22 vor [11].

23 **2.1 Nonresonant ZZ/Z γ^* Production and Decay**

24 Leading-order ZZ production is q \bar{q} -initiated and proceeds through *t*-channel quark
 25 exchange, as shown in Fig. 2.1. At next-to-leading order (NLO; several representative
 26 diagrams are shown in Fig. 2.2), production may have a gluon in the initial state
 27 and may have a quark or gluon in the final state which hadronizes and appears
 28 experimentally as a jet [53–55]. Next-to-next-to-leading order (NNLO) adds gluon-
 29 gluon fusion box diagrams (Fig. 2.3), as well as q \bar{q} -initiated production with two
 30 loops, one loop and a final state jet, and two jets [56, 57]. The NLO and NNLO
 31 corrections are generally large, outside the scale uncertainties of the calculations at
 32 previous orders, because diagrams with new initial states contribute only positively
 33 to the cross section. Quark-gluon scattering diagrams introduced at NLO and gluon-
 34 gluon fusion diagrams introduced at NNLO have large amplitudes—the gg \rightarrow ZZ
 35 process accounts for roughly 60% of the total NNLO correction, for example—due
 36 to the high effective gluon luminosity in multi-TeV proton collisions [56]. Because

37 of the box diagrams' large contribution, “NLO + gg” simulations are often used, in
 38 which NLO $q\bar{q}/qg/\bar{q}g \rightarrow ZZ$ and LO $gg \rightarrow ZZ$ samples are summed even though they
 39 formally contribute at different orders in α_s .

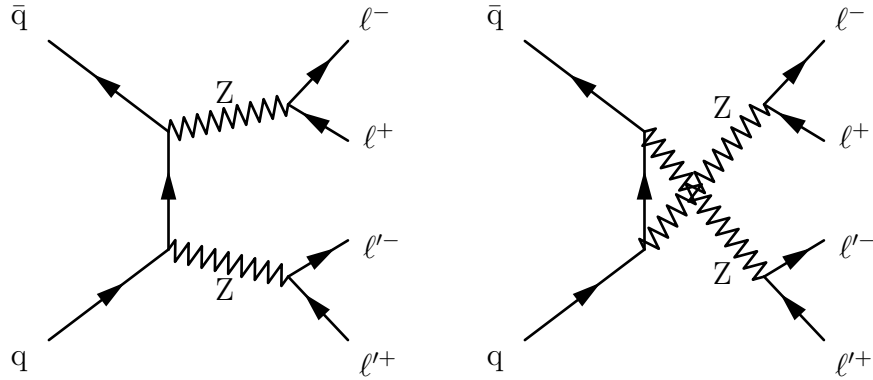


Figure 2.1: Leading order Feynman diagrams for $ZZ \rightarrow 4\ell$ production in pp collisions.

40 Production of pairs of on-shell Z bosons¹ turns on sharply at the kinematic thresh-
 41 old $\sqrt{\hat{s}} = 2m_Z = 182.4$ GeV, and in proton-proton collisions at $\sqrt{s} = 13$ TeV, peaks
 42 around $m_{ZZ} \approx 200$ GeV before falling steeply at higher invariant masses. Continuum
 43 production occurs below the kinematic threshold when one or both Z bosons are re-
 44 placed by a Z^*/γ^* admixture, typically in the form of a $q\bar{q} \rightarrow Z$ event in which one of
 45 the incoming quarks emits a virtual photon as initial state radiation (ISR). Events of
 46 interest in this analysis (see Sections 5.4 and 6.3) generally have one on-shell Z, and
 47 a Z^*/γ^* at a lower mass. Nonresonant $Z\gamma^*$ production is generally flat as a function
 48 of invariant mass between roughly 100 GeV and the doubly resonant threshold.

¹Events with two on-shell Z bosons are often called “doubly resonant,” but are a subset of “nonresonant” production in the sense that the ZZ system is not produced by a resonance. Either term may be used to distinguish “continuum” production from “singly resonant” production from $Z \rightarrow 4\ell$, $H \rightarrow ZZ^*$, or a potential new particle which decays to ZZ.

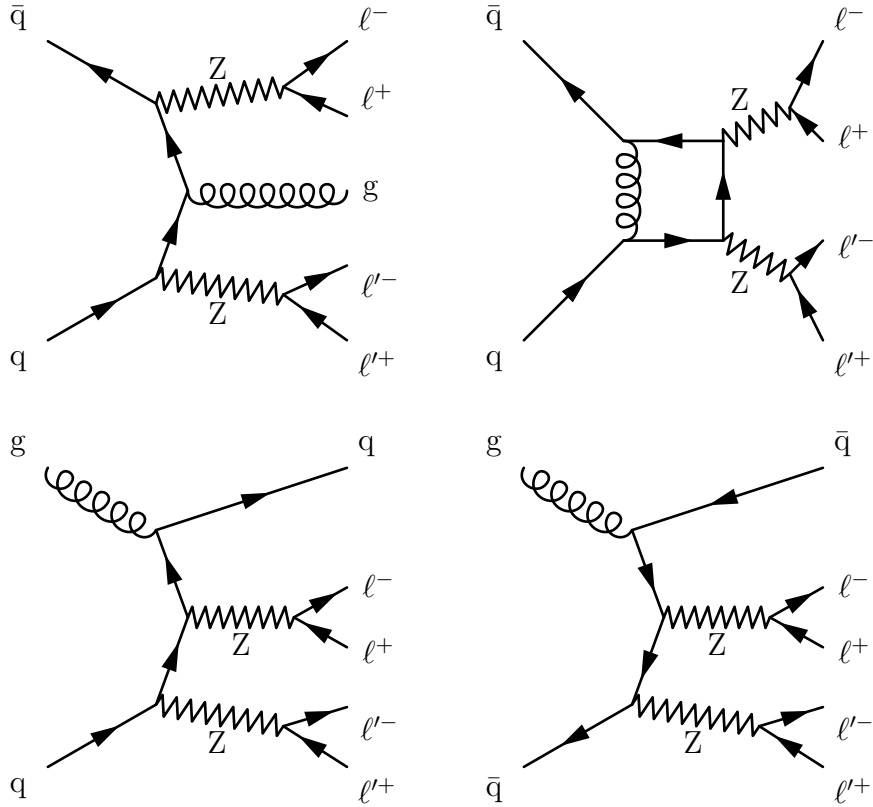


Figure 2.2: Four representative Feynman diagrams that contribute to $ZZ \rightarrow 4\ell$ production in pp collisions at NLO. Clockwise from the top right, the diagrams are examples of one-loop diagrams, real antiquark and quark emission, and real gluon emission. The loop diagram (top right) is formally NNLO, but contributes at NLO through interference with NLO $q\bar{q} \rightarrow ZZ$ diagrams.

⁴⁹ 2.1.1 Vector Boson Scattering

⁵⁰ Vector boson scattering proceeds at hadron colliders through the diagrams shown in
 Fig 2.4, resulting in a $ZZjj$ final state. This fully electroweak (EWK) production
 must be distinguished from the background of QCD-initiated $ZZ + \text{jets}$ events (see
 Section 2.4). The hallmark of the EWK process is a pair of high energy, high rapidity
 jets from the quarks, which retain a high boost along the z -axis even after electroweak
 boson emission and are thus deflected through a small angle in the lab frame. At the
 same time, the ZZ system is produced with low transverse boost compared to QCD-

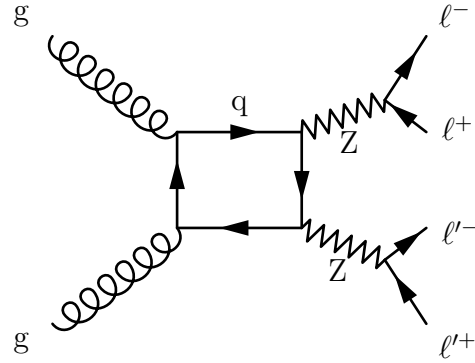


Figure 2.3: A LO box diagram for $ZZ \rightarrow 4\ell$ production through a quark loop in a gluon-gluon fusion event. This is formally an NNLO diagram for ZZ production overall, but is often included in NLO calculations because it accounts for a large fraction of the NNLO correction and its contribution to the ZZ cross section has a similar magnitude to that from the NLO corrections. The $gg \rightarrow ZZ$ amplitude is so large due to the high effective luminosity of gluons with enough energy to produce a Z boson pair in proton collisions at high Q^2 ,

57 initiated $ZZjj$ events, in which the ZZ system recoils against the jets, and somewhat
 58 higher invariant mass on average [58]. Because the hard scattering interaction involves
 59 no color exchange or reconnection [58–60], VBS events are much less likely to have less
 60 energetic jets between the two high-energy quark jets. Useful variables to discriminate
 61 between EWK and QCD production therefore include the angle between the jets, the
 62 jet energies, the dijet invariant mass, the ZZ invariant mass and rapidity, and the
 63 number of central jets (see Section 6.5 for a full list and definitions).

64 2.1.2 Prior Measurements

65 Doubly resonant ZZ production was first observed in e^+e^- collisions at LEP by the
 66 ALEPH, OPAL, L3, and DELPHI experiments, from 183 GeV, just above the thresh-
 67 old center-of-mass energy, to the LEP maximum of 209 GeV [61–66]. Because the ZZ
 68 cross section is very small, these measurements used all possible final states except
 69 those in which all Z decay products were neutrinos or taus. This was possible because

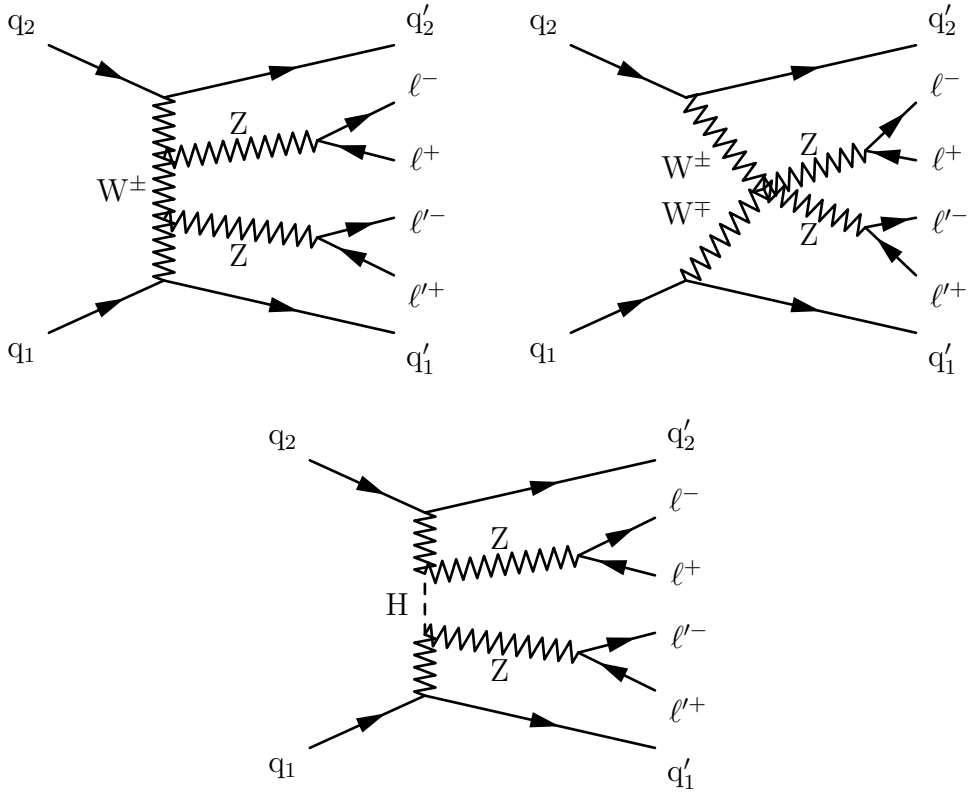


Figure 2.4: The primary ZZ VBS diagrams at hadron colliders. Diagrams also exist with antiquarks and with permutation and crossing of the final state particles. The interaction is only unitary to arbitrarily high energy when all diagrams are considered.

70 e^+e^- collisions do not suffer from the hadronization effect described above, so jets can
 71 be reliably matched to a hard scattering process, allowing identification of $Z \rightarrow q\bar{q}$
 72 decays. The measurements agreed with the SM, but were dominated by statistical
 73 uncertainties. Example measured cross sections from OPAL are shown in Fig 2.5 [65].
 74 Production in hadron collisions was first observed by the CDF and D0 experi-
 75 ments, in 1.96 TeV $p\bar{p}$ events at Tevatron [67–71]. In contrast to the LEP measure-
 76 ments, $p\bar{p}$ colliders cause too many extraneous jets for the hadronic channels to be
 77 seen above the background, so only the 4ℓ and $2\ell 2\nu$ ($\ell = e, \mu$) final states were used.
 78 These fully leptonic decay modes have small branching fractions on top of the small
 79 ZZ cross section of around 1.6 pb [53], but the total Tevatron dataset of roughly 6 fb^{-1}

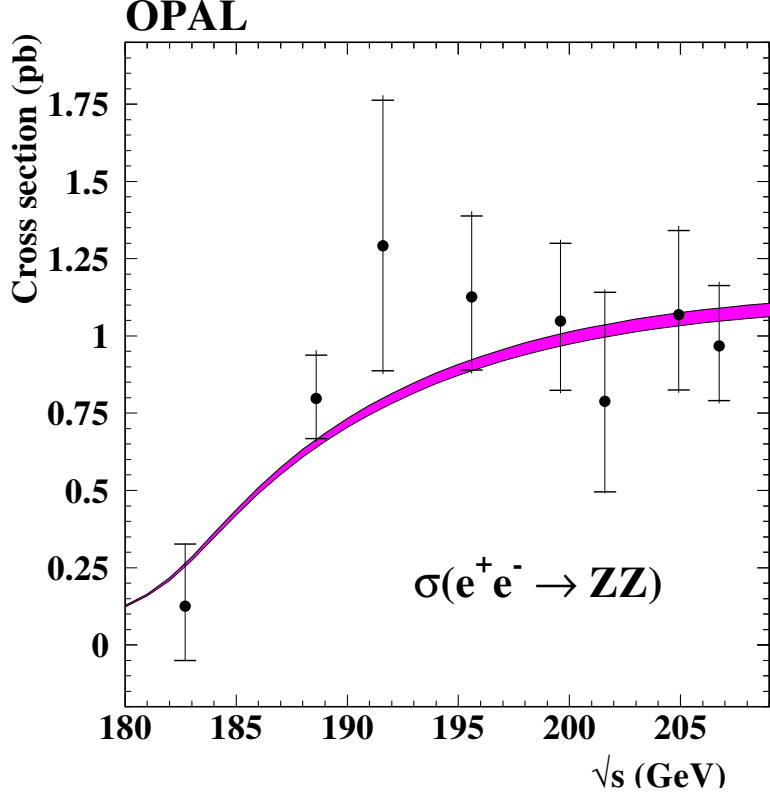


Figure 2.5: Measured $e^+e^- \rightarrow ZZ$ cross sections from the OPAL experiment, reproduced from Ref. [65]. Points represent the measured values. Vertical bars are the total uncertainty with horizontal bars indicating the statistical uncertainties, which dominate. The band is the SM prediction with a 2% theoretical uncertainty.

80 was large enough for CDF and D0 to find a few dozen events each. Results were again
 81 fully consistent with the SM but the statistical uncertainties were large, as can be
 82 seen in the example $m_{4\ell}$ shown in Fig. 2.6 [70].

83 The first run of the LHC (see Section 3.1) produced large datasets of pp collisions
 84 at $\sqrt{s} = 7$ and 8 TeV, producing ZZ events with a higher cross section than at
 85 Tevatron [56] and with a greater integrated luminosity. The primary measurement
 86 channels were again the fully leptonic 4ℓ and $2\ell 2\nu$ decays, and the cross sections were
 87 measured at $\sqrt{s} = 7$ and 8 TeV by both CMS [72–75] and ATLAS [76–78]. With
 88 a dataset of roughly 20 fb^{-1} and signal event counts in the hundreds even for the

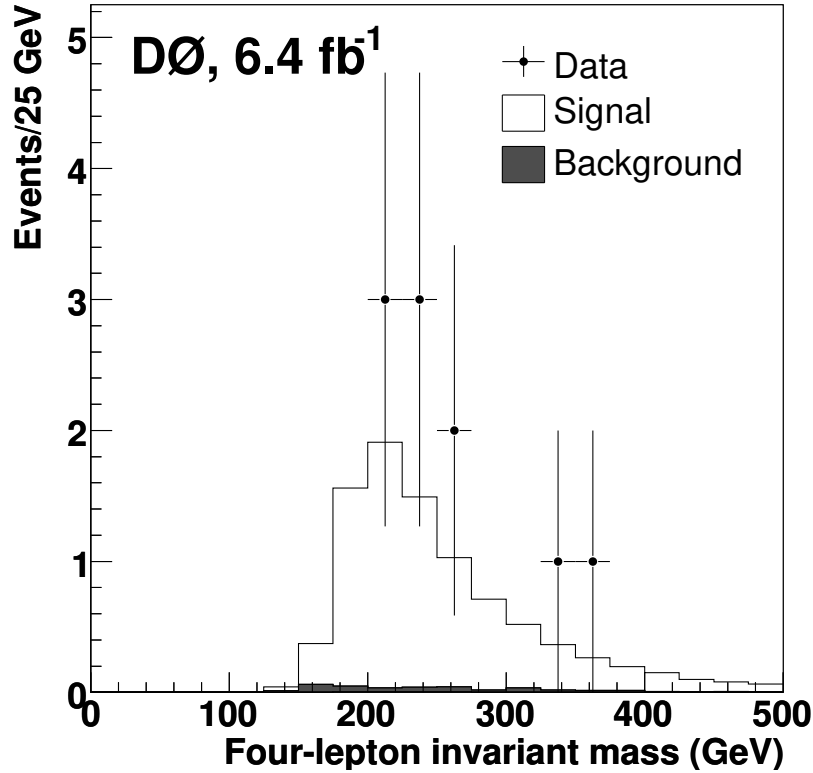


Figure 2.6: Measured $m_{4\ell}$ distribution from ZZ events collected by D0, reproduced from Ref. [70]. Points represent data with vertical bars showing statistical uncertainties, while the histograms show the SM expectation.

89 low-rate 4ℓ channel, the 8 TeV measurements had the statistical power to include
 90 differential cross sections as functions of kinematic observables for the ZZ system
 91 and the associated jets. Statistical uncertainties were still larger than the systematic
 92 uncertainties, but they were at the level of 5–10% for the total cross section, compared
 93 to 30–50% at Tevatron and 15–150% at LEP depending on the experiment and center-
 94 of-mass energy². The four-lepton mass spectra from the CMS and ATLAS ZZ cross
 95 section measurements at 8 TeV are shown in Figs. 2.7 and 2.8, respectively [73, 77]. A
 96 measurement was also performed on CMS data in the ZZ $\rightarrow \ell^+\ell^- b\bar{b}$ and ZZ $\rightarrow \nu\bar{\nu} b\bar{b}$
 97 channels [79].

²Most LEP ZZ cross section measurements had statistical uncertainties around 20–40%; see references given in the text for details.

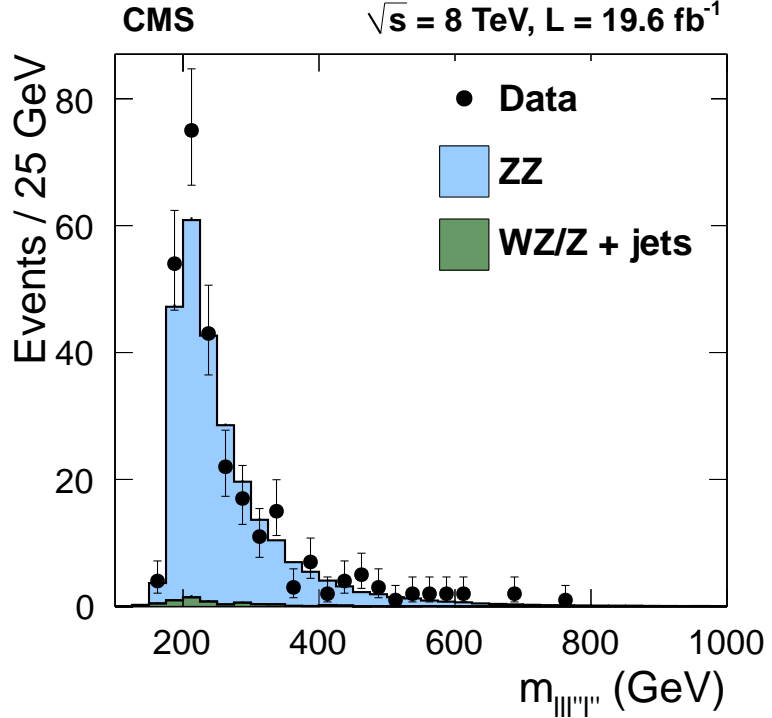


Figure 2.7: Measured $m_{4\ell}$ distribution from ZZ events collected by CMS at $\sqrt{s} = 8$ TeV, reproduced from Ref. [77]. Points represent data with vertical bars showing statistical uncertainties, while the histograms show the SM expectation. The grey hatched band represents the total uncertainty on the prediction.

98 CMS found that the total ZZ cross sections, defined as the cross sections of all
 99 events with two Z bosons in the mass range 60–120 GeV, to be

$$\begin{aligned}\sigma_{ZZ}(7 \text{ TeV}) &= 6.24^{+0.86}_{-0.80} (\text{stat})^{+0.41}_{-0.32} (\text{syst}) \pm 0.14 (\text{lumi}) \text{ pb} \\ \sigma_{ZZ}(8 \text{ TeV}) &= 7.7 \pm 0.5 (\text{stat})^{+0.5}_{-0.4} (\text{syst}) \pm 0.4 (\text{theo}) \pm 0.2 (\text{lumi}) \text{ pb},\end{aligned}\tag{2.4}$$

100 when measured with 4ℓ final states [73, 76], and

$$\begin{aligned}\sigma_{ZZ}(7 \text{ TeV}) &= 5.1^{+1.5}_{-1.4} (\text{stat})^{+1.4}_{-1.1} (\text{syst}) \pm 0.1 (\text{lumi}) \text{ pb} \\ \sigma_{ZZ}(8 \text{ TeV}) &= 7.2 \pm 0.8 (\text{stat})^{+1.9}_{-1.5} (\text{syst}) \pm 0.2 (\text{lumi}) \text{ pb}\end{aligned}\tag{2.5}$$

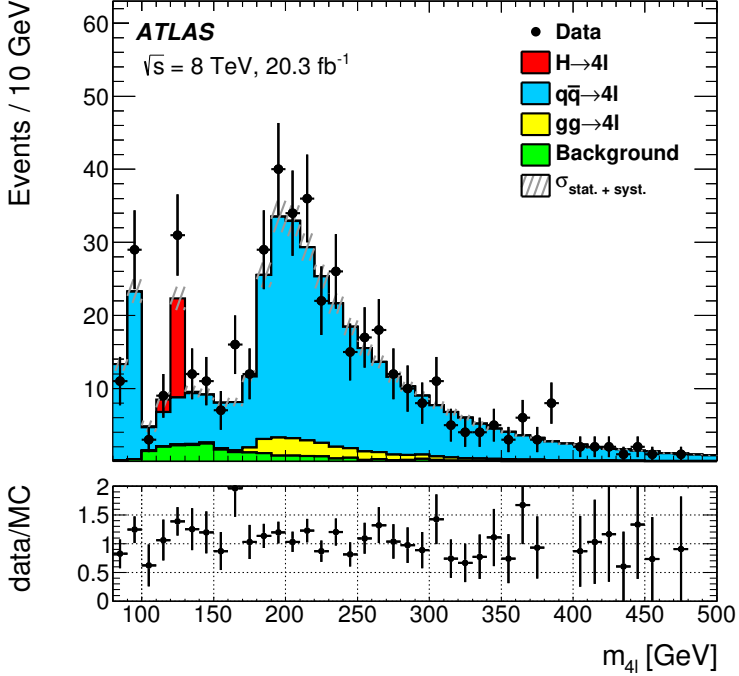


Figure 2.8: Measured m_{4l} distribution from ZZ events collected by ATLAS at $\sqrt{s} = 8$ TeV, reproduced from Ref. [70]. Points represent data with vertical bars showing statistical uncertainties, while the histograms show the SM expectation.

101 when measured with $2\ell 2\nu$ final states [74]. ATLAS found

$$\begin{aligned}\sigma_{ZZ}(7 \text{ TeV}) &= 6.7 \pm 0.7 \text{ (stat)} {}^{+0.4}_{-0.3} \text{ (syst)} \pm 0.3 \text{ (lumi)} \text{ pb} \\ \sigma_{ZZ}(8 \text{ TeV}) &= 7.3 \pm 0.4 \text{ (stat)} \pm 0.3 \text{ (syst)} \pm 0.2 \text{ (lumi)} \text{ pb},\end{aligned}\quad (2.6)$$

102 using 4ℓ final states at 7 TeV [76] and a combination of 4ℓ and $2\ell 2\nu$ events at
103 8 TeV [78]. ATLAS used a slightly different definition of the Z, considering it to
104 have mass in the range 66–116 GeV, which reduces the SM expected cross section
105 by 1.6% [80]. Measured cross sections from both experiments are again consistent
106 with SM predictions of 6.7 ± 0.2 pb at 7 TeV and 8.3 ± 0.2 pb at 8 TeV, both calcu-
107 lated at NNNLO in QCD with MATRIX, with factorization and renormalization scales
108 $\mu_F = \mu_R = m_Z$.

109 Searches for vector boson scattering were first performed at $\sqrt{s} = 8$ TeV. The first

process examined was the low-background same-sign WW process $\text{pp} \rightarrow W^\pm W^\pm jj$ studied at ATLAS, where evidence for electroweak production was observed at the level of a 3.6σ standard deviation excess over the null hypothesis [81], and at CMS, where a 2.0σ excess was found [82]. Subsequent searches for electroweak $Z\gamma jj$ production found a 3.0σ excess above the null hypothesis at CMS [83] and no significant excess at ATLAS [84]. A CMS measurement of $W\gamma jj$ production found a 2.7σ excess above the null hypothesis consistent with electroweak production [85]. Searches for photon-photon VBS were performed as searches for exclusive and quasi-exclusive $\gamma\gamma \rightarrow W^+W^-$ production $\text{pp} \rightarrow p^{(*)}W^+W^-p^{(*)}$, in which the protons do not collide but instead both radiate photons, which scatter. CMS found evidence at the level of 3.4σ above the null hypothesis [86], and ATLAS saw a 3.0σ excess [87]. Roughly contemporaneously with this work, electroweak same-sign WW production was observed at CMS in 13 TeV collisions, with a significance of 5.5σ [88]. No searches for Electroweak ZZ production had been performed prior to the analysis described in the following chapters.

125 **2.2 Resonant ZZ^{*}/γ^{*}γ^{*} Production**

126 Resonant production appears as a sharp peak in the four-lepton invariant mass distribution over the broad spectrum from nonresonant production. There are two known 127 four-lepton resonances: single-Z decays to four leptons around 91 GeV, and Higgs 128 decays to ZZ^{*} around 125 GeV. Another resonance, caused by a new particle, could 129 still be discovered at high mass, or at low mass but with a very small cross section.

131 2.2.1 Z Boson Decays to Four Leptons

132 A single Z boson may decay to a four-lepton final state when a lepton from a normal
 133 $Z \rightarrow \ell^+ \ell^-$ decay radiates a virtual photon, as shown in Fig 2.9. In a window around
 134 the Z mass of $80 < m_{4\ell} < 100$ GeV, t - and u -channel production (the diagrams of
 135 Fig 2.1 with γ^* for both bosons) contribute at the few-percent level (4% at $\sqrt{s} =$
 136 13 TeV). Four-fermion decays were studied in detail at LEP [89]. This included
 137 four-lepton decays, but used all $\ell^+ \ell^- f\bar{f}$ ($\ell = e, \mu, \tau$) final states, where f could be any
 138 fermion except the neutrinos. $Z \rightarrow 4\ell$ decays were also observed at 7 and 8 TeV at
 139 CMS, where the branching fraction was found to be $\mathcal{B}(Z \rightarrow 4\ell) = 4.2^{+0.9}_{-0.8}$ (stat) \pm
 140 0.2 (syst) $\times 10^{-6}$ [90], and at ATLAS, where it was found to be 3.20 ± 0.25 (stat) \pm
 141 0.13 (syst) $\times 10^{-6}$ in a slightly different phase space [91]. After correcting for phase
 142 space differences, the measurements are compatible with each other and with the SM.

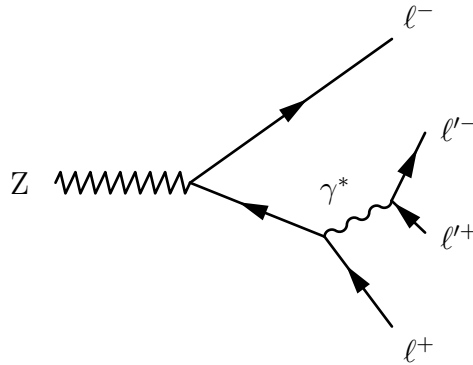


Figure 2.9: Tree-level Feynman diagram for $Z \rightarrow 4\ell$ production. Either initial lepton may radiate the γ^* .

143 2.2.2 Higgs Boson Production

144 The primary Higgs production mechanism in multi-TeV hadron collisions is gluon-
 145 gluon fusion through a quark loop, because of the gluon's high effective luminosity and
 146 the top quark's strong Yukawa coupling. Other mechanisms, in decreasing order by

147 cross section, include vector boson fusion (VBF), vector boson associated production
 148 (VH or “Higgsstrahlung”), and top-antitop associated production ($t\bar{t}H$). Tree-level
 149 Feynman diagrams for all four are shown in Fig. 2.10. The SM cross sections for
 150 the various production mechanisms, and the Higgs branching fractions, are shown as
 151 functions of m_H near the measured mass of 125 GeV in Fig. 2.11. Gluon-gluon fusion
 152 has roughly an order of magnitude higher rate than the others. The VBF process
 153 contributes to the unitarization of vector boson scattering along with the diagrams
 154 in Fig. 2.4. Decays to ZZ^* are heavily suppressed by the fact that, since $m_H < 2m_Z$,
 155 energy conservation requires one of the Z bosons to be far off its mass shell. Decays
 156 to four charged leptons are further suppressed by the small $Z \rightarrow \ell^+\ell^-$ branching
 157 fraction. However, the distinctive signature of four high-energy charged leptons in a
 158 single event is easy to detect with high efficiency and background rejection, and the
 159 momentum of electrons and muons can in general be measured with high precision,
 160 allowing the Higgs resonance to be easily seen as a sharp peak over a small, relatively
 161 flat background, and $H \rightarrow 4\ell$ is one of the most attractive channels for Higgs discovery
 162 and measurement of its properties.

163 **2.2.2.1 Prior Measurements**

164 Higgs boson searches at LEP were for Z-associated production, which has the highest
 165 cross section in e^+e^- collisions. The maximum LEP center-of-mass energy, 209 GeV,
 166 was just under the ZH threshold around 216 GeV. The LEP combined 95% confidence
 167 level (CL) lower limit on m_H was 114.4 GeV [93], and a combination of LEP data and
 168 electroweak precision measurements set an upper limit of 193 GeV [94]. Searches at
 169 the CDF and D0 experiments at the Tevatron were combined to find a 3.0σ local
 170 excess (2.8σ global) consistent with $m_H = 125$ GeV [95], with the $H \rightarrow b\bar{b}$ search
 171 alone finding a local excess of 3.3σ (3.1σ local) [96]. Results from all the Tevatron

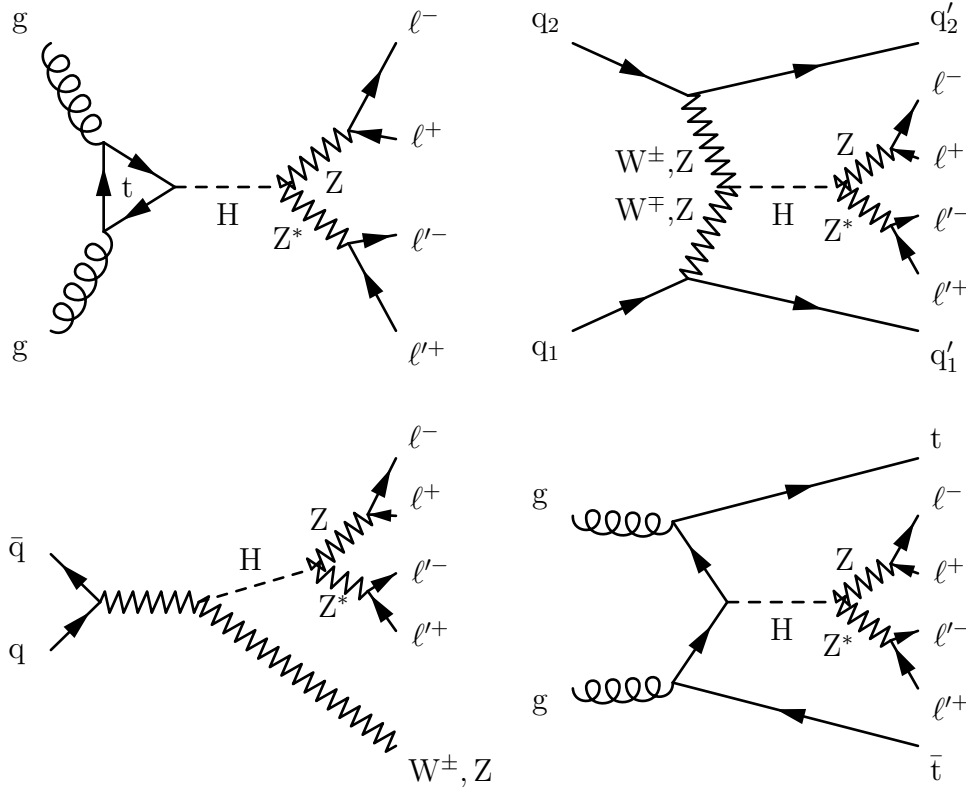


Figure 2.10: Tree-level Higgs production diagrams for gluon-gluon fusion (top left), VBF (top right), VH (bottom left), and $t\bar{t}H$, decaying to four leptons.

and LEP measurements and electroweak precision measurements were combined to place an upper mass limit of 158 GeV at 95% CL [97]. The Higgs was finally discovered simultaneously by the CMS and ATLAS collaborations with a combination of 7 and 8 TeV data [98, 99]. The four-lepton channel was, as anticipated, one of the most important [98, 100]. Its properties were subsequently investigated in detail at both experiments. The Higgs mass was found to be

$$m_H = 125.09 \pm 0.21 \text{ (stat)} \pm 0.11 \text{ (syst)} \text{ GeV} \quad (2.7)$$

based on a combination of data from the two experiments [101], and SM predictions of its properties have been confirmed by a number of measurements [102].

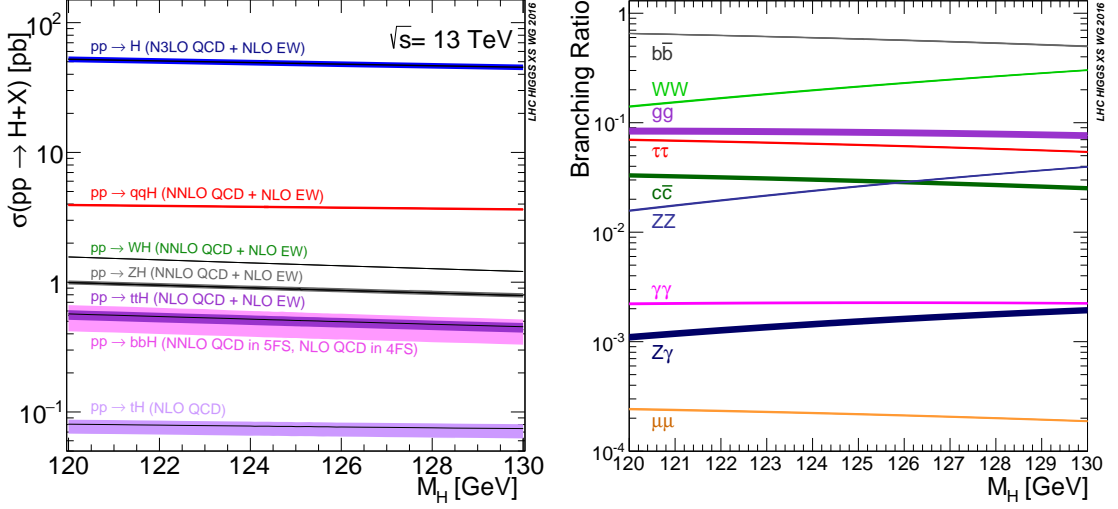


Figure 2.11: The SM cross sections for each Higgs boson production mode (left) and the Higgs branching fraction to several important final states (right), as a function of Higgs mass near the measured mass of 125 GeV. Both plots are reproduced from Ref. [92].

180 2.3 Anomalous Gauge Couplings

181 A primary hallmark of anomalous couplings is an enhanced cross section at center-
 182 of-mass energies of order 1 TeV [42]. The increase in cross section at high $m_{4\ell}$ implies
 183 higher transverse momentum for the outgoing Z bosons and leptons, as shown for two
 184 example aTGC models in Fig. 2.12. Searches for high-mass ZZ events are attractive
 185 because SM continuum production cross sections are extremely small above a few
 186 hundred GeV and all other sources of prompt or nonprompt four-lepton events are
 187 negligible, so even a handful of events would be an unambiguous sign of new physics.
 188 The search for nonzero aTGCs is performed using inclusive ZZ events, because the
 189 aTGC parameters should not have a large effect on jet distributions. The aQGC
 190 search is performed in ZZjj events because it would specifically enhance the VBS
 191 cross section at high mass.

192 The neutral aTGC parameters f_4^V and f_5^V are expected to have almost identi-

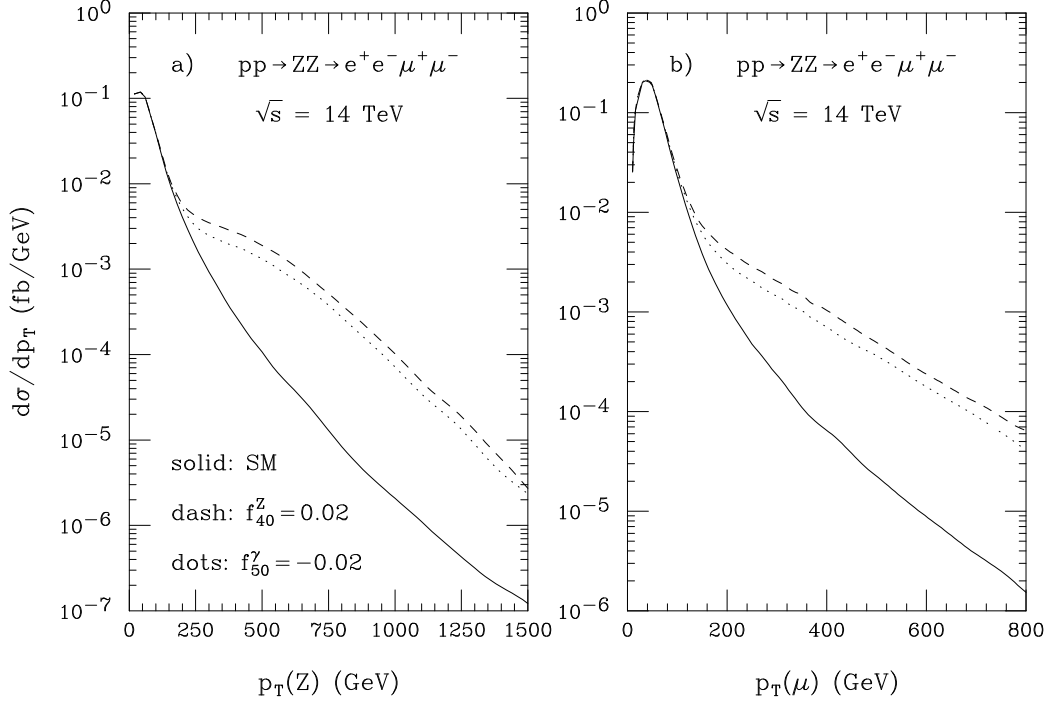


Figure 2.12: Cross section enhancements at high Z and μ momenta caused by example nonzero aTGCs. Reproduced from Ref. [42].

193 cal effects at high energy, so the search variables cannot be used to determine the
 194 relative strengths of the possible anomalous couplings [42]. However, because the
 195 terms governed by f_4^V have opposite behavior to the terms governed by f_5^Z under
 196 parity transformations, they affect the helicity amplitudes of the Z bosons and al-
 197 ter the angular distributions of the final-state leptons. Figure 2.13 shows the cross
 198 section as a function of total angular distance and the azimuthal angular difference
 199 between muons from the same Z decay for several example nonzero aTGCs and for
 200 the SM. These distributions could be used to distinguish between the possible aTGC
 201 parameters and determine the sign of the CP-conserving f_5^V terms.

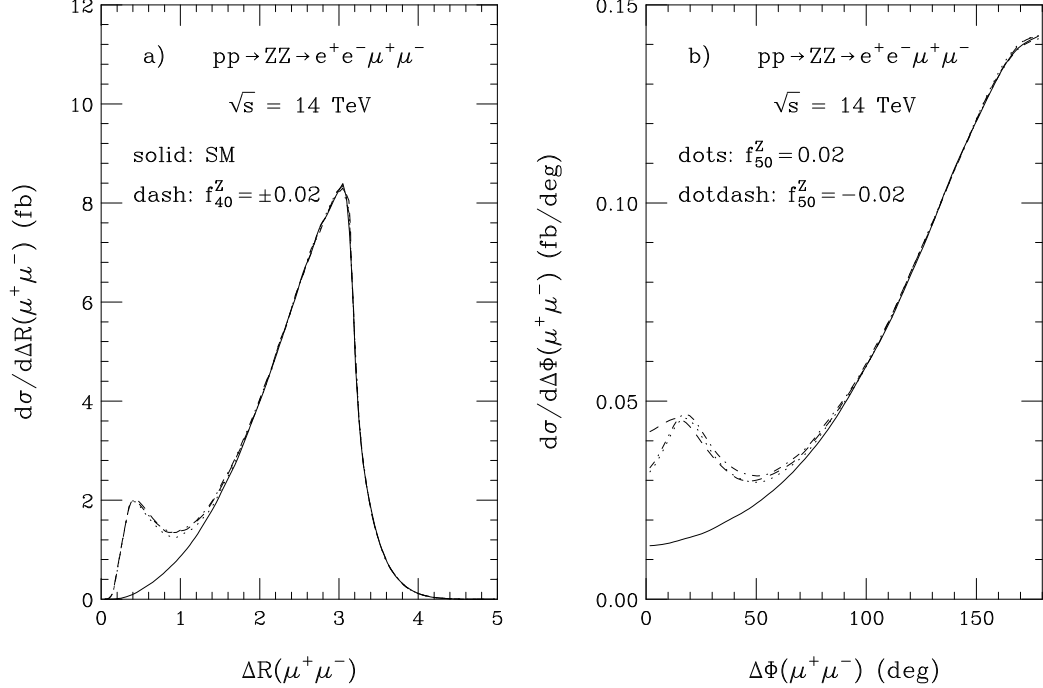


Figure 2.13: Total angular distance and azimuthal angular difference between muons from the same Z decay caused by several example nonzero aTGCs. Reproduced from Ref. [42].

2.3.1 Previous Limits

The first neutral aTGC searches were performed at LEP using ZZ and $Z\gamma$ events [65, 66, 103, 104]. Depending on the experiment and parameter, 95% CL limits were generally $\mathcal{O}(\pm 1)$, and the statistical combination set limits around 0.2–0.4 [94]. The first searches in hadron collisions were performed at Tevatron by CDF collaboration, which set symmetric 95% CL limits in the range ± 0.10 – 0.13 for all parameters [105], and the D0 collaboration, which set symmetric limits around ± 0.20 – 0.31 for all parameters [106]. Both Tevatron experiments used a unitarity-preserving cut-off of $\Lambda = 1.2$ TeV. CMS and ATLAS set 95% CL limits at 7 TeV at $\mathcal{O}(\pm 0.1)$ [72, 76, 107], and $\mathcal{O}(\pm 0.005)$ at 8 TeV [73, 108]. ATLAS presented limits from 7 TeV data with and without a unitarizing form factor; their 8 TeV results, and all CMS results,

213 did not use one. Prior to this work, the most stringent limits on all four neutral
 214 aTGC parameters were set by CMS with a combination of 7 and 8 TeV data [74],

$$\begin{aligned} -0.0022 < f_4^Z < 0.0026, \quad -0.0023 < f_5^Z < 0.0023, \\ -0.0029 < f_4^\gamma < 0.0026, \quad -0.0026 < f_5^\gamma < 0.0027. \end{aligned} \quad (2.8)$$

215 The two-dimensional aTGC limits set by CMS with the 8 TeV dataset are shown in
 216 Fig. 2.14 [73].

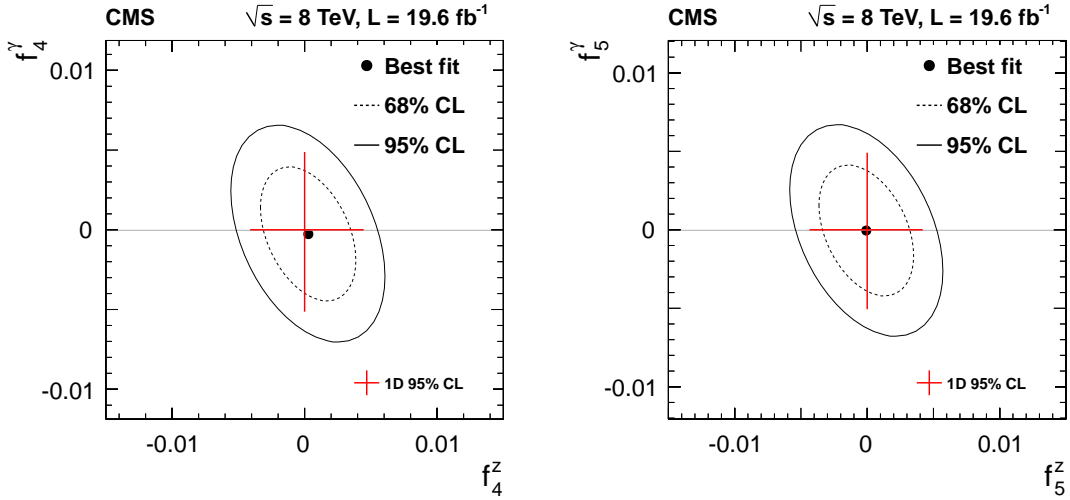


Figure 2.14: Two-dimensional 95% CL aTGC limits set by CMS, reproduced from Ref. [73].

217 No prior aQGC searches were performed using ZZ processes, but both LHC ex-
 218 periments set limits on the ZZ-sensitive effective field theory operators using other
 219 channels. The most stringent limits on f_{T0} were from $\sqrt{s} = 8$ TeV $Z\gamma qq$ events at
 220 ATLAS [84], found to be

$$-3.4 < f_{T0}/\Lambda^4 < 2.9 \text{ TeV}^{-4} \quad (2.9)$$

221 at 95% CL, with similar results produced by CMS [83]. The most stringent limits on
 222 f_{T1} and f_{T2} were set by CMS at 8 TeV using same-sign WWqq events [82], and were

223 found to be

$$-2.1 < f_{T1}/\Lambda^4 < 2.4 \text{ TeV}^{-4} \quad (2.10)$$

224 and

$$-5.9 < f_{T2}/\Lambda^4 < 7.1 \text{ TeV}^{-4}. \quad (2.11)$$

225 CMS and ATLAS produced nearly identical limits on f_{T8} and f_{T9} in the same $Z\gamma qq$
226 searches that set limits on f_{T0} ,

$$-1.8 < f_{T8}/\Lambda^4 < 1.8 \text{ TeV}^{-4} \quad (2.12)$$

227 and

$$-3.9 < f_{T9}/\Lambda^4 < 3.9 \text{ TeV}^{-4}. \quad (2.13)$$

228 2.4 Background Processes

229 Spurious events are categorized as irreducible backgrounds, i.e. those that are ex-
230 pected to have four prompt leptons, and reducible backgrounds, which have two
231 or three prompt leptons and another object that is misidentified as a prompt lep-
232 ton. The only nontrivial irreducible backgrounds to inclusive $ZZ/Z\gamma^*$ production are
233 WWZ triboson events in which all three bosons decay leptonically, and $t\bar{t}Z$ events
234 in which both top quarks and the Z all decay leptonically as shown at tree level in
235 Fig. 2.15. The most prominent reducible backgrounds are $WZ \rightarrow 3\ell\nu$ events in which
236 a jet fragment is misidentified as a prompt lepton, $Z + \text{jets}$ events in which two jet
237 fragments are misidentified, and leptonic $t\bar{t}$ events with two misidentified fragments
238 from the secondary b-jets. For the VBS search, the background is real ZZ events
239 which have two jets, but the jets originate from QCD interactions instead of the fully
240 electroweak processes of Fig. 2.4. An example non-VBS $ZZ + 2\text{jets}$ diagram is also
241 shown in Fig. 2.15.

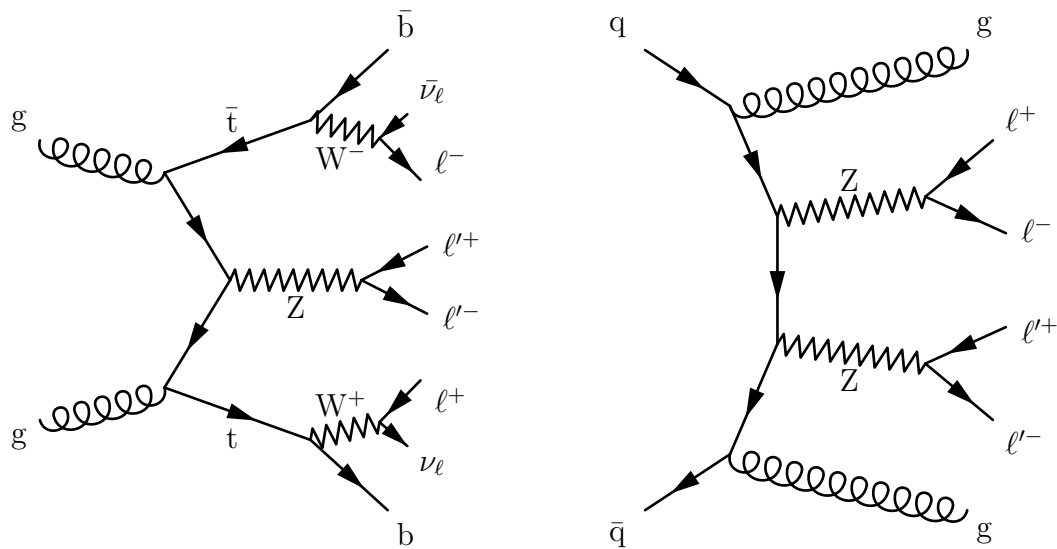


Figure 2.15: An example tree-level $t\bar{t}Z$ diagram (left), which is an irreducible background for inclusive $ZZ/Z\gamma^*$ production, and an example non-electroweak $ZZjj$ diagram (right).

⁰ Chapter 3

¹ The CMS Experiment and the ² CERN LHC

³ Production of controlled high-energy particle collisions, and detection of particles
⁴ created in those collisions, are monumental technical challenges. The apparatus used
⁵ to obtain the results presented in this thesis are the result of decades of work by
⁶ thousands of scientists and engineers, making use of many techniques developed in
⁷ the course of building and operating previous experiments. The LHC [109, 110]
⁸ accelerates pairs of charged hadron (proton or lead ion) beams and collides them
⁹ to provide a source of high energy particle interactions for several fully independent
¹⁰ detectors, including CMS [111], which collected the data used in the studies presented
¹¹ here. Detailed descriptions of the LHC and CMS follow.

¹² 3.1 The CERN Large Hadron Collider

¹³ The LHC, the most powerful particle accelerator and collider ever built, is a 26.7 km
¹⁴ circumference ring of superconducting magnets running through tunnels roughly

15 100 m below the suburbs and countryside near Geneva, Switzerland. It first produced
 16 collisions suitable for collecting physics data in 2010 before generating large datasets
 17 with beam energies of 3.5 TeV in 2011 and 4 TeV in 2012. Following a shutdown
 18 for upgrades and repairs, it operated in 2015 and 2016 to deliver beam energies of
 19 6.5 TeV. Beams collide head-on so that the center-of-mass frame of the proton-proton
 20 system is the rest frame of the detectors, giving proton-proton center-of-mass ener-
 21 gies of 7, 8, and 13 TeV respectively for collisions in 2010–2011, 2012, and 2015–2016.
 22 Each successive energy was the highest ever achieved in controlled hadron-hadron
 23 collisions, giving unprecedented access to extremely high-energy processes at every
 24 step.

25 In addition to increasing collision energies, the LHC increased its rate of collisions
 26 with each new machine configuration. The average event rate dN/dt for a process
 27 with production cross section σ is determined by the instantaneous luminosity \mathcal{L} of
 28 the collider,

$$\frac{dN}{dt} = \mathcal{L}\sigma \quad (3.1)$$

29 so a high instantaneous luminosity enables the observation of rare processes like Higgs
 30 boson production. The LHC’s unprecedented luminosities have allowed collection of
 31 the largest physics datasets in history.

32 The desire for high luminosities drove the decision to collide protons with other
 33 protons instead of with antiprotons as was done at Tevatron, LHC’s predecessor at
 34 Fermilab in Batavia, IL. Antiprotons simply cannot be produced in sufficient quan-
 35 tities for a collider on this scale. Tevatron was designed to study many processes
 36 that are $q\bar{q}$ -initiated, so it is useful to have valence antiquarks available in the col-
 37 lisions. The LHC was designed with Higgs boson production in mind, and the two
 38 most important Higgs production modes are proton/antiproton agnostic. Even for
 39 $q\bar{q}$ -initiated processes, valence antiquarks are less critical at the LHC because, for the

40 same center of mass energy, the effective $q\bar{q}$ luminosity is higher for proton-proton
41 collisions at LHC energies than at Tevatron energies (1.98 TeV center-of-mass energy)
42 as discussed in Section 1.6.

43 In addition to protons, the LHC can accelerate beams of lead nuclei to 2.51 TeV
44 per nucleon, also the highest ever achieved. All studies presented in this thesis were
45 performed on proton-proton collision data, rendering the details of so-called “heavy
46 ion” beams beyond the scope of this document.

47 Beams are maintained and manipulated with magnets, most of them made of
48 superconducting niobium-titanium (NbTi) windings cooled to 1.9 K by superfluid
49 helium. Dipole magnets with fields up to 8.33 T bend the beam around the ring,
50 interspersed with quadrupoles for focusing. More quadrupoles and higher-moment
51 magnets keep the beams focused, squeeze them for collisions, and apply a number
52 of corrections. Superconducting radio frequency (RF) cavities operating at 400 MHz
53 accelerate the beam, maintain it at its final energy, and maintain bunch shape and
54 spacing.

55 3.1.1 Accelerator Chain, Layout, and Detectors

56 The LHC was built in tunnels originally constructed for the Large Electron-Positron
57 Collider (LEP), an e^+e^- collider that operated from 1989 to 2000. Using existing cav-
58 erns, tunnels, and infrastructure was a substantial cost-saving measure, but imposed
59 several important constraints on the LHC’s design. In LEP, the electron and positron
60 beams could be accelerated in opposite directions by the same magnets, because they
61 are oppositely charged. Conversely, proton beams require opposite magnetic fields for
62 the two beams. Because the tunnels were not wide enough to accommodate two com-
63 pletely separate beam lines, most of the magnets in the LHC use a twin-bore design,
64 shown schematically in Fig. 3.1, in which the pipes and windings for the two beams

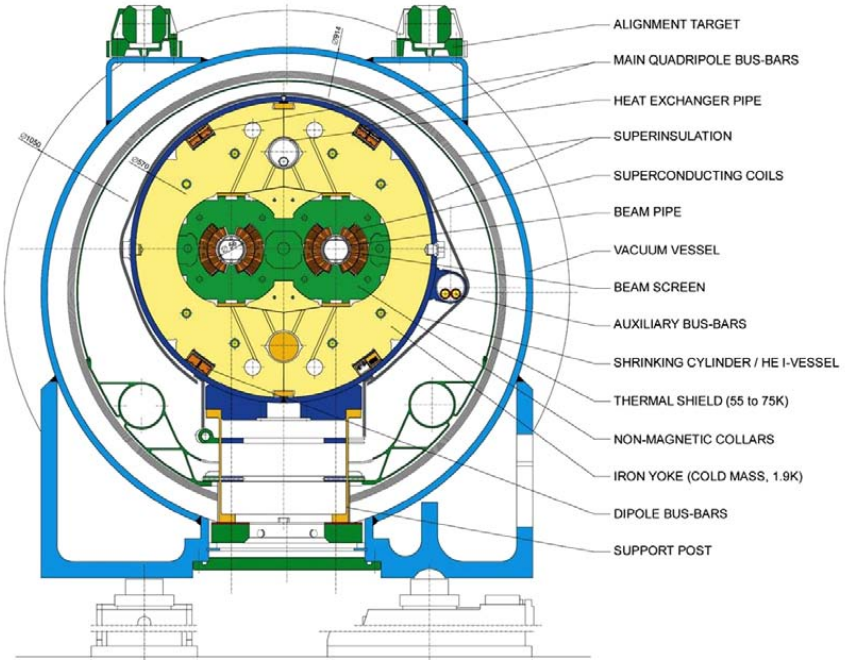


Figure 3.1: Schematic cross section of an LHC dipole and its attendant electrical and cryogenic infrastructure, reproduced from Ref. [109].

65 share a common cryogenic system. The electromagnetic, mechanical, and cryogenic
66 coupling of the two beamlines represents a significant engineering challenge [109, 110].

67 Because no single accelerator has the dynamic range necessary to take a stationary
68 proton to TeV-scale energies, a chain of smaller accelerators repurposed from previous
69 experiments feeds moderate-energy protons into LHC. Protons are obtained by ion-
70 izing hydrogen atoms, then accelerated to 50 MeV by the Linac 2 linear accelerator
71 and injected into the Proton Synchrotron Booster (PSB), the first of several circu-
72 lar accelerators. The PSB feeds 1.4 GeV protons into the Proton Synchrotron (PS),
73 which in turn injects them into the Super Proton Synchrotron (SPS) at 26 GeV. The
74 protons are then accelerated to 450 GeV in the SPS before being injected into LHC.

75 A diagram of the entire accelerator chain is shown in Fig. 3.2.

76 The LHC ring is divided into eight sectors, each of which features a 528 m straight
77 section connected to the adjacent sections by 2.45 km arcs. The straight section length

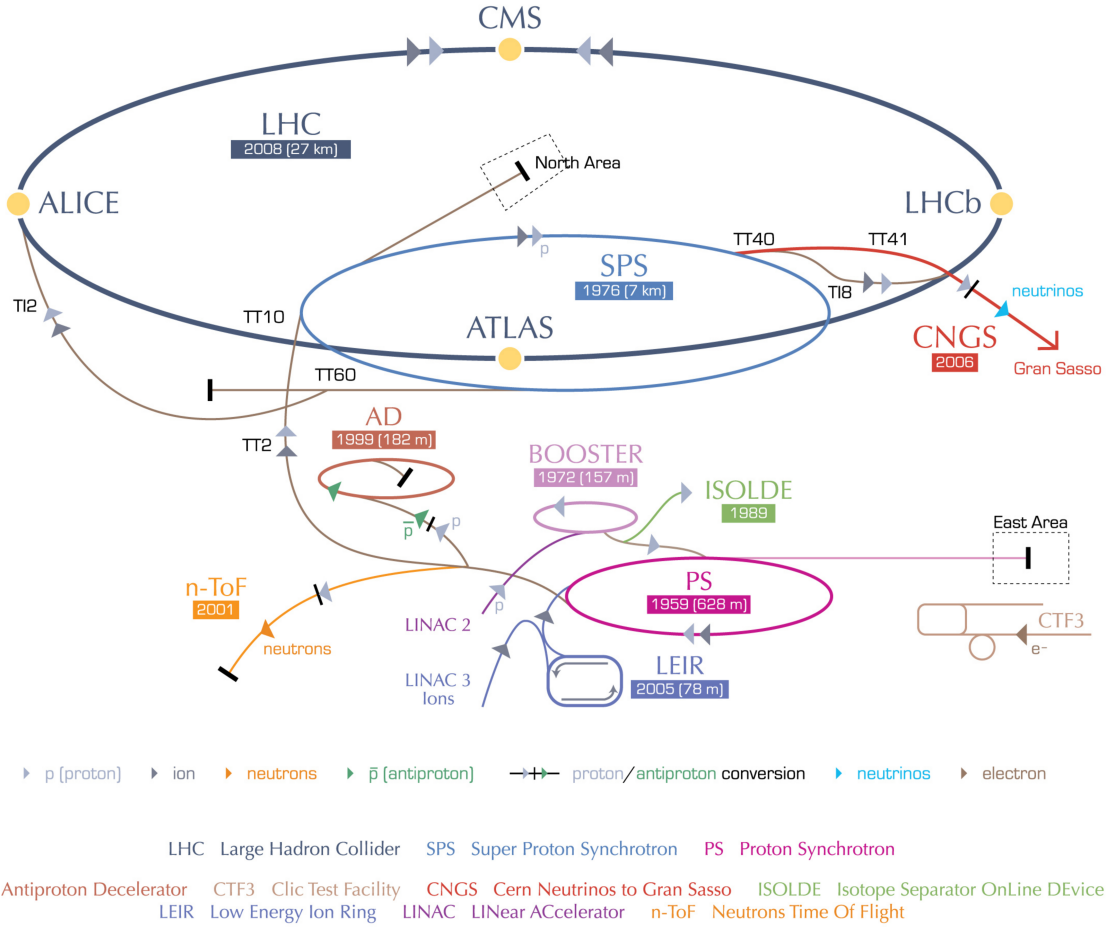


Figure 3.2: A schematic of the LHC accelerator chain and peripheral experiments, reproduced from Ref. [112].

78 was set by the need for RF cavities to accelerate LEP beams to counteract synchrotron
 79 radiation, which is a primary factor limiting electron and positron beam energy. This
 80 is not ideal for proton beams; protons' much higher mass means they radiate less and
 81 need fewer RF cavities. The straight sections feature access points numbered with
 82 Point 1 at the main CERN site in Meyrin, Switzerland, and the rest numbered 2–8,
 83 increasing in the clockwise direction when viewed from above. Points 1, 2, 5, and 8
 84 have beam crossing points and host detectors to study the resulting proton-proton
 85 collisions. Points 3 and 7 feature collimators to reduce momentum and betatron
 86 nonuniformities in the beams. The RF cavities are at Point 4 and the beams are

87 dumped after use or in the event of a magnet quench at Point 6. Beams are disbursed
 88 and deflected into an 8 m long water-cooled graphite absorber by fast kicker magnets
 89 which activate in a 3 μ s-long bunch-free region of the beam known as the abort gap.

90 The CMS detector is at Point 5 in Cessy, France, the furthest point on the ring
 91 from the Meyrin site and Point 1, which houses ATLAS [113], a similar but fully
 92 independent general-purpose particle detector. CMS and ATLAS use complemen-
 93 tary detector technology so that any measurement or discovery by one can be made
 94 concurrently or verified by the other. The other two experimental insertions feature
 95 specialized detectors studying collisions at lower-luminosity beam interaction points.
 96 The LHCb detector [114], at Point 8, studies hadronic physics with an emphasis on
 97 b-hadrons, and ALICE [115] studies heavy ion collisions at Point 2. Three smaller
 98 experiments share interaction points with the larger detectors, with TOTEM [116]
 99 studying proton structure and the total proton-proton interaction cross section next
 100 to CMS; LHCf [117] studying the π^0 energy spectrum and multiplicity near ATLAS;
 101 and MoEDAL [118] searching for magnetic monopoles or other heavy, stable, ionizing
 102 particles at Point 8 with LHCb.

103 3.1.2 Operating Parameters

104 With the beam energy set by the radius of the ring and the strength of available
 105 magnets, the number of interesting physics events produced in LHC collisions depends
 106 only on the integrated luminosity

$$\mathcal{L}_{int} = \int \mathcal{L} dt, \quad (3.2)$$

107 where \mathcal{L} is the instantaneous luminosity defined in Eq. (3.1) and the integral runs
 108 over the time the machine spends in collisions mode. LHC's availability for colli-
 109 sions depends on the electrical and mechanical stability of the accelerators and their

110 support systems, including the cryogenics and the vacuum in the beam pipe. The
 111 instantaneous luminosity while running depends only on the beam parameters. For
 112 symmetric beams which each have n_b colliding gaussian bunches of intensity (i.e. num-
 113 ber of protons in the bunch) N_b , orbiting the ring with frequency f_{rev} and relativistic
 114 factor $\gamma = E_p/m_p$, the instantaneous luminosity is give by

$$\mathcal{L} = f_{rev} \frac{n_b N_b^2 \gamma}{4\pi \beta^* \epsilon_N} R, \quad (3.3)$$

115 where β^* is the amplitude of the beams' betatron oscillations around the nominal
 116 ring path at the interaction point, the normalized emittance ϵ_N is a measure of the
 117 beams' spread in both position and momentum space, and R is a geometrical factor
 118 accounting for the beam crossing angle,

$$R = \sqrt{1 + \left(\frac{\theta_c \sigma_z}{2\sigma^*} \right)^2}. \quad (3.4)$$

119 Here θ_c is the beams' crossing angle, and σ_z and σ^* are respectively the longitudinal
 120 and transverse RMS widths of the bunches in the lab frame.

121 3.1.2.1 Design

122 The machine parameters in the LHC design specification can be seen in the first col-
 123 umn of Table 3.1. Machine parameters during data taking have in general been quite
 124 different, due to both technological advances and technical challenges. In particular,
 125 beam energy and number of colliding bunches are both lower than designed due to
 126 commissioning issues with the magnets and their safety systems [119], but increases in
 127 the number of collisions per bunch crossing (“pileup”) have more than compensated,
 128 leading to a peak instantaneous luminosity in 2016 that was more than 50% higher
 129 than designed. Operating parameters have changed frequently during data taking
 130 and upgrades are always ongoing.

Table 3.1: LHC beam parameters as designed and in practice. As stated in the text, n_b is the number of colliding bunches, N_b is the number of protons in each bunch, β^* is the betatron amplitude at the interaction point, ϵ_N is the normalized emittance, and $\mathcal{L}_{(int)}$ is the instantaneous (integrated) luminosity.

Year	Design		Run I		Run II	
		2010	2011	2012	2015	2016
Energy per beam (TeV)	7	3.5	3.5	4	6.5	6.5
Bunch spacing (ns)	25	150	50	50	25	25
n_b	2808	348	1331	1368	2232	2208
$N_b (10^{11})$	1.15	1.2	1.5	1.7	1.15	1.25
β^* (m)	0.55	3.5	1.0	0.6	0.8	0.4
ϵ_N (mm mrad)	3.75	2.2	2.3	2.5	3.5	3.0
Peak pileup	FIXME	4	17	37	22	49
Peak $\mathcal{L} (10^{34} \text{cm}^{-2}\text{s}^{-1})$	1	0.02	0.35	0.77	0.52	1.53
$\mathcal{L}_{int} (\text{fb}^{-1})$		0.04	6.1	23.3	4.2	41.1

131 3.1.2.2 Run I

132 The LHC came online in 2010 with a beam energy of 3.5 TeV, which was increased
 133 to 4 TeV in 2012. Bunches were spaced 50 ns apart instead of 25 ns to allow full
 134 exploitation of excellent injection chain performance [120]. Beams exiting the SPS
 135 had bunch intensity as much as 50% higher than anticipated in the original LHC
 136 design and beam emittance as low as 67% of nominal. This allowed the LHC to
 137 achieve 77% of its design instantaneous luminosity in 2012 despite having roughly
 138 half as many bunches in each beam.

139 Machine availability was overall good considering the complexity and relative
 140 newness of the LHC, with about 36% of scheduled time spent in stable beams. In all,
 141 LHC delivered 6.1 fb^{-1} to CMS and ATLAS in 2011 and 23.3 fb^{-1} in 2012, enough to
 142 allow discovery of the Higgs boson. The integrated luminosity for each year of LHC
 143 operation is shown as a function of calendar month and day in Fig. 3.3.

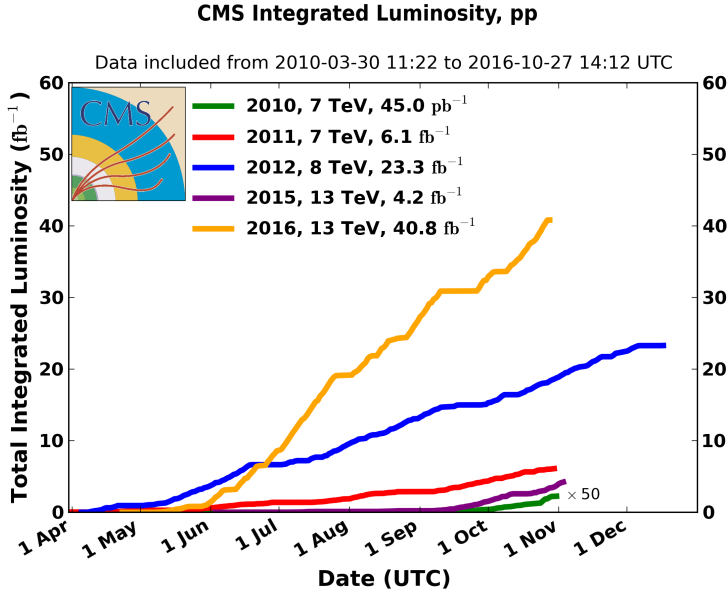


Figure 3.3: The integrated luminosity delivered to CMS in each year of LHC operation, shown as a function of the date within the year.

144 3.1.2.3 Run II

145 The LHC shut down for 2013 and 2014 to allow a number of repairs and upgrades,
 146 including measurements, repairs and upgrades on the electrical connections and cryo-
 147 genic safety systems. Beam energies were increased to 6.5 TeV, close to the nominal
 148 7 TeV. The bunch spacing was decreased to 25 ns while maintaining low emittance
 149 and high bunch intensity with the implementation of the beam compression merging
 150 and splitting (BCMS) scheme in which bunches are merged in the PS before they
 151 are split for injection into SPS, allowing higher bunch intensity [121]. This was offset
 152 by vacuum problems in the SPS beam dump, which limited the total number of col-
 153 liding bunches to around 2200 [122]. Improvements in collimators and beam optics
 154 reduced β^* to 40 cm in 2016, lower than the design β^* of 55 cm. Overall instantaneous
 155 luminosities were substantially higher than originally designed.

156 Machine availability in Run II was excellent, with over 60% of planned time spent
 157 in stable beams [122]. The world's first 13 TeV collisions in 2015 were the subject of

158 a number of measurements and searches, though the 4.2 fb^{-1} integrated luminosity
159 delivered to Points 1 and 5 in 2015 was less than planned due to several mechanical is-
160 sues. The integrated luminosity achieved in 2016, 41.1 fb^{-1} , was far above the roughly
161 25 fb^{-1} expected and more than all previous runs combined, allowing measurements
162 and searches of unprecedented sensitivity and reach, including those presented in this
163 Thesis.

164 **3.2 The Compact Muon Solenoid Detector**

165 The CMS detector [111] is a general-purpose particle detector located in a cavern
166 roughly 100 m below the surface at LHC Point 5. Though designed to do a wide
167 range of physics analyses, CMS was designed specifically with Higgs boson discovery
168 in mind. Primary design goals include

- 169 • High-efficiency reconstruction of charged particles with precise measurement of
170 their trajectories and momenta
- 171 • Good electromagnetic energy resolution, including diphoton and dielectron mass
172 resolution
- 173 • Hermetic calorimetry for good missing transverse energy and dijet mass resolu-
174 tion
- 175 • Good muon identification, momentum resolution (including dimuon mass reso-
176 lution), and charge determination over a broad range of energies

177 To this end, CMS features a silicon tracker, a scintillating crystal electromagnetic
178 calorimeter (ECAL), and a hermetic hadronic calorimeter (HCAL) inside a 3.8 T
179 solenoid magnet surrounded by ionized gas muon tracking devices, all of which can

180 be seen as part of the whole detector in Fig. 3.4. Decisions on which events to read
 181 out are made on-line by a two-level trigger system. Descriptions of these systems
 182 follow.

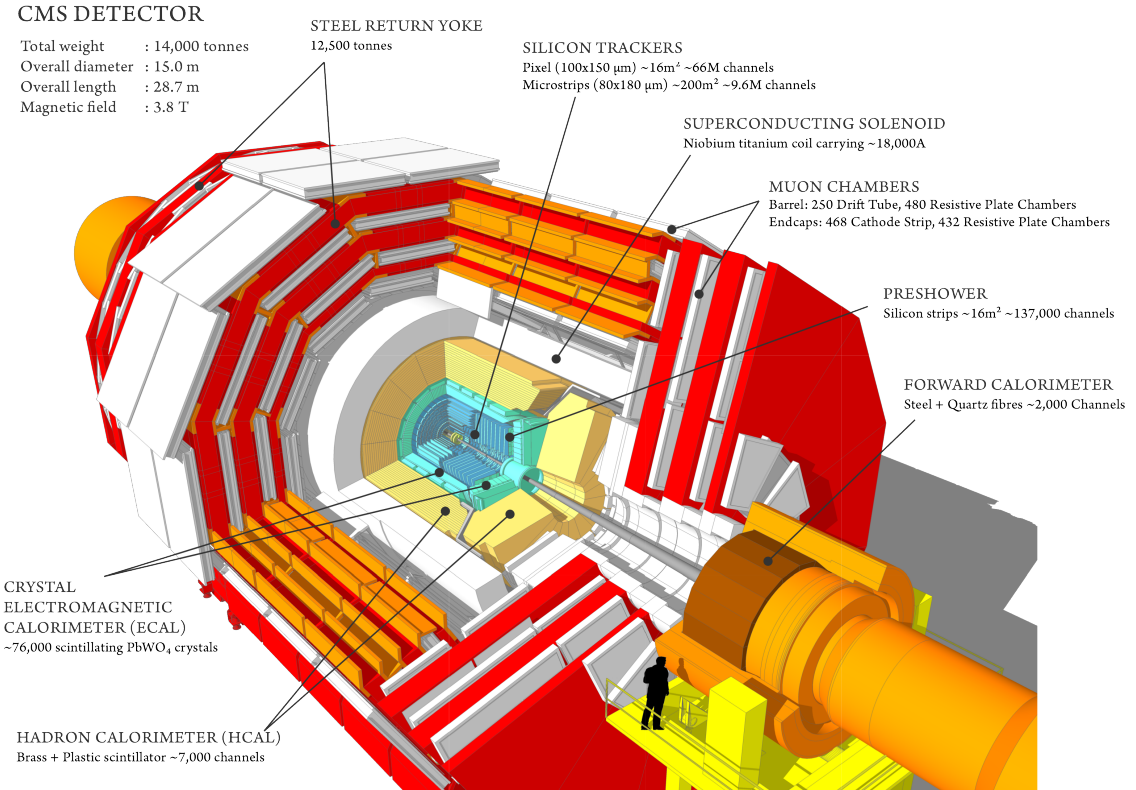


Figure 3.4: Cutout schematic of CMS with all major subdetectors, the beamline, the magnet, and the return yoke visible. Reproduced from Ref. [123].

183 3.2.1 Terminology and Geometry

184 The CMS detector systems are arranged in cylindrical layers with the interaction
 185 point at the center, serving as the origin for the coordinate system. The coordinate
 186 system is defined with the positive- x direction pointing toward the center of the
 187 ring, positive- y pointing vertically up, and positive- z pointing parallel to the beam
 188 in the counterclockwise direction when the LHC ring is viewed from above. Particle

189 momenta are typically expressed in quasicylindrical coordinates (p_T, η, ϕ) . Here p_T is
 190 the magnitude of the particle's momentum transverse to the beam

$$p_T \equiv \sqrt{p_x^2 + p_y^2}, \quad (3.5)$$

191 and ϕ is the azimuthal angle, i.e. the angle from the x -axis to the particle's trajectory
 192 in the x - y plane. The pseudorapidity η is defined as

$$\eta \equiv -\ln \left[\tan \left(\frac{\theta}{2} \right) \right] \quad (3.6)$$

193 where θ is the polar angle measured from the z -axis. The relativistic rapidity

$$y \equiv \frac{1}{2} \ln \left(\frac{E + p_z}{E - p_z} \right), \quad (3.7)$$

194 converges to the pseudorapidity in the limit of massless particles. Pseudorapidity
 195 is preferred to rapidity because it is purely geometrical, with no dependence on the
 196 particle energy. Both are preferred over θ because rapidity differences are invariant
 197 under longitudinal boosts, and because hadron flux at colliders is roughly constant as
 198 a function of rapidity. The transverse energy E_T is the the magnitude of the particle's
 199 four-momentum transverse to the beam, equal to p_T in the limit of massless particles.
 200 Spatial coordinates are expressed as (r, η, ϕ) , where r is the distance from the beam
 201 in the x - y plane.

202 3.2.2 Magnet and Inner Tracking System

203 A particle of charge q moving through a uniform magnetic field of strength B that
 204 points in the z direction will travel in a helix of radius R , given by

$$R = \frac{p_T}{|q|B}, \quad (3.8)$$

205 with the chirality of the helix determined by the sign of q . Thus one can determine the
 206 transverse momentum of the particle by measuring its path through the magnetic field

207 and finding the radius of curvature. In practice, all but the lowest-energy particles
 208 leave too short an arc in the detector for direct measurement of the radius, so the
 209 sagitta of the arc is used instead, given by

$$s = \frac{qBL^2}{8p_T} \quad (3.9)$$

210 where L is the length of the chord spanning the arc (typically equal to the radius of
 211 the tracking system). The transverse momentum resolution varies as

$$\frac{\delta p_T}{p_T} \propto \frac{p_T}{BL^2}, \quad (3.10)$$

212 so a strong field and a large tracking volume are vital to keeping measurements precise
 213 even at high energies.

214 To this end, CMS contains the world's largest superconducting magnet¹, a solenoid
 215 13 m long and 6 m in diameter, which generates a nearly-uniform 3.8 T field in the
 216 centralmost part of the detector [124]. To measure the paths of charged particles in
 217 the field, the volume closest to the interaction point contains layers of silicon sensors
 218 that detect hits from charged particles with high efficiency and excellent position
 219 resolution, between 4.4 cm and 1.1 m from the beam for 2.7 m on either side of the
 220 interaction point. This system, called the inner tracker and shown schematically
 221 in Fig. 3.5, consists of an inner pixel detector surrounded by a larger silicon strip
 222 detector. Both consist of concentric cylinders of sensors covering the barrel of the
 223 detector capped by discs covering the high- η region, up to $|\eta| < 2.5$. With a total of
 224 roughly 200 m² of silicon, the inner tracker is the largest silicon tracker in the world.
 225 Tracks may be reconstructed with hits in as many as 14 layers. The downside of
 226 this is that the tracker and its mechanical support structure represent a substantial
 227 amount of material for electrons and photons to interact with before they reach the

¹Largest in the sense of having the largest stored energy when at constant full field. The largest by size is the ATLAS barrel toroid.

228 calorimeters, with total material budget between 0.4 radiation lengths ($\eta = 0$) and 1.8
 229 radiation lengths ($|\eta| \approx 1.4$), as shown in Fig. 3.6. The tracker-only p_T uncertainty
 230 is around 1.2% at 200 GeV and 15% at 1 TeV. Tracker readout is too slow for it to
 231 be used in the L1 trigger (see Section 3.2.6.1), the first set of trigger decisions must
 232 be made using only information from the calorimeters and outer muon system.

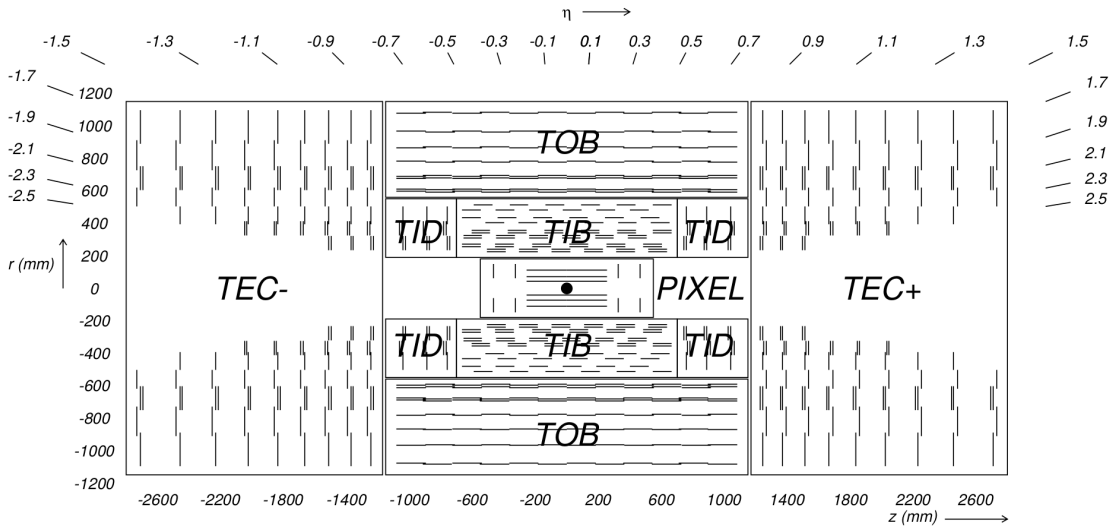


Figure 3.5: Diagram of the inner tracker layout, reproduced from Ref. [111].

233 As the system closest to the interaction point, the inner tracker is subject to
 234 extremely high radiation doses, equivalent to 840 kGy for the innermost pixel layer
 235 over an integrated luminosity of 500 fb^{-1} , so radiation tolerance is a major design
 236 constraint for both the sensors and readout electronics [125]. Leakage currents in
 237 the sensors, which degrade sensor performance, increase linearly with radiation fluence
 238 and exponentially with temperature. Because leakage currents cause self-heating in
 239 the silicon, they can create a dangerous positive thermal feedback loop if the sensors
 240 are not cooled below -10°C during operation. Reverse annealing, a process by which
 241 radiation-induced defects in the silicon can cause further damage months after the
 242 radiation dose is received, can be mitigated by keeping the sensors below 0°C at
 243 all times except for brief maintenance periods [111]. Therefore, to improve tracker

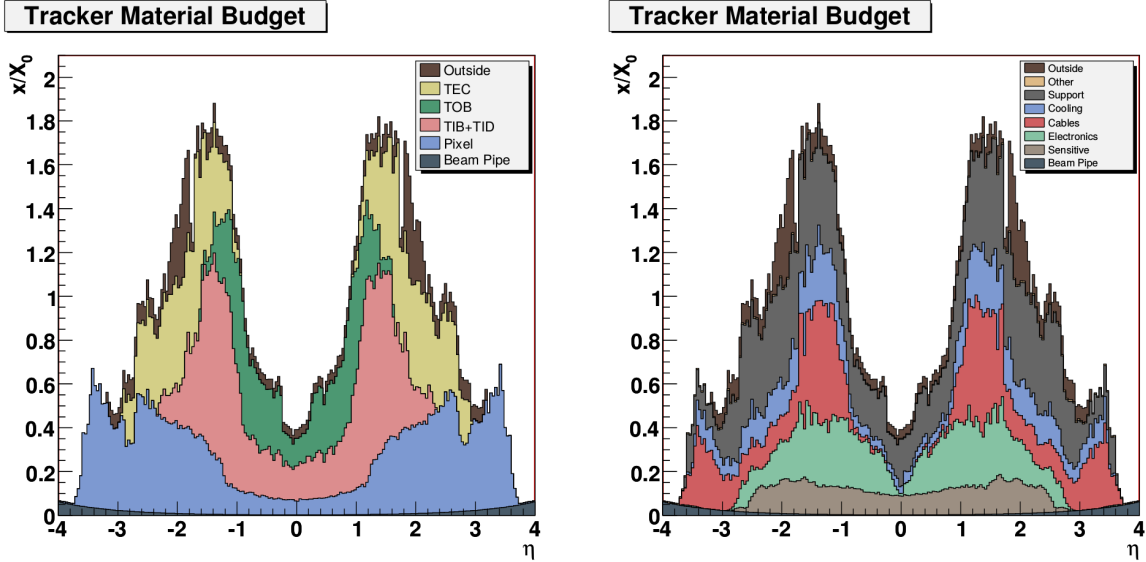


Figure 3.6: Total tracker material budget in units of electromagnetic radiation lengths, as a function of pseudorapidity. At (left) the total is divided by detector subsystem, at (right) by the function of the material. Reproduced from Ref. [111].

244 performance and increase the detectors' lifetimes, a gas cooling system is used to
 245 keep the strip tracker around -15°C and the pixel detector around -20°C during
 246 operation.

247 3.2.2.1 Pixel Detector

248 The pixel detector [125], consisting of three layers in the barrel and two in the endcap,
 249 is responsible for accurate reconstruction of primary proton-proton interaction ver-
 250 tices and secondary vertices from decays of b-hadrons or other long-lived particles, as
 251 well as providing “seed” tracks that may be used in strip tracker reconstruction. As
 252 the system closest to the interaction point, the pixel system experiences the highest
 253 charged-particle flux and therefore must have extremely fine granularity to differen-
 254 tiate between nearby particles. The 66 million pixels in the system have a cell size of
 255 $100 \times 150 \mu\text{m}^2$. Interpolation of the analog signals from the individual pixels allows
 256 a final spatial resolution of $15 \mu\text{m}$ in each direction. The outermost barrel layer is

257 10.2 cm from the beam, and the second endcap disk is 46.5 cm from the interaction
 258 point. The sensor modules are arranged such that at least three sensors cover the
 259 solid angle within the pixel detector's acceptance.

260 **3.2.2.2 Strip Tracker**

261 Outside the pixels is the silicon strip tracker [125], extending out to 1.1 m in the r
 262 direction and ± 2.8 m in the z direction. The tracker is divided into inner and outer
 263 subdetectors, each of which has both barrel cylinders and endcap discs. In total,
 264 there are ten layers in the barrel and nine in each of the endcaps. The inner tracker
 265 uses 320 μm -thick sensors with a typical strip cell size of 10 cm \times 80 μm , leading to
 266 hit resolutions of 23–35 μm . The outer tracker uses 500 μm -thick sensors with typical
 267 strip sizes up to 25 cm \times 180 μm , leading to hit resolutions of 35–53 μm .

268 **3.2.3 Electromagnetic Calorimeter**

269 Outside of the tracker is the electromagnetic calorimeter (ECAL), which is designed
 270 to absorb and measure the energy of electrons and photons. ECAL is made of 68,524
 271 radiation tolerant lead tungstate (PbWO_4) crystals arranged in a cylindrical barrel
 272 (EB) covering $|\eta| < 1.444$ and two endcap discs (EE) covering $1.566 < |\eta| < 3.0$.
 273 The geometry of the ECAL barrel and endcap can be seen in Fig. 3.7; the small
 274 gap between the barrel and endcap is necessary to accommodate cabling and support
 275 structures for the tracker. PbWO_4 crystals scintillate blue-green light and are op-
 276 tically transparent, so the resulting light can be read out by avalanche photodiodes
 277 (APDs) in the barrel and vacuum phototriodes (VPTs) in the endcap. ECAL's gran-
 278 ularity is set by PbWO_4 's small Molière radius of 2.2 cm, which is also the size of the
 279 square front faces of the barrel crystals, which flare out to 2.6 cm at the back, giving

them a truncated pyramid shape covering a roughly 0.0174×0.174 area of $\eta\phi$ space.
 The endcap crystals go from 2.86 cm squares at the front to 3.0 cm at the back.

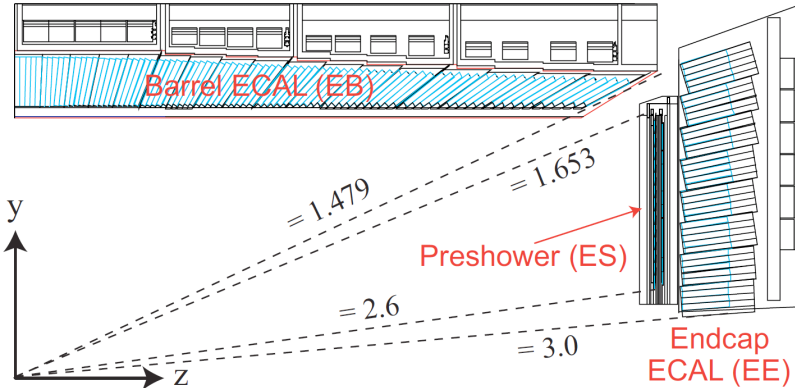


Figure 3.7: Diagram of ECAL geometry, reproduced from Ref. [126].

One of the primary design innovations of CMS—the eponymous compactness—was to place the calorimetry inside the magnet so that tracks can be unambiguously associated with energy deposits in the calorimeters without interference from scattering in the magnet coils. This is possible in part thanks to the high density (8.28 g/cm^3) and short radiation length (0.89 cm) of PbWO_4 , which allow ECAL crystals to be only 23 cm long in the barrel and 22 cm long in the endcap while still spanning 25.8 and 24.7 radiation lengths, respectively. This is enough to ensure that few electrons or photons escape ECAL with any appreciable remaining energy.

The total scintillation light yield is relatively low, averaging just 4.5 photons per MeV deposited. This is partially compensated by the fact that virtually all of ECAL is active material and no energy is lost to uninstrumented absorbers, but Poisson fluctuations in the yield are still the largest contribution to ECAL energy resolution for most electron and photon energies. This statistical uncertainty is represented by the first term in the full resolution equation,

$$\left(\frac{\delta E}{E}\right)^2 = \left(\frac{2.8\%}{\sqrt{E/\text{GeV}}}\right)^2 + \left(\frac{0.12}{E/\text{GeV}}\right)^2 + (0.30\%)^2. \quad (3.11)$$

296 The second term comes from electronic noise and noise from pileup, and the last term
 297 represents intrinsic differences between crystals. The upside to PbWO₄'s scintillation
 298 is that it is fast: roughly 80% of the light is emitted in the 25 ns between bunch
 299 crossings, so energy measurements require integration over only a few bunch crossings.

300 3.2.4 Hadronic Calorimeter

301 Between ECAL and the magnet is the hadronic calorimeter (HCAL), responsible for
 302 measuring the energy of hadronic jets. HCAL is a sampling calorimeter, meaning
 303 that the hadrons pass through dense, uninstrumented material and the products of
 304 the resulting interactions deposit energy in scintillators which are used to measure the
 305 total energy of the original incoming particles. The HCAL barrel (HB, $|\eta| < 1.305$)
 306 and endcap (HE, $1.305 < |\eta| < 3.0$) are made of layers of brass absorber interleaved
 307 with plastic scintillating tiles. The energy resolution in HB and HE is given by

$$\left(\frac{\delta E}{E}\right)^2 = \left(\frac{90\%}{\sqrt{E/\text{GeV}}}\right)^2 + (4.5\%)^2. \quad (3.12)$$

308 The first term is from the stochastic evolution of hadronic showers in the absorber,
 309 the second is from calibration uncertainties.

310 The geometry of HB, HE, and HO is shown in Fig. 3.8. The thickness of HB and
 311 HE is constrained by the size of the magnet, varying from 5.4 nuclear interaction
 312 lengths in the central barrel to more than 10 in the endcaps. Because HB is not thick
 313 enough to absorb all hadrons in the barrel, there is an extra outer HCAL component
 314 (HO) outside of the magnet, consisting of two more layers of scintillator on either
 315 side of a 20 cm-thick iron “tail catcher” covering $|\eta| < 1.3$. With HO and the 1.1
 316 interaction lengths in ECAL considered, no part of the calorimeter system spans
 317 fewer than 11.8 interaction lengths except in the gaps between barrel and endcap,
 318 minimizing the flux of hadronic “punchthrough” interacting with the muon system.

319 The total material budget in front of the layers of the muons systems is shown in
 320 Fig. 3.9.

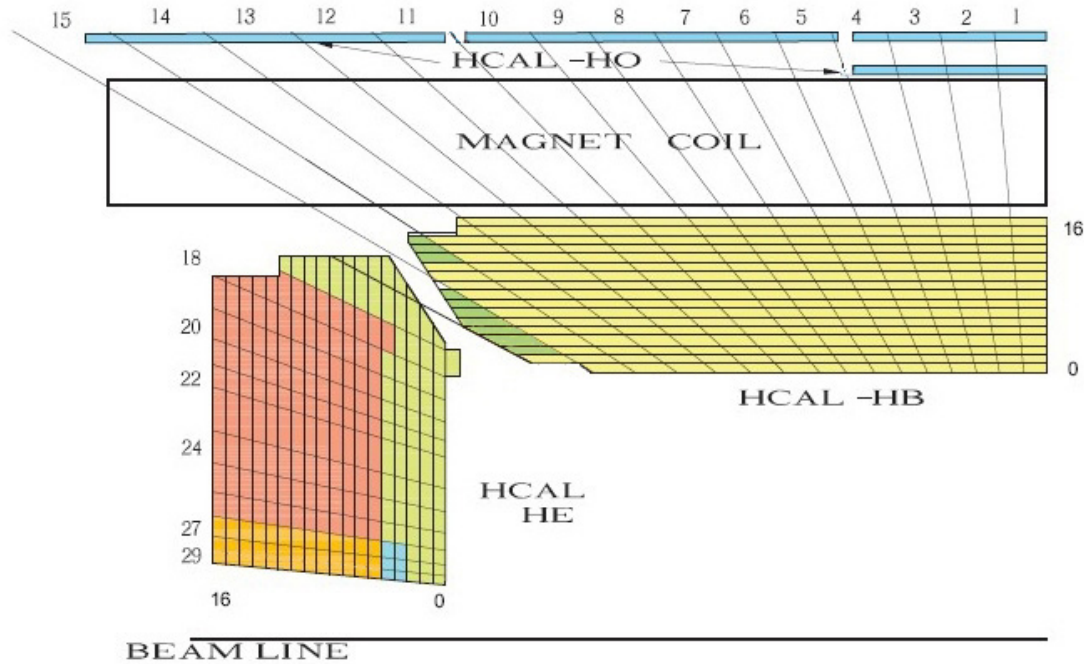


Figure 3.8: Diagram of HCAL geometry, reproduced from Ref. [111].

321 Closer to the beam line on each side, the forward hadronic calorimeter (HF, $3.0 <$
 322 $|\eta| < 5.2$) is made of iron and quartz fibers instead of brass and plastic scintillator to
 323 maximize radiation hardness. It acts as a Cherenkov detector with the quartz fibers
 324 as the active detection element. Half the fibers extend the entire depth of HF, while
 325 the other half start after the hadrons have traversed 22 cm of iron, allowing some
 326 differentiation between electromagnetic and hadronic energy. The energy resolution
 327 in HF is given by

$$\left(\frac{\delta E}{E}\right)^2 = \left(\frac{172\%}{\sqrt{E/\text{GeV}}}\right)^2 + (9\%)^2, \quad (3.13)$$

328 where the terms have the same physical interpretation as those in Eq. (3.12). HF
 329 improves CMS's missing energy resolution by roughly a factor of three.

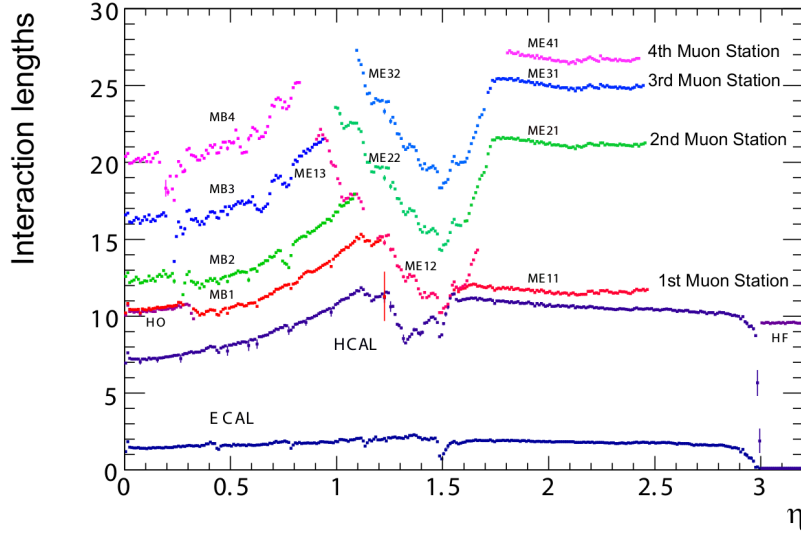


Figure 3.9: Total material budget in units of nuclear interaction lengths, as a function of pseudorapidity, reproduced from Ref. [111].

3.2.5 Muon Spectrometer

Many of the most interesting physics processes at the LHC involve high energy muons, so muon identification, triggering, and momentum measurement are important design goals. Muons leave very little energy in the calorimeters, so ECAL and HCAL cannot be used for triggering and identification as they are for electrons, photons and hadrons, or to improve momentum measurements of high- p_T muons whose tracks are too straight to allow good measurements of their curvature. Instead, these functions are provided for muons by three gas-based systems surrounding the rest of the detector [127, 128]. In all three, ionizing gas chambers provide hits which form a track. The magnetic field for this is provided by the return yoke, a set of steel plates interleaved with the muon chambers which confine the solenoid's magnetic return field. The yoke plates weigh a total of 10,000 t and are fully saturated by the solenoid.

Unlike the inner tracker, the muon systems can be read out fast enough to provide triggering. Because muons above 3 GeV generally traverse the muon system while most other measurable particles are stopped in the calorimeters, magnets, or return

345 yoke, the muon system provides high efficiency, low-background muon identification.
 346 The muon system's momentum measurements are not competitive with the inner
 347 tracker's at low p_T , but a combined fit of the inner track and the muon system
 348 ("standalone") track improves muon p_T resolution above roughly 200 GeV. The
 349 geometry of all three muon systems and the return yoke can be seen in Fig. 3.10.

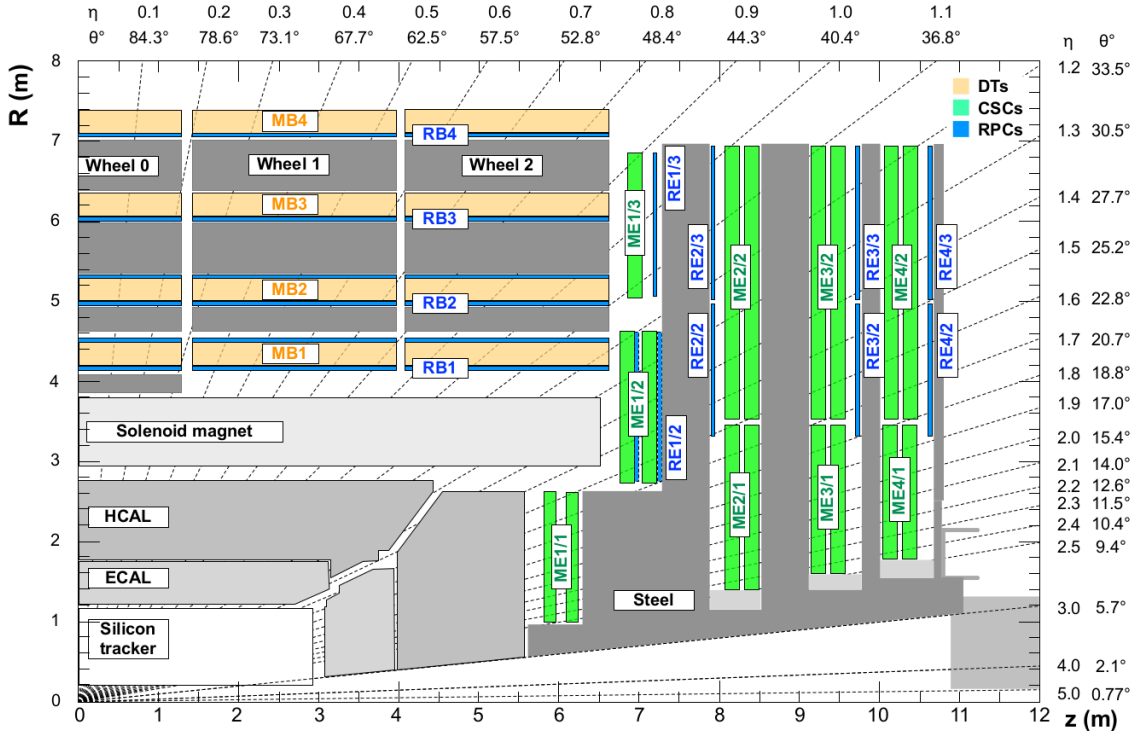


Figure 3.10: Diagram of muon system and return yoke geometry, reproduced from Ref. [128]. The magnet, calorimeters, and inner tracker are also visible.

350 3.2.5.1 Drift Tubes

351 In the barrel ($|\eta| < 1.2$), drift tube (DT) chambers are arranged in four "stations"
 352 separated by the steel layers of the yoke. Stations are made of two or three superlayers
 353 (SLs) of four layers of rectangular drift cells. Adjacent layers are staggered latterally
 354 by half a drift cell width to avoid gaps. Each station has two SLs with wires running
 355 parallel to the beam to measure muon tracks in the $r\phi$ plane, separated by an

356 aluminum honeycomb lattice to provide mechanical rigidity and act as a spacer. The
 357 inner three stations contain an extra SL on the outer side of the spacer with wires
 358 perpendicular to the beam line, to measure muon position along the z -axis.

359 Each drift cell contains a roughly 2.4 m-long wire in gas (85% Ar, 15% CO₂). The
 360 electric field in the cell is provided by aluminum tape glued to the top and bottom
 361 of the cell and held at +1.8 kV relative to the grounded aluminum plates above and
 362 below. Aluminum tape cathodes on the side of the cell are held at -1.2 kV, while the
 363 wires act as +3.6 kV anodes. The width of each cell perpendicular to muon motion,
 364 42 mm, was chosen for a maximum drift time of 380 ns, sufficient to obviate the need
 365 for double-hit readout logic in this low-occupancy region of the detector. The height
 366 of 13 mm set by mechanical and space constraints. Track timing resolution in each
 367 SL is a few nanoseconds when all cells are allowed to read out all deposited charge.
 368 The r - ϕ position resolution available for online use in the trigger is about 1.5 mm in
 369 each SL; offline, for a single wire it is roughly 250 μ m, leading to an overall offline
 370 resolution of 100 μ m at each station.

371 3.2.5.2 Cathode Strip Chambers

372 Muons with $1.2 < |\eta| < 2.4$ are detected by the cathode strip chambers (CSCs).²
 373 The CSC system's trapezoidal chambers are arranged on discs interleaved with the
 374 endcap yoke in four layers. Chambers close to the beamline each cover 20° sections
 375 in ϕ while outer chambers cover 10° sections, with overlap to avoid gaps.

376 A CSC chamber is made of seven panels sandwiched together to make six gaps
 377 filled with a gas mixture (40% Ar, 50% CO₂, 10% CF₄). Six of the plates have cathode
 378 strips milled into one side, varying in pitch from 8.4 mm at the narrow end of the
 379 trapezoid to 16 mm at the wide end, with 0.5 mm gaps between strips. Three panels

²Where the CSCs and DTs overlap ($0.9 < |\eta| < 1.2$), tracks are formed from hits in both.

380 are wrapped with anode wires, alternating with the other panels so that every gas
 381 gap has a plane of wires. Wires are spaced 3.2 mm apart and run azimuthally around
 382 the detector, except for the innermost chamber closest to the interaction point, which
 383 are inside the magnet and must have their wires tilted 29° so that charge collected
 384 by the wires moves parallel to them despite the Lorentz forces from the solenoid.

385 A typical muon will deposit charge in 3–4 cathode strips and a similar number of
 386 anode wires per gas gap, allowing hit position to be interpolated using all these sig-
 387 nals as well as timing information. The single-plane spatial resolution can be as good
 388 as 80 μm but depends strongly on where in the width of the strip the muon hits. The
 389 strips in alternating planes are therefore offset by half their width. Measurements
 390 from all six gas gaps in a chamber are combined into a segment with position reso-
 391 lution in the 30–80 μm range, which depends on the chamber but not where in the
 392 chamber the muon hit.

393 Anodes and cathodes are held 3.6 kV from each other, leading to a drift time of
 394 roughly 300 ns. Single anode planes have an RMS timing resolution of around 11 ns,
 395 insufficient for assigning a hit unambiguously to an individual bunch crossing, as
 396 required for triggering. However, information from all six anode planes in a chamber
 397 can be combined to yield a segment timing resolution around 5 ns. Segments are
 398 therefore the unit of information sent to the trigger. Segment position resolution at
 399 trigger level is 1–2 mm.

400 3.2.5.3 Resistive Plate Chambers

401 To provide a redundant set of muon momentum measurements, as well as precise
 402 timing of muon hits, CMS has six layers of resistive plate chambers (RPCs) in the
 403 barrel and four in the endcap up to $|\eta| < 1.6$. RPC chambers consist of two thin
 404 layers of intert gas (95.2% $\text{C}_2\text{H}_2\text{F}_4$, 4.5% C_4H_{10} , 0.3% SF_6) each between a pair of

405 Bakelite electrodes held at 9.3 kV. The two “gas gaps” are placed on either side of
406 a plane of copper strips. When a passing muon ionizes the gas, the high voltage
407 causes a fast electron avalanche read out by the strips. The narrow gap allows the
408 RPCs to have single-hit timing resolution around 1 ns, but the spatial resolution is
409 limited to about 1 cm by the size of the readout strips. The DTs and CSCs both
410 have better momentum resolution than the RPCs, but RPCs are a simple, robust
411 auxiliary system and the timing resolution can be used in conjunction with the other
412 systems to improve overall muon measurements. The gaps between RPC chambers
413 do not align with the gaps in the other outer muon systems, increasing the muon
414 spectrometer’s geometrical acceptance.

415 **3.2.6 Data Acquisition and Trigger**

416 With a bunch crossing rate of 40 MHz and over 40 collisions possible in each crossing,
417 the collision rate can exceed 1.6 GHz. Event sizes on disk of 1–2 MB mean that the
418 raw data generation rate of CMS could potentially be several PB/s, substantially
419 more than can be read out, stored or analyzed with current technology. However,
420 most events consist only of low-energy, well-understood QCD interactions, so the
421 data rate can be drastically reduced by reading out and storing only events likely to
422 have interesting physics content. CMS reduces the event rate with a two-level trigger
423 system.

424 The level-1 (L1) trigger uses custom hardware operating on trigger primitives
425 (TPs) containing lower-granularity detector information to reduce the event rate to
426 100 kHz or less. The inner tracker’s readout is too slow for use in the trigger, so only
427 the calorimeters and muon systems generate TPs. Events accepted at level-1 are fully
428 read out, digitized, and sent to the high level trigger (HLT), where they are partially
429 reconstructed in software and filtered further, reducing the final rate of stored events

430 to roughly 1 kHz.

431 **3.2.6.1 Level-1 Trigger**

432 LHC beams collide at too high a rate for trigger decisions to be made in software,
 433 so the L1 trigger is instead implemented in custom hardware, with processing done
 434 using field-programmable gate arrays (FPGAs) as much as possible for flexibility, and
 435 application-specific integrated circuits (ASICs) where required. Hardware limitations
 436 of other CMS subsystems—in particular, the inner tracker’s readout speed and buffer
 437 capacity—impose strict constraints on the system. The rate of events passing at
 438 level-1 cannot exceed 100 kHz and the system’s overall latency cannot exceed roughly
 439 4.2 μ s from the proton-proton interaction to data storage at level-1. These goals are
 440 achieved while maintaining high efficiency for interesting physics events by using low-
 441 granularity detector information, to reduce the bandwidth needed within the trigger
 442 system. Information flows through several processing steps, with the data throughput
 443 reduced at each step. Calorimeter and muon information are processed in parallel
 444 and combined only in the final step. Optical links between systems provide high-
 445 bandwidth data transfer and allow flexibility in the overall trigger architecture. The
 446 calorimeter trigger was upgraded with respect to the Run I configuration in 2015,
 447 and the whole trigger system was overhauled in 2016 [129]. Both configurations will
 448 be described here.

449 Calorimeter information is compressed into TPs for use in the trigger by trigger
 450 primitive generators (TPGs). Each TP represents a “tower” consisting of a 5×5
 451 cluster of barrel or endcap ECAL crystals and the HCAL tower behind them, or a
 452 section of the HF. The TP contains an 8-bit transverse energy sum and a quality bit
 453 for each calorimeter, and six bits of error checking and bookkeeping information. In
 454 2015, TPs were sent to the Regional Calorimeter Trigger (RCT) [130], which processed

455 18 portions of the detector (segmented in ϕ with $+\eta$ and $-\eta$ treated separately) in
 456 parallel in separate crates of electronics, using several ASICs and one FPGA in each
 457 crate for processing [131]. Each RCT crate summed the TPs with $|\eta| < 3.0$ into
 458 4×4 tower regions, and found isolated and non-isolated 2×1 tower e/γ and τ
 459 candidates. These objects were sent to Stage 1 Layer 2, which selected the best e/γ
 460 and τ candidates from the entire detector, clustered regions into 3×3 region jet
 461 candidates, and computed global quantities like missing transverse energy and the
 462 scalar sum of transverse momentum for all particles in the event. Pileup subtraction
 463 was performed with a lookup table (LUT) based on the number of regions in the
 464 detector with no energy.

465 In 2016, the whole calorimeter trigger was replaced with a new two-tiered system.
 466 Stage 2 Layer 1 (“CaloL1”) consists of 18 FPGA-based Calorimeter Trigger Proces-
 467 sor 7 (CTP7) cards [132], which calibrate and reformat the TPs before forwarding
 468 them to Stage 2 Layer 2 (“CaloL2”) [131], an FPGA-based time-multiplexed system
 469 which finds e/γ , τ , and jet candidates and computes global quantities for whole events
 470 in parallel using tower-level information.

471 In 2015, the DTs and CSCs fed track segments into track finders (DTTF [133] and
 472 CSCTF [134]) which used pattern recognition algorithms to reconstruct tracks and
 473 measure their p_T , sharing information between the track finders to avoid inefficiency
 474 in the overlap region. The RPCs made their own tracks. Since the 2016 upgrade,
 475 track finding has been done by geometrical region of the detector rather than detector
 476 subsystem alone, with separate track finders for the barrel (BMTF, $|\eta| < 0.85$) using
 477 DT and RPC information [135], the endcap (EMTF, $1.25 < |\eta| < 2.4$) using CSC and
 478 RPC information [129], and the overlap region (OMTF, $0.85 < |\eta| < 1.25$) using all
 479 three muon systems [136]. The track finders feed into the Global Muon Trigger (GMT,
 480 upgraded to μ GMT in 2016) [137, 138], which merges and sorts tracks, analyzes their

481 quality and selects the best ones.

482 The calorimeter and muon trigger systems, which have up to this point worked
 483 entirely in parallel, both send their selected candidates and global quantities to the
 484 Global Trigger (GT, upgraded to μ GT) [139, 140]. The Global Trigger contains the
 485 trigger menu, the configurable set of algorithms used to determine whether an event
 486 is accepted or not. These algorithms can use combinations of the objects from the
 487 calorimeter and muon trigger systems, including imposing topological requirements,
 488 e.g. requiring a large $\Delta\eta$ between muons in a pair. The final decision is a logical OR
 489 of all triggers in the menu, but each trigger may be prescaled, i.e. only included in
 490 the final decision a fraction of the time in order to reduce its rate. When an event is
 491 accepted, a level 1 accept (L1A) signal is sent to all CMS subsystems instructing them
 492 to read out information collected in the accepted event, which is stored in buffers until
 493 it can be read out or safely discarded. A diagram of the whole 2016 L1 trigger system
 494 and its information flow is shown in Fig. 3.11.

495 3.2.6.2 High-Level Trigger

496 After an accepted event is read out and digitized, it must undergo another level
 497 of screening before being stored. The High Level Trigger (HLT) uses full detector
 498 information reconstructed with versions of the normal CMS reconstruction algorithms
 499 specially optimized for speed, running on a large farm of commercial computers [141].
 500 Much of HLT’s power comes from having tracker information, allowing more precise
 501 momentum measurements, isolation calculations and identification algorithms than
 502 are available at L1. For example, the pixels can be used to reconstruct vertices and
 503 tag b-quark jets, and requirements can be placed on the invariant mass of a lepton
 504 pair. However, track reconstructions is slow, so it is typically only done as one of the
 505 last steps in the filtering process, allowing the event to be rejected based on more

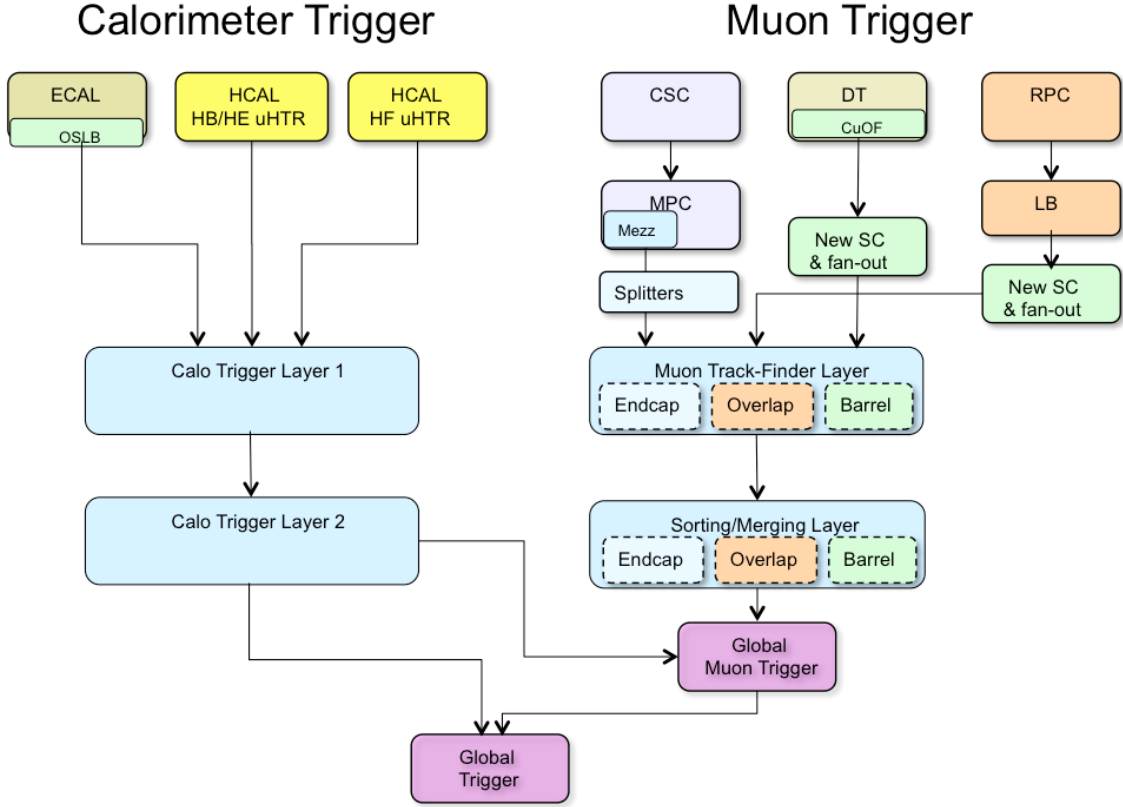


Figure 3.11: Data flow diagram for the CMS L1 trigger after the 2016 overhaul, reproduced from Ref. [129].

506 easily reconstructed objects like tracks in the muon system. Other optimizations
 507 include only reconstructing tracks near objects passed in by the L1 Global Trigger.
 508 The final result is that the rate of events saved for later analysis is around 1 kHz.

509 3.2.7 Luminosity Determination

510 A precise measurement of the luminosity delivered by the LHC is critical to precisely
 511 measuring any cross section. The instantaneous luminosity for n_b colliding bunch
 512 pairs with intensity N_b and orbit frequency f_{rev} is given by

$$\mathcal{L} = \frac{n_b N_b^2 f_{rev}}{A_{\text{eff}}} \quad (3.14)$$

513 where A_{eff} is the effective area of the beam-beam overlap. If beam i has a gaussian
 514 density profile in the u direction of width $\sigma_{i,u}$, and the beam densities are uncorrelated
 515 in each direction, then

$$A_{\text{eff}} = 2\pi \sqrt{\sigma_{1,x}^2 + \sigma_{2,x}^2} \sqrt{\sigma_{1,y}^2 + \sigma_{2,y}^2}. \quad (3.15)$$

516 The beam widths $\sigma_{i,u}$, the only unknowns in Eq. (3.14), are purely geometrical and
 517 can be found with the Van de Meer (VdM) scan method [142, 143]. In a VdM scan,
 518 for which LHC has a special run mode, one beam is held fixed while the position
 519 of the other is scanned in the x - y plane, and detector activity is measured as a
 520 function of beam displacement. Because the width of the interaction rate distribution
 521 is independent of its overall normalization, the detector activity metric may be any
 522 quantity linearly proportional to the interaction rate.

523 Over the course of an LHC run, n_b , N_b , and A_{eff} are all subject to change, and
 524 in fact the VdM scans are performed regularly, so in practice the procedure outlined
 525 above provides a calibration and overall scale for luminosity measurements during
 526 physics collisions. For a given detector metric labeled Q with rate R^Q that peaked
 527 at R_0^Q with no beam displacement, the VdM scan yields a visible cross section, the
 528 constant of proportionality between the rate and the instantaneous luminosity,

$$\sigma_{\text{vis}}^Q \equiv \frac{R^Q}{\mathcal{L}} = \frac{A_{\text{eff}} R_0^Q}{f_{\text{rev}}}. \quad (3.16)$$

529 CMS has several such metrics; the primary one used for measuring integrated lumi-
 530 nosity is the number of pixel hit clusters [144, 145]. The instantaneous luminosity is
 531 given by

$$\mathcal{L} = \frac{\langle N_c \rangle f_{\text{rev}}}{\sigma_{\text{vis}}^{\text{PCC}}} = \frac{\langle N_c \rangle f_{\text{rev}}}{A_{\text{eff}} \langle N_c \rangle_0} \quad (3.17)$$

532 where $\langle N_c \rangle = R^{\text{PCC}} / f_{\text{rev}}$ is the average number of pixel hit clusters at each bunch
 533 crossing and $\langle N_c \rangle_0$ is its peak value during the VdM scan.

534 A number of complications must be accounted for or included in systematic un-
535 certainty estimates. Beam-beam interation effects, correlations between the proton
536 density distributions in the x and y directions, drifts in the beam orbit, and nor-
537 malization uncertainties on the bunch intensity and absolute distance scale from the
538 beam spot must all be handled with care. The result is a total integrated luminosity
539 uncertainty of 2.3% in 2015 [144] and 2.5% in 2016 [145].

⁰ Chapter 4

¹ Simulation

² Comparing data collected by CMS to theoretical predictions is a complex task. The
³ theories described in Chapter 1 are understood in great detail, but using this knowl-
⁴ edge to calculate observables is a nontrivial enterprise. Once calculated, observables
⁵ must be compared to data from a detector with finite resolution and subject to a
⁶ number of experimental effects that do not exist in the rarefied world of quantum
⁷ field theory. The general strategy is to employ numerical simulations of individual
⁸ collision events that involve a physics process of interest, and apply accurate simu-
⁹ lations of the detector’s response to these events to obtain samples that are directly
¹⁰ comparable to data. The success of all steps in this process at a high-luminosity
¹¹ hadron collider is one of the triumphs of the LHC era, with many observables in
¹² interesting processes simulated accurately to the level of a few percent.

¹³ 4.1 Monte Carlo Event Generation

¹⁴ Even in trivial cases, it would be impossible to integrate over the phase space of hard
¹⁵ scattering outcomes determined from theory, convolved with matter interactions, de-

16 tector effects, and other experimental factors, to calculate observables analytically.
 17 Particle interactions are well-understood on a microscopic scale, but it is extremely
 18 difficult to extrapolate from this first-principles understanding to a description of
 19 the macroscopic behavior of an ensemble of particles as needed to make predictions
 20 about fundamentally stochastic processes. Observable spectra are therefore modeled
 21 with the Monte Carlo (MC) method [11, 146], a numerical integration technique so
 22 named because, like a casino, it relies heavily on random numbers¹. The scatter-
 23 ing amplitudes for a process are calculated from theory at a chosen perturbative
 24 order [148], and for each simulated event a configuration of final state particles is
 25 selected at random from this phase space. The final state particles are propagated
 26 through decays, radiation, hadronization, and interaction with other matter—such as
 27 the detector—based on well-understood physics principles, and the outcome of any
 28 stochastic process is chosen at random from a realistic set or distribution of possi-
 29 bilities. In the limit of a large number of simulated events, the distributions from
 30 the simulated detector will converge to be directly comparable to aggregated data.
 31 Individual steps in this process are detailed in the following sections.

32 **4.1.1 Matrix Element and Hard Process Generation**

33 Event generator programs start by calculating the scattering amplitudes for a pro-
 34 cess at a chosen order in perturbation theory. For example, the generator MAD-
 35 GRAPH5_aMC@NLO [149] generates all the relevant Feynman diagrams up to NLO
 36 and calculates the matrix elements for them. Others, like POWHEG [150–152], SHER-
 37 PA [153] and MCFM [53, 54, 154], are not fully general but have a broad range of
 38 physics processes implemented at NLO; SHERPA and MCFM can do some calculations

¹Pseudorandom numbers are actually used, but there is no difference in practice as long as a good pseudorandom number generator (PRNG) is chosen and seeded properly. The Mersenne Twister algorithm [147] is the modern standard among general-purpose PRNGs in physics and elsewhere.

39 at NNLO [155]. Events are generated across the entire allowed phase space, either
 40 uniformly or with the specific distribution dictated by one of several “importance
 41 sampling” techniques [11, 156] which ensure appropriate statistical coverage in re-
 42 gions where the distribution has a large slope or value. Each event is assigned a
 43 weight $w \in (0, 1)$ based on the scattering amplitude in that region of phase space and
 44 the probability of having an appropriate initial state based on the PDFs discussed in
 45 Section 1.6. The sample is then “unweighted” to a subset that is directly comparable
 46 to data by removing events with a probability proportional to $1 - w$.

47 4.1.2 Parton Shower, Hadronization, and Underlying Event

48 Processes generated beyond leading order may have extra radiation, as in the real
 49 emission diagrams of Fig. 2.2. In the case of calculations at higher orders in QCD, the
 50 emissions are quarks and gluons which fragment, hadronize, decay, etc. This process
 51 is handled by a parton shower (PS) MC program such as PYTHIA8 [59] (used for most
 52 simulations used in this analysis), HERWIG [157, 158], or SHERPA [153]. In PYTHIA8,
 53 parton showering is simulated with the Lund string model [11, 159–161], which treats
 54 gluons as strings connecting color charged particles whose tension increases as the
 55 quarks move apart. When a string stretches too far, it breaks, producing a quark
 56 pair at the new string ends.

57 Parton shower programs also handle radiation of soft gluons from color charged
 58 particles and photons from electrically charged particles [162]. The emitter may be
 59 an incoming parton (initial state radiation, ISR), a virtual particle exchanged during
 60 the interaction, or an outgoing particle (final state radiation, FSR). The distinction
 61 between “soft” radiation that should be handled by the PSMC and “hard” emission
 62 present in the matrix element is not well defined, so it is important to avoid double-
 63 counting regions of phase space at the boundary between the processes. This is done

64 with jet matching [11, 149]. At tree level, matching may be achieved by enforcing
 65 a jet energy cutoff: partons from the matrix element must have energy $E > E_{\text{cut}}$,
 66 and the PSMC is responsible for any softer radiation. At NLO, loop diagrams carry
 67 divergences that must be canceled by divergences of opposite sign in the infrared
 68 radiation regime, which the cutoff would prevent, so a more sophisticated scheme must
 69 be used which weights some events negatively to handle destructive interference [149]
 70 or modifies the shower development algorithm [150, 151].

71 When combining showered samples that have different jet multiplicities at the
 72 hard process level, the task becomes even more difficult because the phase space of
 73 events with n jets in the matrix element that gain another from the PS overlaps with
 74 the phase space of events with $n + 1$ jets at matrix element level. This problem can
 75 be solved with one of several jet merging algorithms [149, 163–165]. The MLM [166]
 76 and CKKW [167] algorithms implement merging for tree-level diagrams of different
 77 jet multiplicities by cutting (MLM) or weighting (CKKW) events based on the prob-
 78 ability that such an event would originate from the matrix element or PS. The FxFx
 79 algorithm implements merging when one-loop diagrams are included [168], and there-
 80 fore plays the same role in NLO calculations that the MLM and CKKW algorithms
 81 play in LO calculations.

82 PSMC programs provide several more features that are vital in obtaining a faith-
 83 ful reproduction of data, especially in events with only soft hadronic activity. The
 84 radiation described above affects the p_T of the hard scatter system, so PSMCs must
 85 “retroactively” adjust the kinematics generated by the matrix element MC. The
 86 underlying event and further QCD interactions that happen below the regime that
 87 can be calculated perturbatively are modeled phenomenologically [11, 59]. This in-
 88 cludes soft color exchange between fragments of the colliding hadrons that sends
 89 proton remnants into the detector in the form of extra soft hadrons [169]. There

90 is also a possibility that multiple pairs of partons will undergo hard interactions in
 91 the same proton-proton collision, essentially combining two quasi-independent hard
 92 scatters [162, 170].

93 4.1.3 Pileup Simulation

94 The high per-bunch luminosity of the LHC causes multiple proton-proton collisions to
 95 occur in each bunch crossing. The extra interactions are called pileup. To account for
 96 this effect, CMS simulations include extra minimum-bias collision events overlaid on
 97 top of the primary collision [171, 172]. This includes simulated pileup interactions that
 98 are time evolved to reproduce the effects of “out-of-time” pileup from previous bunch
 99 crossings, because detector electronics generally have relaxation times longer than
 100 a single bunch crossing time so signals overlap. Because MC samples are produced
 101 before the pileup profile can be measured in data, simulated events are reweighted
 102 based on the number of pileup interactions such that the distribution of the number
 103 of reconstructed vertices becomes similar to that in data.

104 4.1.4 Samples Used in this Analysis

105 The $q\bar{q} \rightarrow ZZ$, $qg \rightarrow ZZ$, $gg \rightarrow H \rightarrow ZZ^*$, and $q\bar{q} \rightarrow Z \rightarrow 4\ell$ samples are produced
 106 at NLO with POWHEG 2.0 [55, 150–152, 173] and scaled to the NNLO total cross
 107 section with K factors of 1.7 for the Higgs sample and 1.1 for the others [56]. The non-
 108 Higgs POWHEG samples include ZZ , Z/γ^* , and $\gamma^*\gamma^*$ production with a generator-level
 109 constraint of $m_{\ell\ell} > 4$ GeV for all opposite-charge lepton pairs, to limit the generated
 110 phase space to only regions of interest and far from infrared divergences. For the
 111 inclusive cross sections and differential cross sections in fully leptonic observables,
 112 this POWHEG sample is considered the primary theory prediction. For the differential

113 cross sections in jet-related variables, `MADGRAPH5_aMC@NLO` 2.3.3 [149] is used for
 114 the nominal sample, because it has an extra jet at matrix-element level, merged with
 115 the PS jets using the FxFx scheme. Box diagram $gg \rightarrow ZZ$ samples are generated
 116 with `MCFM` 7.0 at LO [174]; these are scaled to NLO with a K factor of 1.7 [57].

117 Background WZ events are produced with `POWHEG` with the same settings as the
 118 ZZ sample while $t\bar{t}Z$ and WWZ samples are generated at LO with `MADGRAPH5-`
 119 `_aMC@NLO`. Electroweak and non-VBS $ZZjj$ samples are produced with `MADGRAPH-`
 120 `5_aMC@NLO` for the VBS and aQGC searches and with `PHANTOM` 1.2.8 for the cross
 121 section measurements [175]. Samples with nonzero aTGCs are generated at LO with
 122 `SHERPA` 2.1.1 [153] and scaled such that the total yield from the SM `SHERPA` sample
 123 is the same as the yield from the `POWHEG` ZZ sample. Signal samples for the aQGC
 124 search are made with `MADGRAPH5_aMC@NLO`.

125 All samples use the `NNPDF3.0` PDF sets [176]. Parton showering, hadronization,
 126 and underlying event simulation are done with `PYTHIA8` using the CUETP8M1
 127 tune [177] for all samples except the aTGC samples, for which `SHERPA` performs
 128 these tasks.

129 4.2 Detector Simulation

130 To incorporate experimental effects into MC samples, the detector and the final state
 131 particles' interactions with it are simulated with the highest possible level of de-
 132 tail [171, 172]. The detector geometry and material, including both instrumented
 133 and non-instrumented components, are modeled with the `GEANT4` package [178],
 134 which describes microscopic particle interactions with matter over a wide range of
 135 energies and propagates the effects of these interactions to their macroscopic conse-
 136 quences. Stochastic effects are again implemented with Monte Carlo methods that

137 select outcomes at random from realistic distributions of possibilities. The GEANT4
138 simulation includes a detailed model of the magnetic field, so particle trajectories are
139 calculated correctly, and the generation of secondary particles like e^+e^- pairs from
140 photons interacting with tracker material. Charge deposition in silicon, scintillation
141 in clear crystals, hadronic showers from nuclear interactions, and ionization, are all
142 included, among many other processes. Detector signals are derived from microscopic
143 interactions, and GEANT4 simulates signals in the analog front end detector electron-
144 ics and has signal digitization capabilities which ensure that the signals coming out of
145 the simulated detector are exactly those that would be produced by the real detector
146 in the same situation.

147 The simulated signals are fed into the same reconstruction software as is used
148 for data (see Chapter 5). The same analysis strategy may then be used for MC
149 samples and data, and comparing the results is meaningful. Though every effort is
150 made to model the detector accurately, no simulation can incorporate all real effects
151 with perfect fidelity. Monte Carlo samples must be produced before data are actually
152 collected, so the final detector alignment cannot be known exactly, and conditions and
153 calibrations may change mid-run if—for example—a subdetector channel goes dead or
154 LHC beam conditions change. Residual corrections for these small effects are applied
155 to final physics objects in the final steps of the analysis to make distributions of
156 interest, such as dilepton mass around the Z resonance or the overall jet p_T spectrum,
157 match in aggregate. The overall level of agreement between data and simulation may
158 be seen in Fig. 4.1, which shows the invariant mass of e^+e^- events around the Z
159 resonance for simulated samples and data, and their ratio.

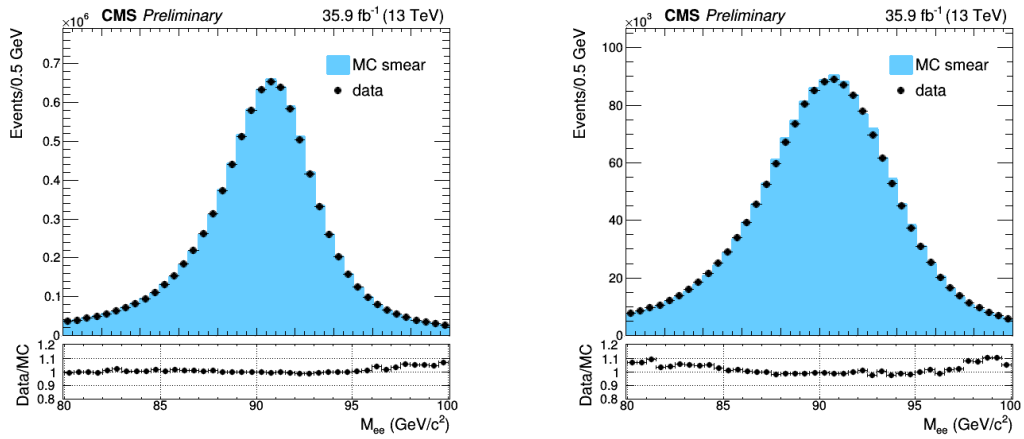


Figure 4.1: The invariant mass of e^+e^- events with both electrons in the barrel (left) and both electrons in the endcaps (right) in the whole 2016 dataset after all corrections are applied. The lower plots show the ratio of data and simulation to show the level of agreement achieved.

0 Chapter 5

1 Object Reconstruction and 2 Selection

3 The raw detector information stored on disk after an event passes trigger selections
4 is not yet suitable for physics analysis. Hits in the tracker and muon systems, and
5 energy deposits in the calorimeters, require significant processing to build physics
6 objects that are interpretable in terms of the physics of the hard scatter. Patterns in
7 the tracker and muon system hits are found and used to construct charged particle
8 and muon tracks, and energy deposits in the calorimeters are grouped into clusters.
9 Final state particles that interact with CMS are reconstructed from the tracks and
10 calorimeter clusters, final state particles are clustered into jets, charged particles are
11 clustered by track origin to find proton-proton collision vertices, and visible particle
12 momenta are summed to find the transverse momentum imbalance from undetectable
13 particles (in the SM, neutrinos). The resulting physics objects undergo selection to
14 determine which represent real particles of interest for the analysis. Selected particles
15 are used to reconstruct the hard interaction from the collision—in the analyses pre-
16 sented here, leptons are paired to form Z/γ^* boson candidates which may be paired

17 to form Higgs or Z boson candidates or nonresonant ZZ candidates, and jets are
18 used to construct hadronic observables and to distinguish electroweak and QCD ZZ
19 production.

20 **5.1 Track Reconstruction and Vertex**

21 **Identification**

22 Tracks are reconstructed in the inner tracker by iterative application of a combina-
23 torial Kalman filter algorithm [179–182]. At each iteration, tracks found in the pixel
24 detector are used as “seeds”, track segments which serve as the initial trajectories on
25 which strip tracker hits from the same particle are expected. The pixel seed supplies
26 the initial parameters for the combinatorial Kalman filter. At each tracker layer, the
27 algorithm predicts where the particle will hit the next layer based on the track’s cur-
28 rent parameters, taking into account the effects of particle interaction with tracker
29 material. The extrapolated trajectory is used to find compatible hits in the next layer
30 with a χ^2 test, and if possible the most compatible hit is added to the track and its
31 parameters are updated accordingly. If no hits are compatible, a “ghost” hit which
32 does not contribute to the track parameters may be added to account for the possibil-
33 ity of a missing hit in the corresponding layer. This procedure is repeated recursively
34 at each tracker layer, from the innermost layer past the seed to the outermost layer
35 of the silicon strip tracker. If two tracks found in an iteration share too many hits,
36 they are assumed to be from the same particle and the one with fewer hits is rejected,
37 using the total χ^2 of all hits as a tiebreaker. The first iterations of the track finding
38 algorithm searches for high- p_T tracks from primary proton-proton interactions, which
39 are easier to find because they are close to straight and originate from the beam line.
40 When a track is found, its constituent hits are removed from consideration in future

41 iterations, reducing the computational complexity of finding the more difficult tracks
 42 from lower- p_T particles and products of b hadron decays which happen away from
 43 the beam line.

44 Because the Kalman filter obtains the final track parameters only at the out-
 45 ermost tracker layer, each track is refit and smoothed with further Kalman filters,
 46 improving track quality and reducing fake rate. Spurious tracks are rejected from the
 47 final collection with requirements on the number of layers hit, the χ^2 of the fit, and
 48 compatibility with a primary vertex.LHC The efficiency for reconstructing tracks of
 49 all prompt charged particles with $p_T > 900$ MeV is around 94% in the barrel and
 50 85% in the endcap; for isolated muons, it is virtually 100% in the whole tracker
 51 acceptance [182].

52 Electrons lose substantially more energy to interactions with the tracker material
 53 than other charged particles, often breaking the assumption of Gaussian energy loss
 54 inherent to the Kalman filter. To mitigate the impact of the resulting poor track
 55 fits, tracks with many missing hits or a poor χ^2 are refit using a Gaussian sum filter
 56 (GSF) [183]. Any Kalman filter or GSF tracks with trajectories that intersect ECAL
 57 energy clusters (see below) are considered electron track candidates and refit with a
 58 second, more complicated GSF. This GSF track collection is used as inputs to the
 59 PF electron reconstruction described below.

60 Proton-proton interaction vertices are found by clustering tracks by minimizing
 61 the figure of merit

$$\chi^2 = \sum_i \sum_j p_{ij} \frac{(z_j^t - z_i^V)^2}{\sigma_j^2}, \quad (5.1)$$

62 where z_i^V is the z position of vertex i , z_j^t is the z position of track j at its closest
 63 point to the beamline, and σ_j^2 is its uncertainty. The track-vertex association matrix
 64 p_{ij} maps tracks to their associated vertices, i.e. $p_{ij} = 1$ if vertex i and track j are
 65 associated, $p_{ij} = 0$ if they are not. Rather than minimize Eq. (5.1) directly with an

66 unknown number of vertices, the CMS clustering algorithm [182, 184] uses a tech-
 67 nique known as deterministic annealing [185], which treats the system as a statistical
 68 ensemble of associations between the tracks and an unknown number of vertices. The
 69 association matrix p_{ij} is then the probability that vertex i and track j are associated.
 70 If every possible set of assignments, for every possible number and arrangement of
 71 vertices, is considered equally probable, this is analogous to a thermodynamic system
 72 at high temperature, with χ^2 playing the role of energy. The system is simulated at
 73 high “temperature” and the analog of free energy is minimized to determine p_{ij} . The
 74 temperature is then lowered in steps, with track-vertex associations deterministic in
 75 the limit of zero temperature.

76 Among the interaction vertices in an event, the one whose associated charged
 77 particles have the highest sum of p_T^2 is labeled the primary vertex (PV). A PV must
 78 be less than 24 cm from the nominal beam spot in the z direction and less than
 79 2 cm from it in the x - y plane. Many commonly-used analysis observables are strongly
 80 dependent on the number of secondary proton-proton interaction vertices in the event,
 81 colloquially called the pileup. The pileup distributions used in Monte Carlo samples
 82 are not the same as the distribution in data, biasing sensitive quantities. Monte
 83 Carlo events are therefore reweighted based on the number of simulated pileup vertices
 84 such that the overall N_{vtx} (number of proton-proton interaction vertices) distributions
 85 match.

86 5.2 Particle Flow Reconstruction

87 The simplest conceivable algorithm would reconstruct each type of particle mostly
 88 with information from single subsystems: muons with the outer muon system, elec-
 89 trons and photons with ECAL (using HCAL to differentiate them from hadrons), jets

90 with the calorimeters aided by inner tracker information to handle b jet vertexing, etc.
 91 This approach is sufficient for many analyses and sophisticated versions of the general
 92 principle have performed admirably at a number of experiments, but it is suboptimal.
 93 It fails to exploit the full detector information for many objects—for example, not
 94 using the inner tracker’s precise measurements of low-energy charged hadrons in jets
 95 made by clustering calorimeter deposits—and misses significant correlations between
 96 detector systems. The CMS collaboration takes a different approach, using a particle
 97 flow (PF) algorithm combining subdetector signals for optimal particle reconstruction
 98 and identification [186–188].

99 Several features of CMS facilitate PF reconstruction, as described in Section 3.2.
 100 The most important is that the calorimeters are inside the magnet and close to the
 101 tracker, so charged particles are much less likely to interact with material between
 102 them. The inner tracker’s precise position measurement and ECAL’s fine segmen-
 103 tation thus allow tracks to be associated to calorimeter clusters even for individual
 104 charged hadrons of modest energy.

105 5.2.1 PF Candidates

106 The inputs to the PF algorithm are inner tracker tracks, muon system tracks, and
 107 clusters of energy deposits in the calorimeters, all of which are calibrated beforehand.
 108 Calorimeter clusters are built independently for each subsystem, with ECAL and
 109 HCAL barrel and endcaps considered separately. Topological clusters are built by
 110 combining adjacent cells with energy deposits over a threshold, using cells that are
 111 local energy maxima as seeds. Within the topological clusters, the final calorime-
 112 ter clusters are built by fitting the energy deposits with the sum of several two-
 113 dimensional Gaussians, one Gaussian for each seed in the topological cluster.

114 The first step of the PF algorithm is to link tracks and clusters across subdetec-

115 tors. Tracks are linked to calorimeter clusters by extrapolating from the track to the
 116 calorimeter cells the particle would be expected to hit. To account for bremsstrahlung
 117 photons from electron interactions with tracker material, GSF tracks are linked with
 118 ECAL clusters compatible ($\Delta\eta < 0.05$) with a tangent to the track where it hit the
 119 tracker. Overlapping ECAL and HCAL clusters are linked outside the inner tracker
 120 acceptance. Inner tracks are linked to muon system tracks if their hits can be propa-
 121 gated onto a common surface and merged into a single track within the resolution of
 122 the muon system (see Section 3.3 of Ref. [188]). The groups of linked objects, called
 123 “PF blocks”, usually originate from one or a few particles and are the basic unit of
 124 PF reconstruction.

125 5.2.1.1 Muons

126 Muon candidates in CMS [189] come in three flavors: “standalone”, “tracker”, and
 127 “global” muons. Standalone muons use only the track from the muon spectrometer
 128 (the “standalone track”), built with a fit to track segments made of clusters of hits in
 129 the DTs, CSCs, and RPCs. Tracker muons use only the inner track, identified as a
 130 muon because the track is compatible with one or more track segments in the muon
 131 system within 3 cm transverse to the track direction, or four standard deviations
 132 of the track’s angular position uncertainty. Global muons use a combined “global
 133 track” made by fitting the hits in an inner track and a compatible standalone track
 134 to a common muon trajectory through the whole detector. By construction, global
 135 muons have corresponding standalone and tracker muons. Tracker muons are merged
 136 into their corresponding global muons, which use the inner track momentum for
 137 muons with $p_T < 200$ GeV and the momentum of the track with the best normalized
 138 χ^2 otherwise. When a muon candidate is reconstructed, its constituent tracks are
 139 removed from the PF block and are therefore not used in further reconstruction.

140 **5.2.1.2 Electrons and Prompt Photons**

141 Electron reconstruction uses GSF tracks linked with ECAL clusters [183, 190]. The
 142 cluster associated with a track and the bremsstrahlung candidate clusters on tangents
 143 to the track are collectively called the “supercluster”. Prompt photons are recon-
 144 structed from superclusters without associated tracks except displaced track pairs
 145 consistent with photon-initiated electron-positron pair production in the tracker ma-
 146 terial [191]. In both cases, the HCAL energy near the supercluster cannot be more
 147 than 10% of the supercluster energy. Non-isolated photons, i.e. those with substan-
 148 tial nearby tracks or calorimeter deposits or a high ratio of HCAL energy to ECAL
 149 energy, are assumed to be from π^0 decays and are described with neutral hadrons in
 150 the next section. Tracks and clusters used to reconstruct electrons and photons are
 151 removed from the PF block and are not used in hadron reconstruction.

152 **5.2.1.3 Charged and Neutral Hadrons**

153 With muon, electron, and prompt photon constituents removed, remaining detector
 154 signals are taken to be from charged and neutral hadrons (including non-prompt
 155 photons) [186, 188]. Clusters in ECAL without associated tracks are taken to be
 156 photons from π^0 decays, because neutral hadrons deposit very little energy in ECAL.
 157 Trackless clusters in HCAL are taken to be neutral hadrons. Both are removed from
 158 the PF blocks, so all that remain are linked clusters and tracks. Paired tracks and
 159 clusters with compatible energies are taken to be charged hadrons. If the track p_T
 160 is much less than the calorimeter-measured p_T , the pair is labeled as overlapping
 161 charged and neutral hadrons.

162 **5.2.2 Jets**

163 Effective clustering of hadrons, non-prompt photons, and non-prompt leptons into jets
 164 is critically important for many physics analyses, including the ZZ + jets differential
 165 cross section measurements and the ZZ VBS search (see Sections 6.5 and 5.4.3).
 166 Clustering must be efficient, to ensure the tagging jets in VBS events are found,
 167 but the clustering algorithm should not tag spurious jets, as the number of jets in
 168 an event is sensitive to higher-order QCD corrections and therefore an interesting
 169 quantity to compare to theoretical predictions. Similarly, the algorithm should not
 170 erroneously cluster particles from the same initial parton into multiple jets or merge
 171 jets from multiple original partons, because the kinematics of the original quarks and
 172 gluons are also of theoretical interest and the detector-level jet kinematics should
 173 accurately reflect them. A clustering algorithm is said to be “infrared safe” if the
 174 presence of low-energy hadrons from soft gluon radiation does not change the number
 175 of jets or have a qualitatively significant effect on jet shapes and kinematics. This
 176 fits with the intuition that a single 1 GeV pion should have essentially no effect in
 177 an event with multiple jets with energies on the order of hundreds of GeV [192].
 178 An algorithm is said to be “collinear safe” if the jets are not changed substantially
 179 by splitting one hadron into two nearly collinear hadrons with the same total four-
 180 momentum. This also fits with physical intuition in that jets deposit energy over
 181 an area significantly larger than the spatial resolution of the detector, so increasing
 182 the detector granularity enough to resolve two very close particles (without changing
 183 their total four-momentum) should have little or no effect on the jet.

184 Infrared and collinear (IRC) safety are critically important for comparing data
 185 to theoretical predictions [193]. Collinear splittings and soft gluon radiation during
 186 jet fragmentation should not affect the dynamics of the TeV-scale hard scattering
 187 processes we wish to probe, but they are nonperturbative and difficult to model

188 (see Section 4.1.2), and experimental analysis can only probe the underlying hard
 189 interaction if it is insensitive to this kind of mismodeling. Experimental detectors'
 190 finite resolution and inability to measure arbitrarily soft particles enforces some level
 191 of IRC safety on any algorithm, but the results of an analysis methods that uses
 192 an IRC unsafe clustering will depend on the complex, detector-dependent details
 193 of this partial IRC regularization. In any case, the most meaningful comparisons
 194 between data and theory should use the same definition of a jet in the experimental
 195 analysis and the perturbative calculation, and perturbative calculations require IRC
 196 safe observables to preserve unitarity.

197 These considerations, and the desire for conical jets with a well-defined area in
 198 the η - ϕ plane, lead most CMS analyses (including this one) to use jets clustered with
 199 the anti- k_T algorithm [194, 195]. The anti- k_T algorithm defines the distance between
 200 two particles i and j as

$$d_{ij} = \min(p_{Ti}^{-2}, p_{Tj}^{-2}) \frac{\Delta_{ij}}{R}, \quad (5.2)$$

201 where Δ_{ij} is the distance in the rapidity-polar angle plane,

$$\Delta_{ij}^2 \equiv (y_i - y_j)^2 + (\phi_i - \phi_j)^2, \quad (5.3)$$

202 and R is a parameter setting the size of the resulting jets. The algorithm proceeds
 203 iteratively. At each iteration, if the smallest d_{ij} between any pair of particles in the
 204 event is smaller than the smallest p_T^{-2} of any single particle, the particles in the pair
 205 are merged into a single particle with their total four-momentum. If the minimum
 206 single-particle p_T^{-2} is smaller than the minimum d_{ij} , the single particle is labeled a
 207 jet and removed from further consideration. Iteration proceeds until all particles are
 208 part of a jet. In this analysis, the size parameter used is $R = 0.4$.

209 Charged hadrons whose tracks originate in pileup interactions are not included in
 210 jet clustering [196]. The contribution of neutral hadrons from pileup is estimated with

211 a jet area technique [197–199] in which the energy density of neutral hadrons from
 212 pileup is calculated event-by-event and multiplied by the area of the jet to estimate
 213 the neutral pileup contribution, which is subtracted from the jet energy. Jets in
 214 Monte Carlo samples have their energy shifted and stochastically smeared such that
 215 the overall energy scale and resolution match that of jets in data [197, 200].

216 5.2.3 Missing Transverse Energy

217 Neutrinos—or, hypothetically, WIMP dark matter or other new particles that do not
 218 decay or interact directly with the detector—escape and cannot be directly measured.
 219 Because the beams have no momentum in the x - y plane, the transverse momentum
 220 of the visible particles must balance the transverse momentum of the invisible ones.
 221 The missing transverse momentum is thus

$$\vec{p}_T^{\text{miss}} = - \sum_{\text{visible}} \vec{p}_T, \quad (5.4)$$

222 where the sum runs over the transverse momenta of all PF candidates in the event.
 223 The missing transverse energy, E_T^{miss} , is its magnitude. The E_T^{miss} is calibrated by
 224 propagating the jet energy scale corrections to the E_T^{miss} calculation [201–203]. All
 225 PF candidates are included in the sum in Eq. (5.4), including those originating from
 226 pileup interactions, because these soft collisions are very unlikely to produce neutrili-
 227 nos, so including them biases the measurement less than trying to determine which
 228 neutral particles should be considered pileup and which should not.

229 5.3 Object Identification and Selection

230 The reconstruction algorithms described above are general purpose in the sense that
 231 they can be used in nearly any analysis, but do not address the specific needs of

any, so further selections are essentially always required to optimize object efficiency and purity for studying a specific physics process. The leptons used in this analysis are required to pass identification requirements on top of those imposed during PF reconstruction, and are required to be isolated from other particles in the event, to reject fake objects from jet fragmentation. Four-lepton processes have low reducible backgrounds, so the selections presented here are generally loose, optimized for high efficiency compared to most CMS analyses.

5.3.1 Electrons

Electrons are required to have $p_T > 7 \text{ GeV}$ and to be in the tracker acceptance, $|\eta| < 2.5$. They must be compatible with the PV, with minimum track-PV distance $d_z < 1 \text{ cm}$ in the z direction and $d_{xy} < 5 \text{ mm}$ in the plane transverse to the beam. Each electron's 3-dimensional impact parameter (IP) $d_{3\text{D}}$ must satisfy a requirement on its significance,

$$\text{SIP}_{3\text{D}} \equiv \frac{d_{3\text{D}}}{\sigma_{d_{3\text{D}}}}, \quad (5.5)$$

where $\sigma_{d_{3\text{D}}}$ is the uncertainty on the IP. The $\text{SIP}_{3\text{D}}$ requirement is $\text{SIP}_{3\text{D}} < 10$ for the ZZ and $Z \rightarrow 4\ell$ cross section measurements and the aTGC search, and $\text{SIP}_{3\text{D}} < 4$ for the Higgs boson measurement and the VBS and aQGC searches. To remove fake electrons arising from muon tracks being associated to photons or other incidental ECAL energy clusters, electrons within $\Delta R < 0.05$ of a muon are vetoed.

To further reduce photon and jet fragment backgrounds while maintaining high prompt electron efficiency, a further selection is applied using a multivariate discriminator made with a boosted decision tree (BDT) [204, 205]. The BDT uses 21 input variables, which fall into three broad categories:

- Track-related observables like the number of hits and normalized χ^2 of the

255 Kalman and GSF tracks and the energy lost to bremsstrahlung according to
 256 the GSF fit. These are intended to discriminate between electrons and charged
 257 hadrons.

- 258 • Calorimetric information including a number of supercluster shape observables
 259 and the amount of HCAL energy near the supercluster, to discriminate electrons
 260 from electromagnetically rich jets.
- 261 • Track-cluster observables comparing the positions and momenta of the particles
 262 seen in the tracker and by ECAL.

263 The BDT training and working point selection are done separately for electron can-
 264 didates with p_T above and below 10 GeV and in three bins of $|\eta|$ (0–0.8, 0.8–1.479,
 265 and 1.479–2.5). The working points are chosen to correspond to 98% efficiency for
 266 single signal electrons in each bin.

267 To ensure that electron candidates are not part of a jet, they are required to be
 268 isolated from other particles in the event. The relative isolation is defined as

$$R_{\text{Iso}} = \left(\sum_{\text{charged}} p_T + \max \left[0, \sum_{\text{neutral}} p_T + \sum_{\text{photons}} p_T - p_T^{\text{PU}}(\ell) \right] \right) / p_T^\ell \quad (5.6)$$

269 where the sums run over the p_T of PF hadrons and photons in a cone of $\Delta R < 0.3$
 270 around the electron trajectory. To mitigate the contribution of pileup to the isolation
 271 calculations, charged hadrons are included only if they originate from the event’s PV.
 272 The estimated neutral contribution to isolation from pileup, $p_T^{\text{PU}}(\ell)$, is defined for
 273 electrons as

$$p_T^{\text{PU}}(e) \equiv \rho \times A_{\text{eff}}, \quad (5.7)$$

274 where the average transverse-momentum flow density ρ is calculated in each event
 275 using the jet area method described above. The effective area A_{eff} is the geometric
 276 area of the isolation cone times an η -dependent correction factor that accounts for

277 the residual dependence of the isolation on pileup. Electrons are considered isolated
 278 if their relative isolations satisfy $R_{\text{iso}} < 0.35$.

279 Efficiencies for GSF track reconstruction, electron reconstruction and identifica-
 280 tion, and electron isolation criteria, are found with a “tag-and-probe” method [206].
 281 In this technique, events are selected which contain at least one high- p_{T} “tag” electron
 282 passing strict ID and isolation requirements, and a “probe” track with the opposite
 283 sign that combines with the electron to have an invariant mass close to the Z boson
 284 mass. The resulting sample is enriched with $Z \rightarrow e^+e^-$ events, so the track is likely
 285 to correspond to a real prompt electron. Unlike all background processes, $Z \rightarrow e^+e^-$
 286 production forms a distinct resonance peak in the $m_{\ell\ell}$ distribution, so shape fits can
 287 be used to find the overall purity of the sample, and thus the number of prompt elec-
 288 trons among the probes. The selection efficiency is then the number of passing probes
 289 divided by the total number of prompt probes. This procedure is performed in bins
 290 of p_{T} and η for data and Monte Carlo events, and residual differences in efficiency in
 291 Monte Carlo samples are corrected to match data by weighting events by the ratio
 292 of data and Monte Carlo efficiency for each electron candidate. Overall electron effi-
 293 ciency varies between roughly 85% in the inner endcap ($|\eta| > 2.0$) to around 95% in
 294 the central barrel ($|\eta| < 0.8$).

295 5.3.2 Muons

296 Muon selection is similar to electron selection, but simpler because muon backgrounds
 297 are much smaller. Candidate muons are required to be tracker or global muons with
 298 $p_{\text{T}} > 5 \text{ GeV}$ within the muon system acceptance ($|\eta| < 2.4$). They are subject to the
 299 same PV compatibility criteria as electrons, $d_z < 1 \text{ cm}$, $d_{xy} < 5 \text{ mm}$, and $\text{SIP}_{3D} < 10$
 300 or 4 depending on the analysis. Muon candidates are further subject to the so-called
 301 “PF ID” criteria, which require them to be isolated from calorimeter deposits or to

302 have high-quality tracks with good fits [188].

303 Isolation is defined as in Eq. (5.6), the same as for electrons except for the defini-
 304 tion of the neutral pileup contribution, which for muons is based on using the known
 305 charged pileup density to estimate the neutral pileup based on the average charge
 306 composition of pileup jets,

$$p_T^{\text{PU}}(\mu) \equiv 0.5 \sum_{\text{charged}} p_T^{\text{PU}}, \quad (5.8)$$

307 where the sum runs over the charged particles from all pileup vertices. As for elec-
 308 trons, the radius of the isolation cone is 0.3 in the η - ϕ plane and the selection criterion
 309 is $R_{\text{iso}} < 0.35$. Muon efficiencies are measured and corrected with the same tag-and-
 310 probe technique as used for electrons, and found to be around 97%.

311 5.3.3 Final State Photon Radiation

312 Final-state radiation (FSR) photons emitted by muons are not included in the PF
 313 momentum reconstruction, and some photons emitted by electrons may be missed,
 314 degrading Z boson reconstruction. Photons are considered FSR candidates if they
 315 have $p_T > 2 \text{ GeV}$, $|\eta| < 2.4$, relative isolation $R_{\text{iso}} < 1.8$ as defined in Eq. (5.6) (with
 316 no neutral pileup correction), and $\Delta R(\ell, \gamma) < 0.5$ with respect to the nearest lepton.
 317 To avoid double counting, photons in electron superclusters are not considered. Be-
 318 cause FSR has a higher energy spectrum than photons from pileup and is expected
 319 to be quasi-collinear with the emitting leptons, a photon is accepted as FSR and
 320 included in the ZZ final state if $\Delta R(\ell, \gamma) / E_{T\gamma}^2 < 0.012$. The performance of this
 321 algorithm is tuned and evaluated with comparisons to generator-level information in
 322 MC samples, and is found to have efficiency around 60% for a purity around 80%.
 323 FSR photons are omitted from the isolation determination for emitting leptons. In

324 the rest of this thesis, the momentum of any FSR photons found is included in Z/γ^*
 325 and ZZ four-momenta unless otherwise stated.

326 **5.3.4 Jets**

327 Jets are considered for analysis if they have $p_T > 30 \text{ GeV}$ and $|\eta| < 4.7$. Loose criteria
 328 are applied to reject spurious jets by requiring they contain multiple particles, and
 329 the particles be a mix of charged and neutral consistent with hadronic jets. Jets are
 330 removed from consideration in the event if a lepton or FSR photon is in its cone
 331 ($\Delta R < 0.4$ with respect to the jet’s total momentum vector).

332 **5.3.5 Misidentified Objects**

333 The reducible background estimation method described in Section 6.1 requires the use
 334 of “loose” lepton candidates which are similar to candidates passing the full selection
 335 but much more likely to be jet fragments or other non-prompt objects. Loose lepton
 336 candidates pass the p_T and η cuts and vertex compatibility criteria, but the other
 337 identification criteria are reduced. The electron BDT discriminator is not applied to
 338 loose electrons. Loose muons must still be tracker or global muons, but the PF ID is
 339 not applied. Isolation requirements are not applied to loose candidates. Depending
 340 on their use, loose candidates may have no further requirements applied, or may be
 341 required to fail the tight ID and/or isolation requirements, as detailed in Section 6.1,
 342 where the fake rates for electrons and muons are shown in Fig. 6.1. Aside from the
 343 ID and isolation criteria, loose leptons are treated the same as their tight cousins,
 344 with FSR recovery performed with the same algorithm. Jets near loose leptons are
 345 only removed if the loose lepton is taken to be one of the four in the ZZ candidate in
 346 the final event interpretation.

³⁴⁷ 5.4 ZZ Candidate and Event Selection

³⁴⁸ Online event selections used single, double, and triple lepton triggers. The double
³⁴⁹ lepton triggers were the primary paths, with single and triple lepton triggers correct-
³⁵⁰ ing for residual inefficiencies to bring the overall trigger efficiency above 99%. Exact
³⁵¹ HLT parameters changed over the course of datataking as instantaneous luminosities
³⁵² changed and trigger rates rose, so many thresholds are shown here as ranges.

³⁵³ • Single muon p_T thresholds were between 20 and 24 GeV for isolated muons.
³⁵⁴ Nonisolated single muons were required to have $p_T > 50$ GeV or $p_T > 45$ GeV
³⁵⁵ and $|\eta| < 2.1$. Single electron p_T thresholds were 25 or 27 GeV depending on
³⁵⁶ ID criteria applied.

³⁵⁷ • Leading lepton p_T thresholds in double lepton paths were 17 or 23 GeV. Trailing
³⁵⁸ lepton thresholds were 12 GeV and 8 GeV for electrons and muons, respectively.
³⁵⁹ Isolation requirements and requirements on the z -axis distance between lepton
³⁶⁰ track origins were added part way through datataking.

³⁶¹ • The p_T requirements in triple lepton paths varied between 5 and 16 GeV, with
³⁶² no isolation or vertex requirements.

³⁶³ An event is considered for the analysis if any of these triggers fires.

³⁶⁴ Several distinct analyses fall under the four-lepton umbrella, each with different
³⁶⁵ requirements and therefore different selection criteria. The sets of selections will be
³⁶⁶ listed here with brief descriptions of their uses, and detailed in full below.

³⁶⁷ • The *full spectrum selection* picks a phase space that encompasses all four-lepton
³⁶⁸ events, and all other selection sets yield strict subsets of the full spectrum phase
³⁶⁹ space.

- 370 • The *singly resonant* ($Z \rightarrow 4\ell$) *selection* picks events with four-lepton mass
 371 around the Z boson resonance.
- 372 • The *Higgs selection* is that used for the Higgs boson discovery and properties
 373 measurements. It is similar to the full spectrum selection but with slightly
 374 tighter requirements on the second Z/γ^* candidate, because $Z \rightarrow 4\ell$ events are
 375 of less interest and some backgrounds may be reduced by excluding events with
 376 an on-shell Z boson and a low mass lepton pair that could be a decay of an Υ
 377 or similar meson.
- 378 • The *on-shell* or *doubly resonant* selection requires both Z candidates to be
 379 compatible with a resonant Z boson. It is used for the ZZ and ZZ + jets cross
 380 section measurements and the aTGC search.
- 381 • The *dijet* (ZZjj) *selection* uses the on-shell selection for the four-lepton system,
 382 and additionally requires at least two jets. It is used for the VBS and aQGC
 383 searches.

384 5.4.1 Z/γ^* Candidate Selection

385 A Z/γ^* candidate is built from a pair of opposite-sign, same-flavor leptons with
 386 invariant mass between 4 and 120 GeV. The Z/γ^* candidate with mass closest to the
 387 nominal Z boson mass is labeled Z_1 , the other is labeled Z_2 . Mass requirements on
 388 the Z/γ^* candidates are among the primary differences between the various analysis
 389 selections. The full spectrum, $Z \rightarrow 4\ell$, and Higgs selections require $m_{Z_1} > 40$ GeV.
 390 The Higgs selection additionally requires $m_{Z_2} > 12$ GeV. The on-shell and dijet
 391 selections require both Z_1 and Z_2 to have $m_{Z_i} > 60$ GeV. The mass range thus
 392 allowed, $60 < m_{Z_{1,2}} < 120$ GeV, serves as the definition of an on-shell Z boson for
 393 purposes of this analysis.

394 5.4.2 ZZ Candidate Selection

395 Four-lepton candidates are built from pairs of Z/γ^* candidates. Among the four lep-
 396 tons in the candidate, all opposite-sign pairs must have invariant mass $m_{\ell^+\ell'^-} > 4 \text{ GeV}$
 397 regardless of flavor, to remove events in which decay products of a light, leptонically
 398 decaying particle like a J/ψ are erroneously paired with the two leptons from a real Z
 399 boson to form two false Z/γ^* candidates by chance when paired incorrectly. The re-
 400 quirement on all pairs does not include FSR photons, because the mesons that would
 401 cause such a problem are generally found in jets which include photons from π^0 decays,
 402 whcih are likely to be misidentified as FSR. All lepton pairs must have $\Delta R > 0.02$
 403 to avoid “ghost” leptons with shared tracks. The leading and lepton among the four
 404 must have $p_T > 20 \text{ GeV}$, and the subleading lepton must have $p_T > 10 \text{ GeV}$ if it is
 405 an electron or $p_T > 12 \text{ GeV}$ if it is an electron. The $Z \rightarrow 4\ell$ selection requires the
 406 candidate to have $80 < m_{4\ell} < 100 \text{ GeV}$, consistent with resonant single- Z production.

407 All allowed pairings of leptons into Z/γ^* candidates are examined separately, so
 408 an event with two electrons and two positrons, for example, will yield two possible
 409 ZZ candidates, with the only difference being how the electrons are paired into Z_1
 410 and Z_2 . In the case that multiple interpretations of the same event pass the full
 411 selection, the one with Z_1 closest to the nominal Z mass is chosen. In the rare case of
 412 further ambiguity, which may arise in events with five or more leptons, Z_2 is chosen
 413 to maximize the scalar p_T sum of the four leptons. This best candidate selection is
 414 done after the full selection is applied, and the other analysis selections are applied to
 415 the disambiguated events in the full spectrum phase space. Like the mass cut on all
 416 opposite-sign lepton pairs, this prevents events with one on-shell Z and one lower-mass
 417 γ^* from passing the on-shell Z mass cuts with an erroneous lepton pairing.

418 The total efficiency of all selections is estimated by finding the fraction of events
 419 in the POWHEG and MCFM ZZ samples which pass both the fiducial cuts at generator

420 level and the full analysis selection after detector simulation and reconstruction. For
421 the doubly on-shell selection ($60 < m_{\ell\ell} < 120$ GeV), the efficiency is 54% for 4e events,
422 65% for 2e2 μ events, and 78% for 4 μ events. For $Z \rightarrow 4\ell$ events, the efficiencies for
423 the 4e, 2e2 μ , and 4 μ channels are, respectively, 24%, 36%, and 73%.

424 5.4.3 Dijet and VBS Signal Selection

425 The dijet selection, used for the VBS and aQGC searches, requires the event to contain
426 two or more jets. The two highest- p_T jets are called the “tagging jets.” The tagging
427 dijet system must have $m_{jj} > 100$ GeV. This criterion is not intended to preferentially
428 select the EWK signal, which is concentrated at much higher dijet masses, but rather
429 to provide a minimal selection for the sample on which to perform the multivariate
430 VBS analysis described in Section 6.5 and the shape-based aQGC analysis described
431 in Section 6.6. No further selections are applied, and the VBS signal efficiency is
432 therefore close to 100%.

⁰ Chapter 6

¹ Analysis Strategy

² 6.1 Background Estimation

3 Reducible backgrounds for four-lepton events typically have two or three prompt
 4 leptons and two or one other objects—typically jet fragments, sometimes photons—
 5 which are misidentified as prompt leptons. The largest source of background contam-
 6 ination is from events in which a Z boson is produced in association with a photon
 7 and a jet, a leptonically-decaying W boson and a jet, or two jets. There is also a
 8 contribution from $t\bar{t}$ events in which both top quarks decay to a lepton, a neutrino,
 9 and a b quark jet. For simplicity, the two sets of processes are not treated separately
 10 in what follows, and are collectively labeled “Z + X” events¹.

11 The contributions of the reducible backgrounds to the selected four-lepton sig-
 12 nal samples are evaluated using the tight-to-loose “fake rates” method, described in
 13 Ref. [207]. In this procedure, the likelihood of a nonprompt (“fake”) object to be
 14 misidentified as a prompt lepton is estimated and applied to control regions enriched
 15 with Z + X events to estimate their contribution to the signal region. The lepton

¹This is a bit of a misnomer, as “Z + X” does not accurately describe $t\bar{t}$ events, but the terminology is retained here for consistency with the CMS papers on these analyses.

16 misidentification rate $f_\ell(p_T^\ell, \eta^\ell)$ is measured from a sample of $Z + \ell_{\text{fake}}$ events, where
 17 the Z boson candidate is selected as in the signal region but with $|m_{\ell\ell} - m_Z| < 10 \text{ GeV}$,
 18 and the ℓ_{fake} object is a lepton candidate that passes relaxed ID requirements as de-
 19 fined in Section 5.3.5, with no isolation or tight ID requirements applied.

20 The misidentification rate is defined as the fraction of ℓ_{fake} candidates which pass
 21 full lepton identification and isolation criteria, in bins of p_T and η . One should note
 22 that the misidentification rate cannot be interpreted as a probability in the usual
 23 sense, and in fact there is no simple physical interpretation of it. Events with three
 24 prompt leptons can contaminate this control region and bias the misidentification
 25 rate, because the non- Z lepton is falsely assumed fake. To mitigate this bias, the
 26 $WZ \rightarrow 3\ell\nu$ yields in the numerator and denominator in each bin are estimated from
 27 a simulated sample and subtracted before the ratio of yields is taken. Figure 6.1
 28 shows the misidentification rates for electrons and muons separately as a function of
 29 p_T and η .

30 To estimate the total reducible background yield, the misidentification rates are
 31 applied to two $Z + X$ enriched control samples, each containing a Z boson candidate
 32 passing all signal region requirements plus two more lepton candidates which pass the
 33 relaxed identification criteria and would make a second Z boson candidate according
 34 to Section 5.4.1 except that one or both fail the full identification or isolation criteria.
 35 The sample with one failing lepton, called the “3P1F” sample for “3 prompt 1 fake,”
 36 covers the contribution from WZ events, while the sample with both leptons in the
 37 second Z boson failing (“2P2F”) covers $Z + \text{jets}$ and $t\bar{t}$ events. The fake object transfer
 38 factor

$$F_\ell(p_T^\ell, \eta^\ell) = \frac{f_\ell(p_T^\ell, \eta^\ell)}{1 - f_\ell(p_T^\ell, \eta^\ell)} \quad (6.1)$$

39 is the ratio of nonprompt objects passing the relaxed and full selection criteria, and
 40 thus serves as a per-lepton extrapolation factor between control sample yields and

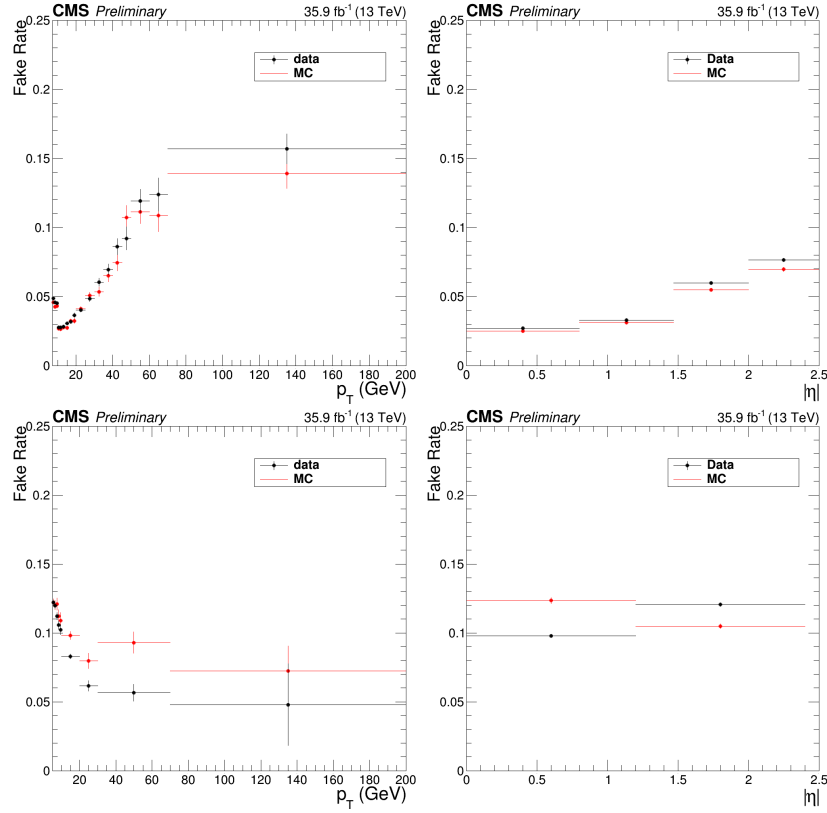


Figure 6.1: Fake rate for electrons (top) and muons (bottom) as a function of p_T (left) and η (right).

41 signal sample yields.

42 The total reducible background yield is thus

$$N_{\text{bkg}} = \sum_{\ell \in \text{3P1F}} F_\ell(p_T^\ell, \eta^\ell) - \sum_{\ell_1, \ell_2 \in \text{2P2F}} F_{\ell_1}(p_T^{\ell_1}, \eta^{\ell_1}) F_{\ell_2}(p_T^{\ell_2}, \eta^{\ell_2}). \quad (6.2)$$

43 The minus sign prevents double-counting of Z+2jets events in which one jet fragment
 44 is misidentified. The failing lepton candidates in the 3P1F and 2P2F control samples
 45 are assumed to truly be jet fragments or other nonprompt objects, but selection
 46 inefficiencies may cause prompt leptons to fail and contaminate the control regions
 47 with signal events. The yield of such signal events in the background control regions is
 48 estimated by applying the same fake factors to failing events in the ZZ signal Monte
 49 Carlo samples, and subtracted from the result of Eq. (6.2).

50 There are also irreducible background contributions from $t\bar{t}Z$ and WWZ events,
 51 which can have four prompt leptons. Expected yields for these processes are taken
 52 from simulation.

53 6.2 Systematic Uncertainties

54 Systematic uncertainties for trigger efficiency are taken to be the difference between
 55 trigger efficiencies in data and in simulated signal events, found to be around 2%
 56 of the final event yield. Because leptons in $Z \rightarrow 4\ell$ events generally have lower p_T ,
 57 the uncertainty increases to 4% for $Z \rightarrow 4e$ events. In both data and simulated
 58 events, trigger efficiencies are found with a tag-and-probe technique [206], performed
 59 on four-lepton events.

60 The lepton identification and isolation efficiencies in simulation are corrected with
 61 scaling factors derived with the tag-and-probe method, performed on $Z \rightarrow \ell^+\ell^-$ events
 62 in data and a single-Z Monte Carlo sample. To find the uncertainties associated with
 63 these corrections, the total yield is recomputed with the scaling factors varied up and
 64 down by one standard deviation of the uncertainties from the tag-and-probe method,
 65 treating all bins as correlated. The resulting changes in the $ZZ \rightarrow 4\ell$ yield, taken to
 66 be the one sigma variations resulting from lepton efficiency uncertainties, are found
 67 to be 6% in the 4e final state, 3% in the 2e2 μ final state, and 2% in the 4 μ final state.
 68 Leptons in $Z \rightarrow 4\ell$ events tend to have lower p_T , and the tag-and-probe samples
 69 for leptons with p_T below about 15 GeV are smaller and more contaminated with
 70 nonprompt objects, so the uncertainties are larger; they are found to be 10%, 6%,
 71 and 7% for the 4e, 2e μ , and 4 μ final states, respectively.

72 The uncertainty on the integrated luminosity of the data sample is 2.5% [145].

73 The uncertainty on lepton fake rates is 40%, which includes both statistical un-

74 certainty and systematic uncertainties associated with the loosened lepton selections
 75 defined in Section 5.3.5 and the differences in the underlying physics processes be-
 76 tween events in the $Z + \ell_{\text{fake}}$, 3P1F, and 2P2F control samples [73]. Statistical uncer-
 77 tainties arising from the limited size of the $Z + X$ control samples are also included
 78 as a systematic uncertainty on the background yield. The total uncertainty on the
 79 background yield varies by channel but is below 1% of the expected total yield.

80 Uncertainties due to the effect of QCD scale on the $ZZ \rightarrow 4\ell$ acceptance are
 81 evaluated with POWHEG and MCFM, by varying the QCD scales up and down by a
 82 factor of two with respect to the default $\mu_R = \mu_F = m_{ZZ}$. Parametric uncertainties
 83 ($\text{PDF} + \alpha_s$) are evaluated according to the PDF4LHC prescription in the acceptance
 84 calculation [208], and with NNPDF3.0 in the cross section calculations. An additional
 85 theoretical uncertainty arises from scaling the $q\bar{q} \rightarrow ZZ$ and $gg \rightarrow ZZ$ simulated
 86 samples to their NNLO and NLO predicted cross sections, respectively, with the
 87 K factors described in Section 4.1.4. The corresponding change in the acceptance,
 88 1.1%, is added to the previous theoretical errors in quadrature.

89 Systematic uncertainties on expected signal yield are summarized in Table 6.1. To
 90 obtain uncertainties in the inclusive cross sections, each uncertainty source is treated
 91 as a nuisance parameter in the fits described in Section 6.3.1. For differential cross
 92 section and other shape uncertainties, the calculation is fully redone for each uncer-
 93 tainty source, with the inputs shifted by one standard deviation in each direction.
 94 Variations across bins are taken to be fully correlated for each uncertainty source.
 95 Lepton and jet momentum scale and resolution uncertainties are taken to be trivial
 96 for the overall yield, but they are considered among the shape uncertainties.

Table 6.1: The contributions of each source of signal systematic uncertainty in the total yields. The integrated luminosity uncertainty and the PDF and scale uncertainties are considered separately. All other uncertainties are added in quadrature into a single systematic uncertainty. Uncertainties that vary by decay channel are listed as a range.

Uncertainty	$Z \rightarrow 4\ell$	$ZZ \rightarrow 4\ell$
Lepton efficiency	6–10%	2–6%
Trigger efficiency	2–4%	2%
MC statistics	1–2%	0.5%
Background	0.6–1.3%	0.5–1%
Pileup	1–2%	1%
PDF	1%	1%
QCD Scales	1%	1%
Integrated luminosity	2.5%	2.5%

97 6.3 Fiducial and Total Cross Section Calculation

98 Inclusive cross section measurements can be treated as simple binned counting experiments,
99 where the bins are the three decay channels ($4e$, $2e2\mu$, and 4μ). If ν events are
100 expected in a given bin, the probability of observing n events is given by the Poisson
101 distribution,

$$f(n; \nu) = e^{-\nu} \frac{\nu^n}{n!}. \quad (6.3)$$

102 In a particle physics analysis like this one, ν takes the form

$$\nu = \nu_s(\vec{\theta}_s) + \nu_b(\vec{\theta}_b) = \mu(\vec{\theta}_s) \mathcal{L}_{int} \sigma_{SM} \epsilon + \nu_b(\vec{\theta}_b) \quad (6.4)$$

103 where ν_s and ν_b are respectively the expected signal and background yields, σ_{SM} is
104 the standard model expectation for the cross section of the signal process and ϵ is our
105 efficiency for detecting and identifying its events. The signal and background nuisance
106 parameter vectors $\vec{\theta}_s$ and $\vec{\theta}_b$ represent hidden quantities that we do not measure
107 directly but which affect our yields, i.e. systematic effects. The signal strength μ

108 compares our expectation to what we actually measure:

$$\mu = \frac{\sigma_{meas}}{\sigma_{SM}}. \quad (6.5)$$

109 Of the variables in Eqs. (6.3) and (6.4), σ_{SM} is known from theoretical calculations,
 110 and ϵ is determined from simulation. The CMS detector is designed to measure n
 111 and \mathcal{L}_{int} , ν_b is estimated from data or simulation, and inferring σ_{meas} is a matter of
 112 finding the most likely value of the signal strength μ given the observed data. Then
 113 the measured cross section is simply

$$\sigma_{meas} = \mu\sigma_{SM}. \quad (6.6)$$

114 One interesting feature of this method is that σ_{SM} is used in the calculation of μ
 115 (Eq. (6.4)) and in the final cross section (Eq. (6.6)) in such a way that it cancels out,
 116 and in fact anything proportional to the true cross section may be used. In practice,
 117 this means that the order at which σ_{SM} is calculated does not matter to the extent
 118 that higher order corrections to the kinematics of the events do not affect ϵ .

119 Typically, σ_{meas} in Eq. (6.6) is the fiducial cross section, the cross section for the
 120 process in a phase space similar to (typically, slightly larger than) the phase space
 121 in which the experimental analysis can in principle detect events. In the four-lepton
 122 case, the fiducial phase space is a space of $2\ell 2\ell'$ ($\ell, \ell' \in e, \mu$) events defined by criteria
 123 on lepton kinematics, dilepton invariant masses, and four-lepton mass. Table 6.2
 124 shows the fiducial definitions for both the $Z \rightarrow 4\ell$ and $ZZ \rightarrow 4\ell$ cross section mea-
 125 surements. Lepton kinematic requirements and an invariant mass requirement on
 126 all opposite-sign, same-flavor lepton pairs in the event are common to both mea-
 127 surements; requirements on the invariant masses of Z/γ^* boson candidates and the
 128 four-lepton system are different.

129 The total ZZ cross section is defined subject to no constraints except the require-
 130 ment that m_{Z_1} and m_{Z_2} be between 60 and 120 GeV, which serves as the definition

131 of a Z boson. The fiducial cross section is related to the total cross section by the
 132 branching fraction \mathcal{B} to the final state in question—here, two factors of the Z/γ^*
 133 branching ratio to electron and muon pairs—and an acceptance factor \mathcal{A} which is the
 134 fraction of events falling in the fiducial phase space,

$$\sigma_{fid} = \mathcal{A}\sigma_{tot} (\mathcal{B}(Z \rightarrow 2\ell))^2. \quad (6.7)$$

135 The acceptance factor \mathcal{A} is determined entirely from theory, and is well known [11], so
 136 it is straightforward to calculate the total cross section once the fiducial cross section
 137 is known. Calculating both fiducial and total cross sections is interesting because
 138 it effectively factorizes experimental and theoretical uncertainties. The experimental
 139 uncertainties are contained entirely in the uncertainties on ϵ , \mathcal{L}_{int} , and ν_b in Eq. (6.4),
 140 which have little or no dependence on theory, while the theoretical uncertainties are
 141 contained entirely in the uncertainty on \mathcal{A} , which is determined with no experimental
 142 input. Thus the uncertainty on σ_{fid} is entirely experimental, and the theoretical
 143 uncertainties enter only in the uncertainty on σ_{tot} .

Table 6.2: Fiducial phase space definitions for the $Z \rightarrow 4\ell$ and $ZZ \rightarrow 4\ell$ cross section measurements. The common requirements apply to both. The $m_{\ell^+\ell'^-}$ criterion is applied to all opposite-sign same-flavor lepton pairs in the event.

Measurement	Fiducial requirements
Common	$p_T^{\ell_1} > 20 \text{ GeV}$, $p_T^{\ell_2} > 10 \text{ GeV}$, $p_T^{\ell_{3,4}} > 5 \text{ GeV}$, $ \eta^\ell < 2.5$, $m_{\ell^+\ell'^-} > 4 \text{ GeV}$
$Z \rightarrow 4\ell$	$m_{Z_1} > 40 \text{ GeV}$, $80 < m_{4\ell} < 100 \text{ GeV}$
$ZZ \rightarrow 4\ell$	$60 < m_{Z_1}, m_{Z_2} < 120 \text{ GeV}$

¹⁴⁴ **6.3.1 Signal Strength Extraction**

¹⁴⁵ The signal strength is found by the method of maximum likelihood [11, 209]. The
¹⁴⁶ likelihood function is the product of the probability distributions across all bins,

$$L \left(\vec{\theta}_s, \vec{\theta}_b \right) = \prod_{bins} f \left(n; \nu \left(\vec{\theta}_s, \vec{\theta}_b \right) \right). \quad (6.8)$$

¹⁴⁷ The most likely value of ν is the one that maximizes L . In practice, $\log L$ is typically
¹⁴⁸ maximized instead because it is easier to work with,

$$\frac{\partial^2 \log L}{\partial \vec{\theta}_s \partial \vec{\theta}_b} = 0. \quad (6.9)$$

¹⁴⁹ This maximization is performed simultaneously for all bins, yielding a single signal
¹⁵⁰ strength across all channels. Systematic uncertainties enter as log-normal constraints
¹⁵¹ imposed on the fit, encoded in $\vec{\theta}_s$ and $\vec{\theta}_b$. The fit is performed numerically.

¹⁵² **6.3.2 $Z \rightarrow 4\ell$ Branching Fraction**

¹⁵³ The total Z cross section can be calculated from the $Z \rightarrow 4\ell$ fiducial cross section
¹⁵⁴ with Eq. (6.7), but it is better measured in the 2ℓ channel, where the larger branching
¹⁵⁵ fraction yields samples several orders of magnitude larger than the $Z \rightarrow 4\ell$ sample
¹⁵⁶ used here. It is therefore more interesting to use $\sigma_{fid}(Z \rightarrow 4\ell)$ for a measurement of the
¹⁵⁷ four-lepton branching fraction $\mathcal{B}(Z \rightarrow 4\ell)$. After applying the acceptance correction
¹⁵⁸ to obtain $\sigma_{tot}(Z \rightarrow 4\ell) = \sigma_{fid}(Z \rightarrow 4\ell) / \mathcal{A}$, the four-lepton branching fraction is given
¹⁵⁹ by

$$\mathcal{B}(Z \rightarrow 4\ell) = \frac{\sigma_{tot}(Z \rightarrow 4\ell)}{\mathcal{C}_{80-100}^{60-120} \sigma(Z \rightarrow 2\ell)} \mathcal{B}(Z \rightarrow 2\ell), \quad (6.10)$$

¹⁶⁰ where $\sigma(Z \rightarrow 2\ell)$ is the dileptonic Z cross section in the 60–120 GeV mass range and
¹⁶¹ $\mathcal{C}_{80-100}^{60-120}$ corrects for the fact that $\sigma(Z \rightarrow 4\ell)$ is found in a mass range of 80–100 GeV.

162 6.4 Differential Cross Sections

163 Measurement of a differential fiducial cross section is also a problem of finding the
164 most likely true distribution given observed yields in multiple bins, estimated back-
165 ground yields, and detector effects understood through simulation. Unlike the inclu-
166 sive cross section, however, finite detector resolution leads to “smearing” effects that
167 cause events to migrate across bins, in addition to the same inefficiencies. The mean
168 detector-level distribution $\vec{\delta}$ is related to the true distribution $\vec{\theta}$ by a response matrix
169 \mathbf{R} :

$$\vec{\delta} = \mathbf{R}\vec{\theta}. \quad (6.11)$$

170 The observed distribution in data \vec{d} is sampled from the Poisson distribution with
171 mean $\vec{\delta}$ independently in each bin. CMS simulation software is sufficiently sophis-
172 ticated to give a good estimate of R , reproducing the real detector’s resolution and
173 smearing effects at the level of a few per cent or better for all distributions of interest.

174 If \mathbf{R} is square and invertible, the maximum likelihood estimate (MLE) of the true
175 distribution, $\hat{\vec{\theta}}$, is given by

$$\hat{\vec{\theta}} = \mathbf{R}^{-1}\vec{d}. \quad (6.12)$$

176 Even when \mathbf{R} is invertible, however, it is frequently ill-conditioned, giving $\hat{\vec{\theta}}$ unphysical
177 features like large bin-by-bin fluctuations or even negative bins as a consequence of the
178 stochastic nature of \vec{d} . It is therefore necessary to use a more sophisticated procedure
179 to ensure the differential cross section distributions obey physics-inspired constraints.

180 The variables used for differential cross sections in this analysis are in general well-
181 measured, so bin-to-bin fluctuations are small and the response matrices are nearly
182 diagonal, but some bins have low occupancy which can still cause pathologies.

183 **6.4.1 Unfolding**

184 The technique used here is an iterative frequentist method developed in high energy
 185 physics by D'Agostini [210] and independently in other fields [211–214], as imple-
 186 mented in ROOUNFOLD [215]. At iteration k , bin j of the predicted true distribution
 187 is set based on its expected contribution to all other bins, weighted by the observed
 188 data yield in each:

$$\begin{aligned}\theta_j^{(k+1)} &= \sum_i \mathbf{R}_{ij} \theta_j^{(k)} \frac{d_i}{\delta_i} \\ &= \sum_i \mathbf{R}_{ij} \theta_j^{(k)} \frac{d_i}{\sum_m \mathbf{R}_{im} \theta_m^{(k)}}.\end{aligned}\tag{6.13}$$

189 After several iterations, $\vec{\theta}^{(k)}$ depends only weakly on the ansatz $\vec{\theta}^{(0)}$.

190 The sequence will converge to the MLE for any non-pathological choice of $\vec{\theta}^{(0)}$ [216]
 191 but again the MLE often displays unphysical behavior. If $\vec{\theta}^{(0)}$ is strictly positive, $\vec{\theta}^{(k)}$
 192 will be strictly positive for all k , and in this case $\hat{\vec{\theta}}$ (as defined in Eq. (6.12)) will be
 193 the asymptotic unfolded distribution as long as it is also strictly positive. Choosing a
 194 smooth function for $\vec{\theta}^{(0)}$ will generally lead to smooth $\vec{\theta}^{(k)}$ for small k ; typical choices
 195 include a flat initial distribution and the truth-level distribution used to construct \mathbf{R}
 196 (used in this analysis). What constitutes “small” k depends on the condition of \mathbf{R} ,
 197 but for most physics distributions of interest, including all those used in this analysis,
 198 nonphysical fluctuations do not arise until after $\vec{\theta}^{(k)}$ is close to convergence. Full
 199 regularization is therefore imposed by ceasing iteration early. For all distributions
 200 shown here, stopping after four iterations was found to obtain a result close to the
 201 asymptotic distribution without artificially increasing the bin-to-bin variance.

202 **6.4.2 Uncertainties**

203 The largest uncertainties in the unfolded distributions arise from the unfolding pro-
 204 cedure itself, which can inflate statistical uncertainties present in the detector-level
 205 distributions. The correlation matrix which gives the full uncertainty—considered
 206 the statistical uncertainty of the unfolded distribution—does not have a closed form
 207 due to the nonlinearity of the method. The covariance matrix is therefore estimated
 208 by propagating the statistical error of the inputs at each iteration of the method, as
 209 laid out in Ref. [210] and improved in Ref. [215]. This procedure does not account for
 210 the bias introduced by regularization, but this is expected to be negligible relative to
 211 other systematic uncertainties for the well-modeled processes studied here.

212 Most systematic uncertainties are propagated through unfolding by recomputing
 213 the response matrix with the training sample shifted or reweighted to reflect a 1σ
 214 shift in the quantity in question. The uncertainty related to that quantity is taken
 215 to be the resulting shape difference in the final unfolded distribution. Systematic
 216 uncertainties are negligible compared to statistical uncertainties in most bins.

217 **6.5 VBS Signal Extraction**

218 The VBS signal search considers events passing the selections described in Sec-
 219 tion 5.4.3. The electroweak yield is insufficient to have sensitivity at 35.9 fb^{-1} , even
 220 with further cut optimization, so a gradient-boosted decision tree (GBDT), imple-
 221 mented with the SCIKIT-LEARN package [217], is used to extract the signal. Hyper-
 222 parameters of the GBDT are optimized with a grid search. Each Monte Carlo sample
 223 used in the VBS search (see Section 4.1.4) is split into a “training” subsample, used to
 224 train the GBDT, and a “test” subsample used to evaluate its performance and make
 225 templates for use in the statistical analysis. The GBDT performance is nearly the

226 same for the test and training samples, a sign that the algorithm is not overtrained.

227 A number of observables have been proposed to discriminate VBS events from
 228 background [58], of which m_{jj} and $\Delta\eta_{jj}$ are the most powerful. Other commonly-used
 229 variables include $m_{4\ell}$, $\eta^{j_1} \times \eta^{j_2}$, $\Delta\phi_{Z_1 Z_2}$, and the so-called Zeppenfeld variables, defined
 230 as

$$\eta_P^* = \eta_P - \frac{\eta_{j_1} - \eta_{j_2}}{2}, \quad (6.14)$$

231 where P may stand for Z_1 , Z_2 , or j_3 , the highest- p_T untagged jet in the event. In ad-
 232 dition to these “traditional” quantities, several other groups of observables have been
 233 examined, including production angles, decay angles, measures of total hadronic ac-
 234 tivity in the event, properties of individual leptons and jets and of the ZZjj system, and
 235 a discriminator designed to distinguish jets originating from quarks and gluons [218].

236 The hadronic activity and quark-gluon tagging variables have some discriminating
 237 power, but they differ significantly depending on the Monte Carlo generator used
 238 and were therefore considered too poorly-modeled to use. New GBDTs were trained,
 239 each with the traditional observables and one other group of observables, and the
 240 groups that improved the GBDT discrimination power significantly were retained.
 241 This procedure yielded 17 observables, including the hard process relative transverse
 242 momentum, defined as the ratio of the p_T of the ZZjj system to the scalar sum of the
 243 p_T of each object,

$$p_T^{rel. hard} = \frac{p_T^{ZZjj}}{\sum_{Z_1, Z_2, j_1, j_2} p_T}, \quad (6.15)$$

244 and the dijet relative transverse momentum,

$$p_T^{rel. jj} = \frac{p_T^{jj}}{\sum_{j_1, j_2} p_T}. \quad (6.16)$$

245 The list of observables was further optimized by retraining the GBDT once with
 246 each variable dropped and eliminating the one with the least discriminating power.
 247 This pruning was repeated until seven observables remained, namely m_{jj} , $\Delta\eta_{jj}$, $m_{4\ell}$,

248 $\eta_{Z_1}^*$, $\eta_{Z_2}^*$, $p_T^{rel.\ hard}$, and $p_T^{rel.\ jj}$. The resulting GBDT performs only marginally worse
 249 (0.2 σ less expected significance on the VBS signal) than a version with all observables
 250 included, and is faster and easier to train, simpler, and less susceptible to biases and
 251 systematic uncertainties from mismodeling.

252 The signal and background yields are extracted from the GBDT output spectrum
 253 with a binned maximum likelihood fit to templates from the test Monte Carlo samples.
 254 To obtain templates with better fit convergence properties, the GBDT output is
 255 mapped to the range [0, 1] with the logistic transformation

$$x \rightarrow \frac{1}{1 - e^{-x}}. \quad (6.17)$$

256 This provides better separation between signal and background and allows uniform
 257 binning in the templates.

258 6.6 Anomalous Gauge Coupling Searches

259 The new physics represented by aGCs would generally manifest as an increase in
 260 events with high invariant mass, so it is natural to use the shape of the $m_{4\ell}$ distribution
 261 for the search. For the aTGC search, the doubly on-shell ZZ selection is used, while
 262 the aQGC search is performed with the ZZjj selection described in Section 5.4.3.

263 Monte Carlo samples with nonzero aTGCs are generated at grids of points in the
 264 $f_4^Z-f_4^\gamma$ and $f_5^Z-f_5^\gamma$ planes. In each bin of the $m_{4\ell}$ distribution, the yields at the various
 265 working points are fit to a function of the form

$$y(f^Z, f^\gamma) = x_0 + x_1 f^Z + x_2 f^\gamma + x_3 f^Z f^\gamma + x_4 (f^Z)^2 + x_5 (f^\gamma)^2 \quad (6.18)$$

266 where $y(f^Z, f^\gamma)$ is the yield in the bin, f^V can be f_4^Z and f_4^γ or f_5^Z and f_5^γ , and x_i
 267 are the parameters to be fit.

268 A similar procedure is performed for the aQGC search. Rather than simulating a
 269 full sample for each working point, which is computationally expensive, events from
 270 `MADGRAPH5_AMC` produced at LO are used to obtain samples for nonzero values
 271 of f_{T0}/Λ^4 , f_{T1}/Λ^4 , f_{T2}/Λ^4 , f_{T8}/Λ^4 , and f_{T9}/Λ^4 by matrix element reweighting [149].
 272 The yields in each $m_{4\ell}$ bin are fit to parabolas as a function of the five aQGC param-
 273 eters separately.

274 A binned profile likelihood method [11] is used to derive the limits. Systematic
 275 uncertainties are taken into account by varying the number of signal and background
 276 events within their uncertainties. Exclusion limits are found by comparing the p-
 277 values of the signal hypothesis and the background only hypothesis

$$CL_s = \frac{p_{s+b}}{1 - p_b} \quad (6.19)$$

278 to set thresholds. Further details on the method can be found in Ref. [219]. The
 279 software for setting limits, implemented with `RooStats`, has been validated and
 280 used extensively by the CMS and ATLAS collaborations [220].

⁰ Chapter 7

¹ Results

2 A number of measurements and analyses fall under the umbrella of four-lepton
3 physics, and results presented in this thesis were originally made public in several
4 journal articles and Physics Analysis Summary documents released by the CMS col-
5 laboration. The first CMS measurement of the ZZ inclusive cross section at 13 TeV
6 used roughly half the 2015 dataset (1.34 fb^{-1}) and was made public in Ref. [221] in
7 December 2015 as one of the first measurements done on 13 TeV collision data. That
8 analysis was expanded to use the whole 2.6 fb^{-1} collected in 2015, and to include
9 the $Z \rightarrow 4\ell$ branching fraction measurement, as reported in Ref. [222], submitted in
10 July 2016 and published the following December. With the full 2016 dataset, the ZZ
11 cross section and $Z \rightarrow 4\ell$ branching ratio were measured again to greater precision in
12 Ref. [80], which also included differential cross section measurements and aTGC lim-
13 its, made public in March 2017. A new paper including these measurements [OUR
14 PAPER] also includes a combination of the 2015 and 2016 inclusive cross section
15 measurements. Differential cross sections with respect to jet-related observables, and
16 searches for EWK ZZ production and aTGCs, were reported in May 2017 in Ref. [223],
17 with a paper on only the VBS and aQGC searches following [224]. The Higgs boson

18 was studied in the four-lepton final state in Refs. [225–227]. In the following, results
 19 for each topic are only shown for 2016 data, which significantly exceed the accuracy
 20 of the results from 2015 data.

21 **7.1 Four-Lepton Yields and Inclusive Cross 22 Sections**

23 **7.1.1 Full Spectrum**

24 The full four-lepton invariant mass spectrum is shown in Fig. 7.1. The single-Z
 25 resonance can be seen below 100 GeV, the Higgs resonance is visible—though it is
 26 not sharply resolved with this binning—in the Z/γ^* region below $2m_Z$, where doubly
 27 resonant ZZ continuum production begins. The dilepton invariant mass spectrum is
 28 shown for both Z/γ^* candidates in Fig. 7.2 and for the Z/γ^* candidate closest to the
 29 nominal Z boson mass (Z_1) in Fig. 7.3. Figure 7.4 shows m_{Z_2} plotted against m_{Z_1}
 30 for data events representative of all four-lepton production. Clusters of events with
 31 zero ($Z \rightarrow 4\ell$ and nonresonant $\gamma^*\gamma^*$ production), one ($H \rightarrow ZZ^*$ and nonresonant $Z\gamma^*$
 32 production), and two (nonresonant ZZ production) on-shell Z bosons can be clearly
 33 seen.

34 **7.1.2 $Z \rightarrow 4\ell$ Resonance**

35 Expected and observed yields for events satisfying the $Z \rightarrow 4\ell$ selection criteria
 36 ($80 < m_{4\ell} < 100$ GeV) are shown in Table 7.1. The invariant mass distribution of
 37 these events is shown in Fig. 7.5. Figure 7.6 shows m_{Z_2} plotted against m_{Z_1} for
 38 all data events consistent with $Z \rightarrow 4\ell$ production. Predictions from Monte Carlo

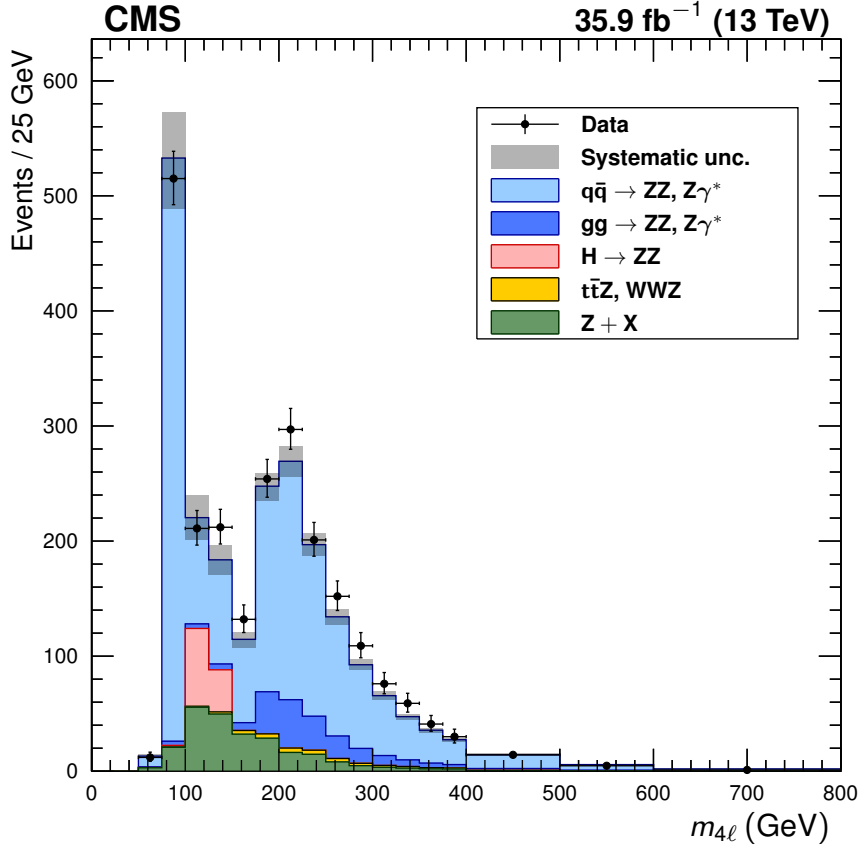


Figure 7.1: Distribution of the four-lepton invariant mass $m_{4\ell}$ of all events in the full spectrum selection. Points represent data, with statistical uncertainty bars. The stack of filled histograms represents the SM signal prediction and background estimate, with a grey band showing the sum in quadrature of the statistical and systematic uncertainties on the total expected yield.

39 samples generally agree well with the data, allowing us to measure the $Z \rightarrow 4\ell$ cross
40 section and branching fraction.

41 The signal strength in the $Z \rightarrow 4\ell$ selection is

$$\mu = 0.980^{+0.046}_{-0.044} (\text{stat})^{+0.065}_{-0.059} (\text{syst}) \pm 0.025 (\text{lumi}), \quad (7.1)$$

42 yielding a fiducial cross section

$$\sigma_{\text{fid}} (\text{pp} \rightarrow Z \rightarrow 4\ell) = 31.2^{+1.5}_{-1.4} (\text{stat})^{+2.1}_{-1.9} (\text{syst}) \pm 0.8 (\text{lumi}) \text{ fb}. \quad (7.2)$$

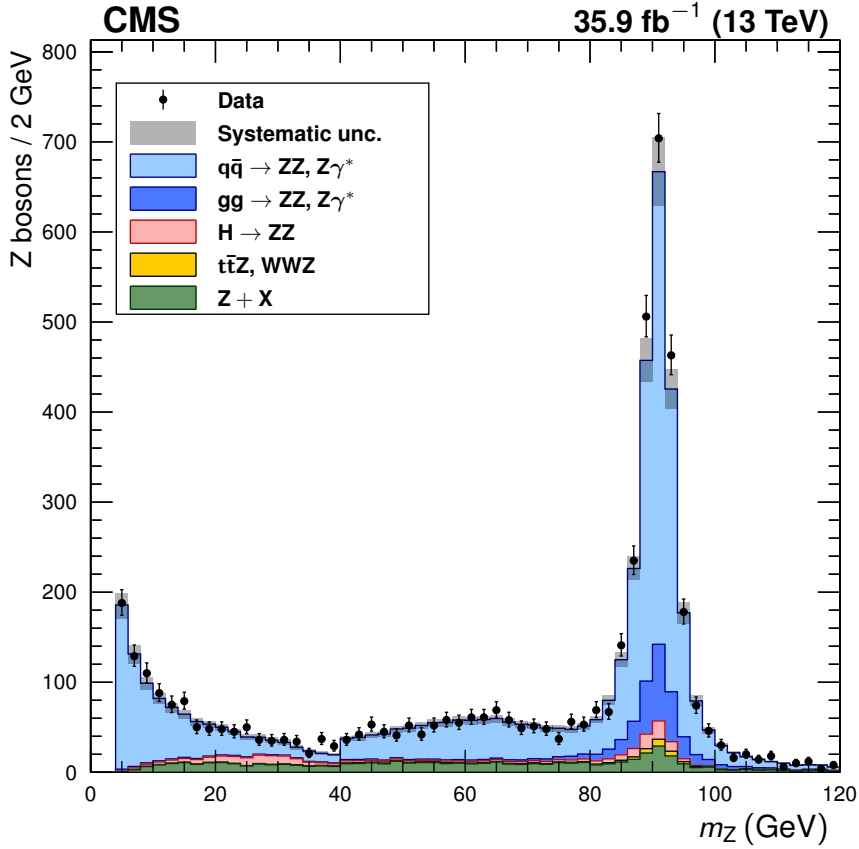


Figure 7.2: Distribution of the dilepton invariant mass of Z/γ^* candidates in all events in the full spectrum selection, regardless of whether the lepton pair is labeled Z_1 or Z_2 . Points represent data, with statistical uncertainty bars. The stack of filled histograms represents the SM signal prediction and background estimate, with a grey band showing the sum in quadrature of the statistical and systematic uncertainties on the total expected yield.

Table 7.1: Observed and expected yields of $Z \rightarrow 4\ell$ events, including expected background yields, shown for each final state and summed to the total. Uncertainties are statistical, then systematic, not including the integrated luminosity uncertainty.

Final state	Expected $N_{4\ell}$	Background	Total expected	Observed
4μ	$224 \pm 1 \pm 16$	$7 \pm 1 \pm 2$	$231 \pm 2 \pm 17$	225
$2e2\mu$	$207 \pm 1 \pm 14$	$9 \pm 1 \pm 2$	$216 \pm 2 \pm 14$	206
4e	$68 \pm 1 \pm 8$	$4 \pm 1 \pm 2$	$72 \pm 1 \pm 8$	78
Total	$499 \pm 2 \pm 32$	$19 \pm 2 \pm 5$	$518 \pm 3 \pm 33$	509

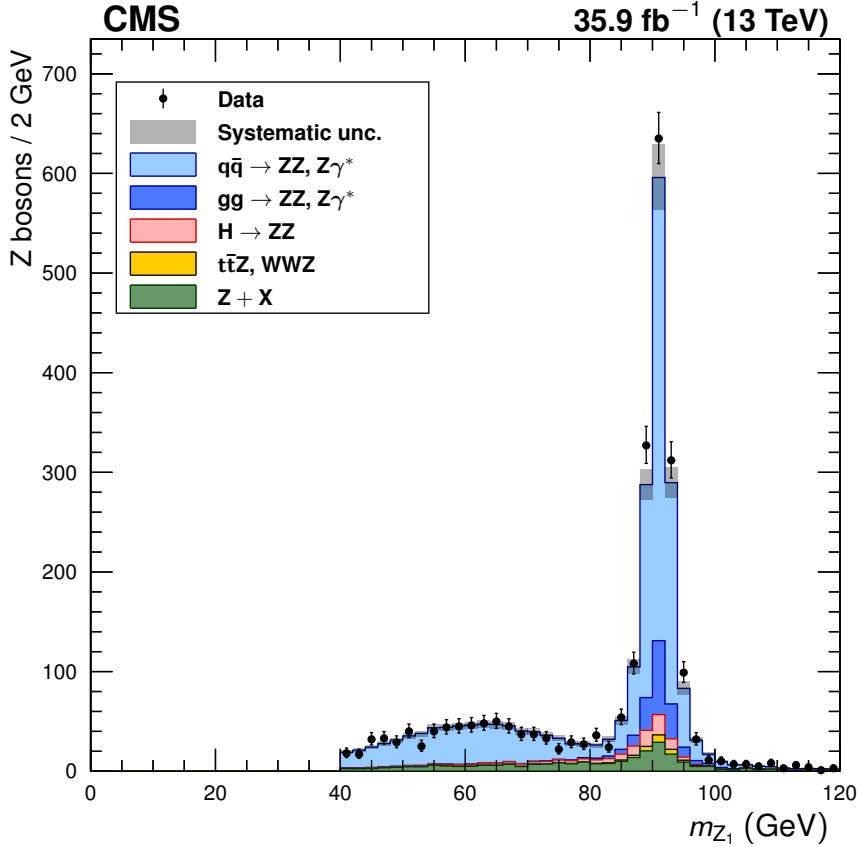


Figure 7.3: Distribution of the dilepton invariant mass of Z_1 , the Z/γ^* candidate in each event closest to the nominal m_Z , in the full spectrum selection. Points represent data, with statistical uncertainty bars. The stack of filled histograms represents the SM signal prediction and background estimate, with a grey band showing the sum in quadrature of the statistical and systematic uncertainties on the total expected yield.

43 This is scaled by an acceptance correction factor $\mathcal{A} = 0.125 \pm 0.002$, estimated with
 44 POWHEG v2.0, to the total $Z \rightarrow 4\ell$ cross section times branching ratio,

$$\sigma(pp \rightarrow Z) \times \mathcal{B}(Z \rightarrow 4\ell) = 249 \pm 8 \text{ (stat)}^{+9}_{-8} \text{ (syst)} \pm 4 \text{ (theo)} \pm 6 \text{ (lumi)} \text{ fb.} \quad (7.3)$$

45 Equation (6.10) is used to calculate the branching fraction. The Z cross section
 46 times dilepton branching ratio is calculated with FEWZ v2.0 [228] at NNLO in QCD
 47 to be $\sigma(Z \rightarrow 2\ell) = 1870^{+50}_{-40}$ pb. The Z mass window correction factor is calculated
 48 with POWHEG and found to be $\mathcal{C}_{80-100}^{60-120} = 0.926 \pm 0.001$. Its uncertainty includes

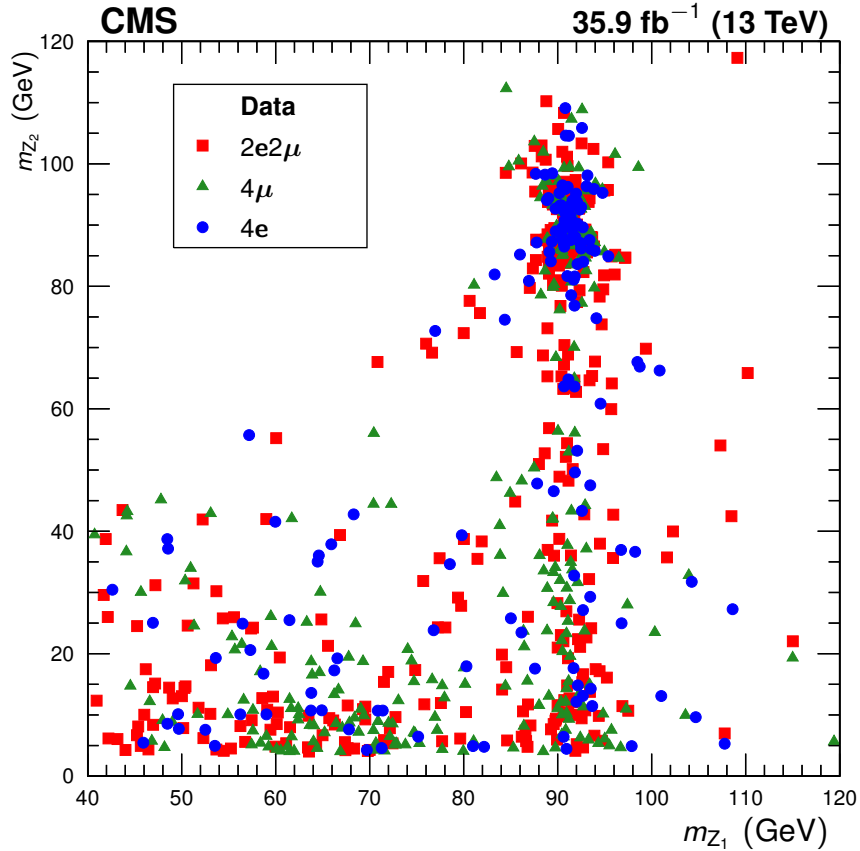


Figure 7.4: The reconstructed m_{Z_2} plotted against the reconstructed m_{Z_1} for data events in the full spectrum selection, with distinctive markers for each final state. For readability, only every fourth event is drawn. Clusters of events from different production modes are visible, as discussed in the text.

49 scale and PDF variations [208]. The nominal Z to dilepton branching fraction is
 50 $\mathcal{B}(Z \rightarrow 2\ell) = 0.03366$ [11]. The four-lepton branching fraction is measured to be

$$\mathcal{B}(Z \rightarrow 4\ell) = 4.8 \pm 0.2 \text{ (stat)} \pm 0.2 \text{ (syst)} \pm 0.1 \text{ (theo)} \pm 0.1 \text{ (lumi)} \times 10^{-6}. \quad (7.4)$$

51 This value is consistent with the theoretical value of 4.6×10^{-6} , calculated with
 52 MADGRAPH5_aMC@NLO v2.3.3, and with previous measurements from CMS and
 53 ATLAS [90, 91, 222], which had uncertainties 2–4 times larger.

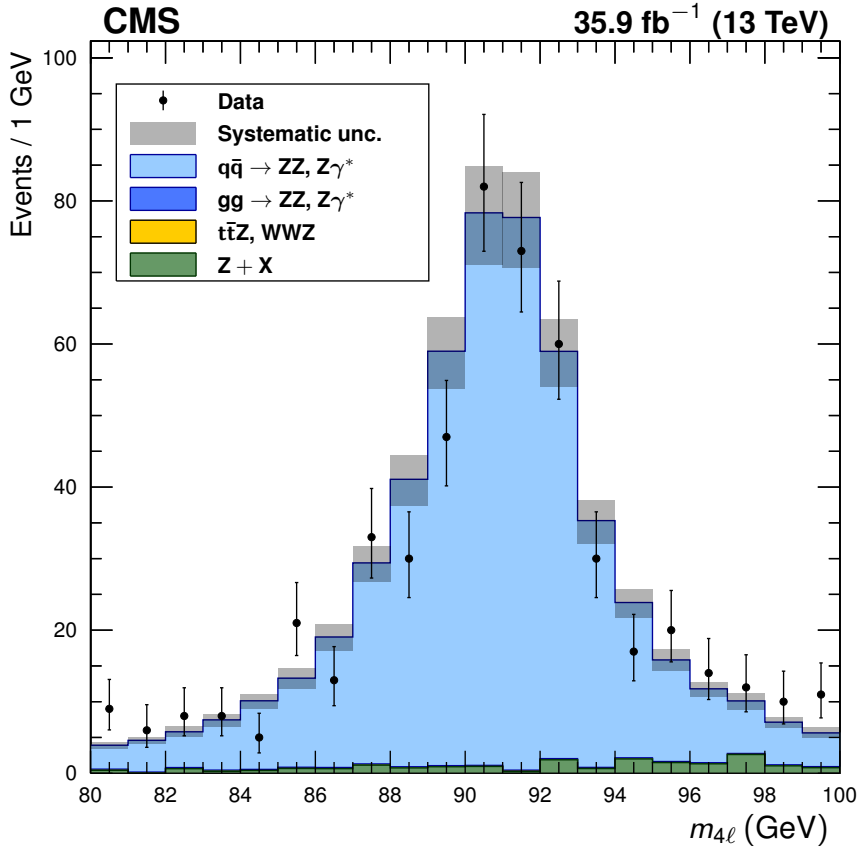


Figure 7.5: Distribution of the four-lepton invariant mass $m_{4\ell}$ of all events in the mass range $80 < m_{4\ell} < 100$ GeV, the $Z \rightarrow 4\ell$ selection. Points represent data, with statistical uncertainty bars. The stack of filled histograms represents the SM signal prediction and background estimate, with a grey band showing the sum in quadrature of the statistical and systematic uncertainties on the total expected yield.

54 7.1.3 Higgs Resonance

55 Figure 7.7 shows the four-lepton invariant mass around the Higgs resonance, which
 56 can be clearly seen above the SM continuum background, for events passing the Higgs
 57 selection ($m_{Z_2} > 12$ GeV, $SIP_{3D} < 4$ for all leptons). Table 7.2 shows the observed
 58 and expected yields in the mass range $118 < m_{4\ell} < 130$ GeV. Here, SM continuum
 59 production—considered signal in all other parts of this analysis—is considered back-
 60 ground. Figures 7.8–7.10 show the Z_1 mass, the Z_2 mass, and the scatter plot of

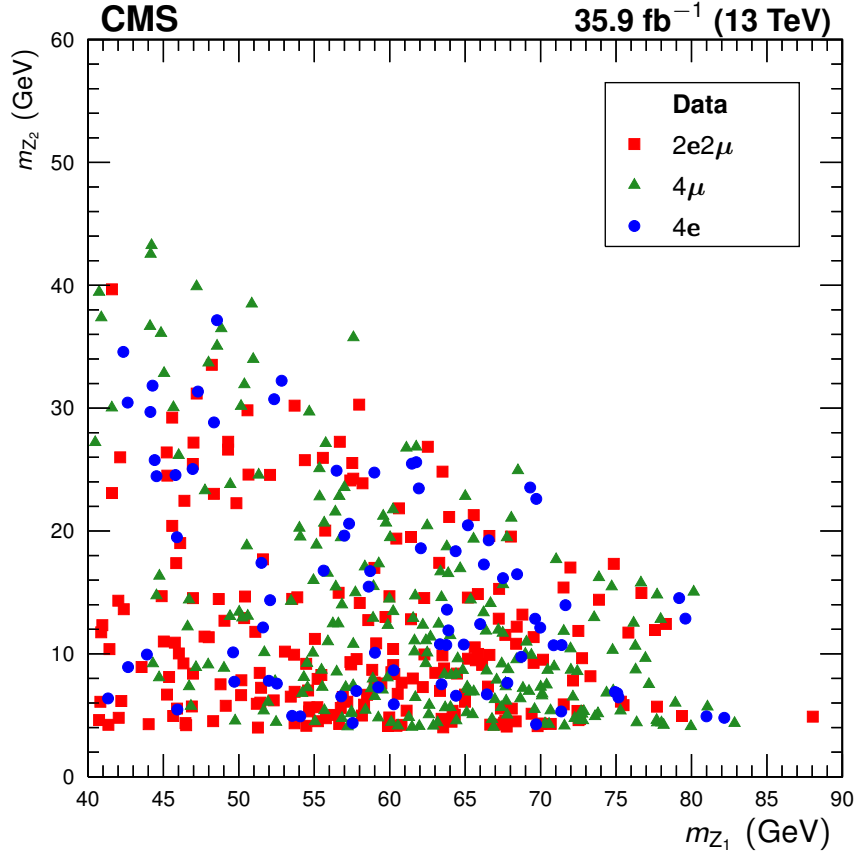


Figure 7.6: The reconstructed m_{Z_2} plotted against the reconstructed m_{Z_1} for all data events with $80 < m_{4\ell} < 100$ GeV, with distinctive markers for each final state.

61 m_{Z_2} against m_{Z_1} , for events in the same four-lepton mass region around the Higgs
 62 resonance. Agreement between predictions and data is again good, allowing measure-
 63 ments of Higgs boson properties, couplings, and production rates. These are beyond
 64 the scope of this thesis, but were reported in Ref. [227].

65 7.1.4 ZZ Production

66 Expected and observed yields for on-shell ZZ events are shown in Table 7.3. The corre-
 67 sponding four-lepton and Z boson candidate invariant masses are shown in Figs. 7.11
 68 and 7.12, respectively. Figure 7.13 shows the distribution of the number of jets (N_{jets})

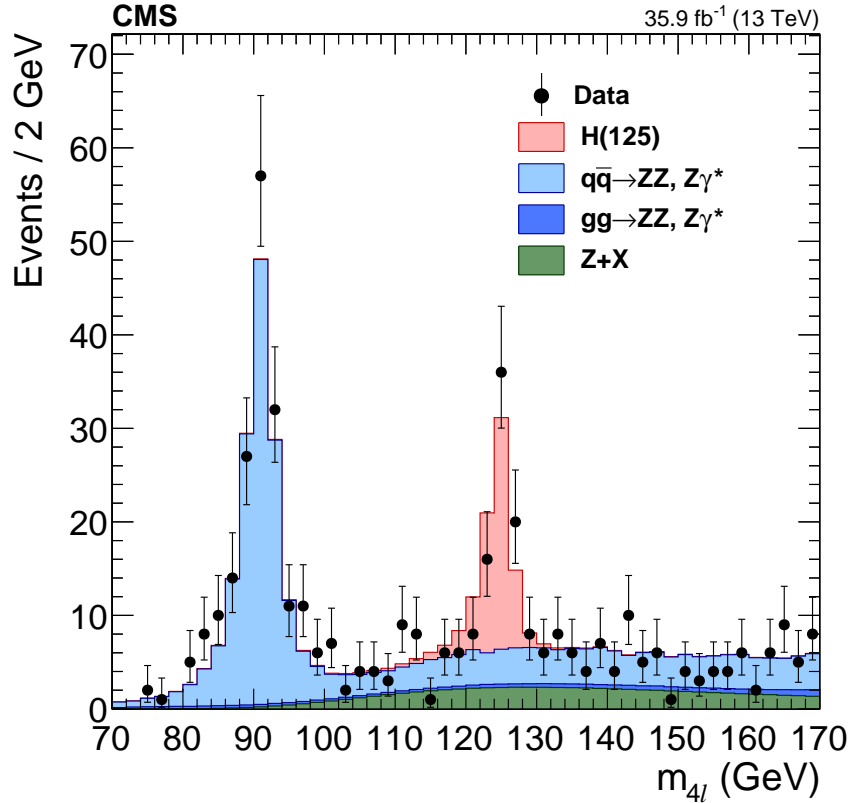


Figure 7.7: Distribution of the four-lepton invariant mass m_{4l} for events in the Higgs selection. Points represent data, with statistical uncertainty bars. The stack of filled histograms represents the signal and SM background predictions and the reducible background estimate.

Table 7.2: Observed and expected yields of $H \rightarrow ZZ^* \rightarrow 4\ell$ events, including expected background yields, for events passing the Higgs selection in the mass range $118 < m_{4l} < 130$ GeV, shown for each final state and summed to the total. Uncertainties are statistical and systematic combined.

Final state	Expected N_H	SM continuum background	$Z + X$	Total expected	Observed
4μ	21.6 ± 1.9	$9.4^{+0.6}_{-0.7}$	$4.7^{+2.0}_{-1.8}$	35.8 ± 2.9	34
$2e2\mu$	26.5 ± 2.3	$11.0^{+0.7}_{-0.8}$	$6.9^{+3.1}_{-2.9}$	$44.4^{+3.7}_{-3.6}$	41
4e	10.2 ± 1.1	3.6 ± 0.3	$1.9^{+0.8}_{-1.0}$	15.8 ± 1.6	19
Total	58.3 ± 5.0	$24.1^{+1.5}_{-1.6}$	$13.5^{+3.7}_{-3.5}$	96.0 ± 6.7	94

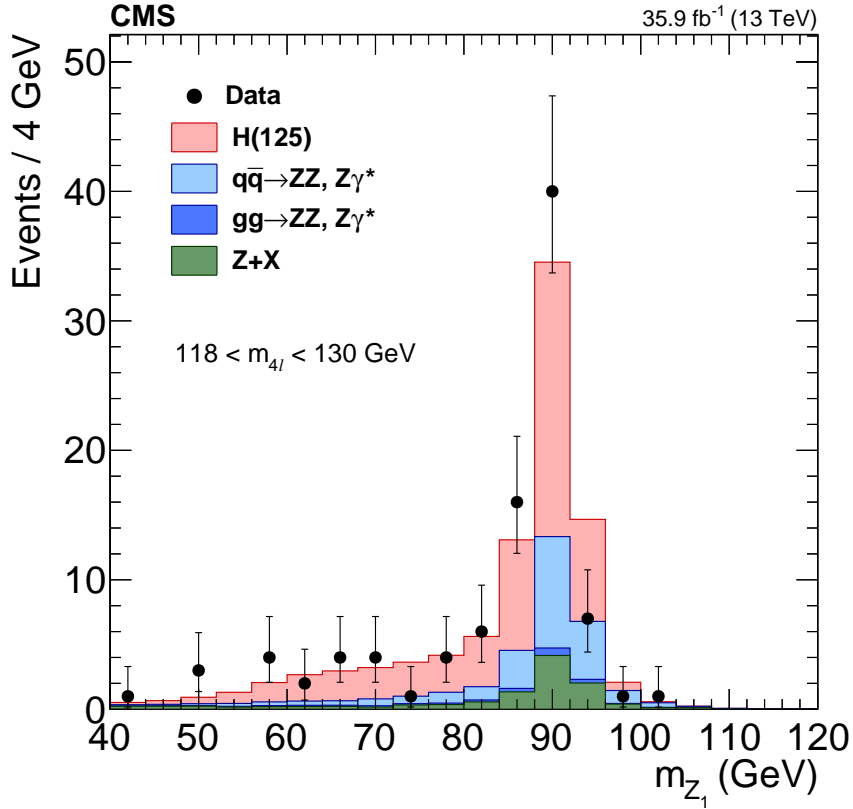


Figure 7.8: Distribution of the dilepton invariant mass of Z_1 , the dilepton candidate in each event closest to the nominal m_Z , in events in the Higgs selection with $118 < m_{4\ell} < 130 \text{ GeV}$. Points represent data, with statistical uncertainty bars. The stack of filled histograms represents the signal and SM background predictions and the reducible background estimate.

in these events. The leading and subleading jet p_T are shown separately in Fig. 7.14, and the leading and subleading jet $|\eta|$ are shown separately in Fig. 7.15, for all events with at least one (leading) or two (subleading) jets. Figures 7.16 and 7.17 show the m_{jj} and $|\Delta\eta_{jj}|$ distributions for tagging jet pairs in the dijet selection. Again, agreement is good overall, indicating that the observables shown are well modeled up to the precision achievable with current data. These are the first such distributions published at $\sqrt{s} = 13 \text{ TeV}$, and statistical uncertainties are smaller than those published at any energy, allowing theorists to make more detailed comparisons to their models

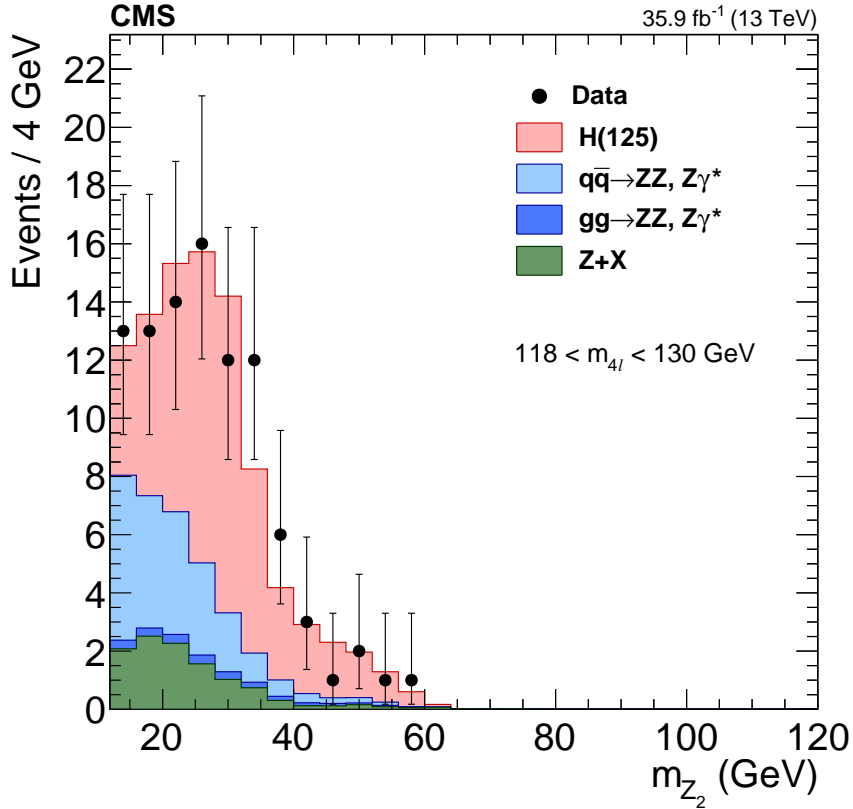


Figure 7.9: Distribution of the dilepton invariant mass of Z_2 , the dilepton candidate in each event farther from the nominal m_Z , in events in the Higgs selection with $118 < m_{4\ell} < 130 \text{ GeV}$. Points represent data, with statistical uncertainty bars. The stack of filled histograms represents the signal and SM background predictions and the reducible background estimate.

77 and, in the case of the jet-related distributions, to QCD and shower modeling.

78 The yields shown in Table 7.3 and the systematic uncertainties of Table 6.1 are
 79 used as inputs to the maximum likelihood method described in Section 6.3.1 to obtain
 80 the on-shell ZZ signal strength across all four-lepton final states,

$$\mu = 1.040^{+0.033}_{-0.032} (\text{stat})^{+0.037}_{-0.035} (\text{syst}) \pm 0.026 (\text{lumi}), \quad (7.5)$$

81 which gives a fiducial cross section

$$\sigma_{\text{fid}}(\text{pp} \rightarrow \text{ZZ} \rightarrow 4\ell) = 40.9 \pm 1.3 (\text{stat}) \pm 1.4 (\text{syst}) \pm 1.0 (\text{lumi}) \text{ fb}, \quad (7.6)$$

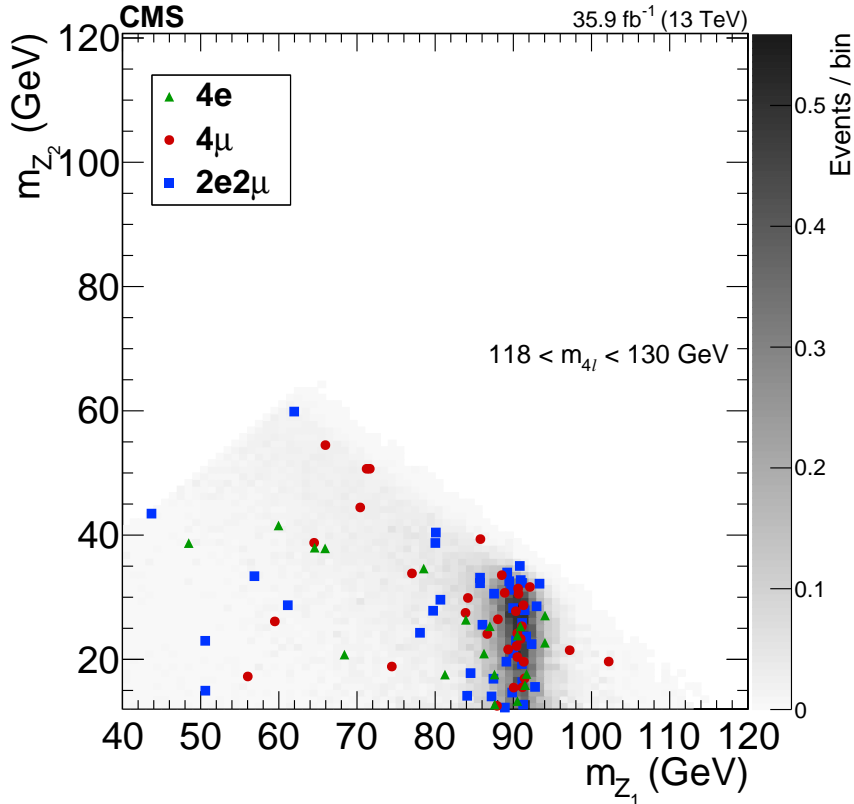


Figure 7.10: The reconstructed m_{Z_2} mass plotted against the reconstructed m_{Z_1} for data events in the Higgs selection with $118 < m_{4\ell} < 130$ GeV, with distinctive markers for each final state. The shading represents the expected number of events in the bin.

Table 7.3: Observed and expected yields of ZZ events, including expected background yields, in the on-shell selection, shown for each final state and summed to the total. Uncertainties are statistical, then systematic, not including the integrated luminosity uncertainty.

Final state	Expected N_{ZZ}	Background	Total expected	Observed
4μ	$301 \pm 2 \pm 9$	$10 \pm 1 \pm 2$	$311 \pm 2 \pm 9$	335
$2e2\mu$	$503 \pm 2 \pm 19$	$31 \pm 2 \pm 4$	$534 \pm 3 \pm 20$	543
4e	$205 \pm 1 \pm 12$	$20 \pm 2 \pm 2$	$225 \pm 2 \pm 13$	220
Total	$1009 \pm 3 \pm 36$	$60 \pm 3 \pm 8$	$1070 \pm 4 \pm 37$	1098

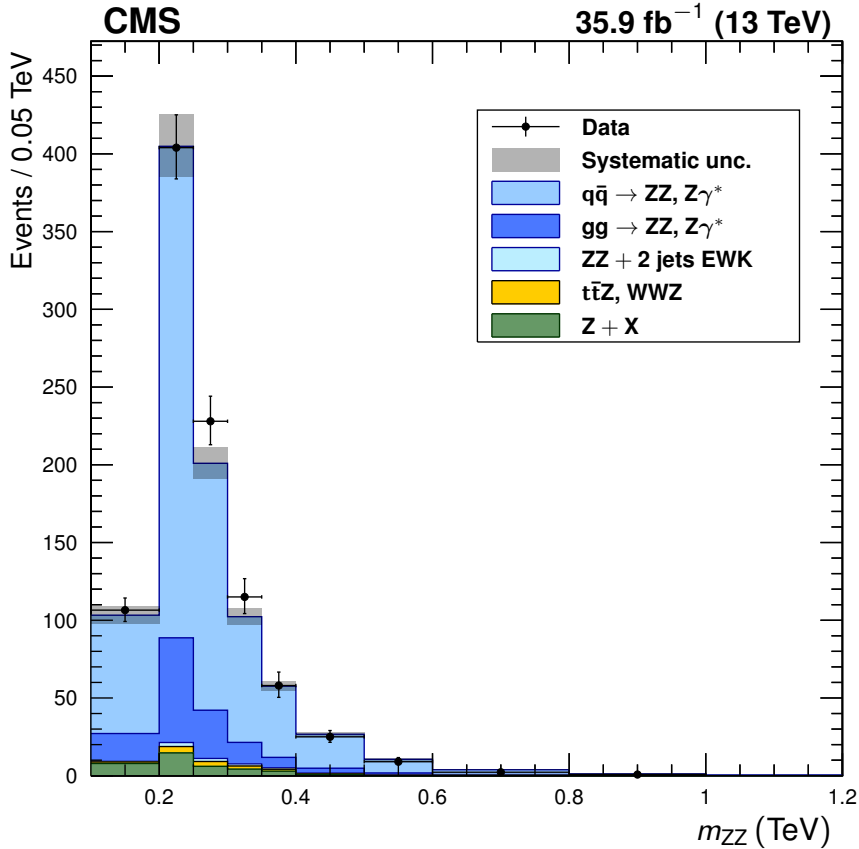


Figure 7.11: Distribution of the four-lepton invariant mass m_{ZZ} of all events in the on-shell selection. Points represent data, with statistical uncertainty bars. The stack of filled histograms represents the SM signal prediction and background estimate, with a grey band showing the sum in quadrature of the statistical and systematic uncertainties on the total expected yield.

82 in the $ZZ \rightarrow 4\ell$ fiducial phase space of Table 6.2. The corresponding total cross
 83 section is

$$\sigma(pp \rightarrow ZZ) = 17.5^{+0.6}_{-0.5} (\text{stat}) \pm 0.6 (\text{syst}) \pm 0.4 (\text{theo}) \pm 0.4 (\text{lumi}) \text{ pb.} \quad (7.7)$$

84 This measurement, on 2016 data, agrees with the result of the 2015 measure-
 85 ment [222],

$$\sigma(pp \rightarrow ZZ) = 14.6^{+1.9}_{-1.8} (\text{stat})^{+0.3}_{-0.5} (\text{syst}) \pm 0.2 (\text{theo}) \pm 0.4 (\text{lumi}) \text{ pb.} \quad (7.8)$$

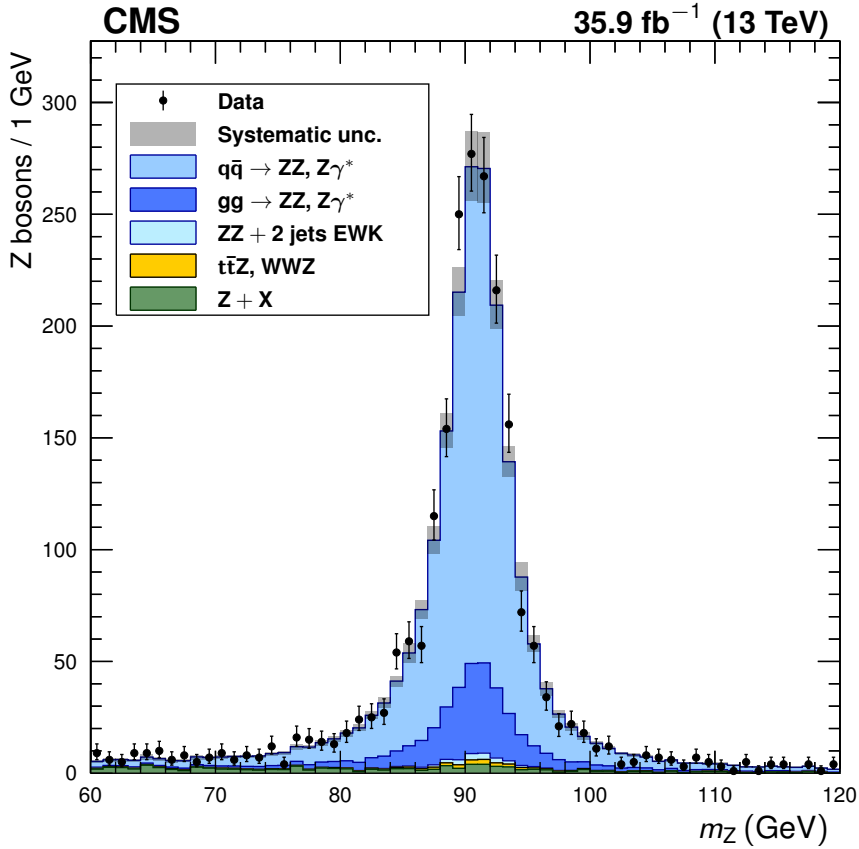


Figure 7.12: Distribution of the dilepton invariant mass of Z candidates in all events in the on-shell selection, regardless of whether the lepton pair is labeled Z_1 or Z_2 . Points represent data, with statistical uncertainty bars. The stack of filled histograms represents the SM signal prediction and background estimate, with a grey band showing the sum in quadrature of the statistical and systematic uncertainties on the total expected yield.

86 One may combine the measurements by doing a six-bin simultaneous fit with the bins
 87 representing the same final state in 2015 and 2016 considered separately. The degree
 88 of correlation between the systematic uncertainties in the 2015 and 2016 runs is not
 89 known, but the 2015 contribution is small enough that the systematic uncertainties
 90 are dominated by those in the 2016 dataset, and the degree of correlation will have
 91 only a small effect on the measurement. We therefore do the fit twice, once treating
 92 the experimental uncertainties as fully correlated between the datasets, and again

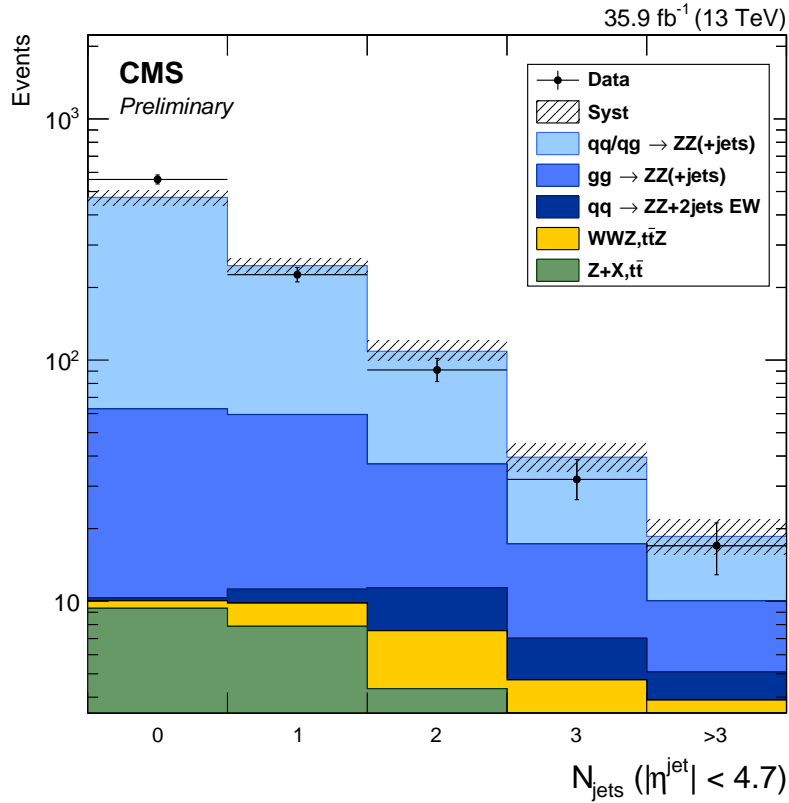


Figure 7.13: Distribution of jet multiplicity in ZZ events. Points represent data, with statistical uncertainty bars. The stack of filled histograms represents the SM signal prediction and background estimate, with a hatched band showing the sum in quadrature of the statistical and systematic uncertainties on the total expected yield.

93 treating them as fully uncorrelated. The small difference in the central value obtained
 94 is added linearly to the systematic error of the result. After the full combination, the
 95 “2015 + 2016” total cross section is found to be

$$\sigma(pp \rightarrow ZZ) = 17.2 \pm 0.5 \text{ (stat)} \pm 0.7 \text{ (syst)} \pm 0.4 \text{ (theo)} \pm 0.4 \text{ (lumi)} \text{ pb.} \quad (7.9)$$

96 These results can be compared to the MATRIX v1.0.0_beta4 prediction of $16.2^{+0.6}_{-0.4}$ pb,
 97 computed at NNLO in QCD, or the MCFM v7.0 prediction of $15.0^{+0.7}_{-0.6} \pm 0.2$ pb, cal-
 98 culated at NLO in QCD with LO gg → ZZ diagrams included. Both predictions use
 99 the NNPDF3.0 PDF sets and fixed scales $\mu_F = \mu_R = m_Z$.

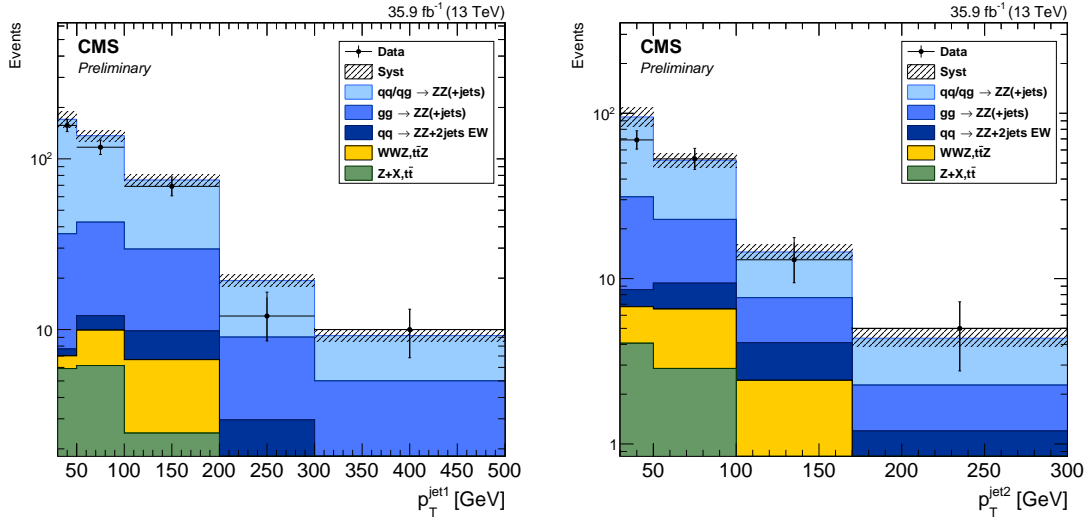


Figure 7.14: Distribution of leading (left) and subleading (right) jet p_T for all ZZ events with at least one jet and at least two jets, respectively. Points represent data, with statistical uncertainty bars. The stack of filled histograms represents the SM signal prediction and background estimate, with a hatched band showing the sum in quadrature of the statistical and systematic uncertainties on the total expected yield.

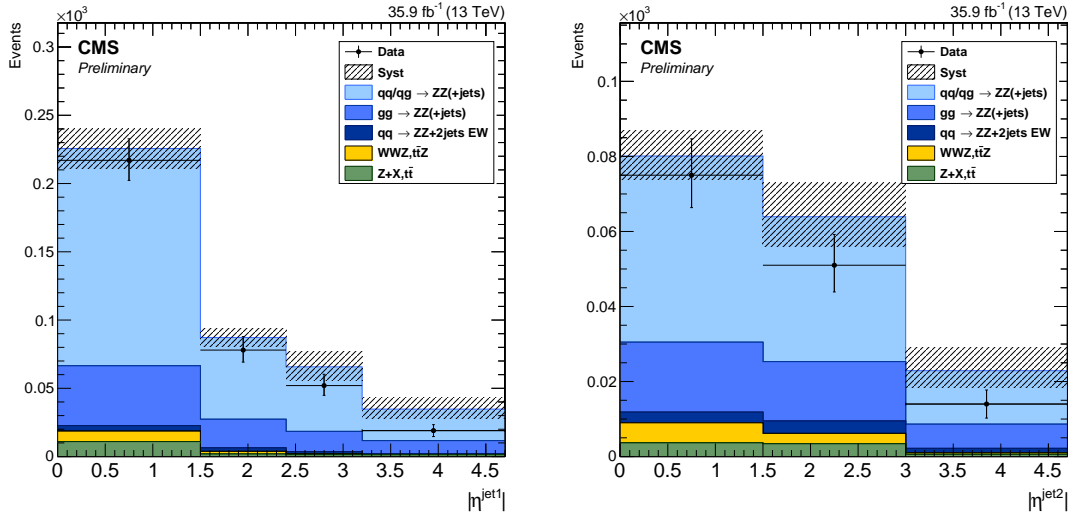


Figure 7.15: Distribution of leading (left) and subleading (right) jet $|\eta|$ for all ZZ events with at least one jet and at least two jets, respectively. Points represent data, with statistical uncertainty bars. The stack of filled histograms represents the SM signal prediction and background estimate, with a hatched band showing the sum in quadrature of the statistical and systematic uncertainties on the total expected yield.

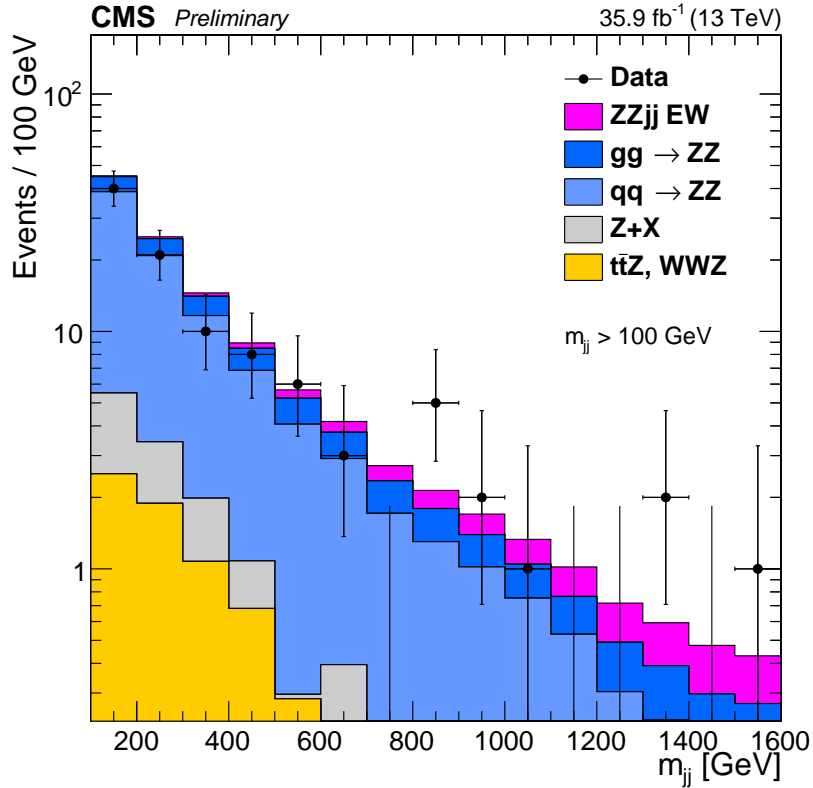


Figure 7.16: Dijet invariant mass m_{jj} of the tag jets in ZZ events passing the dijet selection ($m_{jj} > 100$ GeV). Points represent data, with statistical uncertainty bars. The stack of filled histograms represents the SM signal prediction, including EWK production, and background estimate.

100 The total cross section is shown as a function of \sqrt{s} in Fig. 7.18. Measurements from CMS [72–74, 222] and ATLAS [76, 77, 108] are compared to NLO predictions made with MCFM (with contributions from leading order gluon-gluon fusion diagrams), and NNLO predictions made with MATRIX. Results from both experiments agree with the predictions, verifying this aspect of the SM to within the measurements’ uncertainties.

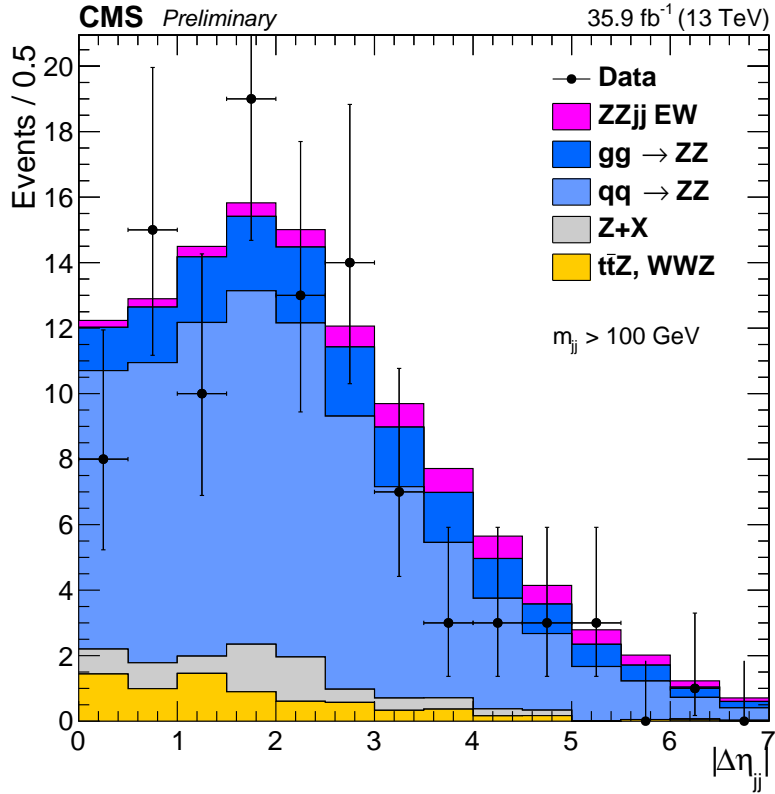


Figure 7.17: Pseudorapidity separation $|\Delta\eta_{jj}|$ of tag jets in ZZ events passing the dijet selection ($m_{jj} > 100$ GeV). Points represent data, with statistical uncertainty bars. The stack of filled histograms represents the SM signal prediction, including EWK production, and background estimate.

¹⁰⁶ 7.2 Differential Cross Sections

¹⁰⁷ Detector-level distributions are unfolded to calculate differential cross sections as de-
¹⁰⁸ scribed in Section 6.4. Figures 7.19–7.30 show measured differential cross sections
¹⁰⁹ and corresponding theory predictions, as functions of different observables. All dis-
¹¹⁰ tributions are normalized to the inclusive fiducial cross section, such that the integral
¹¹¹ of each is unity, including overflow bins (not shown). The observables in Figs. 7.19–
¹¹² 7.24 consider only the four-lepton system. For the calculation of these distributions,
¹¹³ as well as the differential cross section as a function of N_{jets} (Fig. 7.25), all events

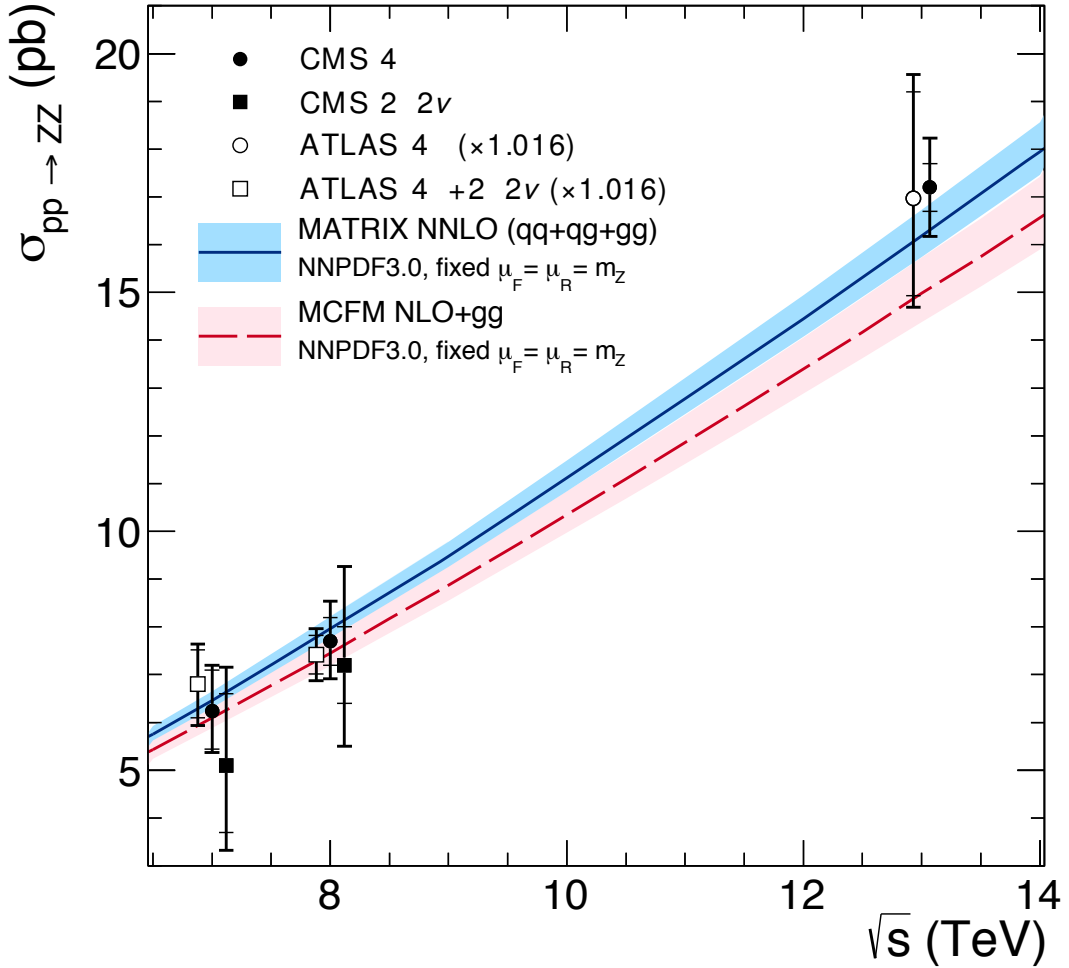


Figure 7.18: The total ZZ cross section is shown as a function of \sqrt{s} . Measurements from CMS and ATLAS are both shown, with the ATLAS numbers adjusted upward by 1.6% to account for differences in Z mass window choice. Points at the same center-of-mass energy are shifted slightly in the horizontal direction for clarity. Experimental measurements are compared to predictions from MCFM at NLO in QCD with additional contributions from LO gluon-gluon fusion diagrams, and MATRIX at NNLO in QCD. Both sets of predictions use the NNPDF3.0 PDF sets and fixed scales $\mu_F = \mu_R = m_Z$.

114 passing the on-shell selection of Table 6.2 are used. Figures 7.26 and 7.27 show m_{jj}
 115 and $|\Delta\eta_{jj}|$ for all ZZ events with at least two jets, while Figs 7.28 and 7.29 show p_T
 116 and η , respectively, for the leading jet in events with $N_{jets} \geq 1$ on the left and the
 117 subleading jet in events with $N_{jets} \geq 2$ on the right. In Fig. 7.30, the phase space is
 118 expanded to the full spectrum selection of Table 6.2 at both detector and true level,
 119 to show the four-lepton differential cross section through all production modes as a
 120 function of $m_{4\ell}$. Measured cross sections overall agree with the theoretical predictions
 121 within their uncertainties, which are dominated by statistical uncertainties in all bins.

122 **7.3 Vector Boson Scattering**

123 Figure 7.31 shows the output of the GBDT discussed in Section 6.5 for events in
 124 the dijet selection. The search procedure finds a modest excess of events compatible
 125 with VBS ZZjj signal, at the level of 2.7 standard deviations over the null hypothesis
 126 of the SM without VBS ZZ production. The expected significance is 1.6 standard
 127 deviations. This corresponds to a VBS fiducial cross section of

$$\sigma_{fid}(pp \rightarrow ZZjj(EWK) \rightarrow 4\ell jj) = 0.40^{+0.21}_{-0.16} (\text{stat})^{+0.13}_{-0.09} (\text{syst}) \text{ fb}, \quad (7.10)$$

128 which is consistent with the SM prediction of $0.29^{+0.02}_{-0.03}$ fb.

129 **7.4 Anomalous Coupling Limits**

130 The ZZ invariant mass is shown in Fig. 7.32 for all events in the on-shell selection,
 131 with two example distributions shown for potential scenarios with nonzero aTGCs,
 132 one of which sets $f_5^\gamma = 0.0019$ and $f_5^Z = 0.0015$, and the other $f_4^\gamma = 0.0019$ and
 133 $f_4^Z = 0.0015$. The limit setting procedure described in Section 6.6 is applied to
 134 each aTGC parameter, with all other couplings fixed to their SM values, to yield

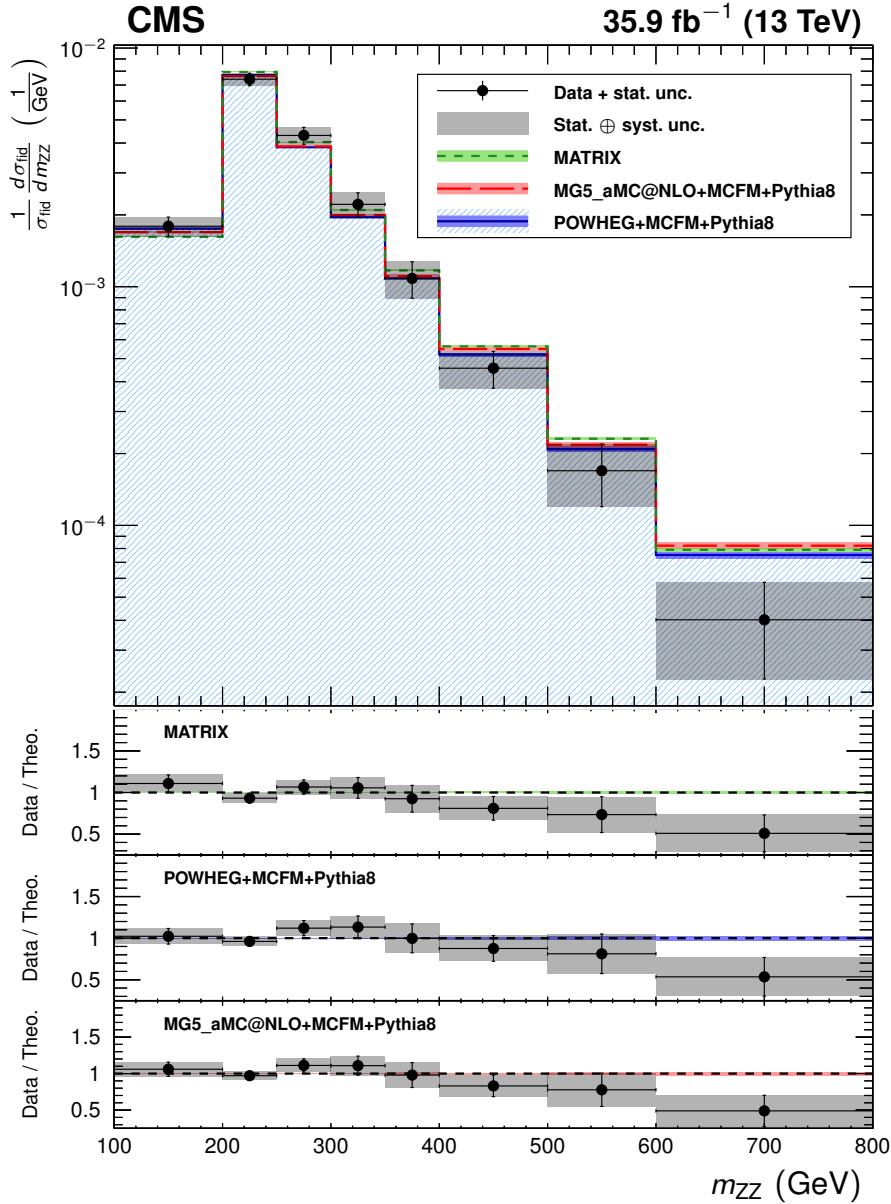


Figure 7.19: The ZZ differential cross section as a function of m_{ZZ} , normalized to the inclusive fiducial cross section. Points represent the unfolded data, with vertical bars showing the statistical uncertainty and a grey band showing the sum in quadrature of the statistical and systematic uncertainties. Blue, red, and green histograms represent the POWHEG+MCFM, MADGRAPH5_aMC@NLO+MCFM, and MATRIX predictions, respectively, with bands around each which represent their combined statistical, scale, and PDF uncertainties. The lower sections of the plot represents the ratio of the measured cross section to each of the predictions.

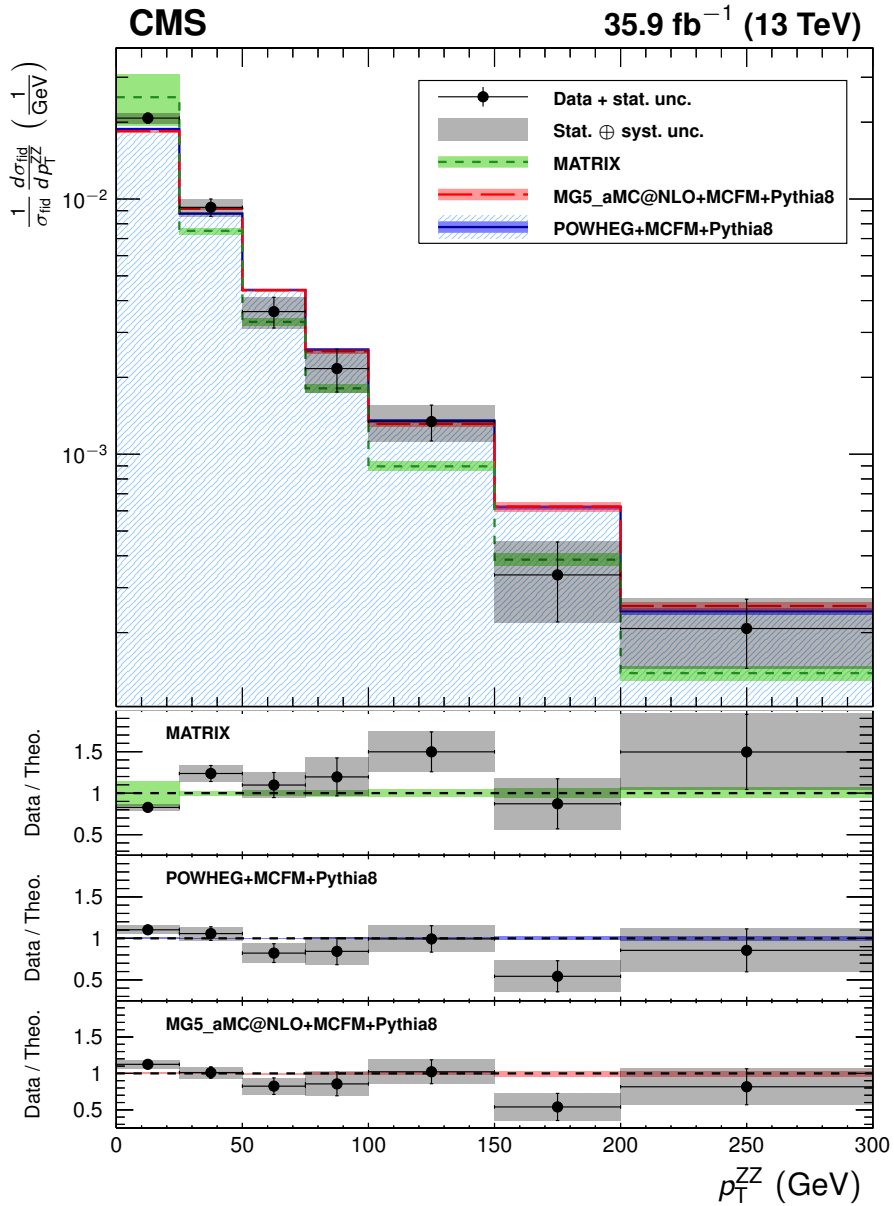


Figure 7.20: The ZZ differential cross section as a function of the four-lepton p_T , normalized to the inclusive fiducial cross section. Points represent the unfolded data, with vertical bars showing the statistical uncertainty and a grey band showing the sum in quadrature of the statistical and systematic uncertainties. Blue, red, and green histograms represent the POWHEG+MCFM, MADGRAPH5_aMC@NLO+MCFM, and MATRIX predictions, respectively, with bands around each which represent their combined statistical, scale, and PDF uncertainties. The lower sections of the plot represents the ratio of the measured cross section to each of the predictions.

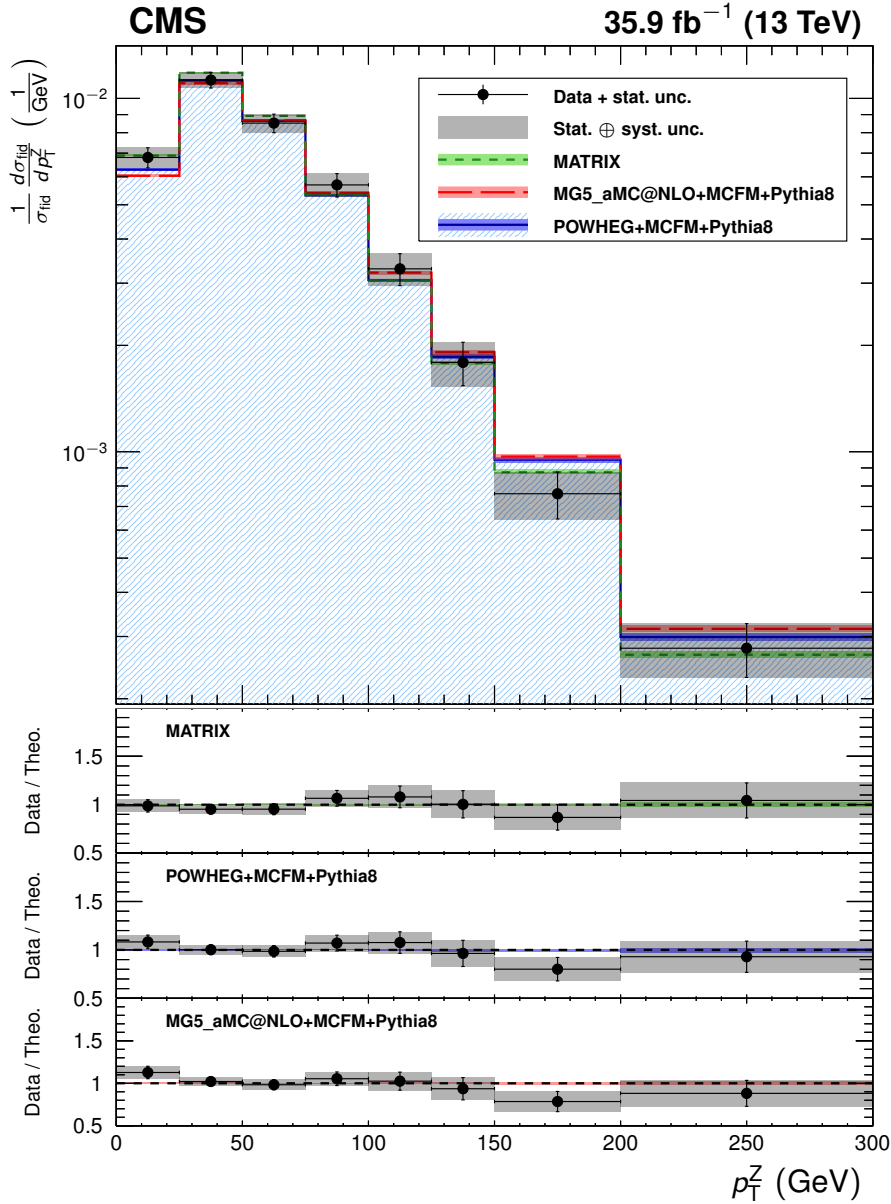


Figure 7.21: The ZZ differential cross section as a function of the p_T of both Z boson candidates, regardless of which one is Z_1 and which is Z_2 , normalized to the inclusive fiducial cross section. Points represent the unfolded data, with vertical bars showing the statistical uncertainty and a grey band showing the sum in quadrature of the statistical and systematic uncertainties. Blue, red, and green histograms represent the POWHEG+MCFM, MADGRAPH5_aMC@NLO+MCFM, and MATRIX predictions, respectively, with bands around each which represent their combined statistical, scale, and PDF uncertainties. The lower sections of the plot represents the ratio of the measured cross section to each of the predictions.

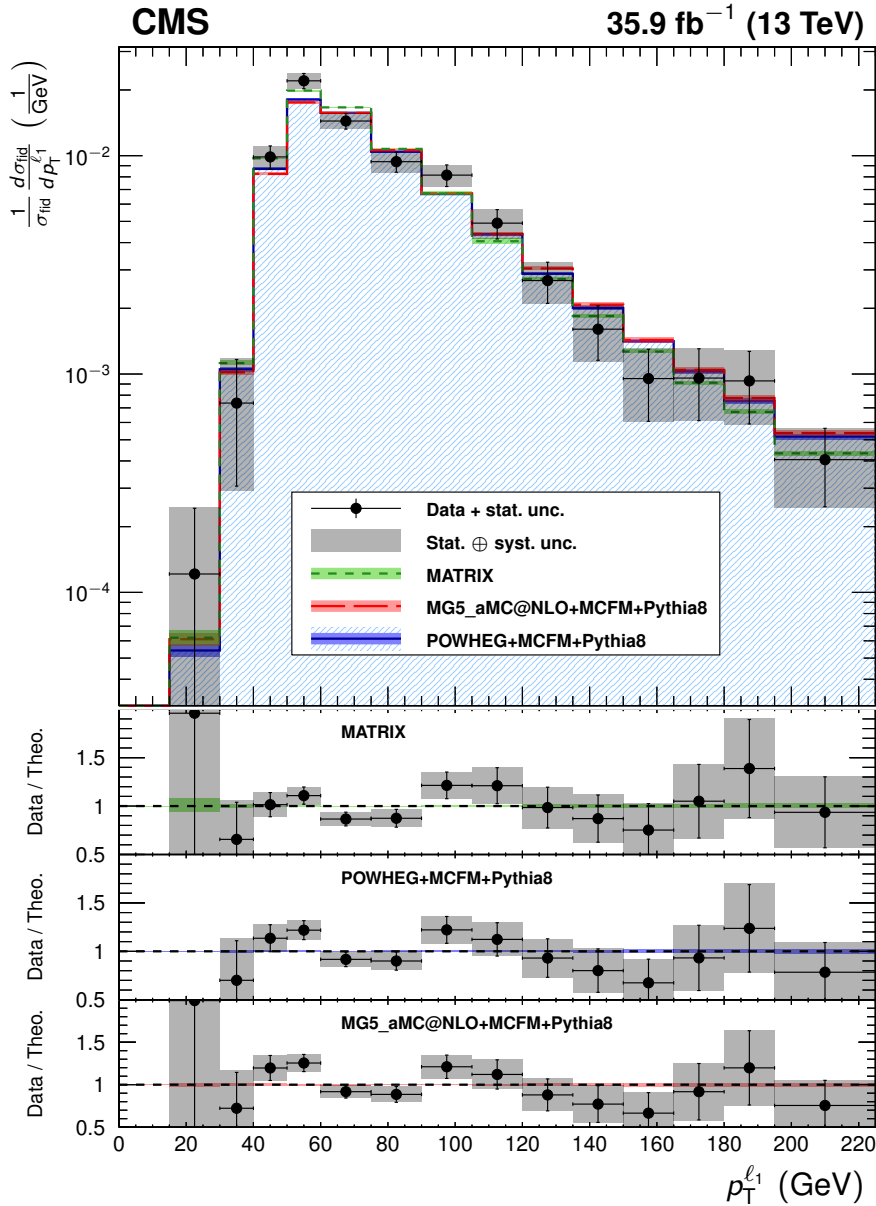


Figure 7.22: The ZZ differential cross section as a function of leading lepton p_T , normalized to the inclusive fiducial cross section. Points represent the unfolded data, with vertical bars showing the statistical uncertainty and a grey band showing the sum in quadrature of the statistical and systematic uncertainties. Blue, red, and green histograms represent the POWHEG+MCFM, MADGRAPH5_aMC@NLO+MCFM, and MATRIX predictions, respectively, with bands around each which represent their combined statistical, scale, and PDF uncertainties. The lower sections of the plot represents the ratio of the measured cross section to each of the predictions.

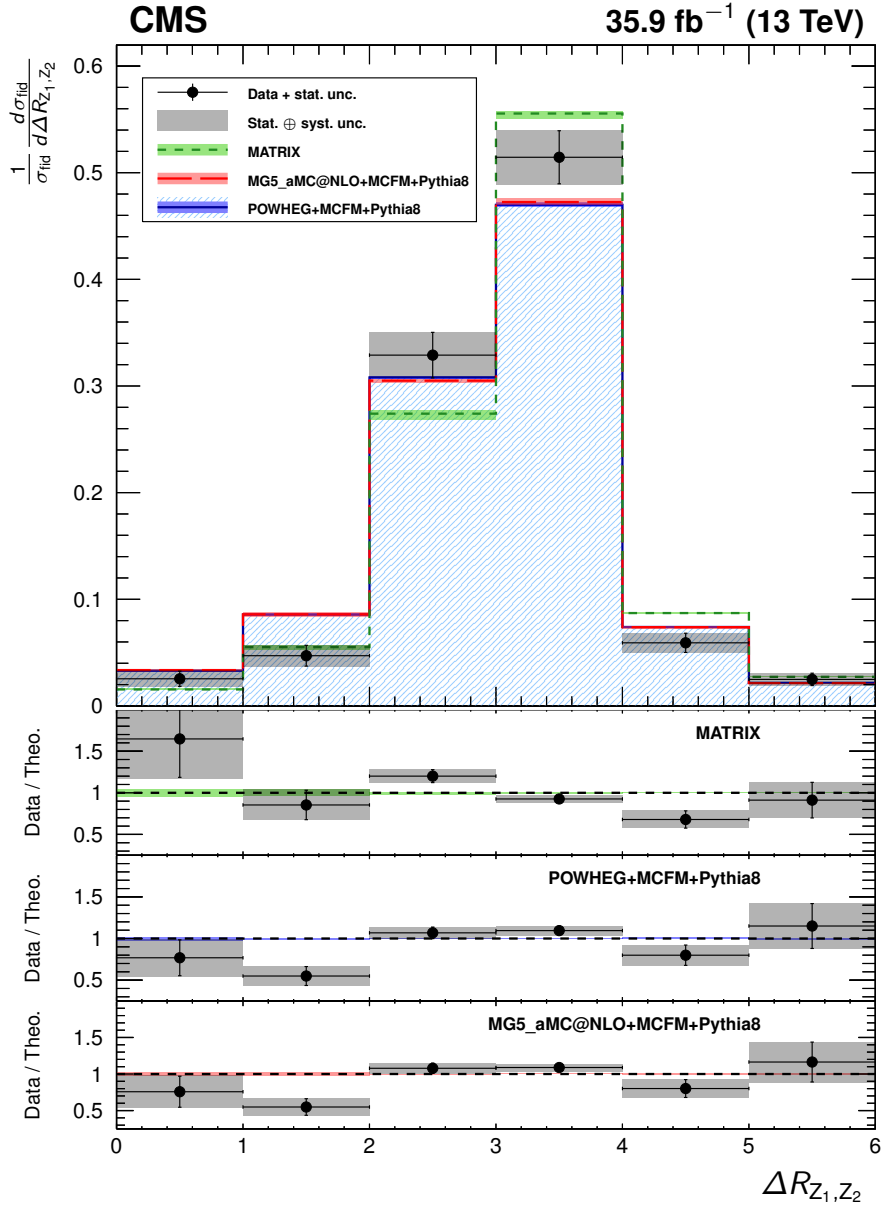


Figure 7.23: The ZZ differential cross section as a function of ΔR between the two Z bosons, normalized to the inclusive fiducial cross section. Points represent the unfolded data, with vertical bars showing the statistical uncertainty and a grey band showing the sum in quadrature of the statistical and systematic uncertainties. Blue, red, and green histograms represent the POWHEG+MCFM, MADGRAPH-5_amc@NLO+MCFM, and MATRIX predictions, respectively, with bands around each which represent their combined statistical, scale, and PDF uncertainties. The lower sections of the plot represents the ratio of the measured cross section to each of the predictions.

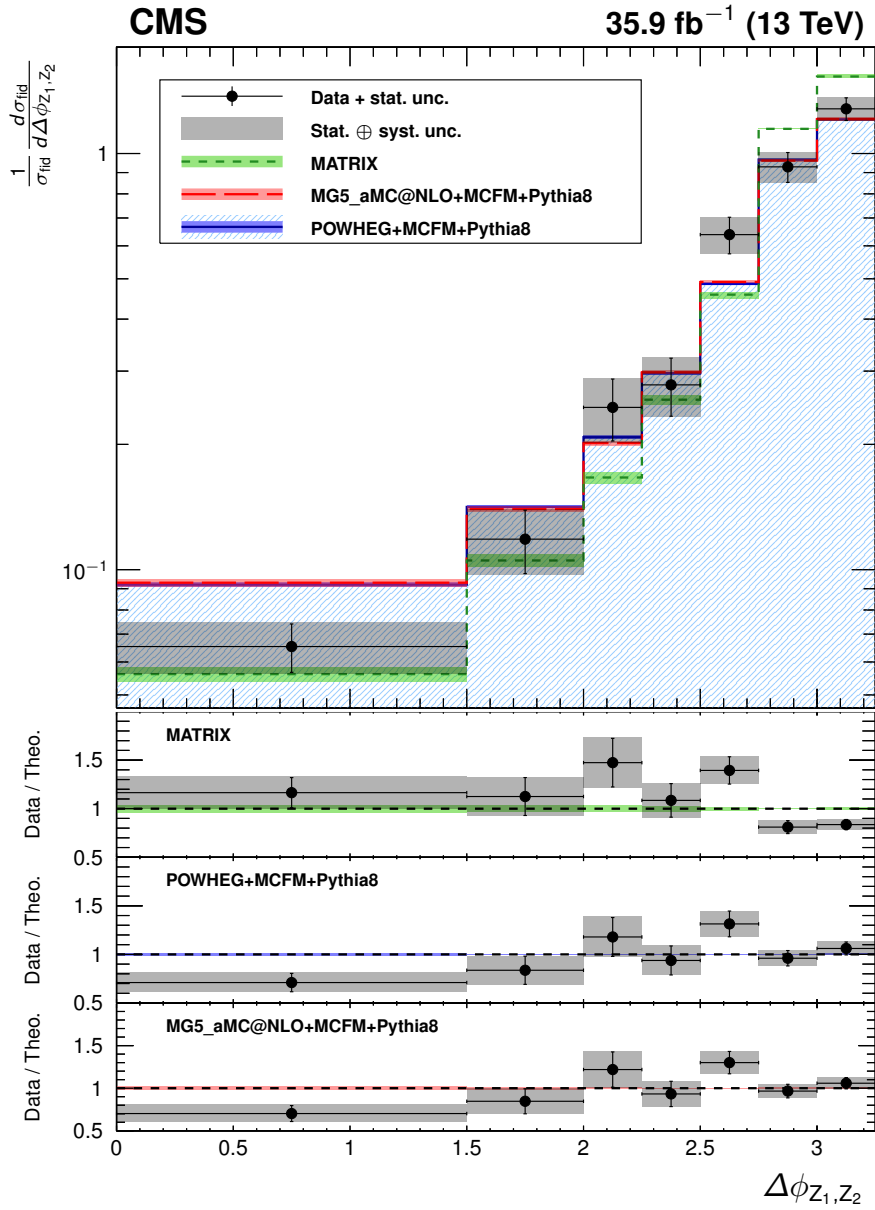


Figure 7.24: The ZZ differential cross section as a function of $\Delta\phi$ between the two Z bosons, normalized to the inclusive fiducial cross section. Points represent the unfolded data, with vertical bars showing the statistical uncertainty and a grey band showing the sum in quadrature of the statistical and systematic uncertainties. Blue, red, and green histograms represent the POWHEG+MCFM, MADGRAPH-5_amc@NLO+MCFM, and MATRIX predictions, respectively, with bands around each which represent their combined statistical, scale, and PDF uncertainties. The lower sections of the plot represents the ratio of the measured cross section to each of the predictions.

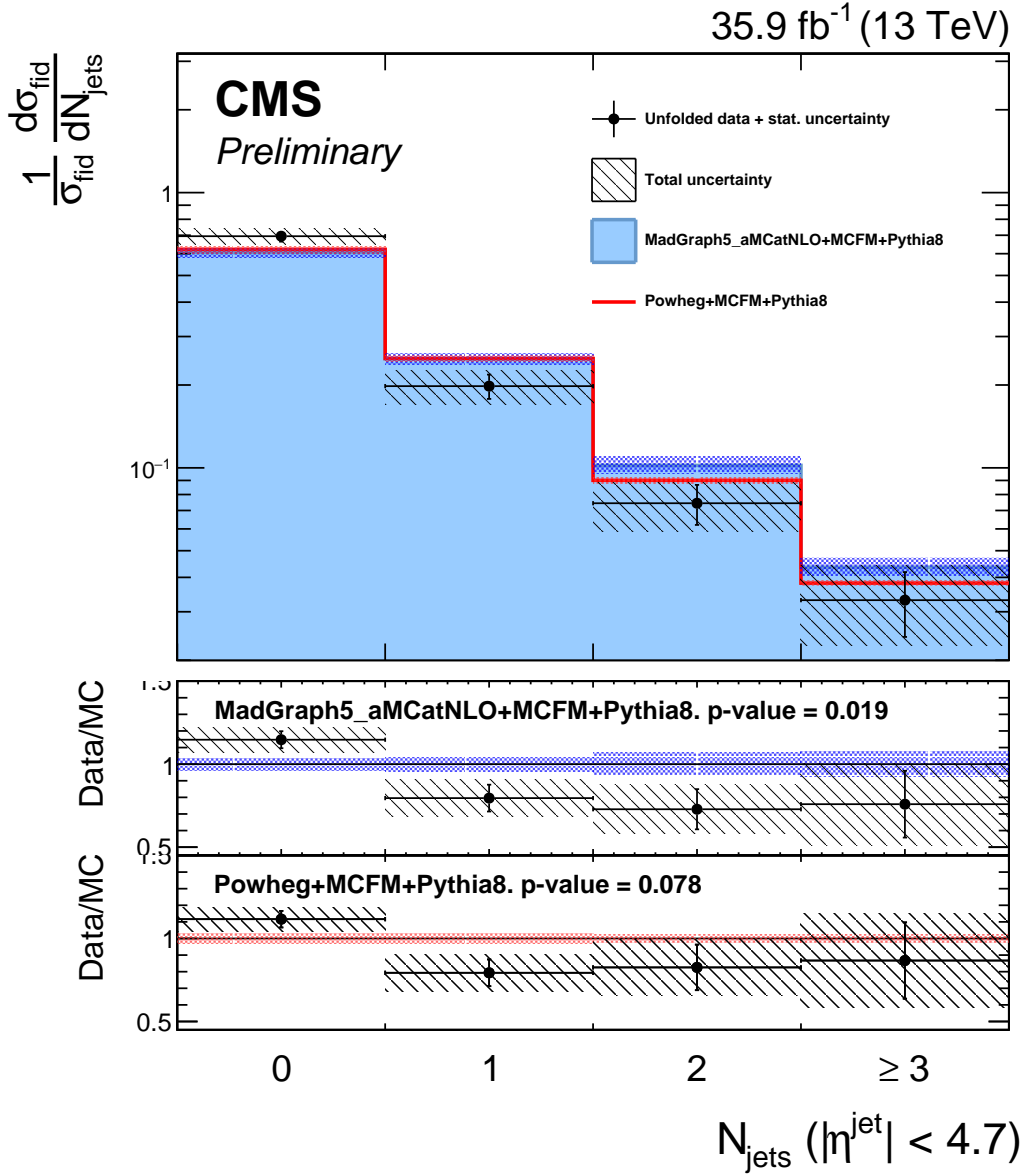


Figure 7.25: The ZZ differential cross section as a function of the jet multiplicity N_{jets} , normalized to the inclusive fiducial cross section. Points represent the unfolded data, with vertical bars showing the statistical uncertainty and a hatched band showing the sum in quadrature of the statistical and systematic uncertainties. Red and blue histograms represent the POWHEG+MCFM and MADGRAPH5_aMC@NLO+MCFM predictions, respectively, with bands around each which represent their combined statistical, scale, and PDF uncertainties. The lower sections of the plot represents the ratio of the measured cross section to each of the predictions.

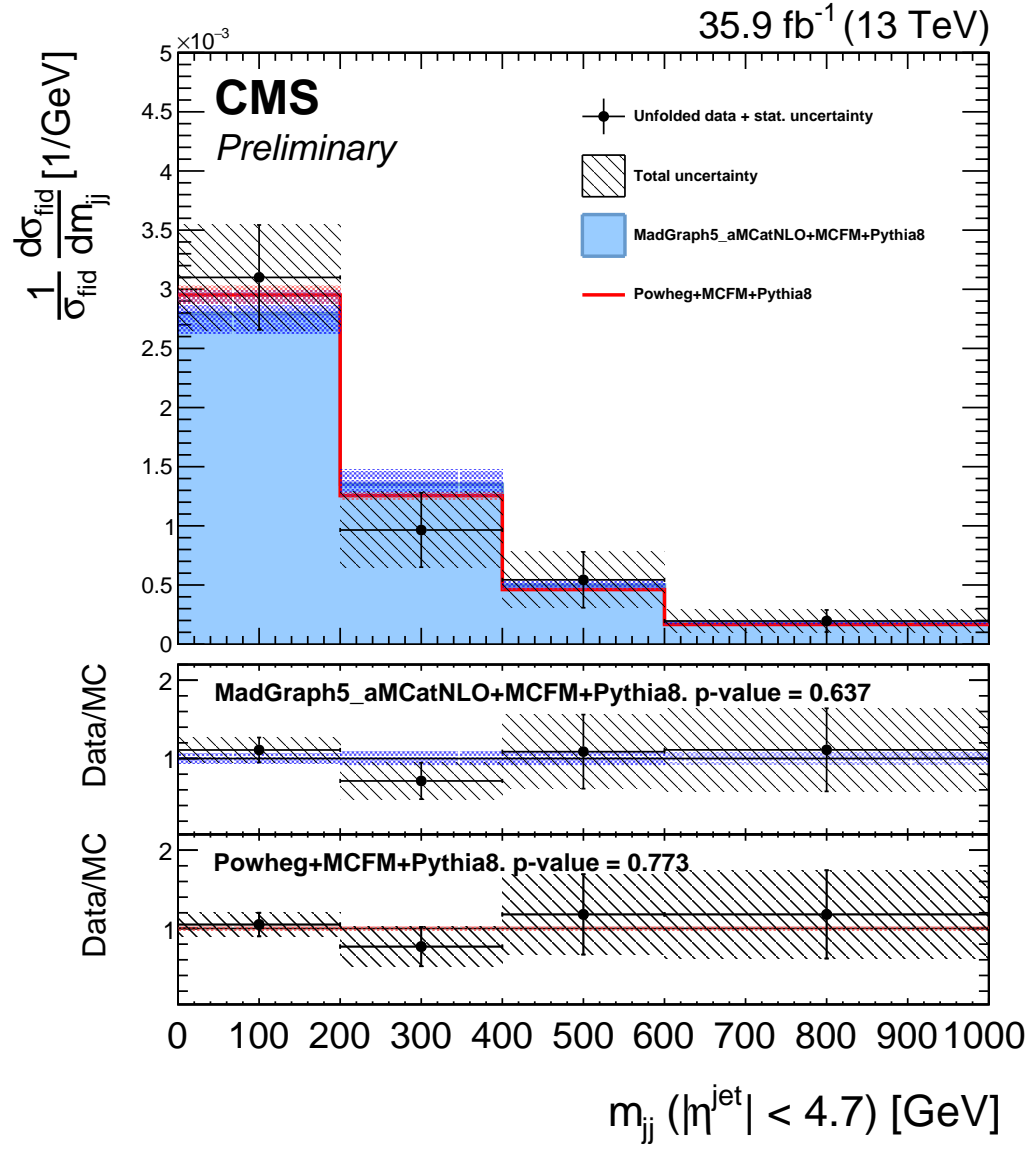


Figure 7.26: The ZZ differential cross section as a function of the invariant mass of the two highest- p_T jets m_{jj} , including all ZZ events with at least two jets, normalized to the inclusive fiducial cross section. Points represent the unfolded data, with vertical bars showing the statistical uncertainty and a hatched band showing the sum in quadrature of the statistical and systematic uncertainties. Red and blue histograms represent the POWHEG+MCFM and MADGRAPH5_aMC@NLO+MCFM predictions, respectively, with bands around each which represent their combined statistical, scale, and PDF uncertainties. The lower sections of the plot represents the ratio of the measured cross section to each of the predictions.

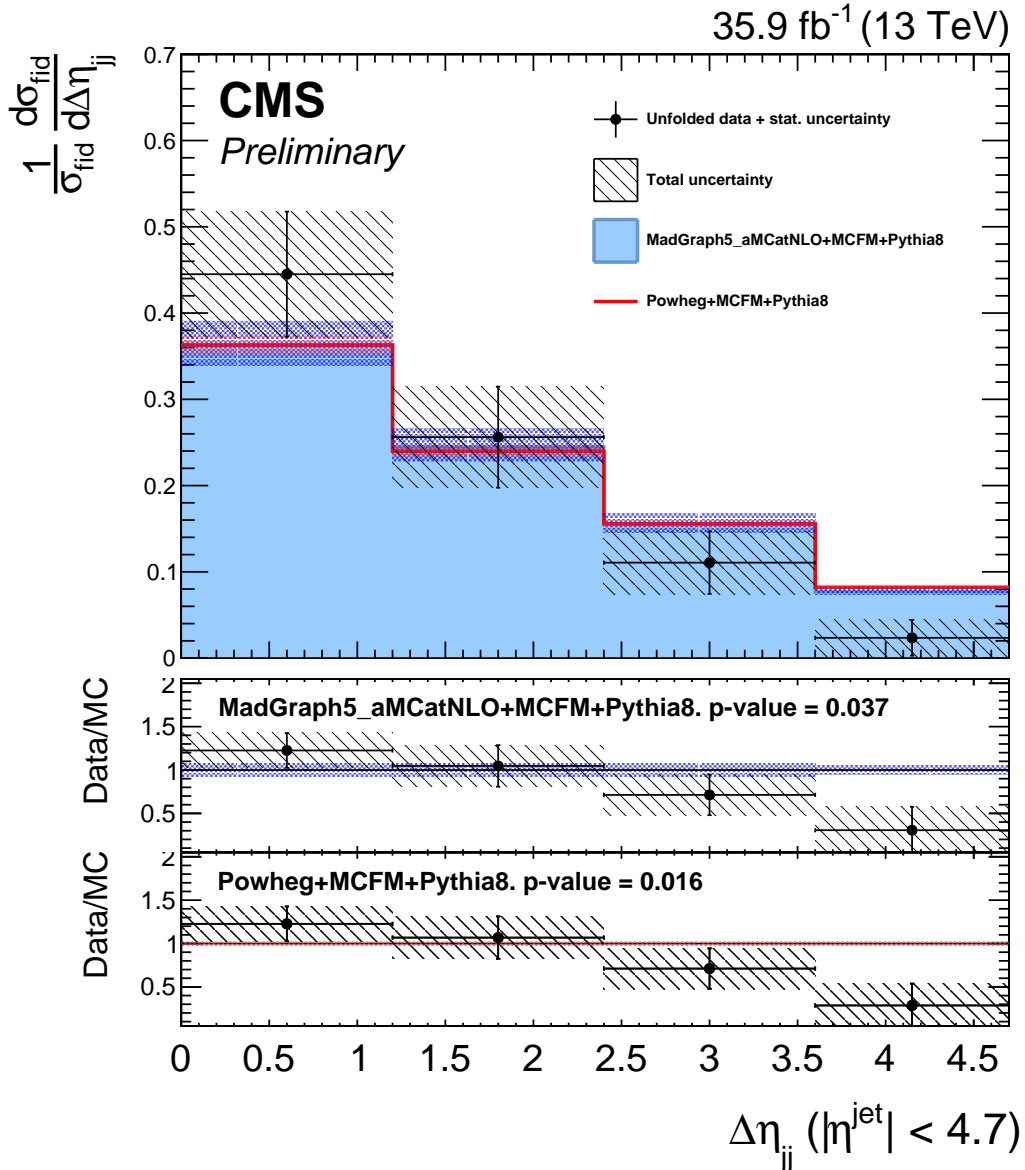


Figure 7.27: The ZZ differential cross section as a function of the absolute pseudo-rapidity separation of the two highest- p_T jets $|\Delta\eta_{jj}|$, including all ZZ events with at least two jets, normalized to the inclusive fiducial cross section. Points represent the unfolded data, with vertical bars showing the statistical uncertainty and a hatched band showing the sum in quadrature of the statistical and systematic uncertainties. Red and blue histograms represent the POWHEG+MCFM and MADGRAPH5_aMC@NLO+MCFM predictions, respectively, with bands around each which represent their combined statistical, scale, and PDF uncertainties. The lower sections of the plot represents the ratio of the measured cross section to each of the predictions.

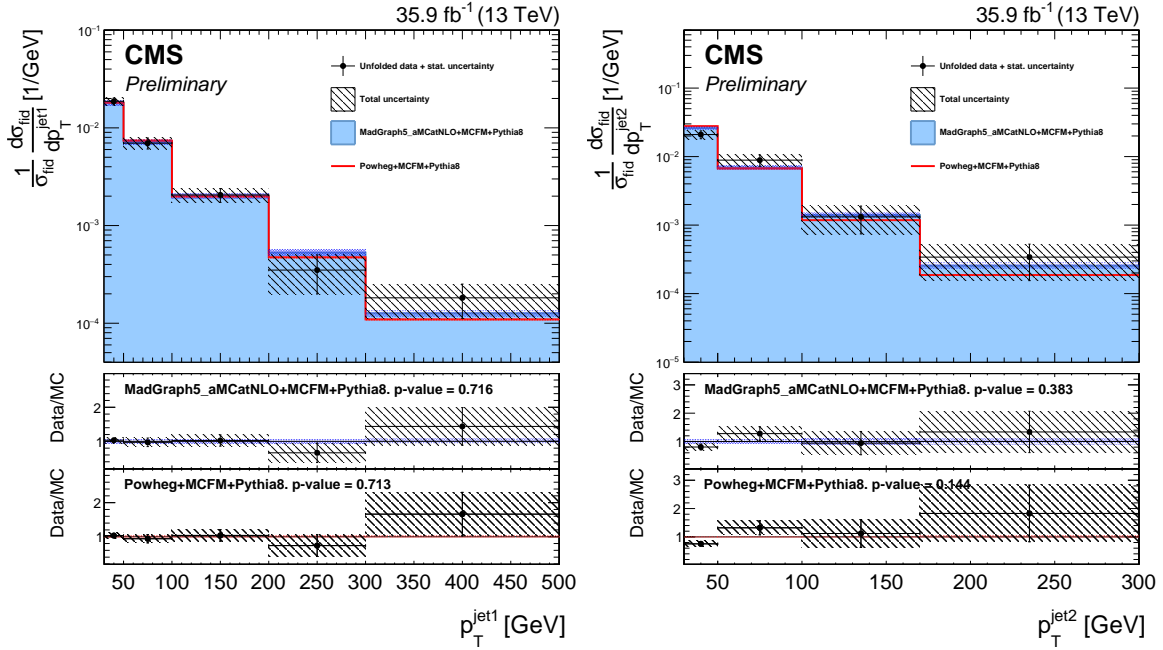


Figure 7.28: The ZZ differential cross section as a function of the leading (left) and subleading (right) jet p_T , in ZZ events with at least one jet and at least two jets respectively, normalized to the inclusive fiducial cross section. Points represent the unfolded data, with vertical bars showing the statistical uncertainty and a hatched band showing the sum in quadrature of the statistical and systematic uncertainties. Red and blue histograms represent the POWHEG+MCFM and MADGRAPH5_aMC@NLO+MCFM predictions, respectively, with bands around each which represent their combined statistical, scale, and PDF uncertainties. The lower sections of the plots represent the ratio of the measured cross section to each of the predictions.

135 one-dimensional 95% CL limits,

$$\begin{aligned} -0.0012 < f_4^Z < 0.0010, \quad -0.0010 < f_5^Z < 0.0013, \\ -0.0012 < f_4^\gamma < 0.0013, \quad -0.0012 < f_5^\gamma < 0.0013. \end{aligned} \tag{7.11}$$

136 These results improve the previous CMS limits, which were the most stringent set
 137 previously, by factors of 2–3 [74] and are the most stringent limits to date on the
 138 parameters in question. Recent preliminary limits from ATLAS using 13 TeV data
 139 are 50–80% looser [229]. Two-dimensional limits are set in the f_4^γ - f_4^Z and f_5^γ - f_5^Z
 140 planes, holding all other parameters to the SM values in each calculation. One- and

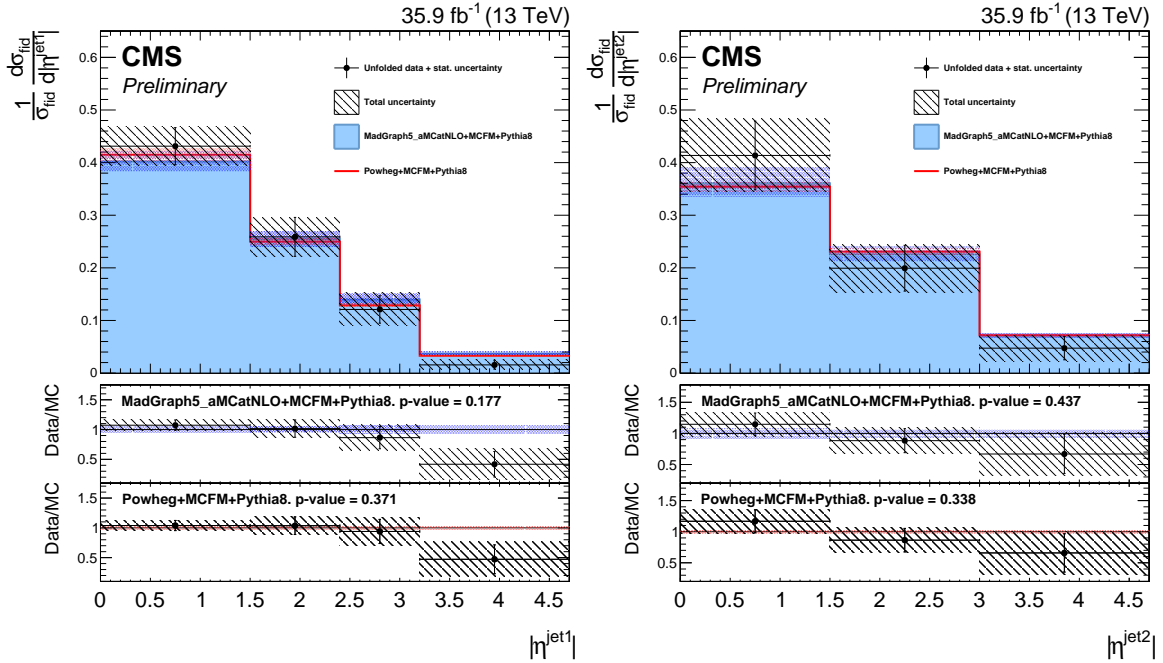


Figure 7.29: The ZZ differential cross section as a function of the leading (left) and subleading (right) jet η , in ZZ events with at least one jet and at least two jets respectively, normalized to the inclusive fiducial cross section. Points represent the unfolded data, with vertical bars showing the statistical uncertainty and a hatched band showing the sum in quadrature of the statistical and systematic uncertainties. Red and blue histograms represent the POWHEG+MCFM and MADGRAPH5_aMC@NLO+MCFM predictions, respectively, with bands around each which represent their combined statistical, scale, and PDF uncertainties. The lower sections of the plots represent the ratio of the measured cross section to each of the predictions.

141 two-dimensional 95% CL limits are shown in Fig. 7.33.

142 No unitarizing form factor (c.f. Section 1.5.1) is applied when calculating the
 143 limits of Eq. (7.11). One way to enforce unitarity without a form factor would be
 144 to restrict the maximum ZZ invariant mass used, and set the limits considering only
 145 events with m_{ZZ} below some cutoff. The limits would then depend on the cutoff
 146 chosen, converging to the nonunitary limits when the cutoff is larger than the energies
 147 accessible in the experiment. The limit computations are repeated with multiple
 148 cutoff values, and the resulting expected and observed limits are shown in Fig. 7.34

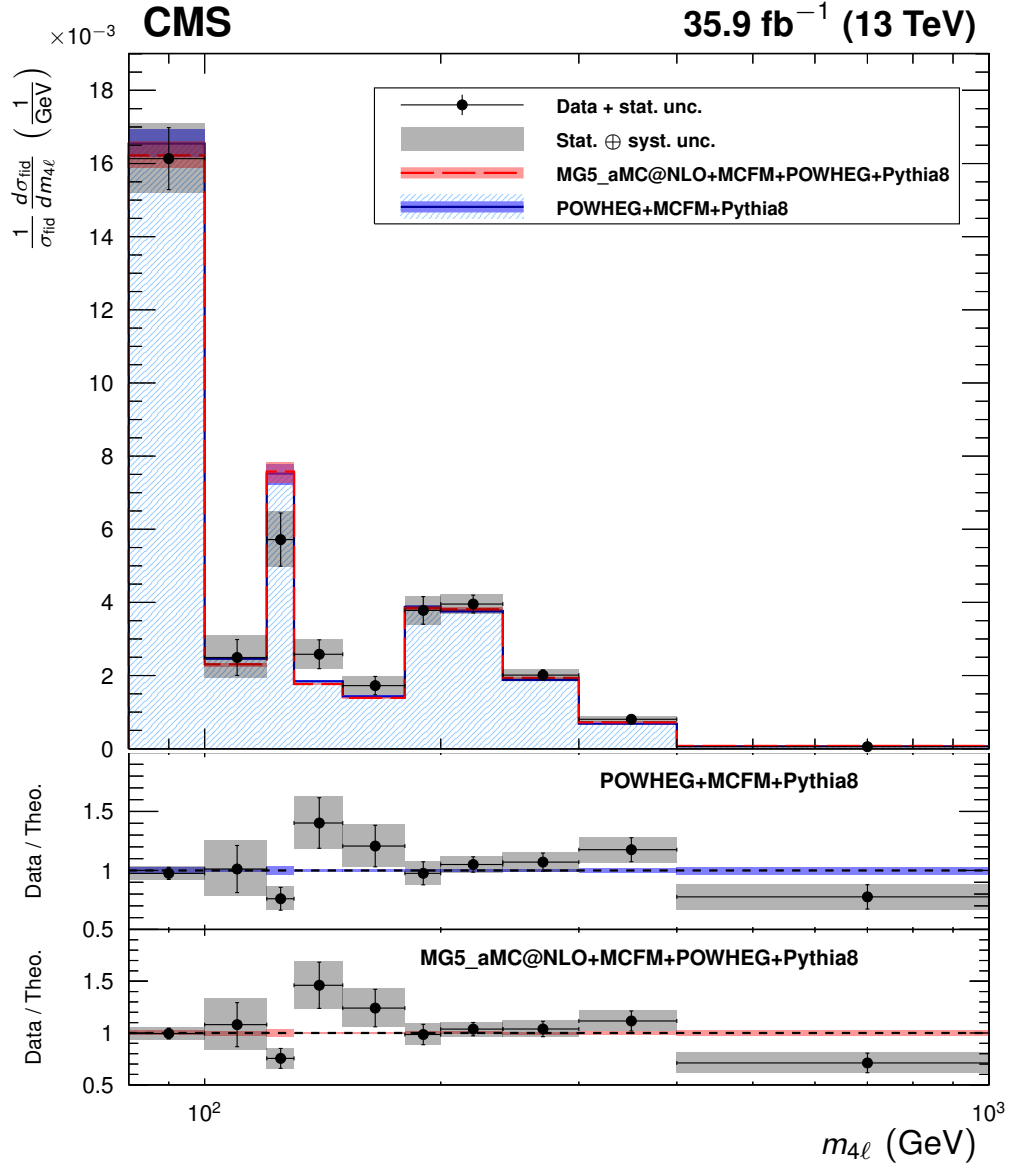


Figure 7.30: The four-lepton differential cross section as a function of $m_{4\ell}$ under the full spectrum selections, normalized to the inclusive fiducial cross section. Points represent the unfolded data, with vertical bars showing the statistical uncertainty and a grey band showing the sum in quadrature of the statistical and systematic uncertainties. Blue and red histograms represent the POWHEG+MCFM and MADGRAPH5_aMC@NLO+MCFM predictions, respectively, with bands around each which represent their combined statistical, scale, and PDF uncertainties. The lower sections of the plot represents the ratio of the measured cross section to each of the predictions.

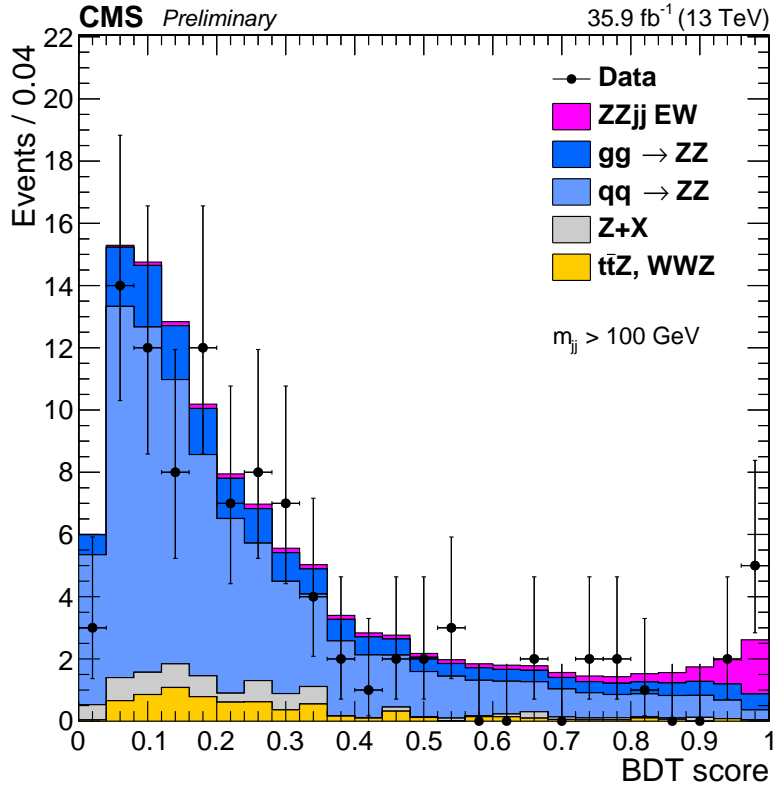


Figure 7.31: Output distribution of the VBS signal extraction GBDT, for events in the dijet selection. Points represent data, with statistical uncertainty bars. The stack of filled histograms represents the SM signal prediction and background estimate.

149 as a function of the maximum m_{ZZ} used.

150 The aQGC search proceeds the same way, but using events in the dijet selection.

151 The observable used for limit setting is again m_{ZZ} , which is shown for these events

152 in Fig. 7.35 along with two example distributions for scenarios with nonzero aQGCs,

153 one with $f_{T8}/\Lambda^4 = 1 \text{TeV}^{-4}$, the other with $f_{T9}/\Lambda^4 = 2 \text{TeV}^{-4}$. In the aQGC search, a

154 unitarity bound is imposed, chosen with VBFNLO [230] to be the value of m_{ZZ} at which

155 the scattering amplitude would violate unitarity if the aQGC parameter in question

156 were set to its 95% CL limit value. While limits are set for each parameter, all other

157 parameters and their unitarity bounds are set to zero. The observed 95% CL limits

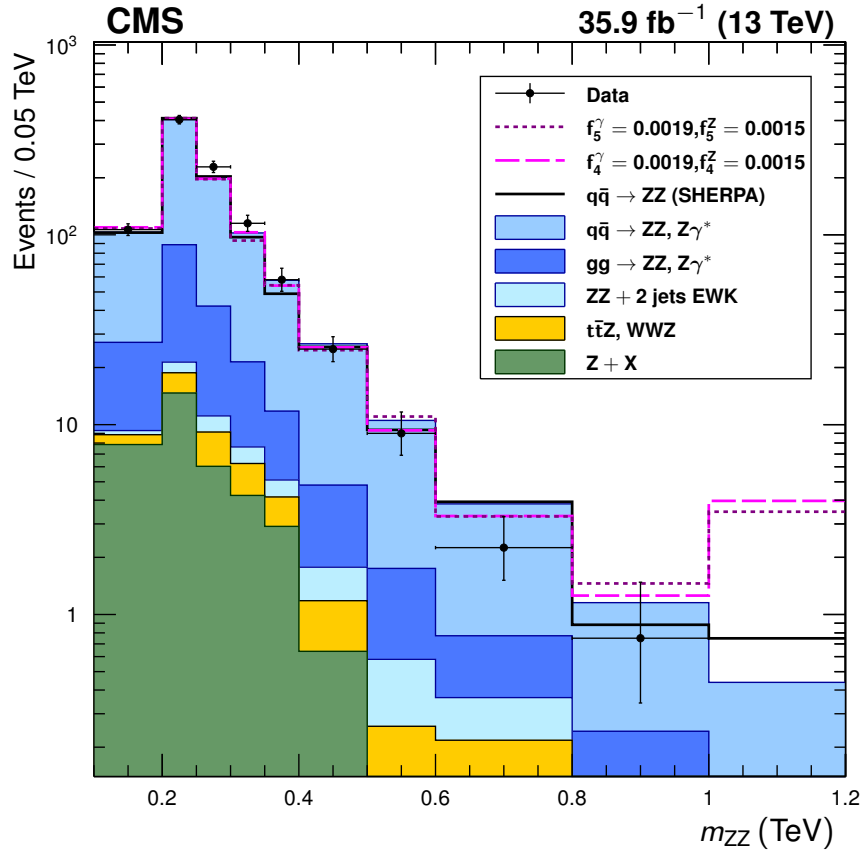


Figure 7.32: Distribution of ZZ invariant mass for all events in the on-shell selection. Points represent data, with statistical uncertainty bars. The stack of filled histograms represents the SM signal prediction and background estimate. The unfilled histograms represent two example SHERPA predictions for nonzero aTGC hypotheses (dashed) and the SHERPA SM prediction (solid), included to illustrate the shape differences between the SHERPA and POWHEG+MCFM SM predictions. The SHERPA distributions are normalized such that the SM prediction's total yield matches that of the other generators. The last bin includes the overflow contributions from events at masses above 1.2 TeV.

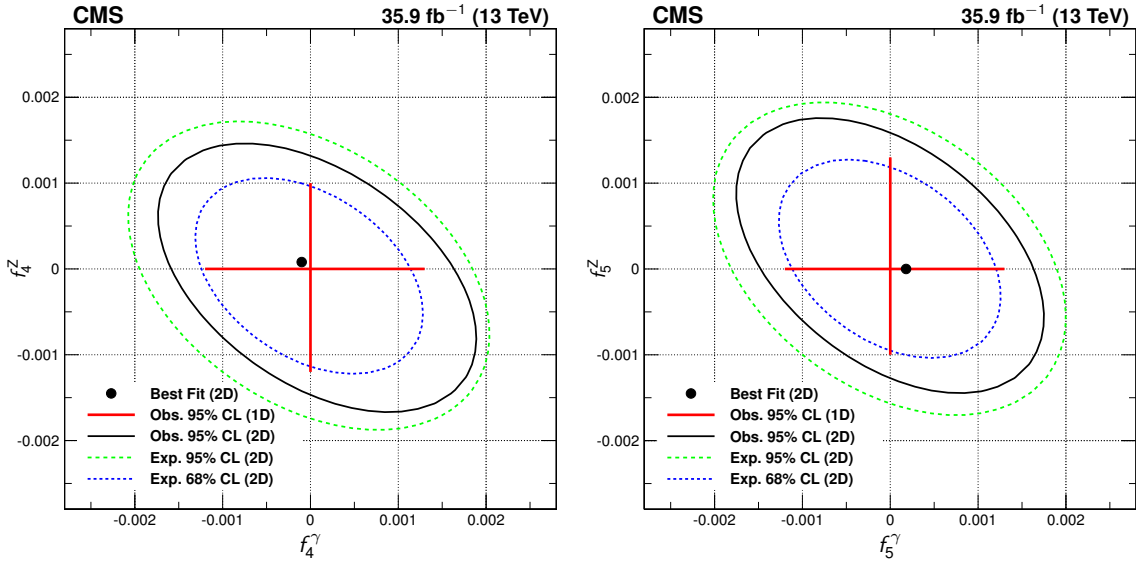


Figure 7.33: Two-dimensional observed 95% CL limits (solid contour) and expected 68 and 95% CL limits (dashed contours) in the f_4^γ - f_4^Z (left) and f_5^γ - f_5^Z (right) planes. The regions outside the contours are excluded at the corresponding confidence level. The dot is the point of maximum likelihood in the two-dimensional fits. Solid, straight lines at the center show the observed one-dimensional 95% CL limits for $f_{4,5}^\gamma$ (horizontal) and $f_{4,5}^Z$ (vertical). No form factor is used.

158 on the coefficients of the effective field theory operators covering ZZjj production

159 are

$$\begin{aligned}
 -0.46 &< f_{T0}/\Lambda^4 < 0.44 \text{ TeV}^{-4}, \\
 -0.61 &< f_{T1}/\Lambda^4 < 0.61 \text{ TeV}^{-4}, \\
 -1.2 &< f_{T2}/\Lambda^4 < 1.2 \text{ TeV}^{-4}, \\
 -0.84 &< f_{T8}/\Lambda^4 < 0.84 \text{ TeV}^{-4}, \\
 -1.8 &< f_{T9}/\Lambda^4 < 1.8 \text{ TeV}^{-4}.
 \end{aligned} \tag{7.12}$$

160 These are the most stringent constraints to date on all five parameters, improving on
 161 the previous best by factors of 2–8 (see Section 2.3.1). This is the first time any of
 162 them have been measured in the ZZjj channel.

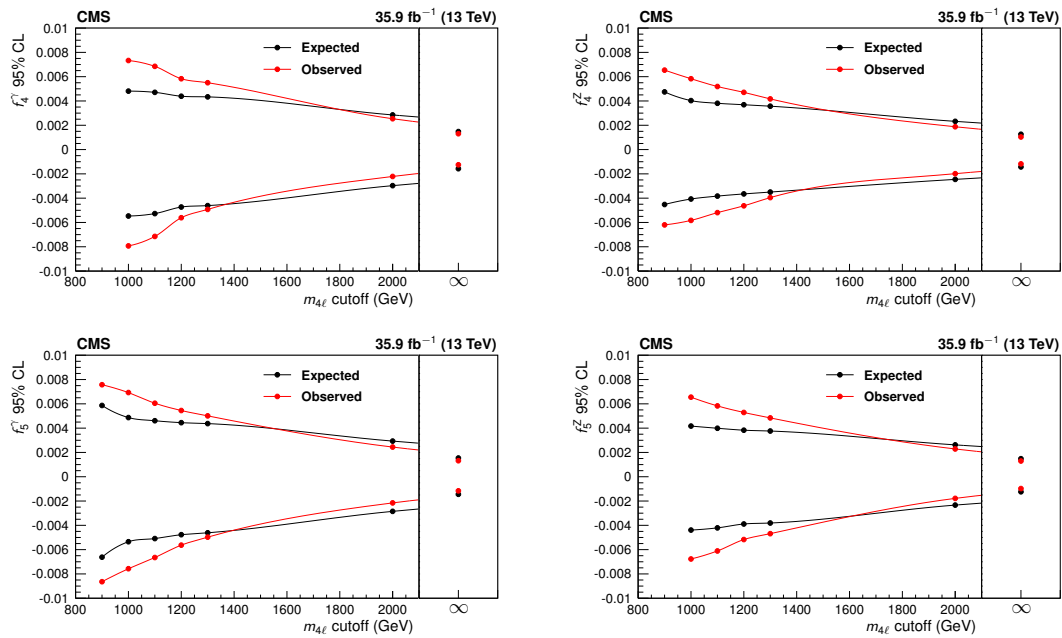


Figure 7.34: Expected and observed one-dimensional limits on the four aTGC parameters, as functions of the m_{ZZ} cutoff used to enforce unitarity. No form factor is used.

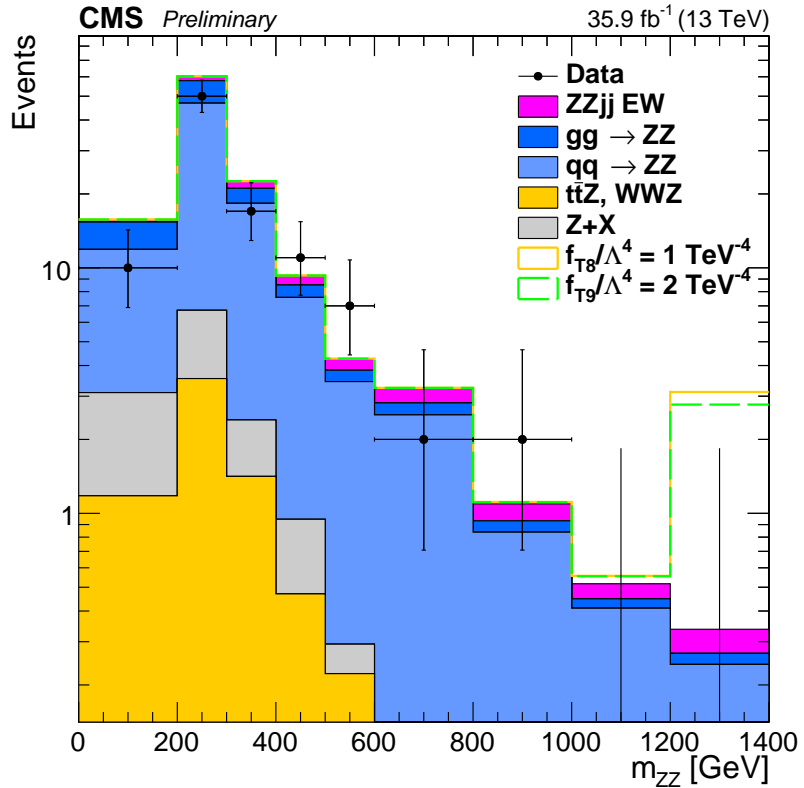


Figure 7.35: Distribution of ZZ invariant mass for events in the dijet selection. Points represent data, with statistical uncertainty bars. The stack of filled histograms represents the SM signal prediction and background estimate. The unfilled histograms represent two example MADGRAPH5_aMC@NLO distributions for nonzero aQGC hypotheses. The last bin includes the overflow contributions from events at masses above 1.4 TeV.

0 Chapter 8

1 Conclusions

2 8.1 Summary

3 Diboson studies in high-energy particle collisions are important probes of the elec-
4 troweak sector of the standard model. In particular, measurements of ZZ , ZZ^* , $Z\gamma^*$,
5 and $\gamma^*\gamma^*$ production shed light on the couplings between the neutral gauge bosons
6 and on the details of electroweak symmetry breaking. Decays to four charged leptons
7 (electrons or muons) are rare, but they can be easily identified and fully reconstructed,
8 and they represent a clean channel with low backgrounds. The LHC at CERN has
9 generated proton-proton collisions with a center-of-mass energy of 13 TeV at record-
10 breaking luminosities, providing an unprecedented opportunity to study such pro-
11 cesses. The CMS detector is well designed for these measurements and collected a
12 high-quality dataset corresponding to an integrated luminosity of 35.9 fb^{-1} . Several
13 studies of four-lepton production were performed with this dataset and reported here.

14 Because the four-lepton channel is so clean, event selections are loose and effi-
15 ciencies are high. Most backgrounds are estimated from data. The full four-lepton
16 spectrum includes resonant single-Z decays ($\text{pp} \rightarrow Z \rightarrow \ell^+\ell^-\gamma^* \rightarrow 4\ell$), resonant Higgs

17 boson decays ($\text{pp} \rightarrow \text{H} \rightarrow \text{ZZ}^* \rightarrow 4\ell$), continuum production of a single Z boson and a
 18 nonresonant lepton pair ($\text{pp} \rightarrow \text{Z}\gamma^* \rightarrow 4\ell$), and continuum production of two on-shell
 19 ($60 < m_{\ell\ell} < 120 \text{ GeV}$) Z bosons ($\text{pp} \rightarrow \text{ZZ} \rightarrow 4\ell$).

20 Both inclusive and differential ZZ cross sections were measured. Inclusive cross
 21 sections were measured with a signal strength found by a maximum likelihood fit.
 22 The measured fiducial ZZ cross section, subject to the requirements of Table 6.2, is

$$\sigma_{\text{fid}}(\text{pp} \rightarrow \text{ZZ} \rightarrow 4\ell) = 40.9 \pm 1.3 \text{ (stat)} \pm 1.4 \text{ (syst)} \pm 1.0 \text{ (lumi)} \text{ fb}. \quad (8.1)$$

23 The total ZZ cross section, subject only to the constraint that both Z bosons be on-
 24 shell, was extrapolated with an acceptance correction and combined with the smaller
 25 (2.9 fb^{-1}) dataset collected in 2015. Its measured value is

$$\sigma(\text{pp} \rightarrow \text{ZZ}) = 17.2 \pm 0.5 \text{ (stat)} \pm 0.7 \text{ (syst)} \pm 0.4 \text{ (theo)} \pm 0.4 \text{ (lumi)} \text{ pb}. \quad (8.2)$$

26 The $Z \rightarrow 4\ell$ branching fraction was measured for events with $80 < m_{4\ell} < 100 \text{ GeV}$
 27 and a requirement of $m_{\ell\ell} > 4 \text{ GeV}$ for all opposite-sign, same-flavor lepton pairs, and
 28 found to be

$$\mathcal{B}(Z \rightarrow 4\ell) = 4.8 \pm 0.2 \text{ (stat)} \pm 0.2 \text{ (syst)} \pm 0.1 \text{ (theo)} \pm 0.1 \text{ (lumi)} \times 10^{-6}. \quad (8.3)$$

29 Differential cross sections were measured as functions of a number of observables
 30 including fully leptonic kinematic variables and quantities related to the production
 31 of associated jets. All results are in agreement with SM predictions.

32 A search was performed for fully electroweak ZZjj production using a gradient-
 33 boosted decision tree. An excess consistent with VBS was found at the level of 2.7
 34 standard deviations above the null hypothesis (1.6σ expected). This corresponds to
 35 a measured electroweak fiducial cross section of

$$\sigma_{\text{fid}}(\text{pp} \rightarrow \text{ZZjj(EWK)} \rightarrow 4\ell\text{jj}) = 0.40^{+0.21}_{-0.16} \text{ (stat)}^{+0.13}_{-0.09} \text{ (syst)} \text{ fb}, \quad (8.4)$$

36 consistent with SM predictions.

37 Searches were performed for anomalous triple and quartic gauge couplings. The
 38 aTGC search, considered in an effective lagrangian framework, used the invariant
 39 mass of inclusive ZZ events to set the most stringent 95% CL limits to date on ZZZ
 40 and ZZ γ couplings,

$$\begin{aligned} -0.0012 < f_4^Z < 0.0010, \quad -0.0010 < f_5^Z < 0.0013, \\ -0.0012 < f_4^\gamma < 0.0013, \quad -0.0012 < f_5^\gamma < 0.0013. \end{aligned} \tag{8.5}$$

41 Two-dimensional limits were also set. The aQGC search, performed in an effective
 42 field theory parameterization with ZZjj events, set the most stringent 95% CL limits
 43 to date on several dimension-8 operators which govern quartic gauge couplings,

$$\begin{aligned} -0.46 &< f_{T0}/\Lambda^4 &< 0.44 \text{ TeV}^{-4}, \\ -0.61 &< f_{T1}/\Lambda^4 &< 0.61 \text{ TeV}^{-4}, \\ -1.2 &< f_{T2}/\Lambda^4 &< 1.2 \text{ TeV}^{-4}, \\ -0.84 &< f_{T8}/\Lambda^4 &< 0.84 \text{ TeV}^{-4}, \\ -1.8 &< f_{T9}/\Lambda^4 &< 1.8 \text{ TeV}^{-4}. \end{aligned} \tag{8.6}$$

44 8.2 Outlook

45 Diboson measurements have great potential to shed further light on the SM or find
 46 deviations from it. In the long term, cross section measurements at higher center-
 47 of-mass energies are of great interest because new physics should be most obvious at
 48 high \sqrt{s} . With no new colliders expected in the near future¹, progress will first come
 49 in the form of precision measurements of processes that are in principle accessible
 50 now. The statistical uncertainties of the measured inclusive cross sections are now

¹The LHC may operate at $\sqrt{s} = 14$ TeV in the near future, which would be useful but only marginally more likely to reveal new physics, in line with the marginal increase in energy.

51 comparable to or smaller than the systematic uncertainties, and systematics should
52 dominate after the inclusion of data collected in 2017, even if new techniques are
53 developed which reduce lepton efficiency and trigger uncertainties somewhat. Un-
54 certainty reductions that can be expected in the short term will make the inclusive
55 measurements somewhat more useful—experimental uncertainties will be comparable
56 to or smaller than theoretical uncertainties, allowing further theoretical improvements
57 to be of interest—but the improvements will overall be limited by the difficulty of
58 reducing systematics in the highly active environments envisioned for future LHC
59 runs.

60 Differential cross sections and searches, however, will be statistically limited for
61 some time and will benefit greatly from additional luminosity at $\sqrt{s} = 13$ TeV. Sta-
62 tistical uncertainties dominate in almost all bins in the differential cross sections.
63 Assuming no deviations from the SM, data collected in 2017 will likely be enough to
64 allow 3σ evidence for VBS, when added to the 2016 data presented here. The statisti-
65 cal power for the aGC searches comes largely from the highest-mass bins, where very
66 few events have been observed—only three above 800 GeV and none above 1 TeV,
67 even in the inclusive selection. Further data collection will improve these limits sub-
68 stantially and place stringent restrictions on BSM neutral gauge boson couplings—or
69 discover them.

70 Bibliography

- 71 [1] D. J. Griffiths, *Introduction to elementary particles; 2nd rev. version*, ser.
72 Physics textbook. New York, NY: Wiley, 2008.
- 73 [2] F. Halzen and A. Martin, *Quarks & Leptons: An introductory course in*
74 *modern particle physics*. New York, USA: John Wiley & Sons, 1984.
- 75 [3] V. Barger and R. Phillips, *Collider Physics*, ser. Frontiers in physics. Avalon
76 Publishing, 1997, ISBN: 9780201149456.
- 77 [4] M. E. Peskin and D. V. Schroeder, *An Introduction to quantum field theory*.
78 Reading, USA: Addison-Wesley, 1995, ISBN: 9780201503975, 0201503972.
- 79 [5] J. F. Donoghue, E. Golowich, and B. R. Holstein, *Dynamics of the Standard*
80 *Model*, ser. Cambridge monographs on particle physics, nuclear physics, and
81 cosmology. Cambridge: Cambridge Univ. Press, 1992.
- 82 [6] O. W. Greenberg, “Spin and unitary-spin independence in a paraquark
83 model of baryons and mesons,” *Phys. Rev. Lett.*, vol. 13, p. 598, 20 1964.
84 DOI: 10.1103/PhysRevLett.13.598. <https://link.aps.org/doi/10.1103/PhysRevLett.13.598>.
- 86 [7] S. L. Glashow, “Quarks with color and flavor,” *Scientific American*, vol. 233,
87 p. 38, 1975. <http://www.jstor.org/stable/24949915>.
- 88 [8] Super-Kamiokande Collaboration, “Evidence for oscillation of atmospheric
89 neutrinos,” *Phys. Rev. Lett.*, vol. 81, pp. 1562–1567, 1998. DOI: 10.1103/
90 PhysRevLett.81.1562. arXiv: [hep-ex/9807003](https://arxiv.org/abs/hep-ex/9807003) [hep-ex].
- 91 [9] SNO Collaboration, “Measurement of the rate of $\nu_e + d \rightarrow p + p + e^-$ interac-
92 tions produced by 8B solar neutrinos at the Sudbury Neutrino Observatory,”
93 *Phys. Rev. Lett.*, vol. 87, p. 071301, 2001. DOI: 10.1103/PhysRevLett.87.
94 071301. arXiv: [nucl-ex/0106015](https://arxiv.org/abs/nucl-ex/0106015) [nucl-ex].

- 95 [10] SNO Collaboration, “Direct evidence for neutrino flavor transformation from
96 neutral current interactions in the Sudbury Neutrino Observatory,” *Phys. Rev.*
97 *Lett.*, vol. 89, p. 011301, 2002. DOI: 10.1103/PhysRevLett.89.011301. arXiv:
98 nucl-ex/0204008 [nucl-ex].
- 99 [11] Particle Data Group, C. Patrignani, *et al.*, “Review of particle physics,”
100 *Chin. Phys. C*, vol. 40, no. 10, p. 100001, 2016. DOI: 10.1088/1674-1137/
101 40/10/100001.
- 102 [12] N. Cabibbo, “Unitary symmetry and leptonic decays,” *Phys. Rev. Lett.*, vol.
103 10, p. 531, 1963. DOI: 10.1103/PhysRevLett.10.531.
- 104 [13] M. Kobayashi and T. Maskawa, “CP-violation in the renormalizable theory
105 of weak interaction,” *Progress of Theoretical Physics*, vol. 49, no. 2, p. 652,
106 1973. DOI: 10.1143/PTP.49.652.
- 107 [14] J. H. Christenson, J. W. Cronin, V. L. Fitch, and R. Turlay, “Evidence for
108 the 2π decay of the K_2^0 meson,” *Phys. Rev. Lett.*, vol. 13, p. 138, 4 Jul. 1964.
109 DOI: 10.1103/PhysRevLett.13.138.
- 110 [15] KTeV Collaboration, “Observation of direct CP violation in $K_{S,L} \rightarrow \pi\pi$
111 decays,” *Phys. Rev. Lett.*, vol. 83, p. 22, 1999. DOI: 10.1103/PhysRevLett.
112 83.22. arXiv: hep-ex/9905060 [hep-ex].
- 113 [16] NA48 Collaboration, “A new measurement of direct CP violation in two
114 pion decays of the neutral kaon,” *Phys. Lett. B*, vol. 465, p. 335, 1999. DOI:
115 10.1016/S0370-2693(99)01030-8. arXiv: hep-ex/9909022 [hep-ex].
- 116 [17] BaBar Collaboration, “Measurement of CP violating asymmetries in B^0
117 decays to CP eigenstates,” *Phys. Rev. Lett.*, vol. 86, p. 2515, 2001. DOI: 10.
118 1103/PhysRevLett.86.2515. arXiv: hep-ex/0102030 [hep-ex].
- 119 [18] Belle Collaboration, “Observation of large CP violation in the neutral B
120 meson system,” *Phys. Rev. Lett.*, vol. 87, p. 091802, 2001. DOI: 10.1103/
121 PhysRevLett.87.091802. arXiv: hep-ex/0107061 [hep-ex].
- 122 [19] LHCb Collaboration, “Observation of CP violation in $B^\pm \rightarrow DK^\pm$ de-
123 cays,” *Phys. Lett. B*, vol. 712, p. 203, 2012, [Corrigendum: DOI: 110.1016/j.
124 physletb.2012.05.060]. DOI: 10.1016/j.physletb.2012.04.060. arXiv:
125 1203.3662 [hep-ex].

- 126 [20] LHCb Collaboration, “First observation of CP violation in the decays of B_s^0
127 mesons,” *Phys. Rev. Lett.*, vol. 110, no. 22, p. 221601, 2013. DOI: 10.1103/
128 PhysRevLett.110.221601. arXiv: 1304.6173 [hep-ex].
- 129 [21] E. Noether, “Invariant variation problems,” trans. by M. A. Tavel, *Gott.
130 Nachr.*, p. 235, 1918, [*Transp. Theory Statist. Phys.*, vol. 1, p. 186, 1971]. DOI:
131 10.1080/00411457108231446. arXiv: physics/0503066 [physics].
- 132 [22] M. Srednicki, *Quantum Field Theory*. Cambridge: Cambridge Univ. Press,
133 2007.
- 134 [23] S. L. Glashow, “Partial symmetries of weak interactions,” *Nucl. Phys.*, vol.
135 22, p. 579, 1961. DOI: 10.1016/0029-5582(61)90469-2.
- 136 [24] S. Weinberg, “A model of leptons,” *Phys. Rev. Lett.*, vol. 19, p. 1264, 1967.
137 DOI: 10.1103/PhysRevLett.19.1264.
- 138 [25] A. Salam, “Weak and electromagnetic interactions,” *Conf. Proc.*, vol. C680-
139 519, p. 367, 1968.
- 140 [26] F. Englert and R. Brout, “Broken symmetry and the mass of gauge vec-
141 tor mesons,” *Phys. Rev. Lett.*, vol. 13, p. 321, 9 Aug. 1964. DOI: 10.1103/
142 PhysRevLett.13.321. <https://link.aps.org/doi/10.1103/PhysRevLett.13.321>.
- 144 [27] P. W. Higgs, “Broken symmetries and the masses of gauge bosons,” *Phys.
145 Rev. Lett.*, vol. 13, p. 508, 16 Oct. 1964. DOI: 10.1103/PhysRevLett.13.508.
146 <https://link.aps.org/doi/10.1103/PhysRevLett.13.508>.
- 147 [28] G. S. Guralnik, C. R. Hagen, and T. W. B. Kibble, “Global conservation
148 laws and massless particles,” *Phys. Rev. Lett.*, vol. 13, p. 585, 20 Nov. 1964.
149 DOI: 10.1103/PhysRevLett.13.585. <https://link.aps.org/doi/10.1103/PhysRevLett.13.585>.
- 151 [29] A. Alboteanu, W. Kilian, and J. Reuter, “Resonances and unitarity in weak
152 boson scattering at the LHC,” *JHEP*, vol. 11, p. 010, 2008. DOI: 10.1088/
153 1126-6708/2008/11/010. arXiv: 0806.4145 [hep-ph].
- 154 [30] V. C. Rubin, “Dark matter in spiral galaxies,” *Scientific American*, vol. 248,
155 p. 96, 1983. DOI: 10.1038/scientificamerican0683-96.
- 156 [31] K. Garrett and G. Duda, “Dark matter: a primer,” *Adv. Astron.*, vol. 2011,
157 p. 968283, 2011. DOI: 10.1155/2011/968283. arXiv: 1006.2483 [hep-ph].

- 158 [32] J. Ellis, “Searching for particle physics beyond the standard model at the
159 LHC and elsewhere,” *AIP Conf. Proc.*, vol. 1446, p. 9, 2012. DOI: 10.1063/
160 1.4727987. arXiv: 1102.5009 [hep-ph].
- 161 [33] H. Georgi, H. R. Quinn, and S. Weinberg, “Hierarchy of interactions in
162 unified gauge theories,” *Phys. Rev. Lett.*, vol. 33, p. 451, 1974. DOI: 10.1103/
163 PhysRevLett.33.451.
- 164 [34] E. Gildener, “Gauge symmetry hierarchies,” *Phys. Rev. D*, vol. 14, p. 1667,
165 1976. DOI: 10.1103/PhysRevD.14.1667.
- 166 [35] A. J. Buras, J. R. Ellis, M. K. Gaillard, and D. V. Nanopoulos, “Aspects of
167 the grand unification of strong, weak and electromagnetic interactions,” *Nucl.
168 Phys. B*, vol. 135, p. 66, 1978. DOI: 10.1016/0550-3213(78)90214-6.
- 169 [36] S. Mele, “The measurement of the number of light neutrino species at LEP,”
170 *Adv. Ser. Direct. High Energy Phys.*, vol. 23, p. 89, 2015. DOI: 10.1142/
171 9789814644150_0004. <http://cds.cern.ch/record/2103251>.
- 172 [37] S. P. Martin, “A supersymmetry primer,” in *Perspectives on Supersymmetry
173 II*. DOI: 10.1142/9789814307505_0001. arXiv: hep-ph/9709356 [hep-ph].
- 174 [38] C. Autermann, “Experimental status of supersymmetry after the LHC run-
175 I,” *Prog. Part. Nucl. Phys.*, vol. 90, p. 125, 2016. DOI: 10.1016/j.ppnp.2016.
176 06.001. arXiv: 1609.01686 [hep-ex].
- 177 [39] H. Georgi and S. L. Glashow, “Unity of all elementary particle forces,” *Phys.
178 Rev. Lett.*, vol. 32, p. 438, 1974. DOI: 10.1103/PhysRevLett.32.438.
- 179 [40] K. Hagiwara, R. D. Peccei, D. Zeppenfeld, and K. Hikasa, “Probing the weak
180 boson sector in $e^+e^- \rightarrow W^+W^-$,” *Nucl. Phys. B*, vol. 282, p. 253, 1987. DOI:
181 10.1016/0550-3213(87)90685-7.
- 182 [41] G. J. Gounaris, J. Layssac, and F. M. Renard, “New and standard physics
183 contributions to anomalous Z and γ self-couplings,” *Phys. Rev. D*, vol. 62,
184 p. 073013, 2000. DOI: 10.1103/PhysRevD.62.073013. arXiv: hep-ph/
185 0003143 [hep-ph].
- 186 [42] U. Baur and D. L. Rainwater, “Probing neutral gauge boson self-interactions
187 in ZZ production at hadron colliders,” *Phys. Rev. D*, vol. 62, p. 113011, 2000.
188 DOI: 10.1103/PhysRevD.62.113011. arXiv: hep-ph/0008063 [hep-ph].

- 189 [43] U. Baur and E. L. Berger, “Probing the weak boson sector in $Z\gamma$ production
 190 at hadron colliders,” *Phys. Rev. D*, vol. 47, p. 4889, 1993. DOI: 10.1103/
 191 PhysRevD.47.4889.
- 192 [44] C. Degrande, N. Greiner, W. Kilian, O. Mattelaer, H. Mebane, T. Stelzer,
 193 S. Willenbrock, and C. Zhang, “Effective field theory: a modern approach to
 194 anomalous couplings,” *Annals Phys.*, vol. 335, p. 21, 2013. DOI: 10.1016/j.
 195 aop.2013.04.016. arXiv: 1205.4231 [hep-ph].
- 196 [45] O. J. P. Éboli, M. C. Gonzalez-Garcia, and J. K. Mizukoshi, “ $pp \rightarrow jj e^\pm \mu^\pm \nu\nu$
 197 and $jj e^\pm \mu^\mp \nu\nu$ at $\mathcal{O}(\alpha_{em}^6)$ and $\mathcal{O}(\alpha_{em}^4 \alpha_s^2)$ for the study of the quartic electroweak
 198 gauge boson vertex at LHC,” *Phys. Rev. D*, vol. 74, p. 073005, 2006. DOI:
 199 10.1103/PhysRevD.74.073005. arXiv: hep-ph/0606118 [hep-ph].
- 200 [46] NNPDF Collaboration, “Parton distributions from high-precision collider
 201 data,” 2017. arXiv: 1706.00428 [hep-ph].
- 202 [47] A. Lazopoulos, K. Melnikov, and F. Petriello, “QCD corrections to tri-boson
 203 production,” *Phys. Rev. D*, vol. 76, p. 014001, 2007. DOI: 10.1103/PhysRevD.
 204 76.014001. arXiv: hep-ph/0703273 [hep-ph].
- 205 [48] T. Binoth, G. Ossola, C. G. Papadopoulos, and R. Pittau, “NLO QCD
 206 corrections to tri-boson production,” *JHEP*, vol. 06, p. 082, 2008. DOI: 10.
 207 1088/1126-6708/2008/06/082. arXiv: 0804.0350 [hep-ph].
- 208 [49] V. Hankele and D. Zeppenfeld, “QCD corrections to hadronic wwz production
 209 with leptonic decays,” *Phys. Lett. B*, vol. 661, p. 103, 2008. DOI: 10.1016/j.
 210 physletb.2008.02.014. arXiv: 0712.3544 [hep-ph].
- 211 [50] F. J. Hasert *et al.*, “Search for elastic ν_μ electron scattering,” *Phys. Lett. B*,
 212 vol. 46, p. 121, 1973. DOI: 10.1016/0370-2693(73)90494-2.
- 213 [51] UA1 Collaboration, “Experimental observation of lepton pairs of invariant
 214 mass around $95 \text{ GeV}/c^2$ at the CERN SPS collider,” *Phys. Lett. B*, vol. 126,
 215 p. 398, 1983. DOI: 10.1016/0370-2693(83)90188-0.
- 216 [52] SLD Electroweak Group, DELPHI Collaboration, ALEPH Collaboration,
 217 SLD Collaboration, SLD Heavy Flavour Group, OPAL Collaboration, LEP
 218 Electroweak Working Group, L3 Collaboration, “Precision electroweak mea-
 219 surements on the Z resonance,” *Phys. Rept.*, vol. 427, p. 257, 2006. DOI: 10.
 220 1016/j.physrep.2005.12.006. arXiv: hep-ex/0509008 [hep-ex].

- 221 [53] J. M. Campbell and R. K. Ellis, “An update on vector boson pair production
222 at hadron colliders,” *Phys. Rev. D*, vol. 60, p. 113 006, 1999. DOI: 10.1103/
223 PhysRevD.60.113006. arXiv: hep-ph/9905386 [hep-ph].
- 224 [54] J. M. Campbell, R. K. Ellis, and C. Williams, “Vector boson pair production
225 at the LHC,” *JHEP*, vol. 07, p. 018, 2011. DOI: 10.1007/JHEP07(2011)018.
226 arXiv: 1105.0020 [hep-ph].
- 227 [55] T. Melia, P. Nason, R. Röntsch, and G. Zanderighi, “ W^+W^- , WZ and ZZ
228 production in the POWHEG BOX,” *JHEP*, vol. 11, p. 078, 2011. DOI: 10.1007/
229 JHEP11(2011)078. arXiv: 1107.5051 [hep-ph].
- 230 [56] F. Cascioli, T. Gehrmann, M. Grazzini, S. Kallweit, P. Maierhöfer, A. von
231 Manteuffel, S. Pozzorini, D. Rathlev, L. Tancredi, and E. Weihs, “ ZZ produc-
232 tion at hadron colliders in NNLO QCD,” *Phys. Lett. B*, vol. 735, p. 311, 2014.
233 DOI: 10.1016/j.physletb.2014.06.056. arXiv: 1405.2219 [hep-ph].
- 234 [57] F. Caola, K. Melnikov, R. Röntsch, and L. Tancredi, “QCD corrections to
235 ZZ production in gluon fusion at the LHC,” *Phys. Rev. D*, vol. 92, p. 094 028,
236 2015. DOI: 10.1103/PhysRevD.92.094028. arXiv: 1509.06734 [hep-ph].
- 237 [58] D. Rainwater, R. Szalapski, and D. Zeppenfeld, “Probing color-singlet ex-
238 change in $Z + 2$ -jet events at the CERN LHC,” *Phys. Rev. D*, vol. 54, p. 6680,
239 11 Dec. 1996. DOI: 10.1103/PhysRevD.54.6680.
- 240 [59] Sjöstrand, Torbjörn and Ask, Stefan and Christiansen, Jesper R. and Corke,
241 Richard and Desai, Nishita and Ilten, Philip and Mrenna, Stephen and Prestel,
242 Stefan and Rasmussen, Christine O. and Skands, Peter Z., “An introduction
243 to PYTHIA 8.2,” *Comput. Phys. Commun.*, vol. 191, p. 159, 2015. DOI: 10.
244 1016/j.cpc.2015.01.024. arXiv: 1410.3012 [hep-ph].
- 245 [60] C. Bierlich and J. R. Christiansen, “Effects of color reconnection on hadron
246 flavor observables,” *Phys. Rev. D*, vol. 92, p. 094 010, 2015. DOI: 10.1103/
247 PhysRevD.92.094010. arXiv: 1507.02091 [hep-ph].
- 248 [61] ALEPH Collaboration, “Measurement of the $e^+e^- \rightarrow ZZ$ production cross-
249 section at center-of-mass energies of 183 GeV and 189 GeV,” *Phys. Lett. B*,
250 vol. 469, p. 287, 1999. DOI: 10.1016/S0370-2693(99)01288-5. arXiv: hep-
251 ex/9911003 [hep-ex].
- 252 [62] OPAL Collaboration, “ Z boson pair production in e^+e^- collisions at $\sqrt{s} =$
253 183 GeV and 189 GeV,” *Phys. Lett. B*, vol. 476, p. 256, 2000. DOI: 10.1016/
254 S0370-2693(00)00197-0. arXiv: hep-ex/0003016 [hep-ex].

- 255 [63] L3 Collaboration, “Z boson pair production at LEP,” *Phys. Lett. B*, vol.
256 572, p. 133, 2003. DOI: [10.1016/j.physletb.2003.08.023](https://doi.org/10.1016/j.physletb.2003.08.023). arXiv: [hep-ex/0308013](https://arxiv.org/abs/hep-ex/0308013) [hep-ex].
- 258 [64] DELPHI Collaboration, “ZZ production in e^+e^- interactions at $\sqrt{s} = 183 - 209$ GeV,” *Eur. Phys. J. C*, vol. 30, p. 447, 2003. DOI: [10.1140/epjc/s2003-01287-0](https://doi.org/10.1140/epjc/s2003-01287-0). arXiv: [hep-ex/0307050](https://arxiv.org/abs/hep-ex/0307050) [hep-ex].
- 261 [65] OPAL Collaboration, “Study of Z pair production and anomalous couplings
262 in e^+e^- collisions at \sqrt{s} between 190 GeV and 209 GeV,” *Eur. Phys. J. c*, vol.
263 32, p. 303, 2003. DOI: [10.1140/epjc/s2003-01467-x](https://doi.org/10.1140/epjc/s2003-01467-x). arXiv: [hep-ex/0310013](https://arxiv.org/abs/hep-ex/0310013)
264 [hep-ex].
- 265 [66] ALEPH Collaboration, “Measurement of Z-pair production in e^+e^- collisions
266 and constraints on anomalous neutral gauge couplings,” *JHEP*, vol. 04, p. 124,
267 2009. DOI: [10.1088/1126-6708/2009/04/124](https://doi.org/10.1088/1126-6708/2009/04/124).
- 268 [67] CDF Collaboration, “First measurement of ZZ production in $\bar{p}p$ collisions at
269 $\sqrt{s} = 1.96$ TeV,” *Phys. Rev. Lett.*, vol. 100, p. 201801, 2008. DOI: [10.1103/PhysRevLett.100.201801](https://doi.org/10.1103/PhysRevLett.100.201801). arXiv: [0801.4806](https://arxiv.org/abs/0801.4806) [hep-ex].
- 271 [68] D0 Collaboration, “ $ZZ \rightarrow \ell^+\ell^-\nu\bar{\nu}$ production in $p\bar{p}$ collisions at $\sqrt{s} =$
272 1.96 TeV,” *Phys. Rev. D*, vol. 78, p. 072002, 2008. DOI: [10.1103/PhysRevD.78.072002](https://doi.org/10.1103/PhysRevD.78.072002). arXiv: [0808.0269](https://arxiv.org/abs/0808.0269) [hep-ex].
- 274 [69] D0 Collaboration, “Observation of ZZ production in $p\bar{p}$ collisions at $\sqrt{s} =$
275 1.96 TeV,” *Phys. Rev. Lett.*, vol. 101, p. 171803, 2008, DOI: [10.1103/PhysRevLett.101.171803](https://doi.org/10.1103/PhysRevLett.101.171803). arXiv: [0808.0703](https://arxiv.org/abs/0808.0703) [hep-ex].
- 277 [70] D0 Collaboration, “Measurement of the ZZ production cross section in $p\bar{p}$
278 collisions at $\sqrt{s} = 1.96$ TeV,” *Phys. Rev. D*, vol. 84, p. 011103, 2011. DOI:
279 [10.1103/PhysRevD.84.011103](https://doi.org/10.1103/PhysRevD.84.011103). arXiv: [1104.3078](https://arxiv.org/abs/1104.3078) [hep-ex].
- 280 [71] CDF Collaboration, “Measurement of ZZ production in leptonic final states
281 at \sqrt{s} of 1.96 TeV at CDF,” *Phys. Rev. Lett.*, vol. 108, p. 101801, 2012. DOI:
282 [10.1103/PhysRevLett.108.101801](https://doi.org/10.1103/PhysRevLett.108.101801). arXiv: [1112.2978](https://arxiv.org/abs/1112.2978) [hep-ex].
- 283 [72] CMS Collaboration, “Measurement of the ZZ production cross section and
284 search for anomalous couplings in $2\ell 2\ell'$ final states in pp collisions at $\sqrt{s} =$
285 7 TeV,” *JHEP*, vol. 01, p. 063, 2013. DOI: [10.1007/JHEP01\(2013\)063](https://doi.org/10.1007/JHEP01(2013)063). arXiv:
286 [1211.4890](https://arxiv.org/abs/1211.4890) [hep-ex].

- 287 [73] CMS Collaboration, “Measurement of the $\text{pp} \rightarrow \text{ZZ}$ production cross section
288 and constraints on anomalous triple gauge couplings in four-lepton final states
289 at $\sqrt{s} = 8 \text{ TeV}$,” *Phys. Lett. B*, vol. 740, p. 250, 2015, [Corrigendum: DOI: 10.
290 1016/j.physletb.2016.04.010]. DOI: 10.1016/j.physletb.2014.11.059.
291 arXiv: 1406.0113 [hep-ex].
- 292 [74] CMS Collaboration, “Measurements of the ZZ production cross sections in the
293 $2\ell 2\nu$ channel in proton–proton collisions at $\sqrt{s} = 7$ and 8 TeV and combined
294 constraints on triple gauge couplings,” *Eur. Phys. J. C*, vol. 75, no. 10, p. 511,
295 2015. DOI: 10.1140/epjc/s10052-015-3706-0. arXiv: 1503.05467 [hep-ex].
- 296 [75] CMS Collaboration, “Measurement of the differential cross sections for pairs
297 of Z bosons produced in association with jets in pp collisions at $\sqrt{s} = 8 \text{ TeV}$,”
298 CERN, Geneva, Tech. Rep. CMS-PAS-SMP-15-012, 2016. <https://cds.cern.ch/record/2209215>.
- 300 [76] ATLAS Collaboration, “Measurement of ZZ production in pp collisions at
301 $\sqrt{s} = 7 \text{ TeV}$ and limits on anomalous zzz and ZZ γ couplings with the ATLAS
302 detector,” *JHEP*, vol. 03, p. 128, 2013. DOI: 10.1007/JHEP03(2013)128.
303 arXiv: 1211.6096 [hep-ex].
- 304 [77] ATLAS Collaboration, “Measurements of four-lepton production in pp collisions
305 at $\sqrt{s} = 8 \text{ TeV}$ with the ATLAS detector,” *Phys. Lett. B*, vol. 753, p. 552,
306 2016. DOI: 10.1016/j.physletb.2015.12.048. arXiv: 1509.07844 [hep-ex].
- 307 [78] ATLAS Collaboration, “Measurement of the ZZ production cross section
308 in proton-proton collisions at $\sqrt{s} = 8 \text{ TeV}$ using the $\text{ZZ} \rightarrow \ell^-\ell^+\ell^-\ell^+$ and
309 $\text{ZZ} \rightarrow \ell^-\ell^+\nu\bar{\nu}$ channels with the ATLAS detector,” *JHEP*, vol. 01, p. 099,
310 2017. DOI: 10.1007/JHEP01(2017)099. arXiv: 1610.07585 [hep-ex].
- 311 [79] CMS Collaboration, “Measurement of wz and zz production in pp collisions
312 at $\sqrt{s} = 8 \text{ TeV}$ in final states with b-tagged jets,” *Eur. Phys. J. C*, vol. 74,
313 p. 2973, 2014. DOI: 10.1140/epjc/s10052-014-2973-5. arXiv: 1403.3047
314 [hep-ex].
- 315 [80] CMS Collaboration, “Measurement of the $\text{pp} \rightarrow \text{ZZ}$ production cross section,
316 $\text{Z} \rightarrow 4\ell$ branching fraction and constraints on anomalous triple gauge couplings
317 at $\sqrt{s} = 13 \text{ TeV}$,” 2017. <https://cds.cern.ch/record/2256100>.
- 318 [81] ATLAS Collaboration, “Evidence for electroweak production of $\text{W}^\pm\text{W}^\pm\text{jj}$ in
319 pp collisions at $\sqrt{s} = 8 \text{ TeV}$ with the ATLAS detector,” *Phys. Rev. Lett.*, vol.
320 113, no. 14, p. 141803, 2014. DOI: 10.1103/PhysRevLett.113.141803. arXiv:
321 1405.6241 [hep-ex].

- 322 [82] CMS Collaboration, “Study of vector boson scattering and search for new
323 physics in events with two same-sign leptons and two jets,” *Phys. Rev. Lett.*,
324 vol. 114, no. 5, p. 051801, 2015. DOI: 10.1103/PhysRevLett.114.051801.
325 arXiv: 1410.6315 [hep-ex].
- 326 [83] CMS Collaboration, “Measurement of the cross section for electroweak pro-
327 duction of $Z\gamma$ in association with two jets and constraints on anomalous qua-
328 ratic gauge couplings in proton–proton collisions at $\sqrt{s} = 8$ TeV,” *Phys. Lett.*
329 *B*, vol. 770, p. 380, 2017. DOI: 10.1016/j.physletb.2017.04.071. arXiv:
330 1702.03025 [hep-ex].
- 331 [84] ATLAS Collaboration, “Studies of $Z\gamma$ production in association with a high-
332 mass dijet system in pp collisions at $\sqrt{s} = 8$ TeV with the ATLAS detector,”
333 *JHEP*, vol. 07, p. 107, 2017. DOI: 10.1007/JHEP07(2017)107. arXiv: 1705.
334 01966 [hep-ex].
- 335 [85] CMS Collaboration, “Measurement of electroweak-induced production of
336 $W\gamma$ with two jets in pp collisions at $\sqrt{s} = 8$ TeV and constraints on anom-
337 alous quartic gauge couplings,” *JHEP*, vol. 06, p. 106, 2017. DOI: 10.1007/
338 JHEP06(2017)106. arXiv: 1612.09256 [hep-ex].
- 339 [86] CMS Collaboration, “Evidence for exclusive $\gamma\gamma \rightarrow W^+W^-$ production and
340 constraints on anomalous quartic gauge couplings in pp collisions at $\sqrt{s} = 7$
341 and 8 TeV,” *JHEP*, vol. 08, p. 119, 2016. DOI: 10.1007/JHEP08(2016)119.
342 arXiv: 1604.04464 [hep-ex].
- 343 [87] ATLAS Collaboration, “Measurement of exclusive $\gamma\gamma \rightarrow W^+W^-$ production
344 and search for exclusive Higgs boson production in pp collisions at $\sqrt{s} = 8$ TeV
345 using the ATLAS detector,” *Phys. Rev. D*, vol. 94, no. 3, p. 032011, 2016. DOI:
346 10.1103/PhysRevD.94.032011. arXiv: 1607.03745 [hep-ex].
- 347 [88] CMS Collaboration Collaboration, “Observation of electroweak production
348 of same-sign W boson pairs in the two jet and two same-sign lepton final state
349 in proton-proton collisions at 13 TeV,” CERN, Geneva, Tech. Rep. CMS-PAS-
350 SMP-17-004, 2017. <https://cds.cern.ch/record/2264525>.
- 351 [89] ALEPH Collaboration, “Study of the four fermion final state at the Z reso-
352 nance,” *Z. Phys. C*, vol. 66, p. 3, 1995. DOI: 10.1007/BF01496576.
- 353 [90] CMS Collaboration, “Observation of Z decays to four leptons with the
354 CMS detector at the LHC,” *JHEP*, vol. 12, p. 034, 2012. DOI: 10.1007/
355 JHEP12(2012)034. arXiv: 1210.3844 [hep-ex].

- 356 [91] ATLAS Collaboration, “Measurements of four-lepton production at the Z
357 resonance in pp collisions at $\sqrt{s} = 7$ and 8 TeV with ATLAS,” *Phys. Rev. Lett.*,
358 vol. 112, no. 23, p. 231806, 2014. DOI: 10.1103/PhysRevLett.112.231806.
359 arXiv: 1403.5657 [hep-ex].
- 360 [92] LHC Higgs Cross Section Working Group Collaboration, “Handbook of LHC
361 Higgs cross sections: 4. deciphering the nature of the Higgs sector,” 2016. DOI:
362 10.23731/CYRM-2017-002. arXiv: 1610.07922 [hep-ph].
- 363 [93] OPAL Collaboration, DELPHI Collaboration, LEP Working Group for Higgs
364 boson searches, ALEPH Collaboration, L3 Collaboration, “Search for the stan-
365 dard model Higgs boson at LEP,” *Phys. Lett. B*, vol. 565, p. 61, 2003. DOI:
366 10.1016/S0370-2693(03)00614-2. arXiv: hep-ex/0306033 [hep-ex].
- 367 [94] DELPHI Collaboration, OPAL Collaboration, ALEPH Collaboration, LEP
368 Electroweak Working Group, L3 Collaboration, “A combination of prelimi-
369 nary electroweak measurements and constraints on the standard model,” 2006.
370 arXiv: hep-ex/0612034 [hep-ex].
- 371 [95] CDF Collaboration, D0 Collaboration, “Higgs boson studies at the Teva-
372 tron,” *Phys. Rev. D*, vol. 88, no. 5, p. 052014, 2013. DOI: 10.1103/PhysRevD.
373 88.052014. arXiv: 1303.6346 [hep-ex].
- 374 [96] CDF Collaboration, D0 Collaboration, “Evidence for a particle produced in
375 association with weak bosons and decaying to a bottom-antibottom quark pair
376 in Higgs boson searches at the Tevatron,” *Phys. Rev. Lett.*, vol. 109, p. 071804,
377 2012. DOI: 10.1103/PhysRevLett.109.071804. arXiv: 1207.6436 [hep-ex].
- 378 [97] Tevatron Electroweak Working Group, CDF Collaboration, DELPHI Collab-
379 oration, SLD Electroweak and Heavy Flavour Groups, ALEPH Collaboration,
380 LEP Electroweak Working Group, SLD Collaboration, OPAL Collaboration,
381 D0 Collaboration, L3 Collaboration, “Precision electroweak measurements and
382 constraints on the standard model,” 2010. arXiv: 1012.2367 [hep-ex].
- 383 [98] CMS Collaboration, “Observation of a new boson at a mass of 125 GeV with
384 the CMS experiment at the LHC,” *Phys. Lett. B*, vol. 716, p. 30, 2012. DOI:
385 10.1016/j.physletb.2012.08.021. arXiv: 1207.7235 [hep-ex].
- 386 [99] ATLAS Collaboration, “Observation of a new particle in the search for the
387 standard model Higgs boson with the ATLAS detector at the LHC,” *Phys.*
388 *Lett. B*, vol. 716, p. 1, 2012. DOI: 10.1016/j.physletb.2012.08.020. arXiv:
389 1207.7214 [hep-ex].

- 390 [100] CMS Collaboration, “Search for the standard model Higgs boson in the decay
391 channel $H \rightarrow ZZ \rightarrow 4$ leptons in pp collisions at $\sqrt{s} = 7$ TeV,” *Phys. Rev. Lett.*,
392 vol. 108, p. 111804, 2012. DOI: 10.1103/PhysRevLett.108.111804. arXiv:
393 1202.1997 [hep-ex].
- 394 [101] ATLAS Collaboration, CMS Collaboration, “Combined measurement of the
395 Higgs boson mass in pp collisions at $\sqrt{s} = 7$ and 8 TeV with the ATLAS and
396 CMS experiments,” *Phys. Rev. Lett.*, vol. 114, p. 191803, 2015. DOI: 10.1103/
397 PhysRevLett.114.191803. arXiv: 1503.07589 [hep-ex].
- 398 [102] ATLAS Collaboration, CMS Collaboration, “Measurements of the Higgs
399 boson production and decay rates and constraints on its couplings from a
400 combined ATLAS and CMS analysis of the LHC pp collision data at $\sqrt{s} = 7$
401 and 8 TeV,” *JHEP*, vol. 08, p. 045, 2016. DOI: 10.1007/JHEP08(2016)045.
402 arXiv: 1606.02266 [hep-ex].
- 403 [103] I. Ots, H. Uibo, H. Liivat, R. Saar, and R. K. Loide, “Possible anomalous $ZZ\gamma$
404 and $Z\gamma\gamma$ couplings and Z boson spin orientation in $e^+e^- \rightarrow Z\gamma$,” *Nucl. Phys.*,
405 vol. B702, pp. 346–356, 2004. DOI: 10.1016/j.nuclphysb.2004.09.019.
- 406 [104] DELPHI Collaboration, “Study of triple-gauge-boson couplings zzz , $ZZ\gamma$ and
407 $Z\gamma\gamma$ at LEP,” *Eur. Phys. J. C*, vol. 51, p. 525, 2007. DOI: 10.1140/epjc/s10052-007-0345-0. arXiv: 0706.2741 [hep-ex].
- 409 [105] CDF Collaboration, D0 Collaboration, “Diboson physics at the Tevatron,”
410 *EPJ Web Conf.*, vol. 28, p. 06001, 2012. DOI: 10.1051/epjconf/20122806001.
411 arXiv: 1201.4771 [hep-ex].
- 412 [106] D0 Collaboration, “Search for ZZ and $Z\gamma^*$ production in $p\bar{p}$ collisions at
413 $\sqrt{s} = 1.96$ TeV and limits on anomalous ZZZ and $ZZ\gamma^*$ couplings,” *Phys. Rev.*
414 *Lett.*, vol. 100, p. 131801, 2008. DOI: 10.1103/PhysRevLett.100.131801.
415 arXiv: 0712.0599 [hep-ex].
- 416 [107] ATLAS Collaboration, “Measurement of the ZZ production cross section
417 and limits on anomalous neutral triple gauge couplings in proton-proton col-
418 lisions at $\sqrt{s} = 7$ TeV with the ATLAS detector,” *Phys. Rev. Lett.*, vol. 108,
419 p. 041804, 2012. DOI: 10.1103/PhysRevLett.108.041804. arXiv: 1110.5016
420 [hep-ex].
- 421 [108] ATLAS Collaboration, “Measurement of the ZZ production cross section in
422 pp collisions at $\sqrt{s} = 13$ TeV with the ATLAS detector,” *Phys. Rev. Lett.*, vol.
423 116, no. 10, p. 101801, 2016. DOI: 10.1103/PhysRevLett.116.101801. arXiv:
424 1512.05314 [hep-ex].

- 425 [109] L. Evans and P. Bryant, “LHC machine,” *JINST*, vol. 3, S08001, 2008. DOI:
426 10.1088/1748-0221/3/08/S08001.
- 427 [110] O. Brüning, H. Burkhardt, and S. Myers, “The Large Hadron Collider,” *Prog.
428 Part. Nucl. Phys.*, vol. 67, no. 3, p. 7054, 2012, ISSN: 0146-6410. DOI: <https://doi.org/10.1016/j.ppnp.2012.03.001>. <http://www.sciencedirect.com/science/article/pii/S0146641012000695>.
- 431 [111] CMS Collaboration, “The CMS experiment at the CERN LHC,” *JINST*, vol.
432 3, S08004, 2008. DOI: 10.1088/1748-0221/3/08/S08004.
- 433 [112] C. Lefèvre, “The CERN accelerator complex. complexe des accélérateurs du
434 CERN,” Dec. 2008, <https://cds.cern.ch/record/1260465>.
- 435 [113] ATLAS Collaboration, “The ATLAS experiment at the CERN Large Hadron
436 Collider,” *JINST*, vol. 3, S08003, 2008. DOI: 10.1088/1748-0221/3/08/
437 S08003.
- 438 [114] LHCb Collaboration, “The LHCb detector at the LHC,” *JINST*, vol. 3,
439 S08005, 2008. DOI: 10.1088/1748-0221/3/08/S08005.
- 440 [115] ALICE Collaboration, “The ALICE experiment at the CERN LHC,” *JINST*,
441 vol. 3, S08002, 2008. DOI: 10.1088/1748-0221/3/08/S08002.
- 442 [116] TOTEM Collaboration, “The TOTEM experiment at the CERN Large
443 Hadron Collider,” *JINST*, vol. 3, S08007, 2008. DOI: 10.1088/1748-0221/3/
444 08/S08007.
- 445 [117] LHCf Collaboration, “The LHCf detector at the CERN Large Hadron Col-
446 linder,” *JINST*, vol. 3, S08006, 2008. DOI: 10.1088/1748-0221/3/08/S08006.
- 447 [118] MoEDAL Collaboration, “The physics programme of the MoEDAL exper-
448 iment at the LHC,” *Int. J. Mod. Phys.*, vol. A29, p. 1430050, 2014. DOI:
449 10.1142/S0217751X14300506. arXiv: 1405.7662 [hep-ph].
- 450 [119] M. Bajko *et al.*, “Report of the task force on the incident of 19th September
451 2008 at the LHC,” CERN, Geneva, Tech. Rep. LHC-PROJECT-Report-1168.
452 CERN-LHC-PROJECT-Report-1168, Mar. 2009. <http://cds.cern.ch/record/1168025>.
- 454 [120] M. Lamont, “Status of the LHC,” *Journal of Physics: Conference Series*,
455 vol. 455, no. 1, p. 012001, 2013. <http://stacks.iop.org/1742-6596/455/i=1/a=012001>.

- 457 [121] Y. Papaphilippou, H. Bartosik, G. Rumolo, and D. Manglunki, “Operational
458 beams for the LHC,” 2014. arXiv: 1412.7857 [physics.acc-ph].
- 459 [122] F. Bordry and C. Pralavorio, “LHC smashes targets for 2016 run,” Nov.
460 2016. <http://cds.cern.ch/record/2235979>.
- 461 [123] T. Sakuma and T. McCauley, “Detector and event visualization with Sketch-
462 Up at the CMS experiment,” CERN, Geneva, Tech. Rep. CMS-CR-2013-379,
463 Oct. 2013. arXiv: 1311.4942. <https://cds.cern.ch/record/1626816>.
- 464 [124] CMS Collaboration, “The magnet project: technical design report,” 1997.
465 <https://cds.cern.ch/record/331056>.
- 466 [125] CMS Collaboration, “The CMS tracker system project: technical design
467 report,” 1997. <http://cds.cern.ch/record/368412>.
- 468 [126] B. Isildak, “Measurement of the differential dijet production cross section
469 in proton-proton collisions at $\sqrt{s} = 7 \text{ TeV}$,” PhD thesis, Bogazici U., 2011.
470 arXiv: 1308.6064 [hep-ex]. <https://inspirehep.net/record/1251416/files/arXiv:1308.6064.pdf>.
- 472 [127] “The CMS muon project: technical design report,” 1997. <http://cds.cern.ch/record/343814>.
- 474 [128] CMS Collaboration, “The CMS muon system in Run2: preparation, status
475 and first results,” *PoS*, vol. EPS-HEP2015, p. 237, 2015. arXiv: 1510.05424
476 [physics.ins-det].
- 477 [129] CMS Collaboration, “CMS technical design report for the level-1 trigger up-
478 grade,” Tech. Rep. CERN-LHCC-2013-011. CMS-TDR-12, Jun. 2013. <https://cds.cern.ch/record/1556311>.
- 480 [130] P. R. K. Chumney, S. Dasu, J. Lackey, M. Jaworski, P. Robl, and W. H.
481 Smith, “Level-1 regional calorimeter trigger system for CMS,” *EConf*, vol.
482 C0303241, THHT003, 2003. arXiv: [hep-ex/0305047](https://arxiv.org/abs/hep-ex/0305047) [hep-ex].
- 483 [131] B. Kreis and others, “Run 2 upgrades to the CMS level-1 calorimeter trigger,”
484 *JINST*, vol. 11, no. 01, p. C01051, 2016. DOI: [10.1088/1748-0221/11/01/C01051](https://doi.org/10.1088/1748-0221/11/01/C01051). arXiv: 1511.05855 [physics.ins-det].
- 486 [132] A. Svetek, M. Blake, M. Cepeda Hermida, S. Dasu, L. Dodd, R. Fobes, B.
487 Gomber, T. Gorski, Z. Guo, P. Klabbers, A. Levine, I. Ojalvo, T. Ruggles, N.
488 Smith, W. Smith, J. Tikalsky, M. Vicente, and N. Woods, “The calorimeter

- 489 trigger processor card: the next generation of high speed algorithmic data
490 processing at CMS,” *JINST*, vol. 11, p. C02011, 2016. DOI: 10.1088/1748-
491 0221/11/02/C02011.
- 492 [133] J. Ero *et al.*, “The CMS drift tube trigger track finder,” *JINST*, vol. 3,
493 P08006, 2008. DOI: 10.1088/1748-0221/3/08/P08006.
- 494 [134] D. Acosta, A. Atamanchuk, V. Golovtsov, A. Madorsky, B. Razmyslovich,
495 B. Scurlock, and S. Wang, “The track-finding processor for the level-1 trigger
496 of the CMS endcap muon system,” 1999.
- 497 [135] J. Ero *et al.*, “The CMS level-1 trigger barrel track finder,” *JINST*, vol. 11,
498 no. 03, p. C03038, 2016. DOI: 10.1088/1748-0221/11/03/C03038.
- 499 [136] W. M. Zabolotny and A. Byszuk, “Algorithm and implementation of muon
500 trigger and data transmission system for barrel-endcap overlap region of the
501 CMS detector,” *JINST*, vol. 11, no. 03, p. C03004, 2016. DOI: 10.1088/1748-
502 0221/11/03/C03004.
- 503 [137] H. Sakulin and A. Taurok, “The level-1 global muon trigger for the CMS ex-
504 periment,” CERN, Geneva, Tech. Rep. CMS-CR-2003-040, Oct. 2003. <https://cds.cern.ch/record/687846>.
- 506 [138] M. Jeitler, J. Lingemann, D. Rabady, H. Sakulin, and A. Stahl, “Upgrade
507 of the CMS global muon trigger,” *IEEE Trans. Nucl. Sci.*, vol. 62, no. 3,
508 pp. 1104–1109, 2015. DOI: 10.1109/TNS.2015.2435060.
- 509 [139] M. Jeitler *et al.*, “The level-1 global trigger for the CMS experiment at LHC,”
510 *JINST*, vol. 2, P01006, 2007. DOI: 10.1088/1748-0221/2/01/P01006.
- 511 [140] J. Wittmann, B. Arnold, H. Bergauer, M. Jeitler, T. Matsushita, D. Rabady,
512 B. Rahbaran, and C.-E. Wulz, “The upgrade of the CMS global trigger,”
513 *JINST*, vol. 11, no. 02, p. C02029, 2016. <http://stacks.iop.org/1748-0221/11/i=02/a=C02029>.
- 515 [141] CMS Collaboration, “The CMS high level trigger,” *Eur. Phys. J. C*, vol. 46,
516 p. 605, 2006. DOI: 10.1140/epjc/s2006-02495-8. arXiv: [hep-ex/0512077](https://arxiv.org/abs/hep-ex/0512077)
517 [hep-ex].
- 518 [142] S. Van der Meer, “Calibration of the effective beam height in the ISR,” 1968.

- 519 [143] CMS Collaboration, “Beams scan based absolute normalization of the CMS
520 luminosity measurement. CMS 2010 luminosity determination,” 2011. <https://cds.cern.ch/record/1357856>.
- 522 [144] CMS Collaboration, “CMS luminosity measurement for the 2015 data-taking
523 period,” CERN, Geneva, Tech. Rep. CMS-PAS-LUM-15-001, 2017. <http://cds.cern.ch/record/2138682>.
- 525 [145] CMS Collaboration Collaboration, “CMS luminosity measurements for the
526 2016 data taking period,” CERN, Geneva, Tech. Rep. CMS-PAS-LUM-17-001,
527 2017. <http://cds.cern.ch/record/2257069>.
- 528 [146] N. Metropolis and S. Ulam, “The Monte Carlo method,” *Journal of the
529 American Statistical Association*, vol. 44, p. 335, 1949. DOI: 10.2307/2280232.
530 <http://www.jstor.org/stable/2280232>.
- 531 [147] M. Matsumoto and T. Nishimura, “Mersenne Twister: A 623-dimensional-
532 ly equidistributed uniform pseudo-random number generator,” *ACM Trans.
533 Model. Comput. Simul.*, vol. 8, p. 3, 1998. DOI: 10.1145/272991.272995.
534 <http://doi.acm.org/10.1145/272991.272995>.
- 535 [148] CTEQ Collaboration, “Handbook of perturbative QCD: version 1.0,” *Rev.
536 Mod. Phys.*, vol. 67, p. 157, 1995. DOI: 10.1103/RevModPhys.67.157.
- 537 [149] J. Alwall, R. Frederix, S. Frixione, V. Hirschi, F. Maltoni, O. Mattelaer,
538 H.-S. Shao, T. Stelzer, P. Torrielli, and M. Zaro, “The automated computation
539 of tree-level and next-to-leading order differential cross sections, and their
540 matching to parton shower simulations,” *JHEP*, vol. 07, p. 079, 2014. DOI:
541 10.1007/JHEP07(2014)079. arXiv: 1405.0301 [hep-ph].
- 542 [150] P. Nason, “A new method for combining NLO QCD with shower Monte
543 Carlo algorithms,” *JHEP*, vol. 11, p. 040, 2004. DOI: 10.1088/1126-6708/
544 2004/11/040. arXiv: hep-ph/0409146 [hep-ph].
- 545 [151] S. Frixione, P. Nason, and C. Oleari, “Matching NLO QCD computations
546 with parton shower simulations: the POWHEG method,” *JHEP*, vol. 11, p. 070,
547 2007. DOI: 10.1088/1126-6708/2007/11/070. arXiv: 0709.2092 [hep-ph].
- 548 [152] S. Alioli, P. Nason, C. Oleari, and E. Re, “A general framework for im-
549 plementing NLO calculations in shower Monte Carlo programs: the POWHEG
550 BOX,” *JHEP*, vol. 06, p. 043, 2010. DOI: 10.1007/JHEP06(2010)043. arXiv:
551 1002.2581 [hep-ph].

- 552 [153] T. Gleisberg, S. Hoeche, F. Krauss, M. Schonherr, S. Schumann, F. Siegert,
553 and J. Winter, “Event generation with SHERPA 1.1,” *JHEP*, vol. 02, p. 007,
554 2009. DOI: 10.1088/1126-6708/2009/02/007. arXiv: 0811.4622 [hep-ph].
- 555 [154] J. M. Campbell, R. K. Ellis, and W. T. Giele, “A multi-threaded version of
556 MCFM,” *Eur. Phys. J. C*, vol. 75, p. 246, 2015. DOI: 10.1140/epjc/s10052-
557 015-3461-2. arXiv: 1503.06182 [physics.comp-ph].
- 558 [155] R. Boughezal, J. M. Campbell, R. K. Ellis, C. Focke, W. Giele, X. Liu, F.
559 Petriello, and C. Williams, “Color singlet production at NNLO in MCFM,”
560 *Eur. Phys. J. C*, vol. 77, p. 7, 2017. DOI: 10.1140/epjc/s10052-016-4558-y.
561 arXiv: 1605.08011 [hep-ph].
- 562 [156] G. P. Lepage, “A new algorithm for adaptive multidimensional integration,”
563 *J. Comput. Phys.*, vol. 27, p. 192, 1978. DOI: 10.1016/0021-9991(78)90004-
564 9.
- 565 [157] M. Bahr *et al.*, “Herwig++ physics and manual,” *Eur. Phys. J. C*, vol. 58,
566 p. 639, 2008. DOI: 10.1140/epjc/s10052-008-0798-9. arXiv: 0803.0883
567 [hep-ph].
- 568 [158] J. Bellm *et al.*, “Herwig 7.0/Herwig++ 3.0 release note,” *Eur. Phys. J. C*,
569 vol. 76, no. 4, p. 196, 2016. DOI: 10.1140/epjc/s10052-016-4018-8. arXiv:
570 1512.01178 [hep-ph].
- 571 [159] B. Andersson, G. Gustafson, and C. Peterson, “A semiclassical model for
572 quark jet fragmentation,” *Z. Phys. C*, vol. 1, p. 105, 1979. DOI: 10.1007/
573 BF01450386.
- 574 [160] B. Andersson, G. Gustafson, and B. Soderberg, “A general model for jet
575 fragmentation,” *Z. Phys. C*, vol. 20, p. 317, 1983. DOI: 10.1007/BF01407824.
- 576 [161] B. Andersson, S. Mohanty, and F. Soderberg, “The lund fragmentation
577 process for a multigluon string according to the area law,” *Eur. Phys. J. C*,
578 vol. 21, p. 631, 2001. DOI: 10.1007/s100520100757. arXiv: hep-ph/0106185
579 [hep-ph].
- 580 [162] Sjöstrand, T. and Skands, Peter Z., “Transverse-momentum-ordered showers
581 and interleaved multiple interactions,” *Eur. Phys. J. C*, vol. 39, p. 129, 2005.
582 DOI: 10.1140/epjc/s2004-02084-y. arXiv: hep-ph/0408302 [hep-ph].
- 583 [163] J. Alwall *et al.*, “Comparative study of various algorithms for the merging
584 of parton showers and matrix elements in hadronic collisions,” *Eur. Phys. J.*

- 585 *C*, vol. 53, p. 473, 2008. DOI: 10.1140/epjc/s10052-007-0490-5. arXiv: 586 0706.2569 [hep-ph].
- 587 [164] J. Alwall, S. de Visscher, and F. Maltoni, “QCD radiation in the production 588 of heavy colored particles at the LHC,” *JHEP*, vol. 02, p. 017, 2009. DOI: 589 10.1088/1126-6708/2009/02/017. arXiv: 0810.5350 [hep-ph].
- 590 [165] M. Rauch, “Vector-boson fusion and vector-boson scattering,” 2016. arXiv: 591 1610.08420 [hep-ph].
- 592 [166] M. L. Mangano, M. Moretti, F. Piccinini, and M. Treccani, “Matching ma- 593 trix elements and shower evolution for top-quark production in hadronic colli- 594 sions,” *JHEP*, vol. 01, p. 013, 2007. DOI: 10.1088/1126-6708/2007/01/013. 595 arXiv: hep-ph/0611129 [hep-ph].
- 596 [167] S. Catani, F. Krauss, R. Kuhn, and B. R. Webber, “QCD matrix elements 597 + parton showers,” *JHEP*, vol. 11, p. 063, 2001. DOI: 10.1088/1126-6708/ 598 2001/11/063. arXiv: hep-ph/0109231 [hep-ph].
- 599 [168] R. Frederix and S. Frixione, “Merging meets matching in MC@NLO,” *JHEP*, 600 vol. 12, p. 061, 2012. DOI: 10.1007/JHEP12(2012)061. arXiv: 1209.6215 [hep- 601 ph].
- 602 [169] Sjöstrand, T. and Skands, Peter Z., “Multiple interactions and the structure 603 of beam remnants,” *JHEP*, vol. 03, p. 053, 2004. DOI: 10.1088/1126-6708/ 604 2004/03/053. arXiv: hep-ph/0402078 [hep-ph].
- 605 [170] A. V. Manohar and W. J. Waalewijn, “A QCD analysis of double parton 606 scattering: color correlations, interference effects and evolution,” *Phys. Rev.* 607 *D*, vol. 85, p. 114009, 2012. DOI: 10.1103/PhysRevD.85.114009. arXiv: 608 1202.3794 [hep-ph].
- 609 [171] S Banerjee, “CMS simulation software,” *Journal of Physics: Conference Se- 610 ries*, vol. 396, p. 022003, 2012. %7Bhttp://stacks.iop.org/1742-6596/ 611 396/i=2/a=022003%7D.
- 612 [172] M Hildreth and V N Ivanchenko and D J Lange and M J Kortelainen, “CMS 613 full simulation for run-2,” *Journal of Physics: Conference Series*, vol. 664, 614 p. 072022, 2015. %7Bhttp://stacks.iop.org/1742-6596/664/i=7/a= 615 072022%7D.

- 616 [173] S. Alioli, P. Nason, C. Oleari, and E. Re, “NLO vector-boson production
617 matched with shower in POWHEG,” *JHEP*, vol. 07, p. 060, 2008. DOI: 10 .
618 1088/1126-6708/2008/07/060. arXiv: 0805.4802 [hep-ph].
- 619 [174] J. M. Campbell and R. K. Ellis, “MCFM for the Tevatron and the LHC,”
620 *Nucl. Phys. Proc. Suppl.*, vol. 205, p. 10, 2010. DOI: 10.1016/j.nuclphysbps.
621 2010.08.011. arXiv: 1007.3492 [hep-ph].
- 622 [175] A. Ballestrero, A. Belhouari, G. Bevilacqua, V. Kashkan, and E. Maina,
623 “PHANTOM : a Monte Carlo event generator for six parton final states at
624 high energy colliders,” *Comput. Phys. Commun.*, vol. 180, p. 401, 2009. DOI:
625 10.1016/j.cpc.2008.10.005. arXiv: 0801.3359 [hep-ph].
- 626 [176] NNPDF Collaboration, “Parton distributions for the LHC Run II,” *JHEP*,
627 vol. 04, p. 040, 2015. DOI: 10.1007/JHEP04(2015)040. arXiv: 1410.8849
628 [hep-ph].
- 629 [177] CMS Collaboration, “Event generator tunes obtained from underlying event
630 and multiparton scattering measurements,” *Eur. Phys. J. C*, vol. 76, p. 155,
631 2016. DOI: 10.1140/epjc/s10052-016-3988-x. arXiv: 1512.00815 [hep-ex].
- 632 [178] GEANT4 Collaboration, “GEANT4: a simulation toolkit,” *Nucl. Instrum.
633 Meth. A*, vol. 506, p. 250, 2003. DOI: 10.1016/S0168-9002(03)01368-8.
- 634 [179] R. Frühwirth, “Application of Kalman filtering to track and vertex fitting,”
635 *Nucl. Instrum. Meth. A*, vol. 262, p. 444, 1987. DOI: 10.1016/0168-9002(87)
636 90887-4.
- 637 [180] P. Billoir and S. Qian, “Simultaneous pattern recognition and track fitting
638 by the Kalman filtering method,” *Nucl. Instrum. Meth. A*, vol. 294, p. 219,
639 1990. DOI: 10.1016/0168-9002(90)91835-Y.
- 640 [181] W. Adam, B. Mangano, T. Speer, and T. Todorov, “Track reconstruction in
641 the CMS tracker,” 2005.
- 642 [182] CMS Collaboration, “Description and performance of track and primary-
643 vertex reconstruction with the CMS tracker,” *JINST*, vol. 9, no. 10, P10009,
644 2014. DOI: 10.1088/1748-0221/9/10/P10009. arXiv: 1405.6569 [physics.ins-
645 det].
- 646 [183] W. Adam, R. Frühwirth, A. Strandlie, and T. Todor, “Reconstruction of
647 electrons with the Gaussian-sum filter in the CMS tracker at the LHC,” 2005.

- 648 [184] T. Speer, K. Prokofiev, R. Fruhwirth, W. Waltenberger, and P. Vanlaer,
649 “Vertex fitting in the CMS tracker,” 2006.
- 650 [185] K. Rose, “Deterministic annealing for clustering, compression, classification,
651 regression, and related optimization problems,” *Proceedings of the IEEE*, vol.
652 86, no. 11, p. 2210, Nov. 1998, ISSN: 0018-9219. DOI: 10.1109/5.726788.
- 653 [186] CMS Collaboration, “Particle-flow event reconstruction in CMS and perfor-
654 mance for jets, taus, and MET,” CERN, Geneva, Tech. Rep. CMS-PAS-PFT-
655 09-001, Apr. 2009. <https://cds.cern.ch/record/1194487>.
- 656 [187] CMS Collaboration, “Commissioning of the particle-flow event reconstruction
657 with the first LHC collisions recorded in the CMS detector,” Tech. Rep. CMS-
658 PAS-PFT-10-001, 2010. <https://cds.cern.ch/record/1247373>.
- 659 [188] CMS Collaboration, “Particle-flow reconstruction and global event descrip-
660 tion with the CMS detector,” 2017, Accepted by *JINST*. arXiv: 1706.04965
661 [physics.ins-det].
- 662 [189] CMS Collaboration, “Performance of CMS muon reconstruction in pp colli-
663 sion events at $\sqrt{s} = 7 \text{ TeV}$,” *JINST*, vol. 7, P10002, 2012. DOI: 10.1088/1748-
664 0221/7/10/P10002. arXiv: 1206.4071 [physics.ins-det].
- 665 [190] S. Baffioni, C. Charlot, F. Ferri, D. Futyan, P. Meridiani, I. Puljak, C. Rovelli,
666 R. Salerno, and Y. Sirois, “Electron reconstruction in CMS,” *Eur. Phys. J. C*,
667 vol. 49, p. 1099, 2007. DOI: 10.1140/epjc/s10052-006-0175-5.
- 668 [191] CMS Collaboration, “Performance of photon reconstruction and identifi-
669 cation with the CMS detector in proton-proton collisions at $\sqrt{s} = 8 \text{ TeV}$,”
670 *JINST*, vol. 10, no. 08, P08010, 2015. DOI: 10.1088/1748-0221/10/08/
671 P08010. arXiv: 1502.02702 [physics.ins-det].
- 672 [192] G. P. Salam and G. Soyez, “A practical seedless infrared-safe cone jet algo-
673 rithm,” *JHEP*, vol. 05, p. 086, 2007. DOI: 10.1088/1126-6708/2007/05/086.
674 arXiv: 0704.0292 [hep-ph].
- 675 [193] G. P. Salam, “Towards jetography,” *Eur. Phys. J. C*, vol. 67, p. 637, 2010.
676 DOI: 10.1140/epjc/s10052-010-1314-6. arXiv: 0906.1833 [hep-ph].
- 677 [194] M. Cacciari, G. P. Salam, and G. Soyez, “The anti- k_T jet clustering algo-
678 rithm,” *JHEP*, vol. 04, p. 063, 2008. DOI: 10.1088/1126-6708/2008/04/063.
679 arXiv: 0802.1189 [hep-ph].

- 680 [195] M. Cacciari, G. P. Salam, and G. Soyez, “FastJet user manual,” *Eur. Phys. J. C*, vol. 72, p. 1896, 2012. DOI: 10.1140/epjc/s10052-012-1896-2. arXiv: 1111.6097 [hep-ph].
- 683 [196] CMS Collaboration, “Study of pileup removal algorithms for jets,” 2014.
- 684 [197] CMS Collaboration, “Jet energy scale and resolution in the CMS experiment
685 in pp collisions at 8 TeV,” *JINST*, vol. 12, no. 02, P02014, 2017. DOI: 10.1088/
686 1748-0221/12/02/P02014. arXiv: 1607.03663 [hep-ex].
- 687 [198] M. Cacciari, G. P. Salam, and G. Soyez, “The catchment area of jets,”
688 *JHEP*, vol. 04, p. 005, 2008. DOI: 10.1088/1126-6708/2008/04/005. arXiv:
689 0802.1188 [hep-ph].
- 690 [199] M. Cacciari and G. P. Salam, “Pileup subtraction using jet areas,” *Phys. Lett. B*, vol. 659, p. 119, 2008. DOI: 10.1016/j.physletb.2007.09.077.
691 arXiv: 0707.1378 [hep-ph].
- 693 [200] CMS Collaboration, “Determination of jet energy calibration and transverse
694 momentum resolution in CMS,” *JINST*, vol. 6, P11002, 2011. DOI: 10.1088/
695 1748-0221/6/11/P11002. arXiv: 1107.4277 [physics.ins-det].
- 696 [201] CMS Collaboration, “Missing transverse energy performance of the CMS
697 detector,” *JINST*, vol. 6, P09001, 2011. DOI: 10.1088/1748-0221/6/09/
698 P09001. arXiv: 1106.5048 [physics.ins-det].
- 699 [202] CMS Collaboration, “Performance of the CMS missing transverse momen-
700 tum reconstruction in pp data at $\sqrt{s} = 8 \text{ TeV}$,” *JINST*, vol. 10, no. 02,
701 P02006, 2015. DOI: 10.1088/1748-0221/10/02/P02006. arXiv: 1411.0511
702 [physics.ins-det].
- 703 [203] CMS Collaboration, “Performance of missing energy reconstruction in 13 TeV
704 pp collision data using the CMS detector,” CERN, Geneva, Tech. Rep. CMS-
705 PAS-JME-16-004, 2016. <http://cds.cern.ch/record/2205284>.
- 706 [204] CMS Collaboration, “Electron reconstruction and identification at $\sqrt{s} =$
707 7 TeV ,” CERN, Geneva, Tech. Rep. CMS-PAS-EGM-10-004, 2010. <https://cds.cern.ch/record/1299116>.
- 709 [205] CMS Collaboration, “Performance of electron reconstruction and selection
710 with the CMS detector in proton-proton collisions at $\sqrt{s} = 8 \text{ TeV}$,” *JINST*,
711 vol. 10, no. 06, P06005, 2015. DOI: 10.1088/1748-0221/10/06/P06005.
712 arXiv: 1502.02701 [physics.ins-det].

- 713 [206] CMS Collaboration, “Measurement of the inclusive W and Z production
714 cross sections in pp collisions at $\sqrt{s} = 7 \text{ TeV}$,” *JHEP*, vol. 10, p. 132, 2011.
715 DOI: 10.1007/JHEP10(2011)132. arXiv: 1107.4789 [hep-ex].
- 716 [207] CMS Collaboration, “Measurement of the properties of a Higgs boson in the
717 four-lepton final state,” *Phys. Rev. D*, vol. 89, no. 9, p. 092007, 2014. DOI:
718 10.1103/PhysRevD.89.092007. arXiv: 1312.5353 [hep-ex].
- 719 [208] J. Butterworth *et al.*, “PDF4LHC recommendations for LHC Run II,” *J. Phys. G*, vol. 43, p. 023001, 2016. DOI: 10.1088/0954-3899/43/2/023001.
720 arXiv: 1510.03865 [hep-ph].
- 722 [209] G. Bohm and G. Zech, *Introduction to statistics and data analysis for physi-
723 cists*. DESY, 2010, ISBN: 9783935702416. <https://books.google.ch/books?id=aQBHcgAACAAJ>.
- 725 [210] G. D’Agostini, “A multidimensional unfolding method based on Bayes’ the-
726 oreom,” *Nucl. Instrum. Meth. A*, vol. 362, p. 487, 1995. DOI: 10.1016/0168-
727 9002(95)00274-X.
- 728 [211] A. P. Dempster, N. M. Laird, and D. B. Rubin, “Maximum likelihood from
729 incomplete data via the EM algorithm,” *J. R. Stat. Soc. B*, vol. 39, p. 1, 1977,
730 ISSN: 00359246. <http://www.jstor.org/stable/2984875>.
- 731 [212] L. B. Lucy, “An iterative technique for the rectification of observed distri-
732 butions,” *Astron. J.*, vol. 79, p. 745, Jun. 1974. DOI: 10.1086/111605.
- 733 [213] W. H. Richardson, “Bayesian-based iterative method of image restoration,”
734 *J. Opt. Soc. Am.*, vol. 62, p. 55, Jan. 1972. DOI: 10.1364/JOSA.62.000055.
735 <http://www.osapublishing.org/abstract.cfm?URI=josa-62-1-55>.
- 736 [214] L. A. Shepp and Y. Vardi, “Maximum likelihood reconstruction for emission
737 tomography,” *IEEE Transactions on Medical Imaging*, vol. 1, no. 2, p. 113,
738 Oct. 1982, ISSN: 0278-0062. DOI: 10.1109/TMI.1982.4307558.
- 739 [215] T. Adye, “Unfolding algorithms and tests using RooUnfold,” in *Proceedings,
740 PHYSTAT 2011 Workshop on Statistical Issues Related to Discovery Claims
741 in Search Experiments and Unfolding*, CERN, Geneva, Switzerland 17–20 Jan-
742 uary 2011, CERN, Geneva: CERN, 2011, p. 313. DOI: 10.5170/CERN-2011-
743 006.313. arXiv: 1105.1160 [physics.data-an]. <https://inspirehep.net/record/898599/files/arXiv:1105.1160.pdf>.

- 745 [216] Y. Vardi, “Empirical distributions in selection bias models,” *Ann. Statist.*,
746 vol. 13, p. 178, Mar. 1985. DOI: 10.1214/aos/1176346585. <http://dx.doi.org/10.1214/aos/1176346585>.
- 748 [217] F. Pedregosa, G. Varoquaux, A. Gramfort, V. Michel, B. Thirion, O. Grisel,
749 M. Blondel, P. Prettenhofer, R. Weiss, V. Dubourg, J. Vanderplas, A. Pas-
750 soss, D. Cournapeau, M. Brucher, M. Perrot, and E. Duchesnay, “Scikit-learn:
751 Machine learning in Python,” *J. Mach. Learn. Res.*, vol. 12, p. 2825, 2011.
- 752 [218] CMS Collaboration Collaboration, “Performance of quark/gluon discrimina-
753 tion in 8 TeV pp data,” CERN, Geneva, Tech. Rep. CMS-PAS-JME-13-002,
754 2013. <https://cds.cern.ch/record/1599732>.
- 755 [219] G. Cowan, K. Cranmer, E. Gross, and O. Vitells, “Asymptotic formulae for
756 likelihood-based tests of new physics,” *Eur. Phys. J. C*, vol. 71, p. 1554, 2011,
757 [Erratum: DOI: 10.1140/epjc/s10052-013-2501-z]. DOI: 10.1140/epjc/
758 s10052-011-1554-0. arXiv: 1007.1727 [physics.data-an].
- 759 [220] CMS Collaboration and ATLAS Collaboration, “Combination of results from
760 the ATLAS and CMS experiments on anomalous triple gauge couplings in ZZ
761 production from pp collisions at a centre-of-mass energy of 7 TeV at the LHC,”
762 CERN, Geneva, Tech. Rep. CMS-PAS-SMP-15-001. ATLAS-CONF-2016-036,
763 2016. <https://cds.cern.ch/record/2202807>.
- 764 [221] CMS Collaboration, “Measurement of the ZZ production cross section in
765 $\ell\ell\ell'\ell'$ decays in pp collisions at $\sqrt{s} = 13$ TeV,” 2015. <https://cds.cern.ch/record/2114822>.
- 767 [222] CMS Collaboration, “Measurement of the ZZ production cross section and
768 $Z \rightarrow \ell^+\ell^-\ell'^+\ell'^-$ branching fraction in pp collisions at $\sqrt{s} = 13$ TeV,” *Phys.*
769 *Lett. B*, vol. 763, p. 280, 2016. DOI: 10.1016/j.physletb.2016.10.054.
770 arXiv: 1607.08834 [hep-ex].
- 771 [223] CMS Collaboration, “Measurements of differential cross sections and search
772 for the electroweak production of two Z bosons produced in association with
773 jets,” 2017. <https://cds.cern.ch/record/2264556>.
- 774 [224] CMS Collaboration, “Measurement of vector boson scattering and constraints
775 on anomalous quartic couplings from events with four leptons and two jets in
776 proton-proton collisions at $\sqrt{s} = 13$ TeV,” 2017, Submitted to *Phys. Lett. B*.
777 arXiv: 1708.02812 [hep-ex].

- 778 [225] CMS Collaboration, “Studies of Higgs boson production in the four-lepton
779 final state at $\sqrt{s} = 13 \text{ TeV}$,” 2016. <https://cds.cern.ch/record/2139978>.
- 780 [226] CMS Collaboration, “Measurements of properties of the Higgs boson and
781 search for an additional resonance in the four-lepton final state at $\sqrt{s} =$
782 13 TeV ,” 2016. <https://cds.cern.ch/record/2204926>.
- 783 [227] CMS Collaboration, “Measurements of properties of the Higgs boson decay-
784 ing into the four-lepton final state in pp collisions at $\sqrt{s} = 13 \text{ TeV}$,” 2017,
785 Submitted to *JHEP*. arXiv: 1706.09936 [hep-ex].
- 786 [228] R. Gavin, Y. Li, F. Petriello, and S. Quackenbush, “FEWZ 2.0: a code
787 for hadronic Z production at next-to-next-to-leading order,” *Comput. Phys.*
788 *Commun.*, vol. 182, p. 2388, 2011. DOI: 10.1016/j.cpc.2011.06.008. arXiv:
789 1011.3540 [hep-ph].
- 790 [229] ATLAS Collaboration, “ $ZZ \rightarrow \ell^+ \ell^- \ell'^+ \ell'^-$ cross-section measurements and
791 aTGC search in 13 TeV pp collisions with the ATLAS detector,” 2017. <http://cds.cern.ch/record/2263045>.
- 793 [230] K. Arnold *et al.*, “VBFNLO: a parton level Monte Carlo for processes with
794 electroweak bosons,” *Comput. Phys. Commun.*, vol. 180, pp. 1661–1670, 2009.
795 DOI: 10.1016/j.cpc.2009.03.006. arXiv: 0811.4559 [hep-ph].